Chirality Transfer from Chiral Solutes and Surfaces to Achiral Solvents: Insights from Molecular Dynamics Studies

by

Shihao Wang

A thesis submitted to the Department of Chemistry

in conformity with the requirements for

the degree of Doctor of Philosophy

Queen's University

Kingston, Ontario, Canada

(September, 2009)

Abstract

Chirality can be induced in achiral solvent molecules located near a chiral molecule or surface, but there have been very few systematic studies in this field either experimentally or theoretically. The focus of this thesis is to study the chirality transfer from chiral molecules to achiral solvents.

To capture the chirality transfer in solvent molecules, a solvent model that is sensitive to the changes in the environment is needed. We developed new polarizable and flexible models based on an extensive series of *ab initio* calculations and molecular dynamics simulations. The models include electric field dependence in both the atomic charges and the intramolecular degrees of freedom. Modified equations of motion are required and we have implemented a multiple time step algorithm to solve these equations. Our methodology is general and has been applied to ethanol as a test. For other solvents in our simulations, such as 2-propanol, limited models are used.

The chirality transfer from chiral solutes to achiral solvents and its dependence on the solute and solvent characteristics are then explored using the new polarizable models in molecular dynamics simulations. The chirality induced in the solvent is assessed based on a series of related chirality indexes originally proposed by Osipov[Osipov *et al*., Mol. Phys.**84**, 1193(1995)]. Two solvents are considered: Ethanol and benzyl alcohol. The solvation of three chiral solutes is examined: Styrene oxide, acenaphthenol, and *n*-(1-(4-bromophenyl)ethyl)pivalamide (PAMD). All three solutes have the possibility of hydrogen-bonding with the solvent, the last two may also form π-π interactions, and the last has multiple hydrogen bonding sites.

The chirality transfer from chiral surfaces to achiral solvents is also explored. Emphasis is placed on the extent of this chirality transfer and its dependence on the surface and solvent characteristics is explored. Three surfaces employed in chiral chromatography are examined: The Whelk-O1 interface; a phenylglycine-derived chiral stationary phase (CSP); and a leucine-derived CSP. The solvents consist of ethanol, a binary *n*-hexane/ethanol solvent, 2-propanol, and a binary *n*-hexane/2-propanol solvent. Molecular dynamics simulations of the solvated chiral interfaces form the basis of the analysis and position dependent chirality indexes are analyzed in detail.

Acknowledgements

First, I would like to thank my supervisor, Dr. Natalie Cann, for providing me with excellent advice throughout my graduate work. Without her help, this thesis and the work within would never have been completed. I would also like to thank Dr. Gang Wu, and Dr. Derek Pratt, for their guidance at my supervisory committee meetings. Many thanks to all members of the Cann group: Dr. Sorin Nita, Dr. Chunfeng Zhao, Rodica Pecheanu, and Mohammad Ashtari, for providing a great working environment.

I would like to thank all my friends for the support and encouragement I received outside of Chernoff Hall. I am also grateful to my parents, who have always been there when I needed them. A special thanks to my fiancée, Fang Gao, for her love, support and understanding.

The last but not the least, financial support from NSERC, Queen's University, and HPCVL scholarships, and computing facilities on SHARCNET, WESTGRID and HPCVL are gratefully acknowledged.

Statement of Originality

I hereby certify that all of the work described within this thesis is the original work of the author under the supervision of Professor Natalie Cann. Any published (or unpublished) ideas and/or techniques from the work of others are fully acknowledged in accordance with the standard referencing practices.

Shihao Wang

September, 2009

Table of Contents

Abstract ii

Acknowledgements iv

Statement of Originality v

Table of Contents vi

List of Tables xi

List of Figures xii

List of Abbreviations xv

Chapter 1 Introduction 1

1.1 Introduction to chirality 1

1.2 Studies on chirality transfer 3

1.3 Polarizable models 7

1.4 Measuring chirality 11

1.5 Thesis organization 15

Chapter 2 Theoretical Methods and Models 16

2.1 Molecular dynamics simulations 16

2.1.1 Potentials 17

2.1.2 Periodic Boundary Conditions 23

2.1.3 Ewald summation 25

2.2 Polarizable Models 29

2.2.1 Fluctuating Charge Model 29

2.2.2 Fluctuating Charge and INTRAmolecular potential model 32

2.3 Equations of motion 37

2.3.1 Verlet Algorithms 37

2.3.2 Nosé-Hoover Thermostat 39

2.4 Reversible Multiple Time Step MD 42

2.5 Quantum Mechanics Methods 48

2.5.1 *Ab initio* calculations 48

2.5.2 Density function theory 49

2.5.3 Basis sets 51

2.5.4 Atomic charges 53

2.5.5 Conformational Minimization 54

2.6 Chirality indexes 55

2.7 Surface representations 58

2.8 Practical considerations 62

Chapter 3 Development of a polarizable and flexible model 64

3.1 Introduction 64

3.2. Methods 67

3.2.1 Assessment of typical electric fields in bulk ethanol 69

3.2.2 *Ab initio* calculations for molecular response 70

3.2.3 Fluctuating Charge Model 74

3.2.4 Lennard-Jones potentials 77

3.2.5 Intramolecular potentials 77

3.2.6 Simulation details 86

3.3. Results and discussion 93

3.3.1 Bulk ethanol 93

3.3.2 Hydrogen bonding 100

3.4. Conclusions 102

Chapter 4 Chirality transfer: The impact of a chiral solute on an achiral solvent 105

4.1. Introduction 105

4.2. Methods 108

4.2.1 Solvent and solute models 108

4.2.2 The assessment of chirality 113

4.2.3. Simulation details 118

4.2.4 Convergence of the chirality transfer 120

4.3. Results and discussion 125

4.3.1 Analyte solvation 125

4.3.2 The solvent representation: Is polarizability important? 129

4.3.3 Chirality transfer and conformational averaging. 132

4.3.4 Contact points and chirality transfer. 138

4.4. Conclusions 144

Chapter 5 Chirality transfer from chiral surfaces to nearby solvents 146

5.1. Introduction 146

5.2. Methods 149

5.2.1 Surface representations 149

5.2.2 Models 149

5.2.3 Chirality indexes 151

5.2.4 Simulation details 155

5.3. Results and discussion 157

5.3.1 Solvation of Chiral Stationary Phases 158

5.3.2 Chirality transfer at interfaces 165

5.3.3 Comparisons between selectors: Conformational chirality 168

5.3.4 Comparisons between selectors: Solvent polarization 175

5.3.5 Comparison of different solvents 179

5.4. Conclusions 182

Chapter 6 Conclusions 184

Bibliography 189

APPENDIX A Evaluation of charge fluctuation parameters $\tilde{\chi}_i^0$ and ζ_i 200

APPENDIX B Evaluation of forces 205

APPENDIX C Details of the potentials for 2-propanol 212

List of Tables

Table 3.1. Average error in the dipole moment, relative to MP2/aug-cc-pVTZ reference calculations (see Eq. [3.2]), for ethanol in 16 electric fields. 73

Table 3.2. Charge fluctuation parameters (see Eq. [2.25]) and Lennard-Jones parameters for the polarizable, flexible fCINTRA ethanol model. 75

Table 3.3. The zero-field bond stretching constants and the field dependence of the equilibrium bond lengths (see Eq. [2.31]) extracted from B3LYP/6-311++G(d,p) calculations of ethanol. 79

Table 3.4. The zero-field angle bending force constant and the field dependence of the equilibrium bond angles (see Eq. [2.32]) extracted from B3LYP/6-311++G(d,p) calculations of ethanol. 82

Table 3.5. Field dependence of the torsional coefficients for rotation about the C(3)-O(2) bond in ethanol (see Eq. [2.33]). 84

Table 3.6. Properties of bulk ethanol as predicted from the polarizable, flexible fCINTRA model are compared with experiment..... 95

Table 3.7. Hydrogen bond statistics evaluated from snapshots of the simulation cell.. 101

Table 4.1. Intramolecular potential parameters for benzyl alcohol..... 110

Table 4.2. Charge fluctuation parameters (see Eq. [2.26]) and zero-field charges for benzyl alcohol. 112

Table 4.3. An analysis of solvent hydrogen-bonding and the average chirality of the solutes. 128

Table 4.4. Average excess chirality for solvent around chiral solute. 136

Table 4.5. Average excess chirality for solvent hydrogen bonded to the chiral solute. 137

Table 5.1. Hydrogen bonding statistics for Whelk-O1, DNB-phenylglycine and DNB-leucine selectors in pure ethanol, pure 2-propanol, 80/20 *n*-hexane/2-propanol, and 80/20 *n*-hexane/ethanol 159

List of Figures

Figure 1.1. Chiral molecules are not super imposable with their mirror images. 1

Figure 1.2. Representation of chiral "zones". The left and right panels illustrate the chiral zone idea around a chiral solute and between chiral surfaces, respectively. 4

Figure 1.3. The Hausdorff Distance. 13

Figure 2.1. Examples of intramolecular degrees of freedom. 18

Figure 2.2. Comparison of Morse potential and harmonic potential for bond stretching. 19

Figure 2.3. Lennard-Jones potential. 22

Figure 2.4. 2-dimensional periodic boundary condition system. 24

Figure 2.5. Discontinuity at the distance of the cut-off radius 24

Figure 2.6. The charge distribution in the Ewald summation. 26

Figure 2.7. Comparison of the Coulomb overlap (solid line) evaluated from Eq. [2.27] with $\frac{1}{r_{ij}}$ (dotted line) and the approximate form in Eq. [2.29] (dashed line). 31

Figure 2.8. The ethanol molecule showing the atom numbering used throughout this thesis. 36

Figure 2.9. The influence of torsional angles on chirality indexes of ethanol. 60

Figure 2.10. Molecular structures and numbering system for (a) Whelk-O1, (b) DNB-leucine, (c) DNB-phenylglycine. 61

Figure 3.1. Flow chart showing the seven steps involved in the design of the polarizable flexible ethanol model 68

Figure 3.2. Statistics on the electric fields collected during the MD simulation using the flexible, non-polarizable Chen *et al*.[134] model of ethanol. 71

Figure 3.3. The impact of the representation of the interatomic Coulomb interaction, $J_{ij}(r_{ij})$. 76

Figure 3.4. The torsional potential, $U^{tor}(\vec{E})$, between H(1)-O(2)-C(3)-C(4) as a function of the dihedral angle. 83

Figure 3.5. The torsional potential, $U^{tor}(\vec{E})$, between O(2)-C(3)-C(4)-H(5) as a function of the dihedral angle. 85

Figure 3.6. The impact of charge "mass" on the diffusion coefficient and radial distribution functions obtained from 20 ps simulations. 89

Figure 3.7. The energy components and the conserved quantity H_{NH} as a function of time. 90

Figure 3.8. The impact of damping on the range of parameter values allowed in the simulation. 92

Figure 3.9. A comparison of radial distributions in bulk ethanol obtained from experiment, a non-polarizable model, and the fCINTRA polarizable model. 94

Figure 3.10. Snapshots of bulk ethanol from the fCINTRA polarizable, flexible model. 101

Figure 4.1. The B3LYP/6-311++G(d,p) optimized structures for the solutes (a-c) and the solvents (d and e). 109

Figure 4.2. The barrier to rotation about the C(3)-O(2) bond of R-acenaphthenol as evaluated from B3LYP/6-31G(d) calculations 113

Figure 4.3. The influence of torsional angles on chirality indexes of benzyl alcohol .. 115

Figure 4.4. The coordinate system used to evaluate chirality indexes for solvent, illustrated for S-PAMD 116

Figure 4.5. Convergence tests for excess chirality 122

Figure 4.6. Structure of ethanol and benzyl alcohol in the bulk and around the solutes. 127

Figure 4.7. The impact of solvent polarizability on chirality transfer: The angle-dependence of $< G_{0S}^{q} >_{\theta,\varphi}$ for ethanol hydrogen-bonded to the oxygen of S-PAMD. ... 131

Figure 4.8. The impact of solute flexibility on chirality transfer. 134

Figure 4.9. Impact of solutes on chirality transferred into hydrogen-bonding ethanol. $< G_{0S}^{q} >_{\theta,\varphi}$ chiral indexes are shown along with illustrative snapshots. 141

Figure 4.10. Impact of solutes on chirality transferred into hydrogen-bonding benzyl alcohol..... 142

Figure 5.1. The influence of torsional angles on chirality indexes of 2-propanol. 153

Figure 5.2. The cylindrical coordinate system used in the spatial breakdown of excess chirality, average atomic charges, and average solvent dipole. 155

Figure 5.3. 2D solvent-selector distributions for potential H-bonding pairs at the Whelk-O1 interface. The position variables, *z* and *r*, are given in Å. 161

Figure 5.4. 2D distributions from 2-propanol/*n*-hexane solvated DNB-phenylglycine and DNB-leucine interfaces..... 164

Figure 5.5. An illustration of the convergence statistics for excess chirality.. 166

Figure 5.6. 2D distributions of average chirality indexes from the 2-propanol/*n*-hexane solvated DNB-leucine interface..... 169

Figure 5.7. 2D distributions of average chirality indexes from the 2-propanol/*n*-hexane solvated DNB-phenylglycine interface. 173

Figure 5.8. 2D distributions of average chirality indexes from the 2-propanol/*n*-hexane solvated Whelk-O1 interface. 174

Figure 5.9. Polarization of 2-propanol at the 2-propanol/*n*-hexane solvated DNB-leucine interface..... 177

Figure 5.10. 2D distributions of charges and average chirality indexes from the ethanol/*n*-hexane, ethanol, 2-propanol/*n*-hexane and 2-propanol solvated Whelk-O1 interface..... 181

List of Abbreviations

2D	2-Dimensional
3D	3-Dimensional
AO	Atomic Orbital
CD	Circular Dichroism
CGTF	Contracted Gaussian-Type Function
CHARMM	Chemistry at HARvard Molecular Mechanics
CHELPG	Charges from Electrostatic Potentials using a Grid based method
CI	Configuration Interaction
CI95	95% Confidence Interval
CN	Coordination Numbers
CSP	Chiral Stationary Phase
DFT	Density Functional Theory
DNB	Dinitrobenzoyl
FC	Fluctuating Charge
fCINTRA	Fluctuating Charge and INTRAmolecular potential
FDA	Food and Drug Administration
GTF	Gaussian-Type Function
HPLC	High-Performance Liquid Chromatography
LJ	Lennard-Jones
MC	Monte Carlo
MD	Molecular Dynamics
MEP	Molecular Electrostatic Potential

MP2	2^{nd} order Moller-Plesset perturbation theory
MPI	Message-Passing Interface
OPLS	Optimized Potential for Liquid Simulations
ORD	Optical Rotatory Dispersion
PAMD	*n*-(1-(4-bromophenyl)ethyl)pivalamide
PBC	Periodic Boundary Conditions
PIPF	Polarizable Intermolecular Potential Function
PP	Peak Position
PPC	Polarizable Point-Charge
RU	Rigid Unit
STO	Slater Type Orbital
UA	United Atom
VCD	Vibrational Circular Dichroism

Chapter 1
Introduction

1.1 Introduction to chirality

The definition of chirality was first stated in Kelvin's Baltimore Lectures on Molecular Dynamics and the Wave Theory of Light in 1904: "I call any geometrical figure, or group of points, chiral, and say it has chirality, if its image in a plane mirror, ideally realized, cannot be brought to coincide with itself" [1]. Chiral molecules don't have mirror planes, centers of inversion, or rotation-reflection axes [2].

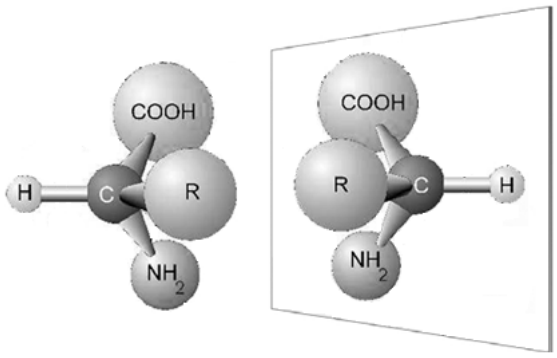

Figure 1.1. Chiral molecules are not super imposable with their mirror images.

Chiral molecules can be found everywhere: in drugs, in agriculture, in electronics, in foods and beverages. Mirror-image chiral molecules are referred to as enantiomers, and two enantiomers are shown in Fig. 1.1. They have the same connectivity and most of the same physical properties, but they have different biological properties. For example, carvone is an important constituent in many plant oils [3]. Its R-isomer has a strong spearmint odor and is essential in oil of mint, while the S-isomer is found in caraway oil

and has a different odor [4]. Similarly, lemon and orange peels both contain limonene. The S-enantiomer and R-enantiomer are found in lemon and orange peels, respectively, and they have different odors [4]. These enantiomers have different scents because of the different interactions between these molecules and our olfactory chiral receptors [5]. In a more extreme case, thalidomide, which was a sedative drug in the late 1950s, caused a tragedy because one enantiomer helped against nausea, while the other caused fetal damage [6]. In 1992, the United States Food and Drug Administration (FDA) released a new policy on chiral drugs, stating that all new drugs would need to be characterized pharmacologically and toxicologically if they are to be marketed as racemic mixtures [7]. As a result of this new policy, the demand for chemical processes that can selectively produce chiral molecules has greatly increased. In 1985, most chiral medicines were sold as racemic mixtures [8]. In 1999, single-isomer chiral drugs accounted for only 32% of the $360 billion pharmaceutical sales [9]. In 2006, in contrast, 75% of new drugs approved by the FDA were single enantiomers [10].

The separation of chiral molecules is often difficult. Chiral pool and chiral resolution are the most widely applied methods in industry [11]. The chiral pool consists of naturally occurring chiral molecules that are enantiomerically pure, such as amino acids, carbohydrates, hydroxy acids, alkaloids and terpenes. It is a very effective way of introducing asymmetry into synthesis and keeping the chirality intact. In the early 1990s, chiral pool materials were used to derive most of the chiral drugs [10]. However, chiral pool synthesis relies heavily on catalysis, which makes it very time consuming, unpredictable and costly [10].

Chromatographic techniques for separation of enantiomers have been developing quickly in the past years. The chromatographic separation of enantiomers can be achieved by various methods, but chiral discriminators or selectors are always needed. There are two types of selectors that can be used: Chiral mobile phase additives and chiral stationary phases (CSP) [12]. In the first case, enantioselective retention is caused by the differences in adsorption properties of the formed diastereomeric complexes to an achiral stationary phase [13, 14]. The chiral selection by CSP is due to differences in the two stereo isomeric complexes that are formed between the enantiomers and the selector [15].

1.2 Studies on chirality transfer

When an achiral solvent molecule is placed near a chiral molecule or surface, its environment becomes chiral and it may respond to the environment in an asymmetric way. In that case, chirality is transferred from the chiral molecule to nearby achiral solvent. This chirality transfer may occur in a zone near the chiral molecule and this defines a "chiral zone", as shown in Fig. 1.2. The size and character of the chiral zone will be critical to understanding chemical reactions involving chiral molecules, the mechanism of chiral chromatography and the results of chiral spectroscopy.

Chirality transfer in liquid crystals has been studied in detail and some chiral dopants are well-known to induce macroscopic chirality in mesogenic hosts [16-22]. Experimental results suggest that the solute influences solvents by polar ordering of the solvent medium and steric hindrance [20]. For example, Lemieux[22] studied the chiral

induction in a smectic liquid crystal phase when doped with molecules with atropisomeric biphenyl cores. It was found that the chirality transferred from chiral dopants heavily depended on the core structure of the liquid crystal host and the mechanism of the chirality transfer was explained by the concepts of host-guest chemistry. Most of the current theoretical studies of this chirality transfer focus on the correlation of solute properties with the experimentally measured helical twisting power[23].

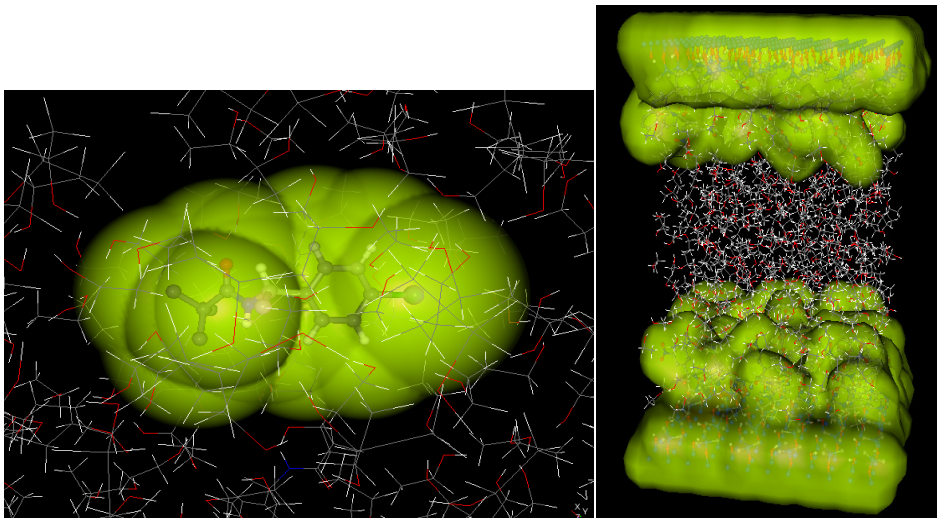

Figure 1.2. Representation of chiral "zones". The left and right panels illustrate the chiral zone idea around a chiral solute and between chiral surfaces, respectively.

Compared to studies of chirality transfer in liquid crystals, isotropic phases are relatively unexplored. However, it is known that solvent effects can greatly influence spectroscopy, such as optical rotatory dispersion (ORD). Solvents can influence the structures of solutes and indirectly affect the spectroscopy. For instance, Kumata *et al.*[24] measured ORD spectra for S-methyloxirane, which is a small and relatively rigid

molecule with a three-membered ring, and observed a significant difference between its optical rotation in water and in benzene. Fischer *et al*.[25] measured the optical rotation of (S)-methylbenzylamine in a wide range of solvents with various concentrations, and very large variations were observed. After comparing the experimental and calculated results, they concluded that hydrogen bonding has large contributions on specific rotation.

Recently, experimental and theoretical studies have begun to focus on the chirality induced in achiral solvent when it surrounds a chiral solute. Yashima *et al*.[26] mentioned, in an NMR study, that the two methyl groups in 2-propanol were not equivalent when they were in the proximity of cellulose tris(4-trimethylsilylphenylcarbamate). Jennings[27] has reviewed the effect of chiral lanthanide shift reagents, such as the tris[3-trifluoromethylhydroxymethylene-d-camphorato]europium(III), on achiral solvents where the appearance of chemical shift nonequivalence was observed in methyl groups of 2-propanol, 2-propylamine and 2-methyl-2-butanol, and the methylene protons in 2,2-dimethylpropanol and 2-methyl-2-butanol. In a recent vibrational circular dichroism(VCD) study, Losada *et al.*[28] found evidence for chirality transfer from methyl lactate to hydrogen-bonded water. It was found that the H–O–H bending modes of the achiral water molecules that are H-bonded to a methyl lactate molecule gave rise to a strong VCD peak. This was further supported by a series of density functional theory (DFT) calculations of methyl lactate-$(H_2O)_n$ complexes and it was concluded that the transfer involved one primary solvent molecule. In contrast, Mukhopadhyay *et al.*[29, 30] suggested that solvent imprinting was a major component of the ORD of methyloxirane in benzene and water. The authors used Monte Carlo (MC) simulations combined with DFT methods and explicit solvent models and

found that the chiral distribution of the solvent molecules exceeded the contribution of the solute itself. They also mentioned that an explicit solvent model was essential in describing the chiroptical properties of molecules in solution. Fidler *et al*.[31] used MD simulations to study the distribution of simple achiral solvent molecules surrounding a chiral solute, and found that achiral solvents can contribute 10-20% of the circular dichroism (CD) intensity. This implies that chirality has been induced in the solvation shell. It was also found that the magnitude of the solvent effect depended strongly on the nature of both the solute and the solvent.

These studies clearly confirm the presence of chirality transfer in solutions. This effect can be important in organic reactions that employ chiral reagents and achiral solvents because the induced chirality in solvents can have an impact on the reaction. Alternatively, chiral chromatography uses binary or ternary achiral solvents in contact with chiral surfaces. The induced chirality in the solvent hasn't been considered in any of the proposed selection mechanisms[15, 32-38], but, at least in principle, it could influence the stereo selectivity if it is significant. Also, except for the examples mentioned above, most of the current theoretical calculations of spectroscopy, such as VCD and ORD, only consider the contributions from the chiral solutes and the solvent effects on solutes, but the solvent molecules are always considered as internally achiral and have no direct impact on the spectra. However, if the chirality transfer is strong enough, the induced chirality in solvents may directly contribute to the spectra and, therefore, can be important when trying to correctly interpret experimental results.

1.3 Polarizable models

Non-polarizable force fields for molecular simulations use effective pairwise potentials for electrostatic interactions and are widely used in simulations of condensed phases and biological systems [39, 40]. However, limitations exist in non-polarizable force fields [39]. Because they use fixed atomic charges and intramolecular potentials, which cannot adjust themselves according to different environments, the molecules are not treated accurately. For instance, solvation free energy calculations indicate that these force fields tend to underestimate the solubility of amino acid side chain analogs [41]. In other studies, non-polarizable flexible models have been found to underestimate the dipole moment of water molecules in bulk [42].

There is no doubt that simulation reliability depends upon the accuracy of the potential functions. In order to study chirality transfer, potential functions should be very sensitive to environmental changes so that asymmetric effects can be reflected. Therefore, non-polarizable models are not sufficient for chirality transfer, and addition of polarizability into the models is necessary.

There have been continuing efforts to incorporate polarization effects into non-polarizable force fields [43-47]. More specifically, molecule's mean response to a field is taken into account by iterative schemes: The charges or dipole moments of molecules can generate fields and the fields will, in turn, influence the charges or dipole moments of each molecule. Gao *et al*.[43] developed a polarizable intermolecular potential function (PIPF) for liquid alcohols. In this model, all atoms are represented explicitly, and the total energy of the system consists of a pairwise term and a nonadditive polarization term. The pairwise term is classical and is also used in non-polarizable models. The

polarization term follows from interactions between induced atomic dipole moments (μ_i) and the electrostatic field at the position of each atom (E_i^0):

$$E^{pol} = -\frac{1}{2}\sum_{i}^{N} \mu_i E_i^0 \qquad [1.1]$$

The induced dipole moment is defined as

$$\mu_i = \alpha_i (E_i^0 - \sum_{j \neq i} T_{ij} \cdot \mu_j) \qquad [1.2]$$

where α_i is the polarizability and T_{ij} is the dipole tensor. The induced dipole moments are calculated self-consistently and 4-5 iterations are typically needed [43]. This model provides a more accurate calculation of intermolecular interactions for heterogeneous systems compared to non-polarizable models. The disadvantage of this model is obvious: Self-consistency requires iterations at each time step, which makes it much more time consuming than non-polarizable models. More importantly, the atomic dipole moment is only conceptual and cannot provide information on real properties such as charge distributions.

Noskov *et al*.[42, 44, 45, 48] include charge carrying Drude particles in their molecular model to allow the molecular dipole to respond to the field. This model, originally proposed by Paul Drude in 1900[49], redistributes the partial charge on a heavy atom, such as oxygen, among a set of massless charged sites connected by a harmonic spring. The positions of these auxiliary sites are self-consistently determined in response to the external field, and the charges and force constants of these fictitious particles are related to the atomic polarizability. Before using the Drude model, the number and distribution of these auxiliary sites should be chosen. This model has been

used to successfully reproduce the vaporization enthalpy, dielectric constant, and self-diffusion of bulk liquids, such as water and ethanol. Similar to the PIPF, this model is computationally expensive because for each simulation step, about 16 iterations are required by the self-consistent procedure [42, 44].

Svishchev *et al.*[47] developed a polarizable point-charge (PPC) model for water. This three-site water model introduced field-dependence to atomic charges and intramolecular structures. In the implementation of this model, the atomic charges are iterated to calculate the self-consistent electrostatic fields and three to four iterations are normally required in each time step. This model has been used to successfully reproduce the static and dynamics properties of liquid water from supercooled to near-critical conditions[47].

Rick *et al*.[46], building upon earlier work by Rappé and Goddard[50], introduced a fluctuating charge (FC) model that uses an extended Hamiltonian approach to allow the molecules to respond to their environment. Specifically, this model was derived on the basis of the principle of electronegativity equalization[50], and starts with the energetic costs of charging an atom. The atomic charges are assigned fictitious masses and the charge values are dynamic variables. The charge fluctuations are dependent on the electrostatic field and subjected to the overall charge constraint, such as charge neutrality for each molecule. This model has been used by a number of groups[51-55] to study condensed phases as well as biological systems, such as peptides, and favorable results have been reported. For instance, average molecular dipole moments predicted by the FC model were found to be higher than those in non-polarizable models and closer to experiments even though the starting dipole moments are consistent with those in the gas

phase [54]. Unlike other polarizable models, the FC model doesn't require any iteration to achieve self-consistency since it is an extended Hamiltonian approach. This makes the cost of the simulation only slightly more than for a non-polarizable model. The disadvantage of this model is that, due to the fast fluctuations of atomic charges, the time step in the simulations is smaller in order to remain on the Born-Oppenheimer surface. A way to improve this is to propagate charge degrees of freedom separately from the nuclear degrees of freedom [56].

Although these models incorporate polarization effects by making electrostatic potentials field-dependent, they all treat the intramolecular potentials to be stationary. However, when molecules are in different environments, their intramolecular potentials, such as the torsional potentials, could be different. A field-dependent intramolecular potential has been developed only once previously, for water [57]. In that model, the HH and OH stretching potentials depended on the field magnitude of oxygen. However, this model is specific to water and the atomic charges were field-independent. Therefore, prior to the current work, a polarizable model that includes field dependence in both the atomic charges and the intramolecular degrees of freedom had not been considered.

In all, polarizable models can accurately describe a molecule's responses to different environments and hence, can increase the accuracy of MD simulations. Both the atomic charges and intramolecular potentials should be polarizable in order to accurately capture rapid changing properties, such as the induced chirality. However, none of the existing methods incorporates all these features. Therefore, a new methodology for developing this polarizable model is needed. The development and implementation of a flexible, polarizable model is discussed in Chapter 3.

1.4 Measuring chirality

The usual way to experimentally measure chirality is to use spectroscopy, such as CD, ORD and VCD [58-60]. These techniques are usually restricted to bulk samples. In a recent study of fluorescence-detected circular dichroism, Hassey *et al*.[61] analyzed dissymmetry parameters of single (bridged triarylamine) helicene molecules, and found that both relatively large positive and negative dissymmetry parameters could be observed although the measured spectra of bulk samples only have very small positive or negative values because of cancellation effects.

The chirality of individual molecules can be quantified by chirality indexes, which have been a subject of continuing interest over the past fifteen years, as summarized in several reviews[62, 63]. Many chiral indexes have been proposed[62, 64-69], but most of them can be divided into two general classes: measures that quantify the difference between a chiral object and an achiral reference[68], and those that quantify the difference between an enantiomer and its mirror image[69].

The first chirality function in chemistry was proposed by Guye *et al*.[70] in 1890. They introduced a function that correlated the optical rotation, which is a pseudoscalar property, with the molecular structure of a chiral molecule [62]. According to Guye, if the masses of the four points in a tetrahedral model are set to be the same, the chirality index P for a tetrahedron can be defined by $P(l) = c\prod_{i>j}^{4}(l_i - l_j)$, where l_j is the distance between the four vertices. In this definition, $P(l)$ is only a function of geometry and is non-zero only in the asymmetric tetrahedron. Therefore, this index indicates the distortion of a simple tetrahedron from its achiral form. Murrayrust *et al*.[71, 72]

improved this chirality function and represented the atomic configuration of a molecule by a point in a multidimensional space. The deformation of the configuration away from the symmetric reference structure can be calculated from the distance from this point to the axis.

In the chiral indexes that quantify the difference between two enantiomers, the common volumes and Hausdorff Distances are the most famous [68, 69]. Let's still take the tetrahedron as an example. When overlapping the tetrahedron with its mirror image, there's a volume that is occupied by both of them. When you rotate one tetrahedron around and get the maximum overlapping volume, that volume is the common volume. When a tetrahedron is achiral, the common volume is equal to the molecular volume. Therefore, this property can be used as a chiral index. A Hausdorff Distance measures how far two subsets of a space are from each other and is defined as:

$$D_H = \max\{\sup_{x\in X}\inf_{y\in Y} d(x,y), \sup_{y\in Y}\inf_{x\in X} d(x,y)\} \qquad [1.3]$$

where sup and inf are supremum and infimum, respectively, and $d(x,y)$ is the distance of two points x and y. Fig. 1.3 illustrates the concept of Hausdorff Distance. The nuclear positions in a rigid molecular model can be represented by a subset of points in three-dimensional space, and the Hausdorff Distance between the original and achiral point sets, indicates the measure of chirality.

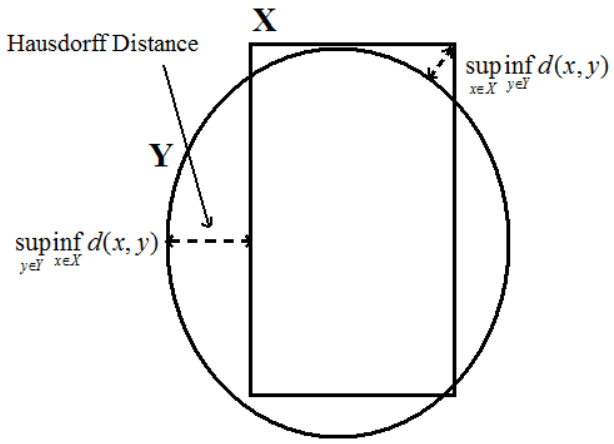

Figure 1.3. The Hausdorff Distance. The set X and Y correspond to all points inside the rectangle and the ellipse, respectively. $\sup_{x\in X}\inf_{y\in Y} d(x,y)$ is the maximum distance from any points in X (rectangle) to the closest point in Y (ellipse). $\sup_{y\in Y}\inf_{x\in X} d(x,y)$ is the maximum distance from any points in Y to the closest point in X. The Hausdorff Distance is the maximum of the two.

More recently, Osipov *et al.*[66] proposed a new chirality index that is different from the previous ones. It does not rely on a comparison to an achiral reference or a mirror image. This chirality index is analogous to the optical activity tensor[66], and has been found to accurately predict the helical twisting power of chiral dopants[73-76] for relatively rigid twisted-core additives. For more flexible additives, the relationship between the chiral index and the twisting power reflected conformational preferences due to interaction with the liquid crystal host[76, 77].

Although chirality indexes are supposed to be non-zero when a molecule is chiral, it has been found that if a chirality index is continuous, there almost always exist chiral zeroes [78]. The rationale for this is based on the following arguments. It is assumed that a molecular structure belongs to a continuous set, and any two structures can be connected by a continuous conversion. Except for some rare cases[79, 80], a chiral

molecule can be converted into its mirror image along a chiral path and all structures on this path are chiral. Since the chirality indexes of the two enantiomers have the same magnitude and opposite signs, there must be at least a point, during the conversion, that the chirality index becomes zero but the molecular structure is still chiral. In fact, there are an infinite number of such points for any molecule. Therefore, special care should be taken to deal with chiral zeroes when selecting chirality indexes.

There are several challenges to assess chirality in molecular dynamics simulations. First, within the simulations, all the molecules are flexible and mobile. The assessed chirality must reflect the conformational changes of each molecule but stay constant for reorientation or translation. Second, achiral molecules will be instantaneously chiral but, over long times, this chirality should average to zero when the molecules are far from a source of chirality. Third, the evaluation of instantaneous chirality must be rapid enough to allow simulations to proceed.

In order to study chirality transfer, it is important to choose proper chirality indexes. The indexes developed by Osipov *et al*[66] are chosen in our study because they fit all our requirements and can be modified to emphasize molecular shape, atomic charges, or atomic masses, etc.. By using multiple indexes, we can focus on different aspects of the molecular structures and charge distributions and prevent chiral zeroes at the same time.

1.5 Thesis organization

The main objective of this thesis is to explore the chirality transfer from chiral solutes and surfaces to achiral solvents. To achieve this goal, a new methodology for building polarizable, flexible models is developed.

This thesis is organized as follows. Chapter 2 presents theoretical methods, simulation algorithms, and details on polarizable models and chirality indexes. Chapter 3 describes the development of polarizable and flexible molecular models based on extensive *ab initio* calculations. In this methodology, intramolecular motion is directly coupled to electrostatic fields. Chapter 4 presents MD simulation results on chirality transfer from chiral solutes to achiral solvents, such as ethanol and benzyl alcohol. Detailed aspects such as the importance of solvent polarizability and solute flexibility, hydrogen-bonding network, and the solvent-solute interaction sites are described. Chapter 5 presents results on chiral induction studies for surfaces used in chiral chromatography, such as the Whelk-O1, leucine- and phenylglycine-based CSPs. The solvents consist of ethanol, 2-propanol, and binary solvents that are commonly used in chromatography, such as n-hexane/ethanol and n-hexane/2-propanol. Emphasis is placed on the location of the chirality transfer zones and the solvent characteristics in these zones. Brief conclusions are presented in Chapter 6.

Chapter 2
Theoretical Methods and Models

2.1 Molecular dynamics simulations

Most of the results in this thesis are obtained from Molecular Dynamics (MD) simulations. The MD simulation technique is used to calculate equilibrium and dynamical properties of many-body systems. It has been used widely from ideal gases and liquids to biomolecules[40, 81]. For every particle in the system, the forces acting upon it are calculated and Newton's equations are used to evolve the system. In the simulations, the coordinates and momenta of all particles are obtained and the physical properties can be calculated using statistical mechanics methods. Therefore, MD is a bridge between theoretical and experimental approaches: It is a computer-based experiment. MD simulation is particularly useful for systems that are too difficult to be studied experimentally or too complicated to be studied by quantum mechanical approaches.

In a classical system of N molecules, the Hamiltonian $H(\vec{q},\vec{p})$ is the sum of kinetic and potential energies and is a function of the coordinates $\vec{q} = (\vec{q}_1, \vec{q}_2, ..., \vec{q}_N)$ and momenta $\vec{p} = (\vec{p}_1, \vec{p}_2, ..., \vec{p}_N)$ of each atom:

$$H(\vec{q},\vec{p}) = K(\vec{p}) + U(\vec{q}) \qquad [2.1]$$

where $K(\vec{p})$ and $U(\vec{q})$ are kinetic and potential energies, respectively. The kinetic energy has the form

$$K(\vec{p}) = \sum_{\alpha}^{N} \sum_{i}^{M} \frac{p_{i\alpha}^2}{2m_{i\alpha}} \qquad [2.2]$$

where N and M are the number molecules and the number of atoms in each molecule, respectively, and $m_{i\alpha}$ is the atomic mass of atom *i* in molecule α. From the Hamiltonian, the equations of motion can be derived:

$$\frac{d\vec{q}_{i\alpha}}{dt} = \frac{\partial H}{\partial \vec{p}_{i\alpha}} = \frac{\vec{p}_{i\alpha}}{m_{i\alpha}} \qquad [2.3]$$

$$\frac{d\vec{p}_{i\alpha}}{dt} = -\frac{\partial H}{\partial \vec{q}_{i\alpha}} = -\frac{\partial U}{\partial \vec{q}_{i\alpha}} \qquad [2.4]$$

Eq. [2.4] can also be written as the total force acting on atom *i* of molecule α:

$$\vec{F}_{i\alpha} = -\frac{\partial U}{\partial \vec{q}_{i\alpha}} = m_{i\alpha} \frac{d^2 \vec{q}_{i\alpha}}{dt^2} = m_{i\alpha} \vec{a}_{i\alpha} \qquad [2.5]$$

In MD simulations, forces are calculated in each time step and the equations of motions are solved to advance the system in time. Therefore, the force calculation is essential to MD simulations.

2.1.1 Potentials

As shown in Eq. [2.5], forces are obtained from first derivatives of the potential ($U(\vec{q})$). Generally, the total potential is divided into two parts: An intramolecular part and an intermolecular part:

$$U = U^{\text{intra}} + U^{\text{inter}} \qquad [2.6]$$

The intramolecular potential in Eq. [2.6] typically consists of four parts: stretching(U^{st}), bending (U^{bend}), torsion (U^{tor}) and improper torsion (U^{imp}), as shown in Fig. 2.1.

Bond-stretching	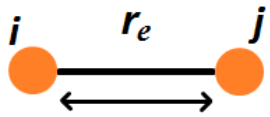
Bond-bending	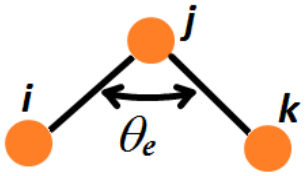
Torsion	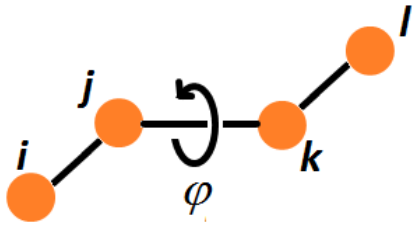
Improper torsion	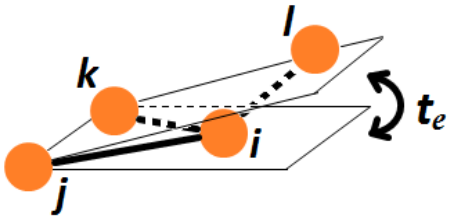

Figure 2.1. Examples of intramolecular degrees of freedom.

Stretching motion can be most accurately defined by a Morse potential[82], which has the form $U^{st}(r) = D_e[1 - e^{-\alpha(r-r_e)}]^2$, where D_e, α and r_e are the well depth (bond dissociation energy), the inverse of potential 'width', and the equilibrium bond distance. However, the Morse potential is computationally expensive and not well suited to MD

simulations. Therefore, a harmonic potential is commonly used to describe the stretching motion:

$$U^{st}(r) = k_s (r - r_e)^2 \qquad [2.7]$$

where k_s and r_e are the stretching force constant and the corresponding equilibrium bond length, respectively. As shown in Fig. 2.2, a harmonic potential provides a good description of the stretching potential near r_e. In MD simulations at 298K, only the bottom of the well (<15kJ/mol) will be important. As a result, fluctuations in bond lengths are generally quite small.

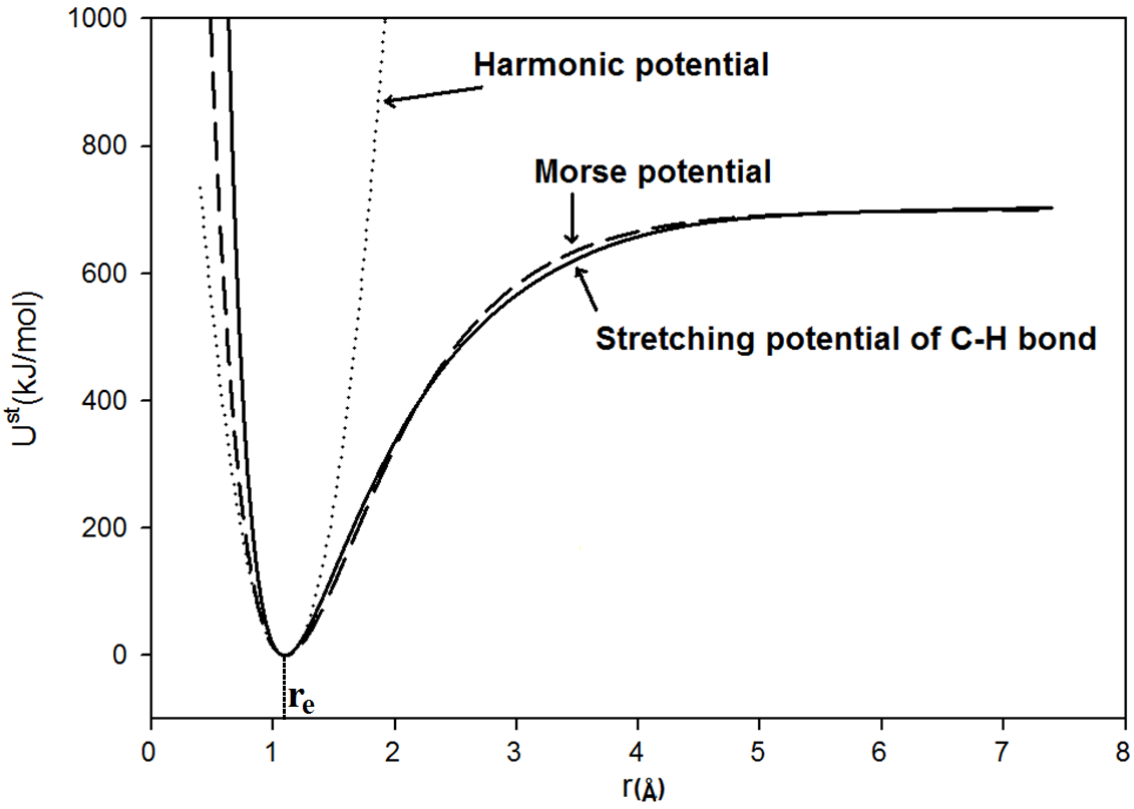

Figure 2.2. Comparison of Morse potential and harmonic potential for bond stretching.

Typical MD simulations keep bond lengths fixed by using the RATTLE[83] or SHAKE[84] algorithms, and a bond stretching potential is only used for some selected bonds.

Bending can also be defined by a harmonic potential,

$$U^{\text{bend}}(\theta) = k_\theta(\theta - \theta_e)^2 \qquad [2.8]$$

where k_θ and θ_e are the bending force constant and the corresponding equilibrium angle, respectively. Other more complicated forms have been employed, but, as with bond stretches, bending motion is limited at typical temperatures and a harmonic potential is usually sufficient.

The torsion potential has the form of a modified Ryckaert-Bellemans potential[85]

$$U^{tor}(\varphi) = \left(\sum_{i=0}^{6} C_i \cos^i(\varphi + \varphi_i)\right) \qquad [2.9]$$

where C_i is the i^{th} torsional coefficient, φ is the dihedral angle and φ_i is the corresponding phase shift. Other forms of torsion potentials are also available[86] and will not be discussed here.

Improper torsion potentials have the form

$$U^{imp}(t) = k_t(t - t_e)^2 \qquad [2.10]$$

where t, t_e, and k_t are the improper torsion angle, the equilibrium value of the angle, and the force constant, respectively.

The intermolecular potential in Eq. [2.6] can be written as

$$U^{\text{inter}} = U^{\text{el}} + U^{\text{LJ}} \qquad [2.11]$$

where U^{el} and U^{LJ} are electrostatic and Lennard-Jones potentials, respectively. The Lennard-Jones (LJ) potential is given by

$$U^{LJ} = \sum_{i\alpha<j\beta} 4\varepsilon_{ij}\left[\left(\frac{\sigma_{ij}}{r_{i\alpha j\beta}}\right)^{12} - \left(\frac{\sigma_{ij}}{r_{i\alpha j\beta}}\right)^{6}\right] \qquad [2.12]$$

where atoms *i* and *j* belong to molecules α and β, respectively. This potential sums over all pairs of atoms from different molecules. ε_{ij} and σ_{ij} are the combined Lennard-Jones energy and length parameters, respectively. In force field development, ε_{ii} and σ_{ii} are parameterized for each atom in a molecule to fit to experimental results, such as the diffusion coefficients [87]. In MD simulations, they are combined to ε_{ij} and σ_{ij} in order to be used in calculation of pair-wise LJ potentials in Eq. [2.12]. A common choice is the Lorentz-Berthelot mixing rules[40]

$$\sigma_{ij} = \frac{\sigma_i + \sigma_j}{2}, \quad \varepsilon_{ij} = \sqrt{\varepsilon_i \varepsilon_j} \qquad [2.13]$$

As shown in Fig. 2.3, ε_{ij} is the magnitude of the minimum potential energy (the well depth) and σ_{ij} is the atomic distance (r_{ij}) when the potential energy is zero.

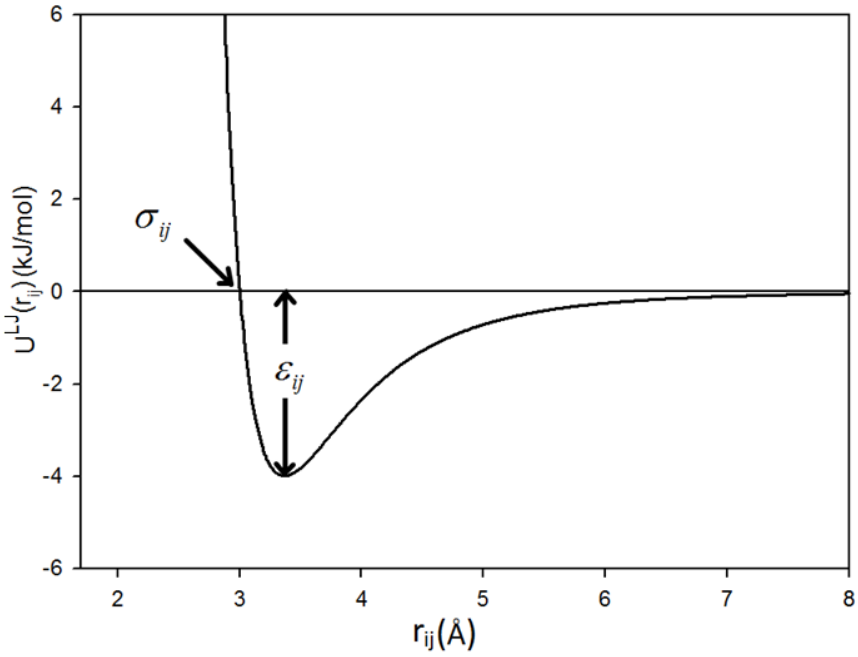

Figure 2.3. Lennard-Jones potential.

The electrostatic potential in Eq. [2.11] in non-polarizable models has the form

$$U^{el} = \sum_{i\alpha<j\beta} \frac{Q_{i\alpha}Q_{j\beta}}{4\pi\varepsilon_0 r_{i\alpha j\beta}} \qquad [2.14]$$

where atoms *i* and *j* belong to molecules α and β, respectively. $Q_{i\alpha}$ is the charge of atom *i* in molecule α, and ε_0 is the dielectric constant. In polarizable models, additional terms are added to Eq. [2.14] and the charges of atoms may not be fixed. This will be discussed in more detail in Section 2.2.1.

For atoms within the same molecule, Eqs. [2.13-2.14] are evaluated only for atom pairs that are separated by four, or more, bonds.

2.1.2 Periodic Boundary Conditions

Computer simulations are usually performed on small systems (with less than 10000 molecules) because of the limitations of computer storage and calculation speed [40]. These molecules are confined to a simulation cell that is space filling when replicated in 3D. A cubic simulation cell is most commonly chosen. For hundreds or thousands of molecules confined to a cube, a large proportion of the molecules are at the surface, and they will experience different forces from the ones in the bulk [88]. In order to overcome this surface effect, periodic boundary conditions (PBC)[88] are usually applied. A 2-dimensional PBC system is shown in Fig. 2.4. The central box is replicated throughout the 2-dimensional space to form an infinite lattice. When an atom in the original box (with thick frame) moves, its periodic images in all boxes move in exactly the same way. If an atom leaves the central box into a neighboring box, such as the atom "a" in figure 2.4, one of its images will enter the central box from another neighboring box through the opposite face, which is shown as a'. With this replication, the simulation volume is effectively infinite and no molecules are at a surface.

When calculating forces on each atom, the influence of atoms in other boxes should also be taken into account. In principle, there are an infinite number of atom pairs to be evaluated in PBC systems, and of course it is impossible to calculate them all. In order to solve this problem, some modifications in the force calculation are necessary. For short-range interactions, such as the LJ potential, the dominating contribution is from the interactions between particles that are close to each other. For example, in Fig. 2.3, the potential energy is almost zero when the atom distance is more than 8Å. Therefore, a cut-off radius (r_c) can be applied to each particle and only the interactions between this

particle and other particles within this radius are evaluated. In MD simulations, the cut-off radius should meet some criteria: it should be large enough so that only negligible interactions are ignored, and it should be smaller than half of the simulation cell length so that each molecule is counted only once (only the original or one of the images should be counted).

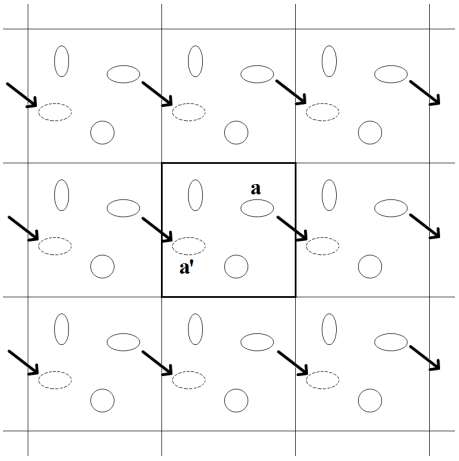

Figure 2.4. 2-dimensional periodic boundary condition system.

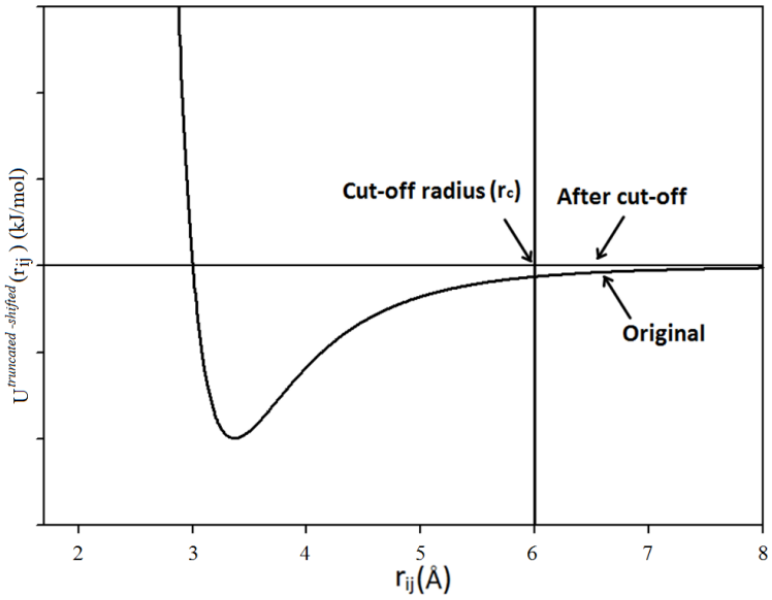

Figure 2.5. Discontinuity at the distance of the cut-off radius

Applying a cut-off radius will introduce a discontinuity at the distance of r_c, as shown in Fig. 2.5. Since forces are obtained from derivatives of the potential, the discontinuity in the potential can cause an infinite force at r_c. The potential is normally shifted after truncation so that it becomes continuous:

$$U^{truncated-shifted}(r_{ij}) = U^{LJ}(r_{ij}) - U^{LJ}(r_c) \quad \text{when } r_{ij} \le r_c$$

$$U^{truncated-shifted}(r_{ij}) = 0 \quad \text{when } r_{ij} \le r_c \qquad [2.15]$$

and the potential and force vary smoothly with distance.

2.1.3 Ewald summation

In MD simulations, the evaluation of long-range interactions (charge-charge, charge-dipole, dipole-dipole) is time consuming. In a cubic simulation cell of side length L with N charged atoms, the Coulombic potential energy is:

$$U^{Coulomb} = \frac{1}{2}\sum_{i=1}^{N} Q_i \Phi(\vec{r}_i) \qquad [2.16]$$

where Q_i and $\vec{r}_i$ are the partial charge and position of atom *i*, respectively, and $\Phi(\vec{r}_i)$ is the electrostatic potential at the position of atom *i*.

$$\Phi(\vec{r}_i) = \sum_{j=1}^{N}\sum_{\vec{n}} \frac{Q_j}{|\vec{r}_{ij} + \vec{n}L|} \qquad [2.17]$$

where $\vec{n} = (n_x, n_y, n_z)$, with n_x, n_y, n_z integers, includes the positions of atoms in the images. The summation omits the case of *i*=*j*, where $\vec{n} = (0,0,0)$ since a charge does not interact with itself. Here, atomic units are used to make the notation more compact.

Unlike LJ potentials, molecules in neighboring cells must be included in the evaluation of $\Phi(\vec{r}_i)$, but the result of this summation depends on the order in which the terms are added up, and thus a direct evaluation of $\Phi(\vec{r}_i)$ suffers from convergence problems [81].

The Ewald summation[89] was introduced many years ago to effectively sum the long-range interactions between an infinite number of particles and all their periodic images. In this approach, each charge is considered to be surrounded by a screening charge distribution (normally Gaussian distribution) of equal magnitude but of opposite sign, as shown in Fig. 2.6.

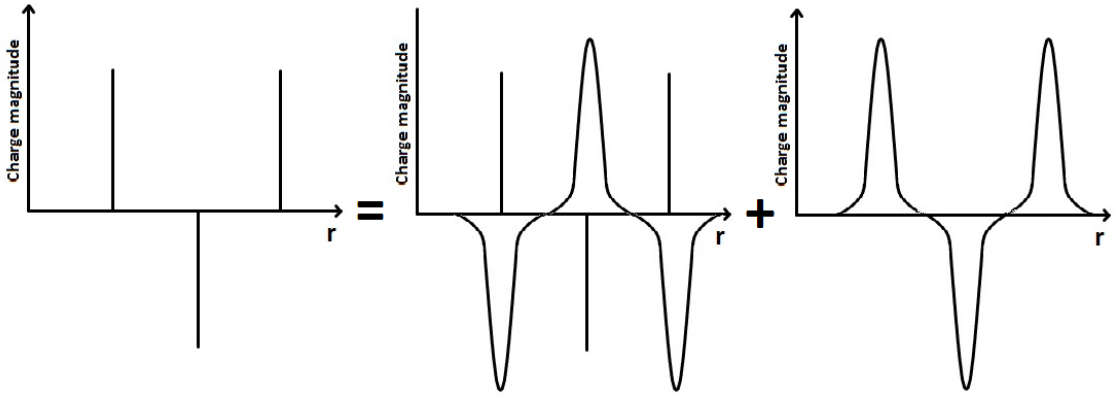

Figure 2.6. The charge distribution in the Ewald summation. Vertical lines represent point charges and Gaussian curves represent screening charge distributions.

In this way, the potential is converted into three terms

$$U^{el} = U^{r} + U^{k} + U^{0} \qquad [2.18]$$

The first term, U^r, is the sum of the interactions between the charges plus the screening distributions, and it is a real space sum[89]:

$$U^r = \frac{1}{2}\sum_{i\neq j}^{N}\sum_{\vec{n}} Q_i Q_j \frac{erfc(\sqrt{\alpha}\,|\vec{r}_{ij}+\vec{n}L|)}{|\vec{r}_{ij}+\vec{n}L|} \qquad [2.19]$$

where α determines the size of the screening distribution and $erfc(x)$ is the complementary error function that decreases monotonically as x increases

$$erfc(x) = \frac{2}{\sqrt{\pi}}\int_{x}^{\infty} e^{-t^2} dt \qquad [2.20]$$

The second term in Eq. [2.18], U^k, exactly counteracts the first screening distribution, and this summation is performed in reciprocal space

$$U^k = \frac{1}{2\pi L^3}\sum_{i,j=1}^{N}\sum_{\vec{k}\neq 0} Q_i Q_j \frac{4\pi}{k^2}\exp(-\frac{k^2}{4\alpha^2})\cos(\vec{k}\cdot\vec{r}_{ij}) \qquad [2.21]$$

where $\vec{k} = (\frac{2\pi n_x}{L}, \frac{2\pi n_y}{L}, \frac{2\pi n_z}{L})$ with n_x, n_y, n_z integers.

The third term in Eq. [2.18], U^0, is a correction term that cancels out the interaction of each of the introduced artificial counter-charges with itself.

$$U^0 = -\sqrt{\frac{\alpha}{\pi}}\sum_{i=1}^{N} Q_i^2 \qquad [2.22]$$

Therefore, Eq. [2.18] can be written as:

$$U^k = \frac{1}{2}\sum_{i\neq j}^{N}\sum_{\vec{n}} Q_i Q_j \frac{erfc(\sqrt{\alpha}\,|\vec{r}_{ij}+\vec{n}L|)}{|\vec{r}_{ij}+\vec{n}L|} + \frac{1}{2\pi L^3}\sum_{i,j=1}^{N}\sum_{\vec{k}\neq 0} Q_i Q_j \frac{4\pi}{k^2}\exp(-\frac{k^2}{4\alpha^2})\cos(\vec{k}\cdot\vec{r}_{ij})$$

$$-\sqrt{\frac{\alpha}{\pi}}\sum_{i=1}^{N} Q_i^2 \qquad [2.23]$$

where α and the number of $\vec{k}$ vectors in the second sum are configurable parameters and they should be carefully chosen so that Eq. [2.23] converges quickly. In practice, α can be chosen such that U^r only requires the central simulation cell and no images are needed.

In Eq. [2.23], it is assumed that the simulation cell is cubic. If the simulation cell is not cubic, an additional shape-dependent correction term, $J(\vec{M}, P)$, should be added,[90] where $\vec{M}$ is the dipole moment of the simulation cell and $\vec{M} = \sum_{i=1}^{N} Q_i \vec{r}_i$. This correction term depends on the summations geometry and has the following form for the rectangular shape cell elongated on the *z* axis:

$$J(\vec{M}) = \frac{2\pi}{V} M_z^{\,2} \qquad [2.24]$$

where M_z and V are the z component of the total dipole moment and the volume of the simulation cell, respectively.

2.2 Polarizable Models

2.2.1 Fluctuating Charge Model

In non-polarizable force fields, fixed atomic charges are used in the molecules. Since the charges are constant, they cannot reflect the changes in electrostatic environments experienced by the molecules during the simulation. Rick *et al*.[46], introduced a fluctuating charge (FC) model that allows the molecules to respond to their environment. In the FC model, the energy of an isolated charged atom, bearing a charge Q_i, can be expanded in a Taylor expansion up to second order:

$$E(Q_i) = E_i(0) + \tilde{\chi}_i^0 Q_i + \frac{1}{2} J_{ii}^0 Q_i^2 \qquad [2.25]$$

where $E_i(0)$ and $\tilde{\chi}_i^0$ are the ground state energy and the electronegativity per unit charge of atom *i*, respectively, and J_{ii}^0 is twice the hardness of the electronegativity of the atom. The values of $\tilde{\chi}_i^0$ and J_{ii}^0 can be obtained from *ab initio* calculations, from empirical forms, or from experiments.

Within the FC model, the electrostatic energy of a system of *M* molecules (with *N* atoms per molecule) is:

$$U^{el} = \sum_{\alpha=1}^{M} \sum_{i=1}^{N_\alpha} \left(E_i(0) + \tilde{\chi}_i^0 Q_{i\alpha} + \frac{1}{2} J_{ii}^0 Q_{i\alpha}^2 \right) + \sum_{i\alpha<j\beta} J_{ij}(r_{i\alpha j\beta}) Q_{i\alpha} Q_{j\beta} \qquad [2.26]$$

where *i* is an atom in molecule α and *j* belongs to molecule β. The first term is the energy for each isolated atom and the second term is the electrostatic energy between all pairs of atoms, both intramolecular and intermolecular. For intermolecular atomic pairs or

intramolecular atomic pairs that are separated by more than three bonds, the atoms are relatively far apart and $J_{ij}(r_{i\alpha j\beta})$ is simply $\frac{1}{r_{i\alpha j\beta}}$. The second term in Eq. [2.26] then becomes the Coulomb potential between two point charges. For intramolecular atomic pairs that are separated by 1-3 bonds, $J_{ij}(r_{i\alpha j\beta})$ is a more complex function of the electron density that includes screening contributions. The $J_{ij}(r_{i\alpha j\beta})$ can be defined as the Coulomb overlap integral[50] between Slater orbitals, $\varphi_{ni}(r_i)$, centered on each atom:

$$J_{ij}(r_{ij}) = \int d\vec{r}_i d\vec{r}_j \, |\varphi_{ni}(r_i)|^2 \, \frac{1}{|\vec{r}_i - \vec{r}_j - \vec{r}_{ij}|} \, |\varphi_{nj}(r_j)|^2 \qquad [2.27]$$

Since this integral is only evaluated for intramolecular atomic pairs, $J_{ij}(r_{i\alpha j\beta})$ is written as $J_{ij}(r_{ij})$, which is a function of two parameters ζ_i and ζ_j and the distances between the two atoms, r_{ij}. As shown in Fig. 2.7, $J_{ij}(r_{ij})$ rapidly approaches the pure Coulomb interaction as the distance between the atoms increases: $J_{ij}(r_{ij})$ converges to the Coulomb potential when the atoms are more than a few Angstroms apart.

The Slater orbitals in Eq. [2.27] have the form[46]

$$\varphi_{ni}(r) = N_i r^{n_i - 1} e^{-\zeta_i r} \qquad [2.28]$$

where n_i is the principal quantum number of the atom, ζ_i is the valence orbital exponent for atom *i*, and N_i is a normalization constant. The value of $J_{ii}(r)$ at $r = 0$ is J_{ii}^0, which appears in the first term in Eq. [2.26] and is trivially related to ζ_i. For example for hydrogen, $n_H = 1$, and it can be shown[46] that $J_{HH}^0 = \frac{5}{8}\zeta_H$. Thus the atomic response

(see Eq. [2.26]) to the presence of an electrostatic field can be expressed in terms of the ζ_i and $\tilde{\chi}_i^0$ parameters.

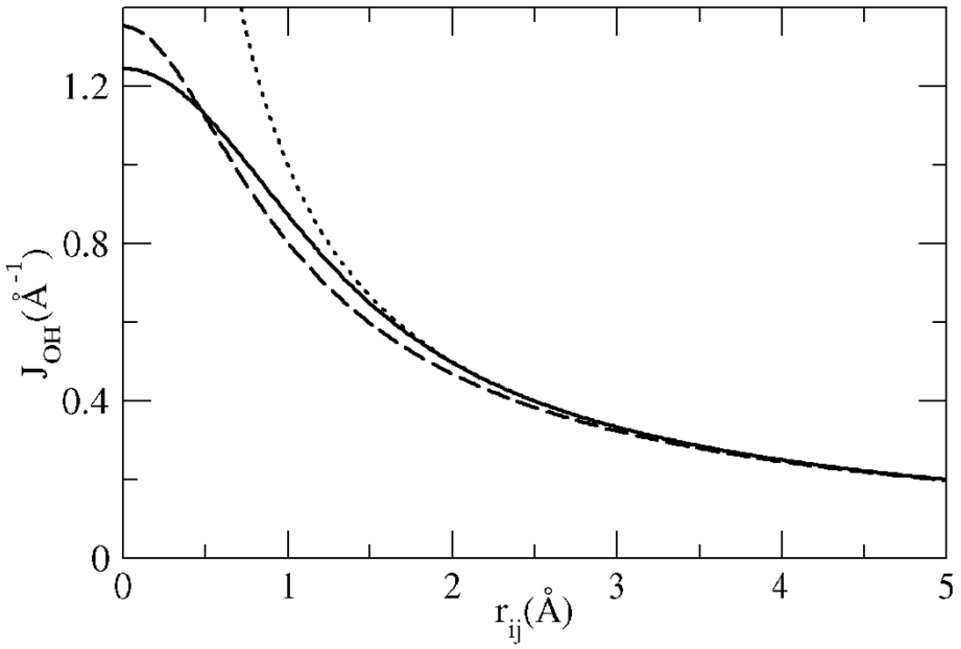

Figure 2.7. Comparison of the Coulomb overlap (solid line) evaluated from Eq. [2.27] with $\frac{1}{r_{ij}}$ (dotted line) and the approximate form in Eq. [2.29] (dashed line).

Since the Coulomb overlap integral in Eq. [2.27] is computationally expensive to calculate, an alternative has been proposed by Patel *et al.*[53] In their approximation, $J_{ij}(r_{ij})$ is

$$J_{ij}(r_{ij}) = \frac{\frac{1}{2}(J_{ii}^0 + J_{jj}^0)}{\sqrt{1+\frac{1}{4}(J_{ii}^0 + J_{jj}^0)^2 r_{ij}^2}} \qquad [2.29]$$

and the requirement for numerical integration (Eq. [2.27]) is avoided.

In Fig. 2.7, the Coulomb overlap evaluated from Eq. [2.27] is compared with $\frac{1}{r_{ij}}$ (Coulomb potential) and the approximate form in Eq. [2.29]. The approximate form in Eq. [2.29] leads to $J_{ij}(r_{ij})$ that are close to the values from Eq. [2.27]. However, it has been found[91] that even small changes in the $J_{ij}(r_{ij})$ lead to large differences in the fluid structure and properties. Therefore, the more accurate form (Eq. [2.27]) is used in our studies. In order to prevent expensive on-the-fly calculations of Eq. [2.27] during the simulations, we evaluate the overlap for 500 interatomic separations, r_{ij}, from 0-5 Å prior to the simulation. During the simulations, the interatomic separations will not normally coincide with a pre-calculated separation, and we employ spline fits to interpolate between calculated potentials and provide the Coulomb overlap at the required separation. The approximation is very accurate because of the large number of interatomic separations that are pre-evaluated and the monotonically decreasing nature of $J_{ij}(r_{ij})$.

2.2.2 Fluctuating Charge and INTRAmolecular potential model

The intramolecular potentials are typically parameterized prior to the simulations and are kept fixed thereafter. However, the potentials could be field sensitive and may change during simulations due to the varying electrostatic environments experienced by the molecules. In this thesis, the development of a new model, the Fluctuating Charge and INTRAmolecular potential (fCINTRA) model, is described. In this model, the environmental effects on atomic charges **and** intramolecular potentials are taken into

account. We have chosen ethanol as a test molecule but note that the principles outlined below are general.

The field-dependent intramolecular potential generally consists of four parts:

$$U^{\text{intra}}(\vec{E}) = U^{st}(\vec{E}) + U^{be}(\vec{E}) + U^{tor}(\vec{E}) + U^{imp}(\vec{E}) . \quad [2.30]$$

where $\vec{E}$ is the electrostatic field, and $U^{st}(\vec{E})$, $U^{be}(\vec{E})$, $U^{tor}(\vec{E})$, and $U^{imp}(\vec{E})$ are the field-dependent stretching, bending, torsion, and improper torsion potentials, respectively. Similar to Eq. [2.7], stretching motion is described by a harmonic potential,

$$U^{st}(\vec{E}) = \sum_{is} k_{s;is}(\vec{E})(r_{is} - r_{e;is}(\vec{E}))^2 \quad [2.31]$$

where $k_{s;is}(\vec{E})$ is the field-dependent stretching force constant, and $r_{e;is}(\vec{E})$ is the corresponding equilibrium bond length. The bending potential is also described by a harmonic potential

$$U^{be}(\vec{E}) = \sum_{ib} k_{\theta;ib}(\vec{E})(\theta_{ib} - \theta_{e;ib}(\vec{E}))^2 \quad [2.32]$$

where $k_{\theta;ib}(\vec{E})$ is the field-dependent bending force constant, and $\theta_{e;ib}(\vec{E})$ is the corresponding equilibrium angle. The torsional potential has the form

$$U^{tor}(\vec{E}) = \sum_{it}\left(\sum_{i=0}^{6} C_{it;i}(\vec{E})\cos^i(\varphi_{it} + \varphi_{0,it}(\vec{E}))\right) \quad [2.33]$$

where φ_{it} is the dihedral angle and $\varphi_{0,it}(\vec{E})$ is the corresponding phase shift. The latter is important in representing the field response of the molecule. Specifically, the potential in

the presence of a field may have a lowest energy conformer at a different torsional angle than the zero-field case and the potential must allow for this shift. Improper torsion potentials have the form

$$U^{imp}(\vec{E}) = \sum_{im} k_{t,im}(\vec{E})(t_{im} - t_{e,im}(\vec{E}))^2 \quad , \qquad [2.34]$$

where t_{im}, $t_{e,im}(\vec{E})$, and $k_{t,im}(\vec{E})$ are the improper torsion angle, the equilibrium value of the angle, and the force constant, respectively.

For ethanol, the intramolecular motion is divided into 8 stretches, 13 bends, and 2 torsions.

The field-dependent coefficients in Eqs. [2.31]-[2.34] are expanded according to "structural" analogs, which include

$$| E_X^1 |, \qquad [2.35]$$

the field magnitude on the indicated atom, for each atom. Pairs of fields contribute via

$$| E_{XY}^{12} | = | \vec{E}_X^1 \, || \, \vec{E}_Y^2 |, \qquad [2.36]$$

the product of the field magnitude on two atoms, and

$$E_{XY}^{12} = \vec{E}_X^1 \bullet \vec{E}_Y^2 \qquad [2.37]$$

the dot product of the fields on two atoms. For ethanol, there are 45 and 36 distinct $| E_{XY}^{12} |$ and E_{XY}^{12} expansion terms, respectively. Fields on three atoms are included in

$$E_{XYZ}^{123} = (\vec{E}_X^3 - \vec{E}_Y^2) \bullet (\vec{E}_Y^2 - \vec{E}_Z^1), \qquad [2.38]$$

corresponding to a field "angle" term on the middle atom, and

$$\hat{E}^{123}_{XYZ} = (\vec{E}^{3}_{X} \times \vec{E}^{2}_{Y}) \bullet (\vec{E}^{2}_{Y} \times \vec{E}^{1}_{Z}) , \qquad [2.39]$$

corresponding to a "dihedral angle" form of E^{123}_{XYZ} . For ethanol, all possible angles are considered, leading to 13 E^{123}_{XYZ} and $\hat{E}^{123}_{XYZ}$ terms. Finally, we include

$$E^{1234}_{XYZA} = ((\vec{E}^{4}_{A} - \vec{E}^{3}_{Z}) \times (\vec{E}^{3}_{Z} - \vec{E}^{2}_{Y})) \bullet ((\vec{E}^{3}_{Z} - \vec{E}^{2}_{Y}) \times (\vec{E}^{2}_{Y} - \vec{E}^{1}_{X})) , \qquad [2.40]$$

which is analogous to a dihedral angle. With all possible torsions considered, twelve four-field terms are obtained for ethanol. The expansion terms in Eqs. [2.35]-[2.40] are invariant to the coordinate system (body-fixed or space-fixed) and, consequently, can be readily evaluated during the simulation without a coordinate transformation.

In principle, coefficients in Eqs. [2.31]-[2.34] can be expanded to many field-dependent terms obtained from Eqs. [2.35]-[2.40]. Symmetry considerations can reduce the number of expressions. Take ethanol as an example, following the numbering in Fig. 2.8, since H(8) and H(9) are related by symmetry, we define

$$E^{123\,X}_{HOCH} = E^{1238}_{HOCH} + E^{1239}_{HOCH} \qquad [2.41]$$

where X is used to represent atoms 8 and 9. Equivalently, for H(5), H(6), and H(7), we have sums of three terms:

$$\hat{E}^{34\,Y}_{CCH} = \hat{E}^{345}_{CCH} + \hat{E}^{346}_{CCH} + \hat{E}^{347}_{CCH} \qquad [2.42]$$

where Y denotes H(5), H(6), and H(7). The summed terms replace the individual ones in the fits to ensure that the expansions are always symmetric with respect to the interchange of these atoms.

The torsional energy for a rotation of φ about the C(3)-O(2) bond should be the same for a rotation of –φ in the field obtained by reflection in the C(4)-C(3)-O(2) plane. That is, the "opposite" field with the "opposite" torsional angle should correspond to the same energy. The cosine terms in Eq. [2.33] are symmetric about 180 degrees and automatically satisfy this constraint. To incorporate this symmetry into the asymmetric coefficients, such as sine terms, we include a multiplicative factor of

$$S_y = E_{y1} + E_{y2} + E_{y3} + E_{y4} \qquad [2.43]$$

in the expansions of these coefficients. In Eq. [2.43], the y-components are in body-fixed coordinates. In this regard, C(3) is at the origin of the body-fixed coordinate system, O(2) lies on the x-axis, and the y-axis is perpendicular to the C(3)-O(2)-H(1) plane. This multiplicative factor enforces the appropriate symmetry in Eq. [2.33].

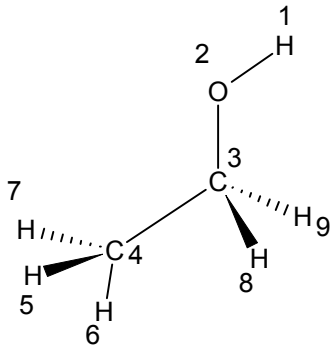

Figure 2.8. The ethanol molecule showing the atom numbering used throughout this thesis.

2.3 Equations of motion

2.3.1 Verlet Algorithms

In MD simulations, equations of motion are integrated to evolve the system after the forces on all particles are calculated. A good integration algorithm should be time reversible, which means that the system can go forward and backward in time symmetrically. One of the most well-known algorithms of integrating the equations of motion is the Verlet algorithm[92], which was derived from the Taylor expansion about the positions $\vec{r}(t)$ at time t:

$$\vec{r}(t+\Delta t) = \vec{r}(t) + \vec{v}(t)\Delta t + \frac{1}{2}\vec{a}(t)\Delta t^2 + ... \qquad [2.44]$$

$$\vec{r}(t-\Delta t) = \vec{r}(t) - \vec{v}(t)\Delta t + \frac{1}{2}\vec{a}(t)\Delta t^2 - ... \qquad [2.45]$$

where $\vec{a}(t)$ is the acceleration at time *t* and is evaluated from the following:

$$\vec{a}(t) = \frac{\vec{F}(t)}{m} \qquad [2.46]$$

where $\vec{F}(t)$ is the total force on the particle at time step *t* and *m* is the particle mass. Adding up Eq. [2.44] and Eq. [2.45] neglecting the high order derivative terms, the following relationship will be obtained:

$$\vec{r}(t+\Delta t) = 2\vec{r}(t) - \vec{r}(t-\Delta t) + \vec{a}(t)\Delta t^2 \qquad [2.47]$$

In this algorithm, the positions $\vec{r}(t+\Delta t)$ only depend on the original positions $\vec{r}(t)$, accelerations $\vec{a}(t)$, and the positions $\vec{r}(t-\Delta t)$ at the previous time step. This equation shows that the Verlet algorithm is time reversible because the $\vec{r}(t+\Delta t)$ and $\vec{r}(t-\Delta t)$ play symmetric roles. This algorithm is also stable in regards to long-time energy conservation. The velocities are not used in the trajectory calculation, but when they are needed to calculate kinetic energy or other properties, they can be easily obtained from the following formula:

$$\vec{v}(t) = \frac{\vec{r}(t+\Delta t) - \vec{r}(t-\Delta t)}{2\Delta t} \qquad [2.48]$$

The errors in Eq. [2.47] and Eq. [2.48] are of the orders Δt^4 and Δt^2, respectively.

The original Verlet algorithm has several equivalent versions that explicitly use velocities in the equations of motion. The most commonly used are the Leap-frog algorithm, where velocities are calculated at half time steps, and the Velocity-Verlet algorithm, where velocities are advanced in a two-step process.

The Velocity-Verlet algorithm has the following form

$$\vec{r}(t+\Delta t) = \vec{r}(t) + \vec{v}(t)\Delta t + \frac{1}{2}\vec{a}(t)\Delta t^2 \qquad [2.49]$$

$$\vec{v}(t+\Delta t) = \vec{v}(t) + \frac{1}{2}\Delta t[\vec{a}(t) + \vec{a}(t+\Delta t)] \qquad [2.50]$$

This algorithm is equivalent to the original Verlet algorithm because when the velocities are eliminated, Eq. [2.49] and Eq. [2.50] will be turned into Eq. [2.47]. The implementation of this algorithm involves two stages. In the first stage, the new positions

are calculated using Eq. [2.49] and the velocities at half time step ($t+\frac{1}{2}\Delta t$) are calculated using

$$\vec{v}(t+\frac{1}{2}\Delta t)=\vec{v}(t)+\frac{1}{2}\vec{a}(t)\Delta t \qquad [2.51]$$

In the second stage, forces ($\vec{F}(t+\Delta t)$) and accelerations ($\vec{a}(t+\Delta t)$) are computed and the velocities are advanced

$$\vec{v}(t+\Delta t)=\vec{v}(t+\frac{1}{2}\Delta t)+\frac{1}{2}\vec{a}(t+\Delta t)\Delta t \qquad [2.52]$$

The appearance of explicit velocities in the equations of motion has some advantages. For instance, it is very easy to transition from the NVE to the NVT ensemble by appropriately scaling the velocities.

2.3.2 Nosé-Hoover Thermostat

In this thesis, all the simulations are performed under constant temperature. There are many ways to do this. Stochastic methods[93], in which the velocity of a random molecule in the system is reset at intervals according to a Maxwell-Boltzmann distribution, and constraint methods[94], in which the velocities of all molecules are rescaled at each time step to get to the desired temperature, are two examples. A more popular method is the extended Lagrangian method[46].

Following Nosé[95] and Hoover's work[96], the Hamiltonian of this extended system is

$$H = \sum_i^N \frac{\vec{p}_i^{\,2}}{2m_i s^2} + \frac{p_s^2}{2Q} + U(\vec{r}^{\,N}) + gk_BT \ln s \qquad [2.53]$$

where s is the additional degree of freedom, and Q and p_s are the effective mass and its momentum. g is the number of degrees of freedom plus 1. Following Hoover, the equations of motion are written as

$$\frac{d\vec{r}_i}{dt} = \frac{\vec{p}_i}{m_i} \qquad [2.54]$$

$$\frac{d\vec{p}_i}{dt} = -\frac{\partial U(\vec{r}^{\,N})}{\partial \vec{r}_i} - \zeta \vec{p}_i \qquad [2.55]$$

$$\frac{d\zeta}{dt} = \frac{1}{Q}\left(\sum_i^N \frac{p_i^2}{m_i} - gk_BT\right) \qquad [2.56]$$

$$\frac{ds}{sdt} = \frac{d \ln s}{dt} = \zeta \qquad [2.57]$$

Eq. [2.54]-[2.56] are a complete set of equations of motion and Eq. [2.57] is used to check the conservation of the system. Specifically, H in Eq. [2.53] should remain constant throughout the simulation.

Separate sets of Nosé-Hoover thermostats are applied to translational motion, rotational motion of rigid units (RUs), and charge fluctuations to define the temperature of each of these degrees of freedom with three thermostats. The relevant conserved quantity in the simulations is

$$H_{NH} = \sum_{\alpha}^{M}\sum_{i}^{N}\frac{\vec{p}_{i\alpha}^{2}}{2m_{i\alpha}} + \sum_{\alpha}^{M}\sum_{i}^{N_{RU}}\frac{I_{i\alpha}\vec{\omega}_{RU;i\alpha}^{2}}{2} + \frac{p_{tr}^{2}}{2W_{tr}} + \frac{p_{rot}^{2}}{2W_{rot}} + g_{tr}k_{B}T_{tr}\ln s_{tr} + g_{rot}k_{B}T_{rot}\ln s_{rot}$$

$$+ \sum_{\alpha}^{M}\sum_{i}^{N}\frac{p_{Q;i\alpha}^{2}}{2m_{Q}} + \frac{p_{fq}^{2}}{2W_{fq}} + g_{fq}k_{B}T_{fq}\ln s_{fq} + U(\vec{E}) \qquad [2.58]$$

where $\vec{p}_{i\alpha}$ is the linear momentum of the i^{th} atom or RU in molecule α and $m_{i\alpha}$ is the corresponding mass. $g_{fq} = M(N-1)$ and $g_{tr} = 3MN - 3$ are the numbers of degrees of freedom associated with charge fluctuation and translational motion, respectively. The former includes a correction since each molecule is constrained to be neutral, while 3 is subtracted from the translational degrees of freedom since the system, as a whole, is stationary. $I_{i\alpha}$ and $\vec{\omega}_{RU}$ are the moment of inertia tensor and angular velocity, respectively, of the RU, in the principal axis system and g_{rot} is the number of degrees of freedom for rotations. A constant temperature ensemble for the atomic positions is obtained with the fictitious variable $\eta_{tr} = \ln s_{tr}$ with a mass of W_{tr} and an associated momentum of $p_{tr} = W_{tr}\dot{\eta}_{tr}$. Similarly, a constant temperature ensemble for the rotation of rigid units is obtained with the fictitious variable $\eta_{rot} = \ln s_{rot}$ with a mass of W_{rot} and an associated momentum of $p_{rot} = W_{rot}\dot{\eta}_{rot}$. Both the translational and rotational temperatures are 298K. The atomic charges, $Q_{i\alpha}$, have a fictitious mass, m_{Q}, and associated momentum $p_{Q;i\alpha} = m_{Q}\dot{Q}_{i\alpha}$. The fictitious variables $\eta_{fq} = \ln s_{fq}$ and $p_{fq} = W_{fq}\dot{\eta}_{fq}$, with associated mass W_{fq} are defined to constrain the charges to a canonical ensemble with a temperature of $T_{fq} = 1K$. This low temperature minimizes the energy transfer between the atomic positions and the atomic charges.

2.4 Reversible Multiple Time Step MD

When the fCINTRA model is applied, the coupling between the rapid changes in atomic charge and the intramolecular potential makes the simulation unstable with typical time steps. In order to solve the problem, the simulation time step should be set to a very small number. However, this is not very efficient because it requires much longer wall time to simulate. Another way to solve the problem is to use multiple time steps and assign different steps to slow and fast motions. Our implementation of a reversible multiple time step algorithm follows from Tuckerman *et al.*[97, 98]. The basic methodology is presented below along with our extensions to the case of polarizable models.

The classical propagator is defined as

$$G(t) = e^{iLt} \qquad [2.59]$$

where $G(t)$ is a unitary operator, and L is the Liouville operator. For example, in 1-D space, the Liouville operator can be defined as

$$iL = \sum_{i=1}^{f} [\dot{x}_i \frac{\partial}{\partial x_i} + F_i \frac{\partial}{\partial p_i}] \qquad [2.60]$$

where *f* is the number of degrees of freedom of the system. The state of the system at time *t* is defined as $\Gamma(t) = \{x_i(t), p_i(t)\}$. The propagation of the system from time *t* to time $(t + \Delta t)$ is given by

$$\Gamma(t + \Delta t) = G(\Delta t)\Gamma(t) \qquad [2.61]$$

If the Liouville operator can be decomposed into two parts

$$iL = iL_1 + iL_2 \qquad [2.62]$$

according to Trotter's theorem[99], the propagator can be written as

$$G(t) = e^{i(L_1+L_2)t} = e^{iL_1\frac{t}{2}} e^{iL_2 t} e^{iL_1\frac{t}{2}} + O(t^3) \qquad [2.63]$$

So Eq. [2.61] can be rewritten as

$$\Gamma(t+\Delta t) = G(\Delta t)\Gamma(t) = (e^{iL_1\frac{\Delta t}{2}} e^{iL_2\Delta t} e^{iL_1\frac{\Delta t}{2}})\Gamma(t)$$

$$= e^{iL_1\frac{\Delta t}{2}} \{e^{iL_2\Delta t}[e^{iL_1\frac{\Delta t}{2}}\Gamma(t)]\} \qquad [2.64]$$

In each time step of an MD simulation, the rightmost operator, $e^{iL_1\frac{\Delta t}{2}}$, is applied to the old state to generate a new state. After that, $e^{iL_2\Delta t}$ is applied to the new state and then the leftmost operator, $e^{iL_1\frac{\Delta t}{2}}$, is used to get the final state at the new time step. Trotter factorization can be expanded to higher orders to improve the accuracy, but this will require the calculation of force derivatives, which may be very time-consuming[97]. Let's take a simple example and set $iL_1 = F(\vec{r})\frac{\partial}{\partial \vec{p}}$ and $iL_2 = \dot{\vec{r}}\frac{\partial}{\partial \vec{r}}$, where $\vec{p} = m\dot{\vec{r}}$. Thus, the propagator is

$$G(\Delta t) = e^{\frac{\Delta t}{2}F(\vec{r})\frac{\partial}{\partial \vec{p}}} e^{\dot{\vec{r}}\Delta t\frac{\partial}{\partial \vec{r}}} e^{\frac{\Delta t}{2}F(\vec{r})\frac{\partial}{\partial \vec{p}}} \qquad [2.65]$$

and each time step is divided into three steps. In the first step, $\dot{\vec{r}}(t)$ is propagated to $\dot{\vec{r}}(t+\frac{\Delta t}{2})$ by $e^{\frac{\Delta t}{2}F(\vec{r})\frac{\partial}{\partial \vec{p}}}$:

$$\dot{\vec{r}}(t+\frac{\Delta t}{2}) = \dot{\vec{r}}(t) + \frac{\Delta t F[\vec{r}(t)]}{2m} \qquad [2.66]$$

In the second step, $\vec{r}(t)$ is propagated to $\vec{r}(t+\Delta t)$ by $e^{\dot{\vec{r}}\Delta t\frac{\partial}{\partial \vec{r}}}$:

$$\vec{r}(t+\Delta t) = \vec{r}(t) + \Delta t\dot{\vec{r}}(\frac{\Delta t}{2}) \qquad [2.67]$$

Finally, $\dot{\vec{r}}(t+\frac{\Delta t}{2})$ is propagated to $\dot{\vec{r}}(t+\Delta t)$ by $e^{\frac{\Delta t}{2}F(\vec{r})\frac{\partial}{\partial \vec{p}}}$:

$$\dot{\vec{r}}(t+\Delta t) = \dot{\vec{r}}(t+\frac{\Delta t}{2}) + \frac{\Delta t F[\vec{r}(t+\Delta t)]}{2m} \qquad [2.68]$$

The full equations of motion can be derived by combining Eqs. [2.66]-[2.68], and it can be seen that they are equivalent to the Velocity Verlet algorithm (Eq. [2.49] and Eq. [2.50]). Since the $G(\Delta t)$ is unitary, and has the relationship $G(-\Delta t) = G^{-1}(\Delta t)$, we can get the following

$$G(-\Delta t)\Gamma(t) = G^{-1}(\Delta t)\Gamma(t) = (e^{-iL_1\frac{\Delta t}{2}}e^{-iL_2\Delta t}e^{-iL_1\frac{\Delta t}{2}})\Gamma(t) = \Gamma(t-\Delta t) \qquad [2.69]$$

Therefore, all the equations of motion derived from it are symmetric in time.

In Eq. [2.65], the momenta are propagated forward in time, by $\Delta t/2$, followed by a full time step propagation of the positions, and finally another half time step propagation of the momenta. This division can be repeated as many times as required[97]

leading to an endless family of propagators of increasing accuracy. We have found that a suitable propagator for polarizable and flexible models is

$$G(\Delta t) = e^{\frac{\Delta t}{2}F_{\vec{r}}(Q,\vec{r})\bullet\vec{\nabla}_{\vec{p}}} e^{\frac{\Delta t}{2}\dot{\vec{r}}\bullet\vec{\nabla}_{\vec{r}}} \times \left(e^{\frac{\delta t}{2}F_Q(\vec{r},Q)\frac{\partial}{\partial p_Q}} e^{\delta t\,\dot{Q}\frac{\partial}{\partial Q}} e^{\frac{\delta t}{2}F_Q(\vec{r},Q)\frac{\partial}{\partial p_Q}} \right)^M \times e^{\frac{\Delta t}{2}\dot{\vec{r}}\bullet\vec{\nabla}_{\vec{r}}} e^{\frac{\Delta t}{2}F_{\vec{r}}(Q,\vec{r})\bullet\vec{\nabla}_{\vec{p}}} \qquad [2.70]$$

where the charge-related operators are placed in the center bracket which will be iterated M times with a smaller time step of $\delta t = \Delta t / M$. In this way, the overall time step Δt is consistent with the time scale for nuclear motion but the charges vary over the smaller time step δt. The propagator in Eq. [2.70] leads to an important reduction in simulation cost since the atomic positions, and associated CPU intensive force calculations, are minimized.

In our simulation, the fictitious variables from Nosé-Hoover thermostats also vary with time and must be included. The complete, reversible propagator is[91]

$$G(\Delta t) = e^{\frac{\Delta t}{2}F_{\eta tr}(\vec{p}_{i\alpha})\frac{\partial}{\partial p_{tr}}} \left[e^{\frac{\Delta t}{4}F_{\vec{r}}(Q,\vec{r})\bullet\vec{\nabla}_{\vec{p}}} e^{-\frac{\Delta t}{2}\dot{\eta}_{tr}\vec{p}\bullet\vec{\nabla}_{\vec{p}}} e^{\frac{\Delta t}{4}F_{\vec{r}}(Q,\vec{r})\bullet\vec{\nabla}_{\vec{p}}} \right] e^{\frac{\Delta t}{2}\dot{\eta}_{tr}\frac{\partial}{\partial\eta_{tr}}} e^{\frac{\Delta t}{2}\dot{\vec{r}}\bullet\vec{\nabla}_{\vec{r}}} \times$$

$$\left(e^{\frac{\delta t}{2}F_{\eta fq}(p)\frac{\partial}{\partial p_{fq}}} \left[e^{\frac{\delta t}{4}F_Q(\vec{r},Q)\frac{\partial}{\partial p_Q}} e^{-\frac{\delta t}{2}\dot{\eta}_{fq}p_Q\frac{\partial}{\partial p_Q}} e^{\frac{\delta t}{4}F_Q(\vec{r},Q)\frac{\partial}{\partial p_Q}} \right] e^{\frac{\delta t}{2}\dot{\eta}_{fq}\frac{\partial}{\partial\eta_{fq}}} e^{\delta t\,\dot{Q}\frac{\partial}{\partial Q}} e^{\frac{\delta t}{2}\dot{\eta}_{fq}\frac{\partial}{\partial\eta_{fq}}} \times \right.$$

$$\left. \left[e^{\frac{\delta t}{4}F_Q(\vec{r},Q)\frac{\partial}{\partial p_Q}} e^{-\frac{\delta t}{2}\dot{\eta}_{fq}p_Q\frac{\partial}{\partial p_Q}} e^{\frac{\delta t}{4}F_Q(\vec{r},Q)\frac{\partial}{\partial p_Q}} \right] e^{\frac{\delta t}{2}F_{\eta fq}(p)\frac{\partial}{\partial p_{fq}}} \right)^M$$

$$\times e^{\frac{\Delta t}{2}\dot{\vec{r}}\bullet\vec{\nabla}_{\vec{r}}} e^{\frac{\Delta t}{2}\dot{\eta}_{tr}\frac{\partial}{\partial\eta_{tr}}} \left[e^{\frac{\Delta t}{4}F_{\vec{r}}(Q,\vec{r})\bullet\vec{\nabla}_{\vec{p}}} e^{-\frac{\Delta t}{2}\dot{\eta}_{tr}\vec{p}\bullet\vec{\nabla}_{\vec{p}}} e^{\frac{\Delta t}{4}F_{\vec{r}}(Q,\vec{r})\bullet\vec{\nabla}_{\vec{p}}} \right] e^{\frac{\Delta t}{2}F_{\eta tr}(\vec{p}_{i\alpha})\frac{\partial}{\partial p_{tr}}} \qquad [2.71]$$

where time derivatives are identified by superscript dots, square brackets identify single applications of Trotter's rule[99], round brackets isolate the inner loop with the smaller time step, and $M\delta t = \Delta t$. The variables associated with the charges are advanced in the inner loop with the small time step of δt. The force associated with charge fluctuations, $F_Q(\vec{r}, Q)$, is evaluated in the inner loop and requires the charge dependence of the electrostatic energy, the field dependence of the intramolecular potential, and the charge dependence of the field. These terms can each be evaluated efficiently since, although they are complex, their dependence on charge is straightforward. The application of Eq. [2.71] can be divided into three stages: the advancement of positions, momenta, η, and $\dot{\eta}$ by $\Delta t/2$; the iterative inner loop advancement, in steps of δt ,of the charges, their associated momenta, η_{fq}, and $\dot{\eta}_{fq}$; and the final advancement of positions, momenta, η, and $\dot{\eta}$. The equations of motion are given explicitly below. In the first stage, the equations of motion are

$$p_{tr}(t+\Delta t/2) = p_{tr}(t) + \frac{\Delta t}{2} F_{\eta_{tr}}(t) \quad \vec{p}_{i\alpha}(t+\Delta t/2) = [\vec{p}_{i\alpha}(t) + \frac{\Delta t}{4} F_{\vec{r}}(t)] e^{-p_{tr}(t+\Delta t/2)\frac{\Delta t}{2W_{tr}}} + \frac{\Delta t}{4} F_{\vec{r}}(t)$$

$$\eta_{tr}(t+\Delta t/2) = \eta_{tr}(t) + \frac{\Delta t}{2W_{tr}} p_{tr}(t+\Delta t/2)$$

$$\vec{r}_{i\alpha}(t+\Delta t/2) = \vec{r}_{i\alpha}(t) + \frac{\Delta t}{2m_{i\alpha}} \vec{p}_{i\alpha}(t+\Delta t/2)$$

where $F_{\vec{r}}(t)$ is the force on the atomic positions evaluated in the previous time step. $F_{\eta_{tr}}(t)$ is given by

$$F_{\eta_{tr}}(t) = \sum_{\alpha}^{M} \sum_{i}^{N} \frac{\vec{p}_{i\alpha}^{2}(t)}{m_{i\alpha}} - g_{tr} k_B T_{tr} .$$

The second stage consists of the following steps:

$$p_{fq}(t'+\delta t/2) = p_{fq}(t') + \frac{\delta t}{2} F_{\eta_{fq}}(t')$$

$$p_{Q;i\alpha}(t'+\delta t/2) = [p_{Q;i\alpha}(t') + \frac{\delta t}{4} F_Q(t')] e^{-p_{fq}(t'+\delta t/2)\frac{\delta t}{2W_{fq}}} + \frac{\delta t}{4} F_Q(t')$$

$$\eta_{fq}(t'+\delta t) = \eta_{fq}(t') + \frac{\delta t}{2W_{fq}} p_{fq}(t'+\delta t/2)$$

$$Q_{i\alpha}(t'+\delta t) = Q_{i\alpha}(t') + \delta t \frac{p_{Q;i\alpha}(t'+\delta t/2)}{m_Q}$$

$$p_{Q;i\alpha}(t'+\delta t) = [p_{Q;i\alpha}(t'+\delta t/2) + \frac{\delta t}{4} F_Q(t'+\delta t)] e^{-p_{fq}(t'+\delta t/2)\frac{\delta t}{2W_{fq}}} + \frac{\delta t}{4} F_Q(t'+\delta t/2)$$

$$p_{fq}(t'+\delta t) = p_{fq}(t'+\delta t/2) + \frac{\delta t}{2} F_{\eta_{fq}}(t'+\delta t) .$$

These steps are iterated M times to yield $Q_{i\alpha}(t+\Delta t)$, $p_{q;i\alpha}(t+\Delta t)$, $\eta_{fq}(t+\Delta t)$, and $\dot{\eta}_{fq}(t+\Delta t)$. The force on the charges $F_Q(t')$ is evaluated at each step of the inner loop. The force $F_{\eta_{fq}}(t')$ is given by

$$F_{\eta_{fq}}(t') = \sum_{\alpha}^{M} \sum_{i}^{N} \frac{p_{Q;i\alpha}^{2}(t')}{m_Q} - g_{fq} k_B T_{fq} .$$

The third stage is similar to the first, and consists of the following sequence of time steps:

$$\vec{r}_{i\alpha}(t+\Delta t) = \vec{r}_{i\alpha}(t+\Delta t/2) + \frac{\Delta t}{2m_{i\alpha}} \vec{p}_{i\alpha}(t+\Delta t/2)$$

$$\eta_{tr}(t+\Delta t) = \eta_{tr}(t+\Delta t/2) + \frac{\Delta t}{2W_{tr}} p_{tr}(t+\Delta t/2)$$

$$\vec{p}_{i\alpha}(t+\Delta t) = [\vec{p}_{i\alpha}(t+\Delta t/2) + \frac{\Delta t}{4} F_{\vec{r}}(t+\Delta t)] e^{-p_{tr}(t+\Delta t/2)\frac{\Delta t}{2W_{tr}}} + \frac{\Delta t}{4} F_{\vec{r}}(t+\Delta t)$$

$$p_{tr}(t+\Delta t) = p_{tr}(t+\Delta t/2) + \frac{\Delta t}{2} F_{\eta_{tr}}(t+\Delta t).$$

2.5 Quantum Mechanics Methods

2.5.1 *Ab initio* calculations

Ab initio, or first principles, calculations predict the properties of molecular systems without using any empirical data. In this thesis, *ab initio* calculations are used for intramolecular potentials, atomic charges, and to parameterize polarizable force fields. A main disadvantage of this approach is that it is very time consuming.

The theory starts with the Schrödinger equation that governs the behavior of the system:

$$\hat{H}\Psi = E\Psi \qquad [2.72]$$

where E is the total energy of the system and Ψ is the wavefunction

$$\Psi = \Psi(\vec{R}_1, \vec{R}_2, ..., \vec{R}_n, \vec{r}_1, \vec{r}_2, ..., \vec{r}_m) \qquad [2.73]$$

where $\vec{R}$ and $\vec{r}$ are the positions of the nuclei and electrons, respectively, and n and m are the number of nuclei and electrons in the system, respectively. $\hat{H}$ is the Hamiltonian operator that is given by

$$\hat{H} = -\frac{\hbar^2}{2m_e}\sum_i \nabla_i^2 - \frac{\hbar^2}{2}\sum_k \frac{\nabla_k^2}{M_k} + \frac{1}{2}\sum_{i\neq j}\frac{e^2}{|r_i - r_j|} + \frac{1}{2}\sum_{k\neq l}\frac{Z_k Z_l}{|R_k - R_l|} - \sum_{k\neq l}\frac{eZ_k}{|r_i - R_k|}$$

[2.74]

where *i*,*j* and *k*,*l* refer to electrons and nuclei, respectively, m_e and M_k are the electron and nucleus masses, respectively, and atomic units are used. Eq. [2.74] can be written as

$$\hat{H} = \hat{T}_e + \hat{T}_n + \hat{U}_{ee} + \hat{U}_{nn} + \hat{U}_{en} \qquad [2.75]$$

where $\hat{T}_e$ and $\hat{T}_n$ are kinetic energies of the electrons and nuclei, respectively, and $\hat{U}_{ee}$, $\hat{U}_{nn}$, and $\hat{U}_{en}$ are the potential energies of electron-electron, nucleus-nucleus, and electron-nucleus interactions. Because nuclei weigh about 2000 times more than electrons, Schrödinger equation can be roughly divided into nuclear and electronic equations. This approximation is the well-known Born-Oppenheimer approximation. Focusing on the electronic Hamiltonian, one has

$$\hat{H}_e = -\frac{\hbar^2}{2m_e}\sum_i \nabla_i^2 + \frac{1}{2}\sum_{i\neq j}\frac{e^2}{|r_i - r_j|} - \sum_{k\neq l}\frac{eZ_k}{|r_i - R_k|} \qquad [2.76]$$

2.5.2 Density function theory

DFT is a very popular method for electronic structure calculations in chemistry and solid-state physics. In DFT, the Hohenberg-Kohn theorem[100] states that the expectation value of any operator depends only on the ground state electronic density. Kohn and Sham[101] developed a method to find the ground state density and energy. In the theory, the energy of the real system with respect to the electron density, $n(\vec{r})$, is given by

$$E[n] = T[n] + V[n] + U[n] \qquad [2.77]$$

where $T[n]$ is the kinetic energy, $U[n]$ is the two-body electron-electron interaction, and $V[n] = \int V(\vec{r})n(\vec{r})d^3\vec{r}$ is the energy due to the external potential from the nuclei. To minimize the energy functional, it can be written as a density functional of non-interacting particles:

$$E_s[n] = \langle \psi_s[n] \,|\, T_s + V_s \,|\, \psi_s[n] \rangle \qquad [2.78]$$

where T_s is the kinetic energy of the non-interacting electrons, V_s is the external potential, and the density of the non-interacting system, $n_s(\vec{r})$, is equal to the density of interest, $n(\vec{r})$. The full ground state energy of a real system is written as

$$E_0 = E[n_0] = -\sum_{\alpha} Z_\alpha \frac{n_0(\vec{r}_1)}{r_{1\alpha}} d\vec{r}_1 - \frac{1}{2}\sum_i \left\langle \theta_i^{KS}(1) \,|\, \nabla_1^2 \,|\, \theta_i^{KS}(1) \right\rangle + \frac{1}{2}\iint \frac{n_0(\vec{r}_1)n_0(\vec{r}_2)}{r_{12}} d\vec{r}_1 d\vec{r}_2 + E_{xc}[n_0] \qquad [2.79]$$

The first three terms are the electron-nuclear interaction energy, the average ground state kinetic energy of non-interacting electrons, and the electron-electron interaction energy, respectively. The last term, $E_{xc}[n_0]$, is the Kohn-Sham exchange-correlation energy. The exchange-correlation potential is the derivative of the exchange-correlation energy

$$V_{xc}(\vec{r}) = \frac{\delta E_{xc}[n_0(\vec{r})]}{\delta n_0(\vec{r})} \qquad [2.80]$$

The spatial part of Kohn-Sham orbital, θ_i^{KS}, is determined by solving the Kohn-Sham equations of the non-interacting system iteratively:

$$[-\frac{1}{2}\nabla_i^2 + V_s(\vec{r})]\theta_i^{KS}(\vec{r}) = \varepsilon_i \theta_i^{KS}(\vec{r}) \qquad [2.81]$$

where ε_i are Kohn-Sham orbital energies and the electron density is given by $n(\vec{r}) = \sum_i |\theta_i^{KS}(\vec{r})|^2$.

An important problem of this method is that the Kohn-Sham exchange-correlation functional E_{xc} is unknown. One of the most popular exchange-correlation functionals is the B3LYP, which is a hybrid functional combining the local-spin-density approximation exchange functional[102], the Lee-Yang-Par correlation functional[103], and the Becke's exchange functional[98], which is combined with the exact energy from Hartree-Fock theory.

DFT generally gives accurate results for most properties such as molecular geometries, frequencies and dipole moment, and is much more efficient than perturbation theory, coupled cluster methods and Configuration Interaction method.

2.5.3 Basis sets

In quantum calculations, the molecular orbitals are represented by linear combinations of basis functions:

$$\phi_i = \sum_i c_i \chi_i \qquad [2.82]$$

where χ_i are atom-centered basis functions and c_i are the variational coefficients. There are many choices of basis functions. Slater type orbitals (STOs) are a natural choice, but they are computationally expensive and impractical for nonlinear polyatomic systems. An alternative to STOs is the Gaussian-type functions (GTFs). A Cartesian Gaussian centered on a nucleus is defined as $g_{i,j,k} = Nx^i y^j z^k e^{-\alpha r^2}$, where N is the normalization coefficient, α is a positive orbital exponent, *i*,*j*,*k* are nonnegative integers, and *x*, *y*, *z* are Cartesian coordinates with the origin at the nucleus. However, a single GTF cannot reproduce an STO very well, because it has no cusp at the nucleus and decays to zero too quickly. Thus, the contracted Gaussian-type functions (CGTFs) are more commonly used. CGTFs, often referenced to as primitives, are linear combinations of GTFs and can better reproduce the STOs. For example, in the STO-3G basis set, each STO is reproduced by three GTFs. The minimal basis set has one basis function for each occupied atomic orbital. Multiple-zeta basis set has multiple CGTFs for each occupied atomic orbital. For instance, cc-pVDZ represents two CGTFs for each atomic orbital. A more popular type of basis set is the split valence basis set, which applies multiple-zeta basis functions to valence orbitals and single-zeta basis functions to core orbitals.

In molecules, atomic orbitals (AOs) are distorted. In order to account for this shape distortion, additional Gaussian functions with high angular momenta, called polarization functions, are required. For instance, 6-311G(d,p) basis set has 6 primitive Gaussians for each inner-shell AO, and each valence-shell AO is represented by 3 CGTFs, one formed by three pieces composed of three Gaussian primitives, one Gaussian primitive, and one Gaussian primitive. The "(d,p)" denote that a set of 6 d-type Gaussian functions is added to nonhydrogen atoms and a set of 3 p-type Gaussian functions is

added to hydrogen atoms. For some molecules, such as anions and those with lone pairs, the electron density is still very significant at large distances from the nuclei. To improve the accuracy of treating such molecules, highly diffuse functions with a very small orbital exponent can be added. For instance, the aug-cc-pVDZ basis set augments the cc-pVDZ basis by additional slowly decaying s, p and d Gaussian functions.

2.5.4 Atomic charges

There are many different definitions and algorithms to assign atomic charges [104-109]. Mulliken population analysis approach [104-106, 108] is one of the most often used. In this approach, atomic charges are assigned on the basis of atomic orbital populations.

Another approach of obtaining atomic partial charges is to fit the molecular electrostatic potential (MEP). The MEP at position $\vec{r}_1$ is:

$$\phi(\vec{r}_1) = \sum_{\alpha} \frac{Z_\alpha}{r_{1\alpha}} - \int \frac{n(\vec{r}_2)}{r_{12}} d\vec{r}_2 \qquad [2.83]$$

where Z_α and $n(\vec{r}_2)$ are the charge on nucleus α and the charge density at position $\vec{r}_2$, respectively, and the first and second terms are the nuclear and electronic part, respectively. The atomic partial charges are fitted to reproduce the MEP at a number of points:

$$\phi^{fitting}(\vec{r}_1) = \sum_{\alpha} \frac{Q_\alpha}{r_{1\alpha}} \qquad [2.84]$$

and the charges are obtained by least square fit to minimized the following

$$f = \sum_{i=1}^{N} [\phi^{fitting}(\vec{r}_i) - \phi^{calculated}(\vec{r}_i)]^2 \qquad [2.85]$$

where N is the total number of points used in the MEP.

In this thesis, the CHarges from Electrostatic Potentials using a Grid based method (CHELPG) scheme[110], which is one of the most common schemes, is used to obtain atomic charges. We choose this scheme because the charges calculated by CHELPG depend on the environment and the actual potential, which is a feature we want to integrate into our simulation.

2.5.5 Conformational Minimization

In order to obtain the most stable molecular structures, conformational minimization is needed to get the local energy minima. The potential energy surface of a molecule has 3N-6 degrees of freedom, where N is the number of atoms in the molecule. Starting from the input geometry, the potential energy and its first derivatives are calculated and then the 3N-6 degrees of freedom are changed to get a lower potential energy. This procedure is iterated until a local minimum is found. Large molecules normally have many local minima, and in order to locate the global minimum, it is necessary to repeat the search procedure for different starting geometries.

In this thesis, DFT calculations are used to obtain equilibrium structures and intramolecular potentials of solvents, such as ethanol, benzyl alcohol, and 2-propanol. B3LYP/6-311++G(d,p), B3LYP/6-311G(d,p) and B3LYP/aug-cc-pVDZ calculations are performed for ethanol, benzyl alcohol, and 2-propanol, respectively. For ethanol, the intramolecular motion is divided into 8 stretches, 13 bends, and 2 torsions. For benzyl

alcohol, since the aromatic ring is very rigid, only 5 stretches, 9 bends, 2 torsions, and 1 improper torsion are chosen to represent the molecular flexibility. For 2-propanol, 19 bends and 3 torsions are employed to represent intramolecular motion.

Each stretching force constant is extracted from nine energy calculations, as the bond is compressed and stretched away from the equilibrium value. Bending potentials are obtained by least squares fits to nine energy calculations where the angle is varied within sixteen degrees of the equilibrium value. For torsion potentials, the angle is varied from 0 to 360^{o}, in steps of 10 degrees. Each of the improper torsion potentials is obtained from nine restricted geometry optimizations.

DFT calculations are also used to obtain the FC and fCINTRA parameters. The details will be described in Chapter 3.

2.6 Chirality indexes

The aim of this thesis is to study the transfer of chirality from chiral solutes or surfaces to achiral solvents. Therefore, it is very important to find a way to quantify the chirality. As introduced in the previous chapter, chirality indexes have been a subject of continuing interest over the past fifteen years. Most of the proposed measures are not suited to this particular study since the chirality measure employed here should be evaluated from individual solvent molecules. The measure should also be unchanged by a simple translation or rotation of the solvent, should change signs upon reflection, should average to zero for solvent in an achiral environment, and should be fast to calculate since millions of calculations will be required in MD simulations. With these considerations, we use a chirality index which was originally developed by Osipov *et*

al[66]. Our implementation includes a modification introduced by Solymosi *et al*.[111] to partially correct for a strong dependence on the number of atoms *N* in the molecule. The chiral index is defined as:

$$G_{0S}^{w} = \frac{8}{N!}\left[\sum_{i,j,k,l=1\ldots N} w_i w_j w_k w_l \times \frac{[(\vec{r}_{ij} \times \vec{r}_{kl}) \cdot \vec{r}_{il}](\vec{r}_{ij} \cdot \vec{r}_{jk})(\vec{r}_{jk} \cdot \vec{r}_{kl})}{(r_{ij} r_{jk} r_{kl})^{n} r_{il}^{\ m}}\right] \qquad [2.86]$$

where the sum runs over all combinations of four atoms in the molecule. The superscript of G_{0S}^{w} shows the type of atomic weights, where *1*, *q* and *m* correspond to unity, atomic charges and atomic masses, respectively. From Eq. [2.86], G_{0S}^{w} has a strong dependence on molecular structure, as reflected by the presence of interatomic vectors. Dependence on other properties can be included via the atomic weights, w_i , that can be chosen to be atomic charges, van der Waals radii, atomic masses, and so on. The powers *n* and *m* in the denominator of Eq. [2.86] can be chosen to emphasize the contributions from atoms well separated within the molecule (small values for *m* and *n*) or atoms that are close together (large values for *m* and *n*).

A strictly shape-dependent index can be obtained by choosing all weights equal to unity in Eq. [2.86]. The resulting index, G_{0S}^{1} , gives equal weighting to all the atoms and reflects only the asymmetry of the atomic positions. In addition to this index, we explore indexes G_{0S}^{m} and G_{0S}^{q} , where the weights are atomic masses and atomic charges, respectively. The former will de-emphasize the hydrogen atoms and, for the ethanol, 2-propanol, and benzyl alcohol solvents, terms involving the oxygen and carbon atoms will contribute most to G_{0S}^{m}. The latter index, where the terms are weighted by the atomic charges, will place greater emphasis on the alcohol group of the solvents where the

atomic charges are largest. For G^1_{0S}, when the powers *m* and *n* in Eq. [2.86] are set to 1 and 2, respectively, the index becomes dimensionless.

Regardless of the choice of atomic weights, or *m* and *n,* in Eq. [2.86], the indexes are zero for an achiral solvent structure. To see the response of G^w_{0S} to reflection, consider the term $[(\vec{r}_{12}\times\vec{r}_{34})\cdot\vec{r}_{14}](\vec{r}_{12}\cdot\vec{r}_{23})(\vec{r}_{23}\cdot\vec{r}_{34})$ in Eq. [2.86]. If the mirror operation is performed, $[(\vec{r}_{12}\times\vec{r}_{34})\cdot\vec{r}_{14}]$ will change sign but $(\vec{r}_{12}\cdot\vec{r}_{23})$ and $(\vec{r}_{23}\cdot\vec{r}_{34})$ will stay the same, and the whole term will change sign. Thus, all indexes obtained from Eq. [2.86] will change sign for the mirror-image molecule. Within the simulations, this symmetry ensures that all indexes will average to zero for solvents in an achiral environment. In addition, translational and rotational invariance follows from Eq. [2.86] since the indexes are determined from dot products of interatomic vectors and these are unchanged by translation and molecular reorientation. Thus, as required, the instantaneous index reflects the shape of the molecule but not its position or orientation.

Despite these important advantages, there is one important concern with the use of G^w_{0S}. As discussed by Solymosi[111], the index depends on the number of atoms in the molecule: They introduced the *N!* term in Eq. [2.86] to partially eliminate this dependence. Nonetheless, a residual dependence remains and we cannot compare the magnitude of the excess chirality $< G^w_{0S} >$ for the two different solvents. However, we are most interested in the impact of various chiral solutes on a given solvent and, for this, $<G^w_{0S}>$ can be compared.

G_{0S}^{w} will generally have units, and its magnitude depends on the molecule under examination, on the weights chosen in Eq. [2.86], and on the values for *m* and *n*. Take ethanol as an example, to ascertain "typical" values for the indexes, Fig. 2.9 presents $G_{0S}^{1}, G_{0S}^{q}, G_{0S}^{m}$ for a single ethanol molecule as a function of two torsional angles. Clearly, the indexes respond differently to changes in the molecular conformation. When the molecule is in an achiral environment, each index in Fig. 2.9 will be sampled over time to yield an excess chirality of zero. In a chiral environment, complete cancellation will not occur and a non-zero excess chirality will be achieved. When the solvent happens to have an instantaneously achiral structure, all three indexes will be simultaneously zero.

2.7 Surface representations

In this thesis, the interfacial chirality transfer is studied for three brush-type selective interfaces that include amide linkages and DNB (dinitrobenzoyl) groups: Whelk-O1, based on a 1-(3,5-dinitrobenzamido)-1,2,3,4-tetrahydrophenanthrene chiral selector; DNB-phenylglycine, based on a N-(3,5-dinitrobenzoyl)-phenylglycine selector; and DNB-leucine, based on a N-(3,5-dinitrobenzoyl)-leucine selector are considered. These three selectors are shown in Fig. 2.10. The atom numbering provided in the figure will be used throughout this thesis. The Whelk-O1 selector (Fig. 2.10(a)) consists of a dinitrophenyl group and a 1,2,3,4-tetrahydrophenanthrene group joined by an amide linkage. The selector includes two chiral carbons [C(9) and C(10) in Fig. 2.10(a)], one connecting the 1,2,3,4-tetrahydrophenanthrene group to the amide linkage and the other joining the selector to the alkyl tether that, in turn, connects to the underlying surface. As shown in Fig. 2.10(b) and (c), DNB-leucine and DNB-phenylglycine selectors are

structurally similar: the two selectors consist of a dinitrophenyl group, a chiral carbon [C(15) in Figs. 2.10(b) and 2.10(c)] located between two amide linkages, a lateral group (a phenyl ring for DNB-phenylglycine and an isobutyl chain for DNB-leucine), and a tether that bonds the selector to the surface. Despite their similarity *ab initio* calculations[112] indicate that the difference in the lateral group is sufficient to significantly alter the conformational energetics of the selectors [112]. In particular, these two selectors have distinct minimum energy conformers, DNB-leucine has several low energy conformers whereas DNB-phenylglycine has only one conformer within 12.0 kJ/mol of the global energy minimum. More detailed descriptions of all three selectors can be found elsewhere [112, 113].

A side view of a typical simulation cell is shown in Fig. 2.10(d). The simulation cell includes two interfaces, with solvents in between. In order to be consistent with experiment[114-116], the model interface includes silanol groups and trimethylsilyl end caps on the silicon surface. For all three model CSPs, the selector surface coverage is 1.07μmol/m^2, the surface density of trimethylsilyl end-caps is 3.20 μmol/m^2, and silanol groups are present at a density of 4.26μmol/m^2. A selective surface consists of a total of 9 selectors, 27 trimethylsilyl end caps, 36 silanol groups, and an underlying layer of 72 silicon atoms, with a Si-Si distance of 3.2Å. Empty space is placed above the top layer and below the bottom layer in order to minimize interactions between the periodic images in z direction, and the simulation cell is duplicated in three dimensions. Ewald summations with a correction for the rectangular prism shape of the simulation cell[40] are used to evaluate electrostatic interactions.

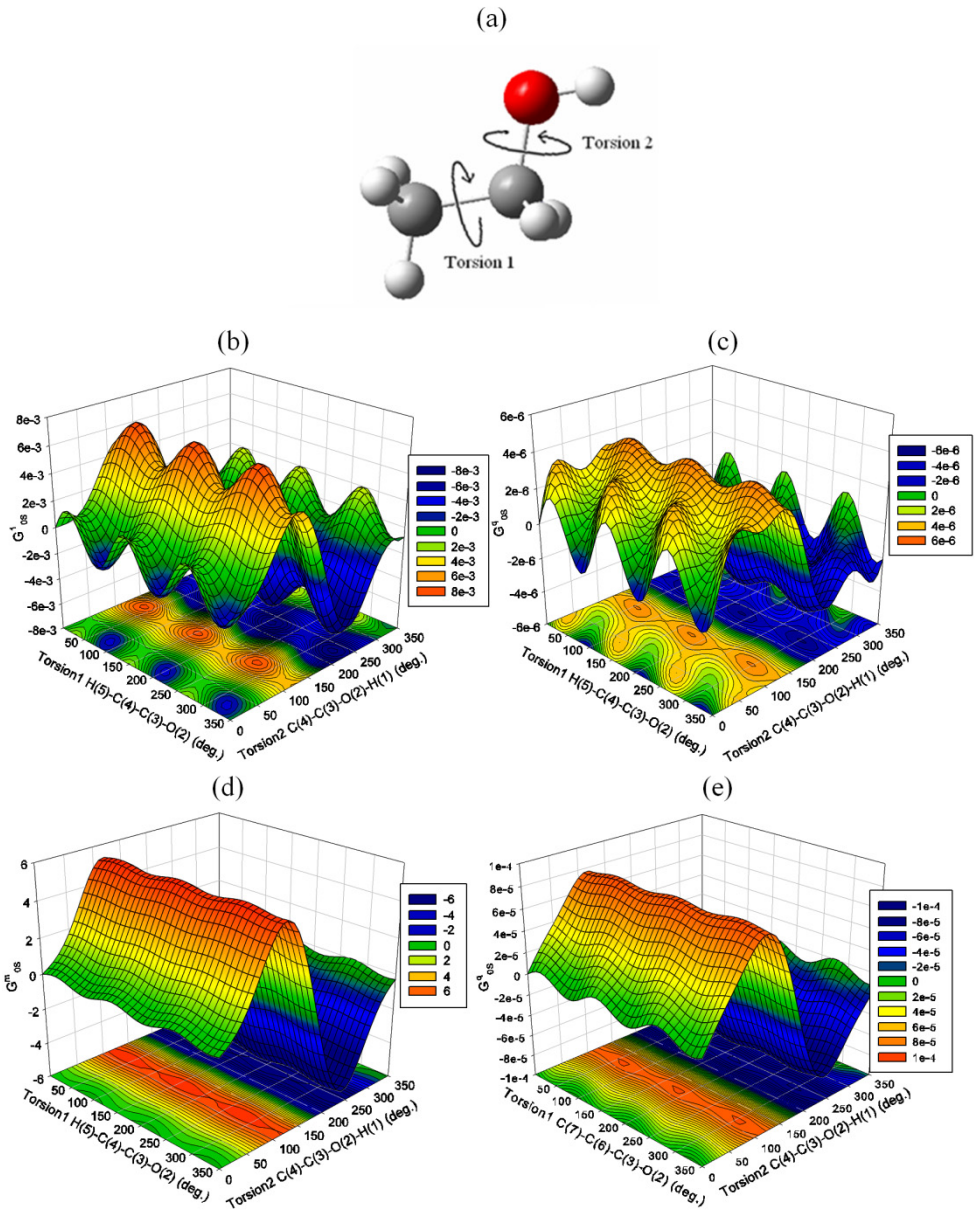

Figure 2.9. The influence of torsional angles on chirality indexes of ethanol. Panel (a) shows the two torsions under consideration. For the conformation shown in Panel (a), both torsion 1 and torsion 2 are 180 degrees. Panels (b), (c), and (d) show G^{1}_{OS}, G^{q}_{OS}, G^{m}_{OS}, respectively, as the torsional angles vary. The atomic charges from the *ab initio* calculations are used for (b). Panel (e) presents G^{q}_{OS} for a different set of average atomic charges observed in the simulations.

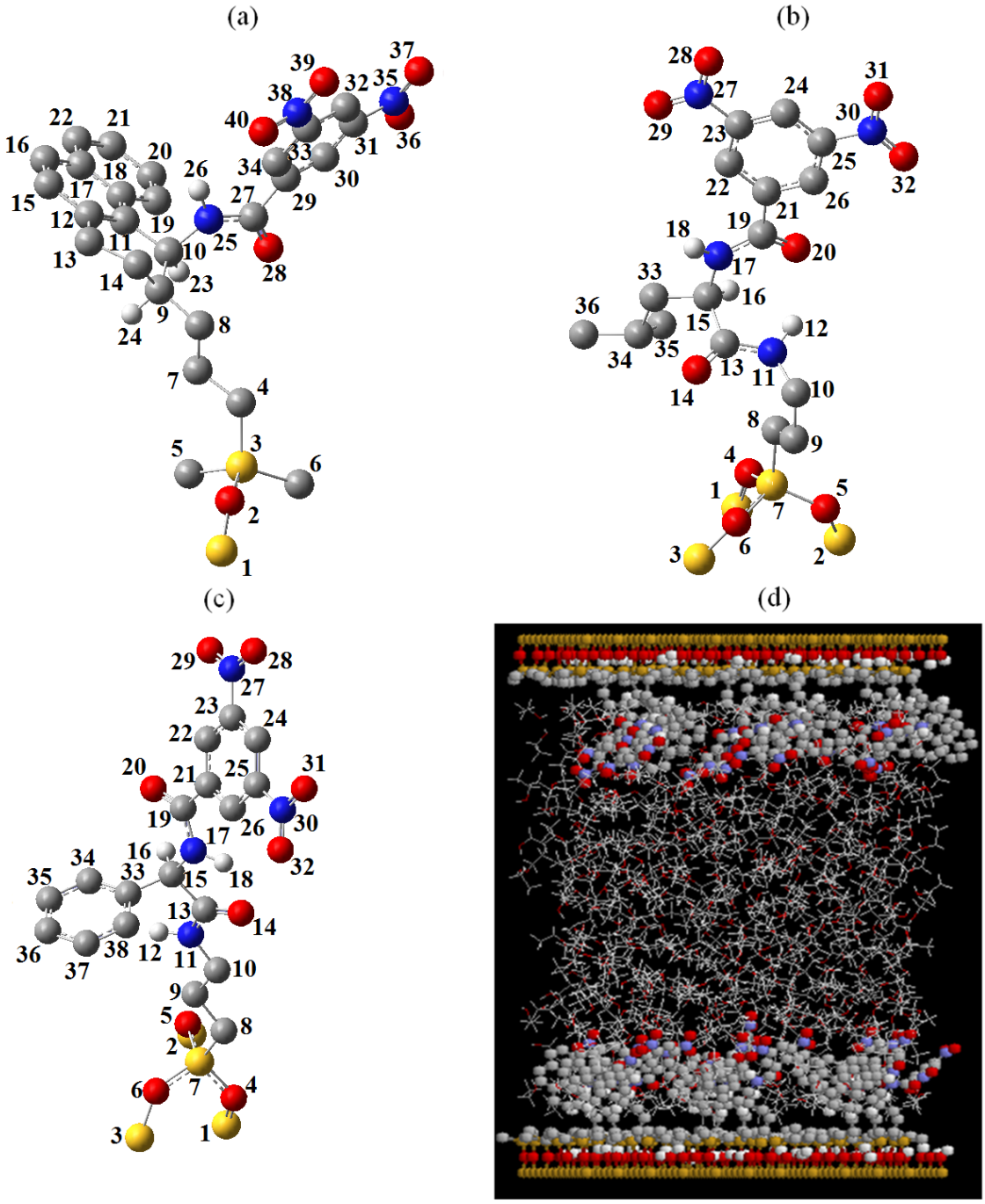

Figure 2.10. Molecular structures and numbering system for (a) Whelk-O1, (b) DNB-leucine, (c) DNB-phenylglycine. The atom numbering will be used throughout this chapter. Panel (d) provides a side view of a typical simulation cell. In this case, the Whelk-O1 surface in the presence of ethanol is shown. Silicon, oxygen, hydrogen, nitrogen, and carbon are shown in yellow, red, white, blue, and grey respectively. Solvent atoms are shown in wireframe. Please note that the hydrogen atoms connected to achiral carbons are omitted for simplicity.

Within the simulations, the chiral selectors are semi-flexible. In particular, the rings are kept rigid while the rest of the molecule is flexible. The atoms within these rigid units do not move relative to each other but rather they collectively translate and rotate according to their aggregate forces. The conserved quantity in the simulations is the Nosé-Hoover Hamiltonian (H_{NH}), which is defined in Eq. [2.58].

2.8 Practical considerations

All the simulations were performed using the MDMC program that originated from our group. Prior to this work, the MDMC program had been applied to simulations of bulk phases and interfacial systems using non-polarizable models. To achieve the objectives of this thesis, the program has been modified extensively to include the charge fluctuation model, the field-dependent intramolecular potential, the multiple time step algorithm, and chirality index collection.

The charge fluctuation model requires additional force calculations and new equations of motion, so the relevant part of the program has been modified. The field-dependent intramolecular potential requires new force calculation subroutines and a multiple time scale approach. For the latter, each inner step requires force calculations, which is very time-consuming. Therefore, much effort has been used to improve the efficiency of the calculations.

The non-bonding force calculations and the evaluation of forces from the field-dependent intramolecular potential are the most time-consuming aspects of the

computation. We have parallelized this segment of the code to allow for rapid computation of the forces. More specifically, the message-passing interface (MPI) has been employed. The message passing model is defined as a set of processes that have local memory and communicate with each other by sending and receiving messages. In the simulation program, a master/slave model is used. All the serial work, such as the initialization and input/output, is done on the master node. Also, the computationally inexpensive parts of the simulation, such as the intramolecular force calculation and integration of equations of motion, are done on the master node. The time-consuming parts of the simulation, such as the LJ forces and Ewald summation, are implemented in parallel on both master and slave nodes. In each time step, the master node distributes the task evenly on all processes and sends the necessary information to all the slave nodes using broadcast statements. After calculations are done, all nodes send their part back to the master node, which then sums up the results. The implementation of MPI in the simulation has been optimized to minimize the communication time. Our simulations are performed on High Performance Computing Virtual Laboratory (HPCVL), Westgrid and SHARCNET high performance computing facilities. Most of the single processor simulations are performed on Westgrid (Glacier) and most of the MPI simulations are performed on Requin and Narwhal clusters of SHARCNET. Our parallel simulations use 8 processors and are about 7.5 times as fast as simulations with single processor. About 20-30 independent simulations are performed for each solute/solvent and surface/solvent pair and, as a rough guide, each simulation requires roughly two weeks of simulation time.

Chapter 3
Development of a polarizable and flexible model

Intuitively, chirality transfer and polarization are closely related. In this chapter, methodology for developing a polarizable and flexible model (the fCINTRA model) is discussed in detail. All aspects of the model design are discussed along with details of the simulations, including the implementation of a multiple time step molecular dynamics algorithm. This methodology is general and can be applied to any molecules. In this chapter, an example has been provided for ethanol and the results of MD simulations with this model are analyzed and compared with experiments and other popular models.

3.1 Introduction

Hydrogen bonding in alcohols is complex and quite different from bulk water [117]. Neutron diffraction[118], *ab initio* calculations[119], and simulations[120] show that bulk methanol under supercritical conditions is characterized by monomers and small hydrogen-bonded rings. Under ambient conditions, it has been suggested[121] that methanol prefers closed-chain hydrogen-bonded hexamers. The situation is less clear for ethanol[117, 122] where hydrogen-bonded networks have been assumed to prefer tetrameric loops, hexameric loops, U-shapes, or coils. A recent neutron diffraction[123] study, along with previous X-ray[124] and neutron diffraction[125] work on ethanol, provides increasingly accurate experimental interatomic distributions in the bulk. Ethanol has also been the subject of several statistical mechanics studies [43, 45, 126,

127]. The simplest molecular models for ethanol[128, 129] have fixed-charges on the atoms and are pairwise-additive. Fixed-charge transferable potentials, such as OPLS[127], have been well studied for alcohols[127]. The use of fixed charges means that the molecules are not polarized by the local electric field: An important effect for hydrogen-bonded liquids[47].

The importance of polarizability, and the impact of its inclusion, are well understood for water where a variety of polarizable models have been designed [42, 46, 47, 130]. In this thesis, we employ the FC model to govern the atomic charge fluctuations in bulk ethanol. Relative to other polarizable models, ours is unique in one important respect: It includes field dependence in both the atomic charges and the intramolecular degrees of freedom. In this way, the model reflects the field-induced redistribution of electrons that results in instantaneous changes to atomic charges and to the potential energy surface that defines intramolecular motion. This is particularly important for the torsional motion governing the position of the hydrogen-bonding hydrogen: We find that this potential is highly field-dependent and, in some fields the minima appear at very different angles relative to the zero-field potential. Thus, the optimal position of the hydrogen depends on the field experienced by the molecule and this will, in turn, influence the hydrogen bonding structure in the fluid. As mentioned in Chapter 1, a field-dependent intramolecular potential has been attempted only once previously. In that study, the HH and OH stretching potentials of water depended on the magnitude of the field of oxygen but the atomic charges were field-independent [57]. Aside from this one exception, existing polarizable flexible models fully separate the molecular flexibility from the field response.

Persuasive arguments for a systematic application of the FC method have been presented by Patel and Brooks[53] and Banks *et al.*[131] Our implementation of the FC method differs primarily in that we rely exclusively on *ab initio* results to describe the atomic charge fluctuations. The field-dependent intramolecular potentials are also derived strictly from *ab initio* results. Overall, we have placed considerable emphasis on developing a methodology that can be readily extended to other molecules. In particular, relatively few parameters remain to be determined empirically and these are optimized by comparison with experimental interatomic distributions for bulk ethanol[123] and by comparison with the measured self-diffusion coefficient[87], dielectric constant[132], and enthalpy of vaporization[133]. The simultaneous implementation of field-dependent atomic charges and intramolecular potentials impacts the equations of motion for the fluid and the simulations are significantly more lengthy than for corresponding non-polarizable models.

Results from extensive molecular dynamics simulations of bulk ethanol are reported. In particular, the hydrogen bonding network is examined in detail. We compare our results with a non-polarizable ethanol model, a partially polarizable model where the intramolecular motion is field-independent but atomic charges respond to the electric field, and a partially polarizable model where the atomic charges are field-independent but the intramolecular potential responds to the electric field.

This chapter is organized as follows. Section 3.2 outlines the methods we have used to arrive at the polarizable flexible model for ethanol. Section 3.3 analyzes the fluid structure and properties, with an emphasis on hydrogen bonding. Concluding remarks are given in Section 3.4.

3.2. Methods

The full field-dependent potential, $U(\vec{E})$, is written as

$$U(\vec{E}) = U^{el}(\vec{E}) + U^{\text{intra}}(\vec{E}) + U^{LJ} \quad [3.1]$$

where the evaluation of the electrostatic energy, $U^{el}(\vec{E})$, is discussed in Section 3.2.3. The field-dependent intramolecular potential, $U^{\text{intra}}(\vec{E})$, is the subject of Section 3.2.5. The Lennard-Jones contribution to the energy, U^{LJ}, is not field-dependent and has been discussed in Chapter 2.

Fig. 2.8 shows the atom labeling employed throughout this chapter. The model developed in this chapter is referred to as the Fluctuating Charge and INTRAmolecular potential (fCINTRA) model. A flowchart summarizing our procedure for ethanol model development is given in Fig. 3.1.

The process begins by assessing the range and frequency of fields experienced in bulk ethanol. As shown in Fig. 3.1, molecular dynamics simulations using a non-polarizable model are used to provide an estimate of "typical" fields in bulk ethanol. The second and third steps in our procedure involve the analysis of the collected fields and the selection of a representative subset. Steps 1-3 in Fig. 3.1 are discussed in detail in Section 3.2.1 below. The field-response of ethanol molecules is assessed via an extensive series of *ab initio* calculations. A very large number of calculations is required and, as a result, the *ab initio* method chosen to evaluate field response must be efficient as well as accurate. Thus, benchmarking against high level calculations is a necessary step to choose the appropriate basis set and method used to quantify the molecular response. The discussion of the *ab initio* calculations is provided in Section 3.2.2. Following these

preliminary steps to select appropriate fields and gauge the molecular response, the polarizable model is developed as discussed in Sections 3.2.3, 3.2.4, and 3.2.5.

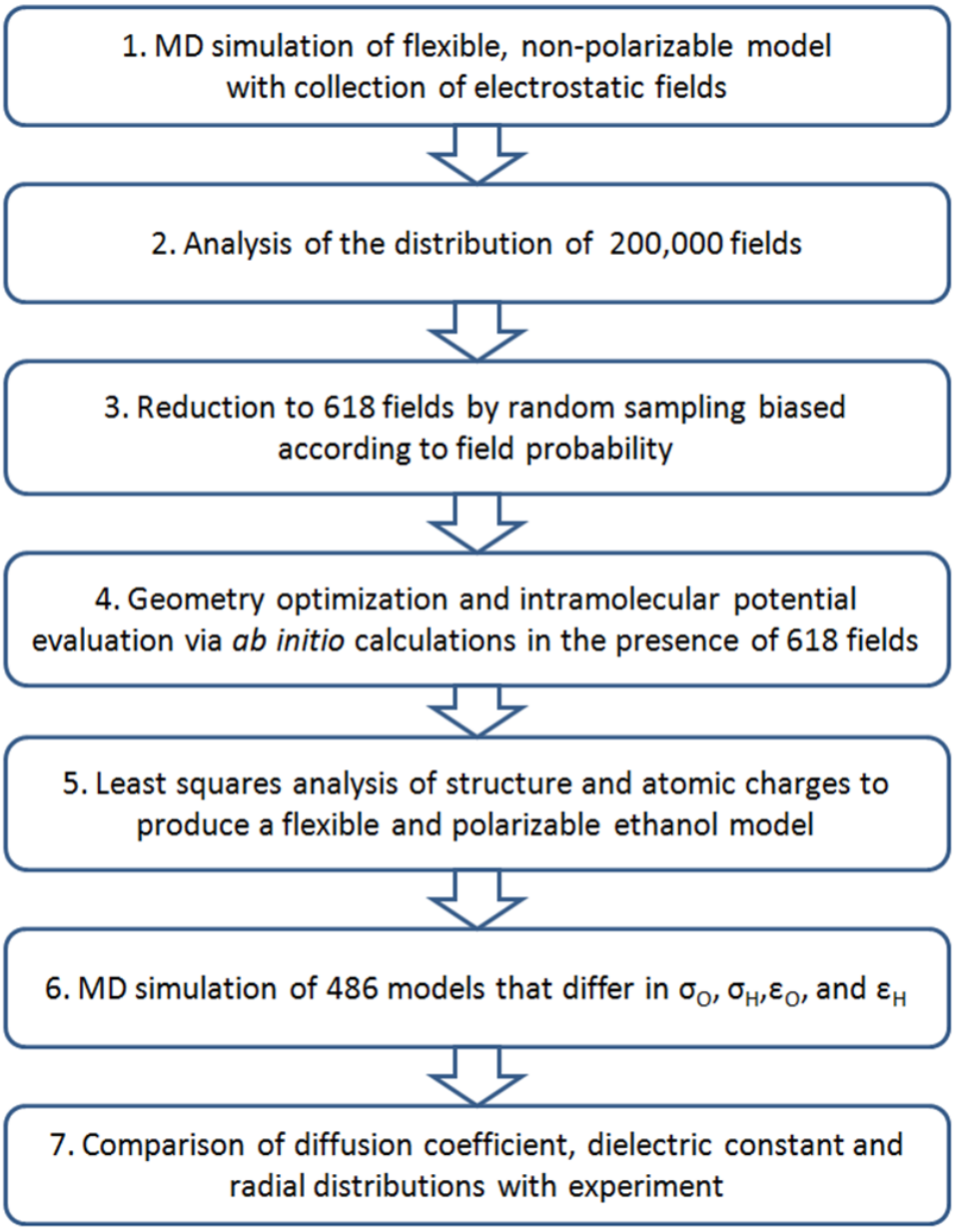

Figure 3.1. Flow chart showing the seven steps involved in the design of the polarizable flexible ethanol model.

3.2.1 Assessment of typical electric fields in bulk ethanol

In the parameterization of a polarizable model, a limited number of fields can be explicitly considered. We chose to proceed by directly assessing the fields a typical ethanol molecule experiences in the bulk. Specifically, a lengthy molecular dynamics simulation of bulk ethanol was undertaken. The flexible non-polarizable model of Chen *et al*.[134] was employed with fields recorded every 500 time steps. The simulations were performed in the NVE ensemble, for 2000 molecules, over 50000 iterations, and with a time step of 0.127 fs. Ewald[90] sums were employed, with tinfoil boundary conditions, a convergence parameter α of 0.1609 $Å^{-1}$, and a momentum space cutoff of $k^{*2} \leq 27$.

Throughout the simulation, the field on the C(3), O(2), and H(1) atoms of each molecule were monitored. Information was not gathered for the other atoms since C(4) is uncharged in the Chen *et al*.[134] model and the other hydrogens do not appear explicitly in the model. The end result, summarized in Fig. 3.2, is a distribution of electric fields in bulk ethanol, as predicted from a non-polarizable ethanol model. While the field distributions will change for a polarizable model, Fig. 3.2 provides a rough estimate of the range of fields experienced by ethanol molecules in the bulk, and the probability of a given field. It is important to note that long-ranged contributions to these fields are substantial. Thus, the intuitive process of generating fields by placing charges at hydrogen-bonding sites[131], or other local sites, will not produce typical fields experienced by ethanol molecules in the bulk liquid.

The 200,000 fields summarized in Fig. 3.2 are too numerous to consider directly. The number of fields is reduced to 618 as follows. Figs. 3.2(a), 3.2(b), and 3.2(c) are

individually employed to select 350, 158, and 110 fields, respectively, from the 200000 possibilities. Consider Fig. 3.2(a). We divide the magnitude of the field squared, E^2, on C(3) into 2000 equal segments. For a given E^2 range, 405 to 405.5 say, the height of the curve is compared to the maximum. If a random number is less than this ratio then one of the fields with an E^2 in this range will be selected for further analysis. In this way, the field selection is biased by the frequency of occurrence of the field. The procedure is repeated for Figs. 3.2(b) and 3.2(c). Note that the broader peak in Fig. 3.2(a) results in a larger number of selected fields. Distributions corresponding to the 618 fields are shown in Fig. 3.2. The desired result has been achieved: a manageable number of fields, representative of typical fields experienced by ethanol molecules in the bulk.

3.2.2 *Ab initio* calculations for molecular response

The parameterization of molecular response to a given field requires that the field be reproduced in the *ab initio* calculation. Here, the field is obtained by placing four point charges around a single ethanol molecule with the magnitudes and positions of the charges chosen to reproduce the fields at C(3), O(2), and H(1). In practice, the charges must be far enough from the molecule so that the molecule responds to an overall field rather than to individual charges. We accomplish this by excluding the charges from the volume defined by a box of dimensions $2(x^{max},y^{max},z^{max})$, where x^{max}, y^{max}, and z^{max} are the largest components of the atomic positions. This procedure is repeated for 618 fields and a set of four point charges is obtained for each field.

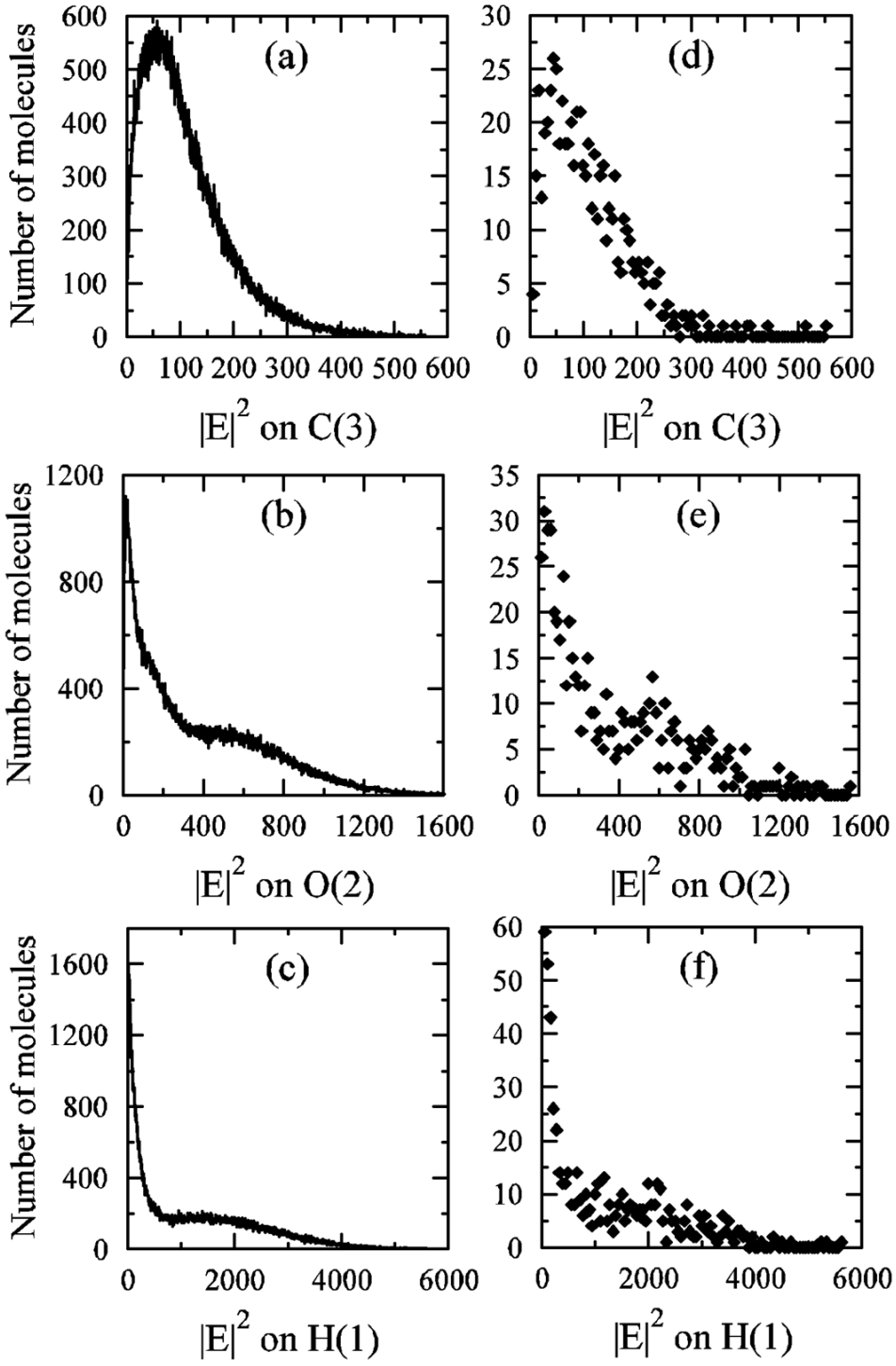

Figure 3.2. Statistics on the electric fields collected during the MD simulation using the flexible, non-polarizable Chen *et al.*[134] model of ethanol. Panels (a)-(c) each summarize 200000 measurements of the electric field on C(3), O(2), and H(1), respectively. Panels (d)-(f) show the corresponding distributions for the 618 selected electric fields. The field magnitudes are in reduced units.

In a bulk liquid, the molecule cannot rotate or translate fast enough to respond to an instantaneous change in the field, but its atomic charges and potential surface change. That is, the electrons rapidly move about the molecule to respond to the field but the nuclei respond much more slowly. A full optimization of the molecular structure in the presence of a field would lead to translation and rotation. In order to prevent this, C(3) is forced to remain at the origin, O(2) must lie on the z-axis, and H(1) is in the *xz* plane during the optimization. These constraints prohibit translation and, to a large extent, rotation due to the field. Other than these constraints, the molecule is fully optimized.

All *ab initio* calculations are performed using Gaussian 03[135]. Before selecting a basis set and method, benchmark calculations were performed. Specifically, 16 fields were selected randomly and the molecular structure was optimized in each of these fields, for 20 functional/basis set combinations. In addition, for each field, a benchmark calculation was performed using 2nd order Moller-Plesset perturbation theory[136] (MP2) with the augmented correlation consistent triple-zeta (aug-cc-pVTZ) basis set of Dunning *et al*.[137, 138] Table 3.1 shows the average error in the molecular dipole, relative to the benchmark, for the 20 functional/basis set combinations. Specifically, for each combination, the ratio

$$\frac{1}{16}\sum_{F=1}^{16}\frac{(\mu^{Method,F}-\mu^{MP2,F})^2}{(\mu^{MP2,F}-\mu^{MP2,0})^2} \qquad [3.2]$$

is calculated. $\mu^{Method,F}$ and $\mu^{MP2,F}$ are the dipole moments obtained in the field for the selected functional/basis set combination and for the benchmark, respectively, and $\mu^{MP2,0}$ is the zero-field dipole. Table 3.1 clearly shows the importance of basis set on the response: All of the basis sets are large, but additional polarization and diffuse functions

improve the dipole prediction. In particular, for the cc-pVDZ and cc-pVTZ basis sets[137], a deficit in diffuse functions resulted in optimized structures significantly in error for 2 of the 16 fields under consideration and this raised their overall average in Eq. [3.2].

Table 3.1. Average error in the dipole moment, relative to MP2/aug-cc-pVTZ reference calculations (see Eq. [3.2]), for ethanol in 16 electric fields. Errors are reported for four functionals and five basis sets.

	6-311G(d,p) [139, 140]	**aug-cc-pVDZ [138]**	**cc-pVDZ [137]**	**cc-pVTZ [137]**	**6-311++G(d,p) [139, 140]**
B3LYP[141]	0.5740	0.5151	2.1598	1.0070	0.0298
B97-2[142, 143]	0.6875	0.7436	2.0186	1.3059	2.0682
PBE1PBE[144]	0.6756	0.723	1.9964	1.2630	0.9359
PBEPBE[144]	1.0741	1.0435	3.0747	1.7321	2.0156

From Table 3.1, the B3LYP functional[141] with the 6-311++G(d,p) basis set[139, 140] predicts dipoles in closest agreement with the MP2 benchmark. We find that a measure similar to Eq. [3.2], but based on atomic positions, also indicates that the B3LYP/6-311++G(d,p) combination is superior. In addition, the zero-field optimized structure from B3LYP/6-311++G(d,p) gives a dipole of 1.706D which is in close agreement to the experimental gas phase value of 1.71D[145]. Based on these results, all further *ab initio* calculations employ the B3LYP functional with the 6-311++G(d,p) basis set.

The evaluation of the field-dependence of intramolecular motion begins with a series of geometry optimizations in the presence of the individual fields. At each field, one full geometry optimization and a series of 122 restricted geometry optimizations are

performed. The final field-dependent potentials for ethanol are extracted from 76014 B3LYP/6-311++G(d,p) calculations.

3.2.3 Fluctuating Charge Model

The FC model has been discussed in detail in Chapter 2. In this section, we briefly introduce our implementation. Appendix A describes our methodology for extracting the charge response parameters from *ab initio* calculations.

Our ethanol-specific FC parameter values are compared with CHARMM transferable parameters[53] in Table 3.2. Our calculations predict electronegativities ($\tilde{\chi}_i^0$) that are consistently larger than for CHARMM[53], and hardnesses (J_{ii}^0) of the atomic polarizabilities that are larger than the CHARMM values except for H(5)-H(9) where the values are 5-10% smaller.

The parameters in Table 3.2 for a given atom incorporate the effects of the other atoms in the molecule. That is, the parameterization reflects the response of the atom *within* the ethanol molecule. In this thesis, the parameters for chemically equivalent hydrogens (H(5), H(6), H(7)) and (H(8), H(9)) have been constrained to be equal. Symmetry arguments dictate that H(8) and H(9) should have the same parameters, and interconversion of the methyl hydrogens (H(5)-H(7)) during the simulation requires that these three have the same response parameters. In Appendix A we discuss our method for imposing symmetry on the hydrogen parameters. As a result of these symmetry constraints, the final zero-field atomic charges in the fCINTRA model (see Table 3.2) give a dipole moment of 1.734D, slightly larger than the gas-phase B3LYP/6-311++G(d,p) dipole moment of 1.706D.

Table 3.2. Charge fluctuation parameters (see Eq. [2.25]) and Lennard-Jones parameters for the polarizable, flexible fCINTRA ethanol model. The fCINTRA parameters are compared with polarizable CHARMM[53] values. For comparison with CHARMM, the $\tilde{\chi}_i^0$ have been shifted to give an H(1) value of zero in the sixth column. J_{ii}^0 are given in kJ/(mol |e|^2) and $\tilde{\chi}_i^0$ are reported in kJ/(mol |e|). The LJ parameters for H(1) and O(2) were optimized for the fCINTRA model while the remaining values are from CHARMM[53].

	ζ_i **fCINTRA (nm^{-1})**	J_{ii}^0 **fCINTRA**	J_{ii}^0 **CHARMM**	$\tilde{\chi}_i^0$ **fCINTRA**	$\tilde{\chi}_i^0$ **(shifted) fCINTRA**	$\tilde{\chi}_i^0$ **CHARMM**	ε_{ii} **(kJ/mol)**	σ_{ii} **(nm)**	Q_i^0 **fCINTRA (|e|)**
H(1)	26.24	2278.6	2164.2	-264.0	0.0	0.0	0.1	0.1	0.40
O(2)	29.31	1479.3	1286.2	262.4	526.4	444.9	1.3	0.295	-0.71
C(3)	21.54	1087.0	874.2	-2.7	261.3	207.5	0.251	0.358	0.48
C(4)	21.30	1075.1	1005.6	-8.2	255.7	233.7	0.305	0.360	-0.19
H(5)	23.52	2042.7	2098.0	-34.3	229.7	216.7	0.09614	0.235	0.051
H(6)	23.52	2042.7	2098.0	-34.3	229.7	216.7	0.09614	0.235	0.051
H(7)	23.52	2042.7	2098.0	-34.3	229.7	216.7	0.09614	0.235	0.051
H(8)	22.13	1921.6	2098.0	-35.7	228.3	228.0	0.1338	0.239	-0.066
H(9)	22.13	1921.6	2098.0	-35.7	228.3	228.0	0.1338	0.239	-0.066

As described in Chapter 2, $J_{ij}(r_{i\alpha j\beta})$ can be defined as a Coulomb overlap integral (Eq. [2.27]) or using an approximation form (Eq. [2.29]). In Fig. 3.3, we compare the H(1)-H(1) radial distribution from two simulations that differ only in the form of $J_{ij}(r_{ij})$ for intramolecular atomic pairs separated by less than four bonds. From the figure, even small changes in the $J_{ij}(r_{ij})$ lead to important differences in the fluid structure. In particular, the fluid is less structured when Eq. [2.29] is employed and the average dipole is 1.9 D. The experimental dipole moment in the bulk is 3.04 D[145] and the use of $J_{ij}(r_{ij})$ from Eq. [2.27] gives an average dipole of 2.64 D. It appears that seemingly small differences in the Coulomb overlaps can lead to significant differences in the fluid structure and properties.

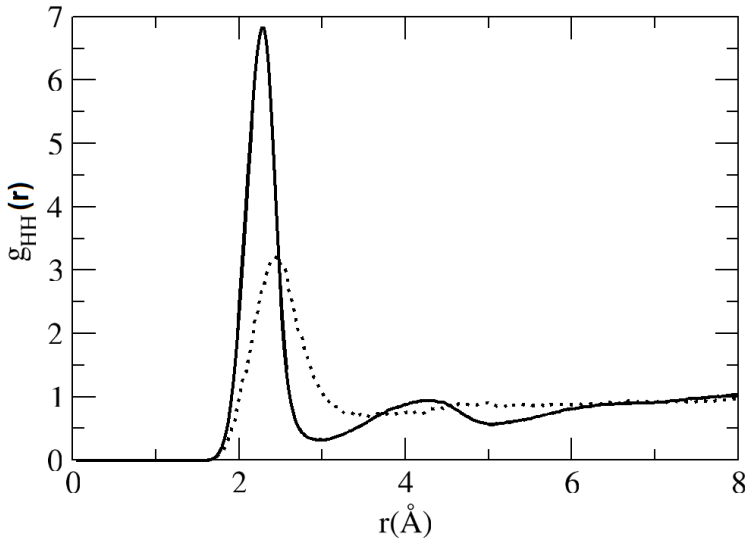

Figure 3.3. The impact of the representation of the interatomic Coulomb interaction, $J_{ij}(r_{ij})$. The H(1)-H(1) radial distribution is shown for bulk ethanol at ρ=0.787 g/cm^3 and T=298K. Results for the fCINTRA model with the overlap integral (Eq. [2.27]) form of the Coulomb interaction are given by a solid line, while use of Eq. [2.29] leads to the distribution identified by the dotted line.

3.2.4 Lennard-Jones potentials

The Lennard-Jones energy and length parameters, ε_{ij} and σ_{ij}, are the only adjustable parameters in our simulations: All other parameters are extracted from B3LYP/6-311++G(d,p) calculations. In fact, we adjust only the LJ parameters for O(2) and H(1), all others are taken from the CHARMM force field[53].

3.2.5 Intramolecular potentials

The functional forms for the stretch, bend, and torsion potentials have been introduced in Chapter 2. For ethanol, we divide the intramolecular motion into 8 stretches, 13 bends, and 2 torsions, and the corresponding potentials are described by Eqs. [2.31]-[2.33]. For Eq. [2.33], a form with a slight variation is used

$$U^{tor}(\vec{E}) = \sum_{it=1}^{2} \left(\sum_{i=0}^{6} C_{it;i}(\vec{E}) \cos^{i} \varphi_{it} + C_{it;7}(\vec{E}) \cos^{3}(\varphi_{it} - 90^{o}) + C_{it;8}(\vec{E}) \cos^{5}(\varphi_{it} - 90^{o}) \right), \quad [3.3]$$

The *ab initio* energies used to define the potentials should be corrected[146], prior to further analysis, by removing contributions from atoms separated by more than 3 bonds. For ethanol, this contribution is only from H(1) interacting with H(5)-H(7). Bond lengths and angles do not change much during a simulation and the corrections will be slowly varying over the relevant parameter range. Consequently, we have not corrected the *ab initio* potentials for stretches and bends. Consider the torsions. The largest contribution to the correction is expected from electrostatic interactions between the hydrogens. We correct the *ab initio* energies as follows. For each torsional angle and field, we subtract the electrostatic contribution to the energy, U^{el}, as given in Eq. [2.26].

The atomic charges required for this correction are obtained by solving the equations of motion for the charges (see Section 3.2.6 and Appendix B) for a single molecule constrained to the appropriate geometry and in the chosen field. In this way, the electrostatic contribution to the energy from atoms separated by more than three bonds, as it is evaluated during a simulation, is removed from the *ab initio* energy.

The incorporation of field dependence in the coefficients of Eqs. [2.31]-[2.33] is challenging. As a first step, we fitted power series in the fields at each atom, the field components at each atom, and products between field components. While the resulting fits were of acceptable quality, most of the individual terms were not physically meaningful and the fitted potentials did not reproduce expected symmetry in the potentials. Rather than pursue this approach, we have chosen to expand the field-dependent parameters in Eqs. [2.31]-[2.33], according to "structural" analogs. These terms are listed in Eqs. [2.35]-[2.43]. With these considerations in mind, the parameters in Eqs. [2.31]-[2.33] are expanded using the terms in Eqs. [2.35]-[2.43] and the multiplicative coefficients are obtained by least-squares fits with the SPSS package (Version 13.0). The coefficients are prioritized and only the most significant are kept, so that expansions for the individual coefficients are relatively short (11 terms or less). For example, the equilibrium bond angle of H(1)-O(2)-C(3) is expanded as follows

$$\theta_e(\vec{E}) = 108.7 - 1.43\times10^{-4}(|E_{HH}^{15}|+|E_{HH}^{16}|+|E_{HH}^{17}|) - 1.08\times10^{-3}|E_{HO}^{12}|+... \quad [3.4]$$

Table 3.3 gives the expansion coefficients describing the field dependence of the bond lengths. As described in Eqs. [2.41]-[2.42], X is used to represent atoms 8 and 9, and Y denotes H(5), H(6), and H(7). Only the first term contributes in the absence of the

field, and the coefficient listed for this term is simply the zero-field equilibrium bond length. The expansions generally produce an $R^2 \geq 0.8$. As is evident from the magnitude of the coefficients in the table, the bond lengths do not change significantly with the field.

Table 3.3. The zero-field bond stretching constants and the field dependence of the equilibrium bond lengths (see Eq. [2.31]) extracted from B3LYP/6-311++G(d,p) calculations of ethanol. B_{HO}^{AB} identifies the bond: the superscripts follow the atom numbering shown in Fig. 2.8, while the subscripts are added for convenience and identify the atom types. k_s is the zero-field bond stretching force constant, and r_e is the corresponding zero-field equilibrium bond length. The terms, and the coefficients, are given for each bond. The minimum and maximum bond lengths observed in the 618 fields are provided in the 4th and 5th rows, respectively. Note that $A(-n) = A \times 10^{-n}$.

Bond	B_{HO}^{12}	B_{OC}^{23}	B_{CC}^{34}	B_{CH}^{4Y}	B_{CH}^{3X}
k_s(kJ/Å^{2}mol)	251105.1	132438.5	128123.6	157499.1	148234.4
r_e(Å)	0.962	1.430	1.517	1.093	1.099
r_{min}(Å)	0.961	1.416	1.514	1.092	1.094
r_{max}(Å)	0.978	1.464	1.526	1.098	1.102
Term	$\lvert E_H^1 \rvert$ 1.07(-4)	$\lvert E_H^X \rvert$ 1.61(-4)	$\lvert E_{HH}^{XX} \rvert$ 1.84(-6)	$\lvert E_C^3 \rvert$ 2.61(-5)	$\lvert E_H^1 \rvert$ 1.68(-5)
Term	$\lvert E_O^2 \rvert$ -7.37(-5)	$\lvert E_{HH}^{11} \rvert$ 1.04 (-5)	$\lvert E_{OC}^{24} \rvert$ -2.60(-6)	E_{OH}^{2X} -8.76(-7)	$\lvert E_C^3 \rvert$ -1.24(-4)
Term	$\lvert E_{HH}^{11} \rvert$ 6.93(-7)	$\lvert E_{OO}^{22} \rvert$ 2.78(-5)	$\lvert E_{HC}^{14} \rvert$ 1.98(-6)	E_{CH}^{31} 7.77(-7)	$\lvert E_{HH}^{XX} \rvert$ 9.22(-7)
Term	E_{CCO}^{432} -8.79(-7)	$\lvert E_{HH}^{XX} \rvert$ -6.11(-6)	$\lvert E_{HH}^{89} \rvert$ -2.77(-6)	E_{CH}^{3X} 1.98(-6)	$\lvert E_{OH}^{2X} \rvert$ -6.37(-7)
Term	E_{HCO}^{X32} -1.52(-6)	$\lvert E_{HH}^{YX} \rvert$ 6.82(-7)	E_{OH}^{2Y} -4.34(-7)	E_{HH}^{89} -2.35(-6)	$\lvert E_{CO}^{32} \rvert$ 4.32(-6)
Term	E_{HCC}^{X34} 1.02(-6)	E_{OH}^{21} -3.53(-5)	E_{HH}^{1Y} 7.13(-7)	E_{HCH}^{Y4Y} 1.18(-6)	$\lvert E_{CH}^{3Y} \rvert$ -1.79(-7)
Term	E_{HCH}^{839} -3.70(-6)	E_{HCH}^{Y4Y} -4.27(-6)	E_{HCC}^{Y43} 2.51(-6)	E_{HCO}^{X32} 8.42(-10)	E_{OC}^{24} -1.80(-5)
Term	$\widehat{E}_{COH}^{321}$ -4.69(-10)	E_{HCO}^{X32} -7.71(-6)	$\hat{E}_{HCH}^{Y4Y}$ -6.01(-10)	$\widehat{E}_{HCH}^{Y4Y}$ -2.14(-10)	E_{OH}^{2Y} 4.64(-6)
Term	$\widehat{E}_{CCO}^{432}$ 5.63(-10)	$\widehat{E}_{HCO}^{X32}$ -8.98(-9)	$\widehat{E}_{HCO}^{X32}$ 1.26(-9)	$\widehat{E}_{HCO}^{X32}$ 8.42(-10)	E_{HH}^{89} 6.22(-7)
Term	$\widehat{E}_{HCC}^{X34}$ 9.46(-10)	$\widehat{E}_{HCC}^{X34}$ -4.93(-9)	$\widehat{E}_{HCC}^{X34}$ 2.13(-9)	$\widehat{E}_{HCH}^{839}$ 1.12(-9)	$\widehat{E}_{HCO}^{X32}$ 6.18(-10)

Table 3.4 gives the expansion coefficients for the field-dependence of the equilibrium angles. The first coefficient in Table 3.4 is constrained to be the equilibrium angle in the absence of a field. The other coefficients are obtained by regression. In general, the fitted potentials provide a good representation of the bend potentials with the exception of the H(1)-O(2)-C(3) angle. Even with a substantial number of expansion terms the R^2 is roughly 0.4. However, as indicated by the θ_{min} and θ_{max} values, this angle does not vary much in the course of the simulation.

Consider the torsion about the O(2)-C(3) bond. This motion reflects the ease with which the hydrogen-bonding hydrogen can rotate and will clearly be relevant to the hydrogen bonding characteristics in the fluid. Fig. 3.4 shows this torsional potential in six different fields. The uncorrected *ab initio* potential, the corrected potential obtained by subtraction of the intramolecular electrostatic contribution, and the fitted potential are compared. From the figure, the corrected and *ab initio* potentials are qualitatively similar. However, the corrected potential has a higher barrier for rotation through the eclipsed conformation in most fields. It is clear from the figure that some fields radically change the characteristics of the torsion potential. For instance, in Fig. 3.4(d), in the presence of this particular field, the minimum at 180^0 has nearly disappeared. On the other hand, many fields leave the potential virtually unchanged, as illustrated in Fig. 3.4(b). The fitted potentials shown in the figure illustrate the overall quality of the fitted potentials: very good agreement with the corrected *ab initio* potentials is shown in Figs. 3.4(a)-(c) and poorer agreement is evident in Figs. 3.4(d) and 3.4(f). It is important to realize that the curves are not fitted individually, rather a single functional form of the torsional potential, Eq. [2.33], is used to model the response to all fields. That is, for 618 fields

and 35 energies on each potential curve a total of 21630 energies have been evaluated and these are fitted simultaneously. As illustrated in Figs. 3.4(e) and 3.4(f), even for the poorest fits, the fitted and corrected *ab initio* potentials are qualitatively similar. The overall R^2 value is 0.90. If we rank each field according to the quality of the fitted torsional potential, then 390 fields have R^2 values above 0.8. Only 94 fields have R^2 values below 0.6. The expansion coefficients for the O(2)-C(3) torsion are given in Table 3.5.

The field dependence of the torsion potential for rotation about the CC bond is shown in Fig. 3.5. The methyl hydrogens are interchanged by this torsion and, regardless of the applied field, interconversion of the hydrogens by a 120 degree rotation forces the potential to return to its original value. The fields selected for the figure illustrate the range of variability found for this potential. Clearly, the field has little impact on this motion. As a result, we employ only the zero-field coefficients and these have the following values (in kJ/mol): $C_{2;0} = 7.183$, $C_{2;1} = -21.798$, $C_{2;3} = 30.625$, and $C_{2;5} = -1.644$. All other coefficients in Eq. [2.33] are zero for this torsion and this field-independent potential yields and R^2 value of 0.975.

Within our simulations, we have focused on the more strongly field-dependent motions. As a result, we have not considered the field dependence of the stretching force constants, $k_{s;is}(\vec{E})$, or the equilibrium bond lengths. After a detailed exploration of the bending potentials in the presence of the fields, we found that the field dependence of $k_{\theta;ib}(\vec{E})$ was weak. Consequently, we have only used the zero-field force constants in the bending potentials. Finally, field dependence has not been included for the torsion

about C(3)-C(4). Field-dependence remains in the equilibrium bond angles, and the torsion about C(3)-O(2).

Table 3.4. The zero-field angle bending force constant and the field dependence of the equilibrium bond angles (see Eq. [2.32]) extracted from B3LYP/6-311++G(d,p) calculations of ethanol. The terms, and the coefficients, are given for each bend. The minimum and maximum bond angles observed in the 618 fields are provided in the 4th and 5th rows, respectively. Note that $A(-n) = A \times 10^{-n}$.

	A^{123}_{HOC}	A^{234}_{OCC}	$A^{34\,Y}_{CCH}$	$A^{23\,X}_{OCH}$	$A^{Y\,4\,Y}_{HCH}$	$A^{43\,X}_{CCH}$	A^{938}_{HCH}
k_θ **(kJ/deg²mol)**	0.064392	0.113844	0.066162	0.090502	0.06207	0.074054	0.064054
θ_e **(deg)**	108.7	107.8	110.5	110.2	108.4	110.2	107.8
$\theta_{\min}$ **(deg)**	106.1	107.6	109.5	106.9	105.4	109.0	106.7
$\theta_{\max}$ **(deg)**	111.9	112.8	113.7	111.2	109.7	111.9	109.4
Term	$\lvert E^{1Y}_{HH} \rvert$ -1.43(-4)	$\lvert E^{Y}_{H} \rvert$ 7.06(-3)	$\lvert E^{1}_{H} \rvert$ 7.45(-3)	$\lvert E^{1Y}_{HH} \rvert$ -2.11(-4)	$\lvert E^{14}_{HC} \rvert$ -1.10(-4)	$\lvert E^{11}_{HH} \rvert$ 3.58(-4)	$\lvert E^{1}_{H} \rvert$ -2.88(-2)
Term	$\lvert E^{12}_{HO} \rvert$ -1.08(-3)	$\lvert E^{24}_{OC} \rvert$ -1.25(-3)	$\lvert E^{3}_{C} \rvert$ -6.43(-3)	$\lvert E^{2Y}_{OH} \rvert$ 1.02(-4)	$\lvert E^{YX}_{HH} \rvert$ 1.73(-5)	$\lvert E^{2X}_{OH} \rvert$ 8.26(-5)	$\lvert E^{2}_{O} \rvert$ 3.03(-2)
Term	$\lvert E^{4Y}_{CH} \rvert$ 8.79(-4)	$\lvert E^{1Y}_{HH} \rvert$ 2.21(-4)	$\lvert E^{11}_{HH} \rvert$ -6.93(-5)	$\lvert E^{YX}_{HH} \rvert$ 5.36(-4)	E^{14}_{HC} 9.50(-5)	$\lvert E^{1Y}_{HH} \rvert$ 7.93(-5)	$\lvert E^{11}_{HH} \rvert$ 4.44(-4)
Term	E^{21}_{OH} 1.24(-3)	$\lvert E^{YX}_{HH} \rvert$ 5.02(-5)	$\lvert E^{14}_{HC} \rvert$ 6.40(-5)	$\lvert E^{14}_{HC} \rvert$ -8.76(-5)	$E^{Y\,43}_{HCC}$ -5.59(-4)	$\lvert E^{YY}_{HH} \rvert$ -2.72(-5)	$\lvert E^{22}_{OO} \rvert$ 3.17(-4)
Term	E^{YY}_{HH} -8.11(-4)	E^{1Y}_{HH} 1.57(-4)	$\lvert E^{YX}_{HH} \rvert$ -1.46(-5)	E^{321}_{COH} 9.86(-4)	E^{839}_{HCH} 7.52(-4)	E^{13}_{HC} -7.11(-4)	$\lvert E^{21}_{HH} \rvert$ -6.98(-4)
Term	E^{321}_{COH} 1.84(-3)	E^{89}_{HH} -5.08(-4)	$E^{Y\,43}_{HCC}$ 5.84(-4)	$E^{X\,34}_{HCC}$ -2.51(-4)	$\widehat{E}^{Y\,4\,Y}_{HCH}$ -1.21(-7)	E^{321}_{COH} -1.94(-3)	$\lvert E^{34}_{CC} \rvert$ 1.60(-4)
Term	E^{432}_{CCO} 7.39(-4)	E^{321}_{COH} 7.14(-4)	E^{839}_{HCH} -2.72(-4)	$\widehat{E}^{432}_{CCO}$ -1.50(-7)	$E^{Y\,432}_{HCCO}$ -5.43(-7)	$E^{Y\,4\,Y}_{HCH}$ -3.11(-4)	E^{89}_{HH} -3.56(-4)
Term	$\widehat{E}^{321}_{COH}$ -5.15(-7)	$\widehat{E}^{X\,32}_{HCO}$ -7.45(-7)	$\widehat{E}^{432}_{CCO}$ -1.24(-7)	$\widehat{E}^{Y\,4\,Y}_{HCH}$ -1.54(-7)	$E^{X\,321}_{HCOH}$ -2.12(-7)	$E^{X\,32}_{HCO}$ -8.06(-4)	E^{321}_{COH} -8.10(-4)
Term	$\widehat{E}^{X\,34}_{HCC}$ 7.23(-7)	$E^{X\,321}_{HCOH}$ 3.65(-7)	$\widehat{E}^{Y\,4\,Y}_{HCH}$ 1.28(-7)	$\widehat{E}^{X\,32}_{HCO}$ 1.04(-6)		E^{839}_{HCH} -7.20(-4)	$E^{X\,32}_{HCO}$ 6.74(-4)
Term	$\widehat{E}^{839}_{HCH}$ 1.70(-6)	$E^{X\,34\,Y}_{HCCH}$ -3.65(-6)	$\widehat{E}^{X\,32}_{HCO}$ -1.18(-7)	$\widehat{E}^{839}_{HCH}$ 1.22(-6)		$E^{Y\,432}_{HCCO}$ -9.32(-7)	$\widehat{E}^{X\,32}_{HCO}$ -1.12(-7)

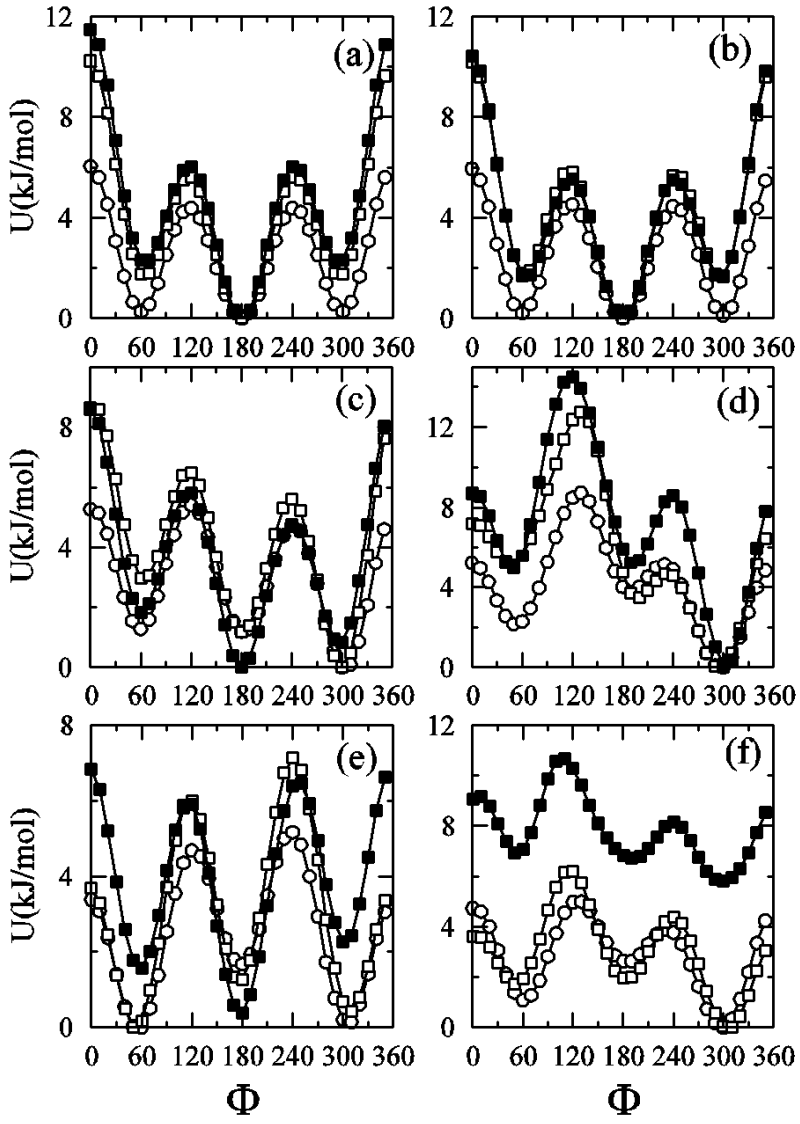

Figure 3.4. The torsional potential, $U^{tor}(\vec{E})$, between H(1)-O(2)-C(3)-C(4) as a function of the dihedral angle. For convenience, each vertical scale is shifted so that the *ab initio* curve minimum corresponds to an energy of zero. The B3LYP/6-311++G(d,p) results are shown with open circles, corrected *ab initio* results are open squares, and least-squares fits to the corrected *ab initio* results are filled squares. The sequence of panels shows the dependence of the potential on the field. In reduced units: (a) $|\vec{E}_H^1|$=0.00, $|\vec{E}_O^2|$=0.00,$|\vec{E}_C^3|$=0.00; (b) $|\vec{E}_H^1|$=2.50,$|\vec{E}_O^2|$=2.23,$|\vec{E}_C^3|$=2.15; (c) $|\vec{E}_H^1|$=7.19,$|\vec{E}_O^2|$=7.32, $|\vec{E}_C^3|$=7.55; (d) $|\vec{E}_H^1|$=24.64, $|\vec{E}_O^2|$=17.24,$|\vec{E}_C^3|$=12.16; (e) $|\vec{E}_H^1|$=18.14, $|\vec{E}_O^2|$=16.61, $|\vec{E}_C^3|$=12.85; and (f) $|\vec{E}_H^1|$=31.37,$|\vec{E}_O^2|$=25.28,$|\vec{E}_C^3|$=18.33.

Table 3.5. Field dependence of the torsional coefficients for rotation about the C(3)-O(2) bond in ethanol (see Eq. [2.33]). The minimum and maximum values for the coefficients in 618 fields are given in the 2nd and 3rd rows, respectively. The third row gives the coefficients in the absence of a field and the following rows list the field-dependent terms. $A(-n) = A \times 10^{-n}$.

	$C_{1;0}$	$C_{1;1}$	$C_{1;2}$	$C_{1;3}$	$C_{1;4}$	$C_{1;5}$	$C_{1;7}$	$C_{1;8}$
Cmin	-1.67	-13.41	-12.78	-2.45	-2.48	-4.07	-8.60	-13.88
Cmax	19.41	-3.26	6.46	17.09	4.69	13.60	9.89	11.84
Term	5.01	-6.93	0.00	10.20	0.00	2.41	0.00	0.00
Term	$\lvert E_H^1 \rvert$ -3.41(-2)	$\lvert E_O^2 \rvert$ -1.13(-2)	$\lvert E_H^X \rvert$ 4.32(-2)	$E_{HCC}^{Y\,43}$ -4.21(-3)	$\lvert E_C^3 \rvert$ -2.35(-1)	$\lvert E_C^3 \rvert$ -1.43(-1)	$\lvert E_H^X \rvert$ 9.50(-4)	$\lvert E_{HC}^{14} \rvert$ -5.17(-5)
Term	$\lvert E_C^4 \rvert$ -7.14(-2)	$\lvert E_H^1 \rvert$ 4.20(-2)	$\lvert E_{CO}^{32} \rvert$ 5.86(-3)	E_{HCH}^{839} -1.54(-3)	$\lvert E_H^X \rvert$ 1.28(-1)	$\lvert E_{CC}^{33} \rvert$ 2.35(-2)	$\lvert E_{OH}^{2Y} \rvert$ 1.06(-5)	
Term	$\lvert E_H^X \rvert$ -4.02(-2)	$\lvert E_{HH}^{11} \rvert$ -4.41(-4)	$\lvert E_{CH}^{3Y} \rvert$ 2.78(-3)	$\widehat{E}_{COH}^{321}$ -2.47(-6)		$\lvert E_{HH}^{YY} \rvert$ 5.26(-4)		
Term	$\lvert E_{HH}^{XX} \rvert$ 1.06(-2)	E_{OH}^{2X} -2.78(-3)	$\lvert E_{OH}^{2Y} \rvert$ -1.68(-3)			$\lvert E_{HH}^{89} \rvert$ -4.46(-3)		
Term	$\lvert E_{HH}^{1X} \rvert$ -6.44(-4)	E_{HH}^{1X} 2.71(-3)	E_{OH}^{2X} -7.60(-4)			E_{CH}^{3Y} -2.89(-3)		
Term	$\lvert E_{OC}^{24} \rvert$ 1.37(-3)		E_{CH}^{4X} -2.21(-2)			E_{OH}^{2X} -5.07(-3)		
Term	$\lvert E_{CH}^{4X} \rvert$ -2.81(-3)		E_{HH}^{YX} 5.37(-3)			$E_{HCH}^{Y\,4Y}$ 1.35(-3)		
Term	$\lvert E_{HH}^{89} \rvert$ -2.65(-3)		E_{CCH}^{431} 3.79(-3)			$\widehat{E}_{COH}^{321}$ 1.77(-6)		
Term	E_{HH}^{89} -7.50(-3)		E_{HCH}^{839} -9.18(-3)					
Term	E_{HCH}^{839} -8.72(-3)		$\widehat{E}_{HCC}^{X\,34}$ 2.29(-6)					
Term	$\hat{E}_{HCH}^{Y\,4Y}$ 8.05(-7)							

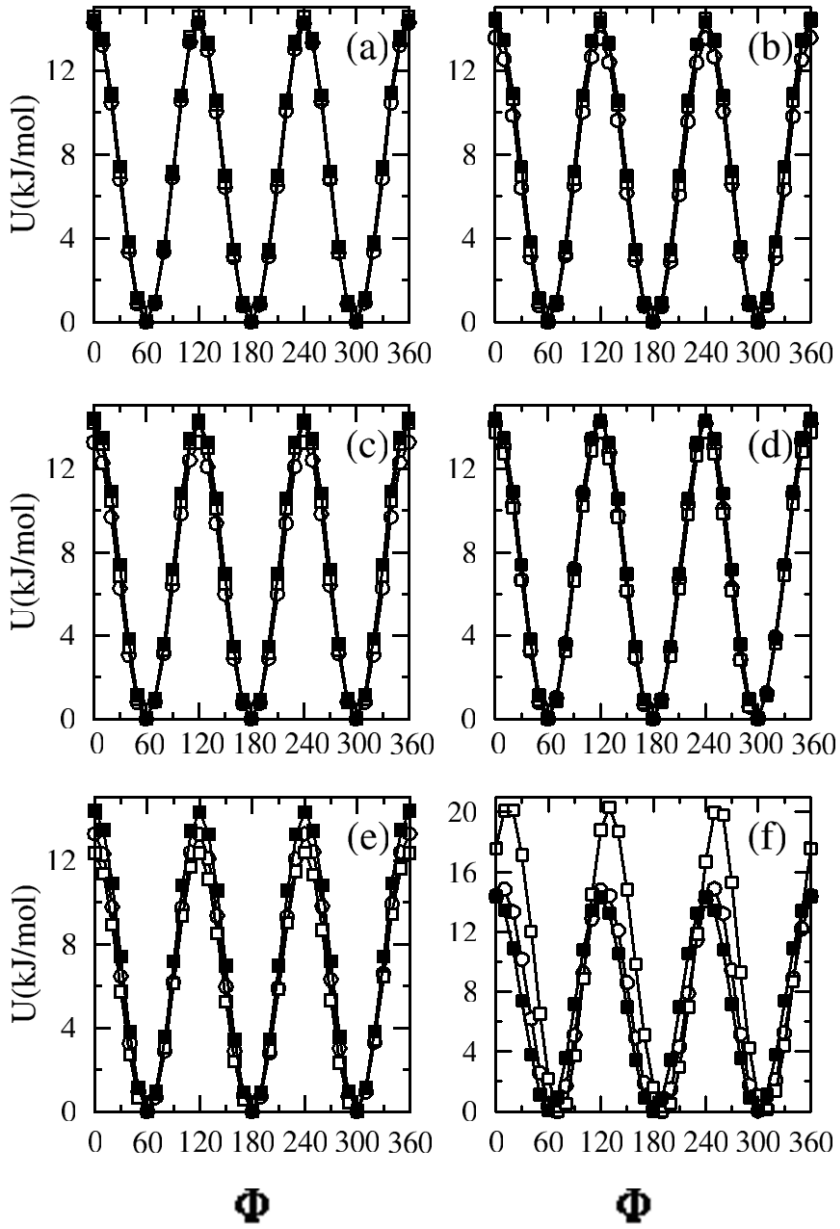

Figure 3.5. The torsional potential, $U^{tor}(\vec{E})$, between O(2)-C(3)-C(4)-H(5) as a function of the dihedral angle. For convenience, each vertical scale is shifted so that the *ab initio* curve minimum corresponds to an energy of zero. The B3LYP/6-311++G(d,p) results are shown with open circles, corrected *ab initio* results are open squares, and the field-independent fit to the corrected *ab initio* results are filled squares. The panels show the dependence of the potential on the field. In reduced units: (a) $|\vec{E}_H^1|$=0.00, $|\vec{E}_O^2|$=0.00, $|\vec{E}_C^3|$=0.00; (b) $|\vec{E}_H^1|$=27.10, $|\vec{E}_O^2|$=26.83, $|\vec{E}_C^3|$=25.63; (c) $|\vec{E}_H^1|$=14.88, $|\vec{E}_O^2|$=11.85, $|\vec{E}_C^3|$=10.47; (d) $|\vec{E}_H^1|$=18.12, $|\vec{E}_O^2|$=18.99, $|\vec{E}_C^3|$=11.62; (e) $|\vec{E}_H^1|$=16.12, $|\vec{E}_O^2|$=9.49, $|\vec{E}_C^3|$=6.17; and (f) $|\vec{E}_H^1|$=30.72, $|\vec{E}_O^2|$=18.35, $|\vec{E}_C^3|$=12.29.

3.2.6 Simulation details

The canonical (NVT) ensemble is employed for MD simulations of 200 ethanol molecules, at a density of 0.787 g/cm^3 and a temperature of 298 K. Periodic boundary conditions are employed together with a spherical cut-off for LJ interactions.

The fluid structure is particularly sensitive to the parameters chosen for H(1) and O(2). This is expected based on the importance of hydrogen bonding in the fluid. Simulations were performed for 486 models differing in the Lennard-Jones parameters for O(2) and H(1). Specifically, ε_o=(0.7, 0.9, 1.1, 1.3, 1.5, 1.7), σ_o=(0.25, 0.27, 0.29, 0.295, 0.3, 0.305, 0.31, 0.33, 0.35), ε_H=(0.1, 0.2, 0.3), and σ_H=(0.02, 0.05, 0.10). We initially perform 20 ps simulations for the 486 parameter combinations and assess the fluid structure based on peak positions and coordination numbers, versus neutron diffraction results[123]. We also require that the charge on O(2) be less than -1.0|e| and that the diffusion coefficient is within a factor of three of the experimental value[87], 1.2×10^{-9} m^2/s. With these criteria, 25 parameter sets were selected for further consideration. 50 ps simulations were undertaken for these parameter sets, and the 5 sets with diffusion coefficients closest to experiment were selected. For the remaining five models, 1 ns simulations were performed and the final model has been chosen based on the predicted dielectric constant. Our optimal LJ parameters are given in Table 3.2.

EWALD summations[90], with conducting boundary conditions, are applied for the long-ranged electrostatic interactions. The additional contributions from the charge fluctuations are included in the EWALD contribution to the energy by first computing the EWALD contribution for an atomic fluid and then removing the contribution for the intramolecular pairs where Eq. [2.26] differs from the point-charge Coulombic potential.

For these atomic pairs, the electrostatic energy is calculated from Eq. [2.26]. The results reported below correspond to a position space cut-off of $\alpha = 0.26685$ Å^{-1}, and a momentum space cutoff of $k^{*2} \leq 27$.

The procedure employed to generate the starting configuration has been discussed in detail elsewhere[147]. Briefly, an excess of molecules is placed in the simulation cell and some are removed at random until the desired number (200) remains. These molecules are oriented randomly within the simulation cell. Finally, the system is expanded to reduce any strong repulsions, and Monte Carlo cycles are performed (assuming that the molecules are rigid and non-polarizable) while the cell is gradually recompressed to the desired volume. The molecules are then assigned random linear and angular velocities, consistent with the desired temperature. Following this, the equations of motion for the charges are equilibrated and the corresponding field-dependent intramolecular potentials are calculated. In this way, the starting configuration is liquid-like and each ethanol molecule begins the simulation with distinct intramolecular potentials and atomic charges.

We compare four different simulations to evaluate the importance of charge fluctuations and field-dependent intramolecular motion. First, we consider bulk ethanol, as represented by a non-polarizable flexible molecular model. Second, we allow the charges to respond to the molecular field but use the zero-field intramolecular potentials. Third, we consider electric-field dependent charges and intramolecular motion but, in the evaluation of forces, we treat the intramolecular contribution as though it is field-independent. With this approximation, the simulation time increases only marginally while the intramolecular potential still responds to the field. Of course, dynamical

motion will not be correct but we explore the accuracy of the equilibrium fluid structure. Finally, we simulate the full model and include forces due to the field-dependence of the atomic charges and intramolecular potential.

Nosé-Hoover thermostatting[95, 96] was used to generate canonical averages. Following Rick *et al*.[46], extended Lagrangian equations of motion are also applied to the charges. The relevant conserved quantity in our simulations is shown in Eq. [2.58]. The mass m_Q is set to 3 x 10^{-5} kcal/mol (ps/e)^2, a very small value chosen to allow the atomic charges to rapidly respond to changes in atomic positions. Since these fluctuations are intended to capture electronic reorganization, it is expected that the variations in charge should be much faster than atomic motion. Fig. 3.6 shows the impact of m_Q on the fluid structure and diffusion coefficient. The diffusion coefficients in the figure are evaluated from the slope of the mean square displacement[40] for 20 ps simulations. The mass chosen in this work is identified by (a) in the figure. From the figure, the diffusion coefficient's dependence on the charge mass can be characterized by a plateau region at very small mass (rapid response region), followed by a sharp peak, then a drop down to very small values and a gradual rise to the fixed-charge limit. Clearly, the value of m_Q has an important impact on the fluid structure: a very small value allows the charges to fully respond to changes in nuclear positions, a large value suppresses the charge fluctuations, but at intermediate values the charges drastically alter the fluid properties, either by reducing the intermolecular structure, or by greatly enhancing it. For the simulations m_Q must be chosen carefully since an exceedingly small value will negatively impact the time step of the simulation but a large value will

lead to unphysical results. In particular, the hydrogen bonding structure will only be accurately predicted if the chosen mass allows a sufficiently fast charge response.

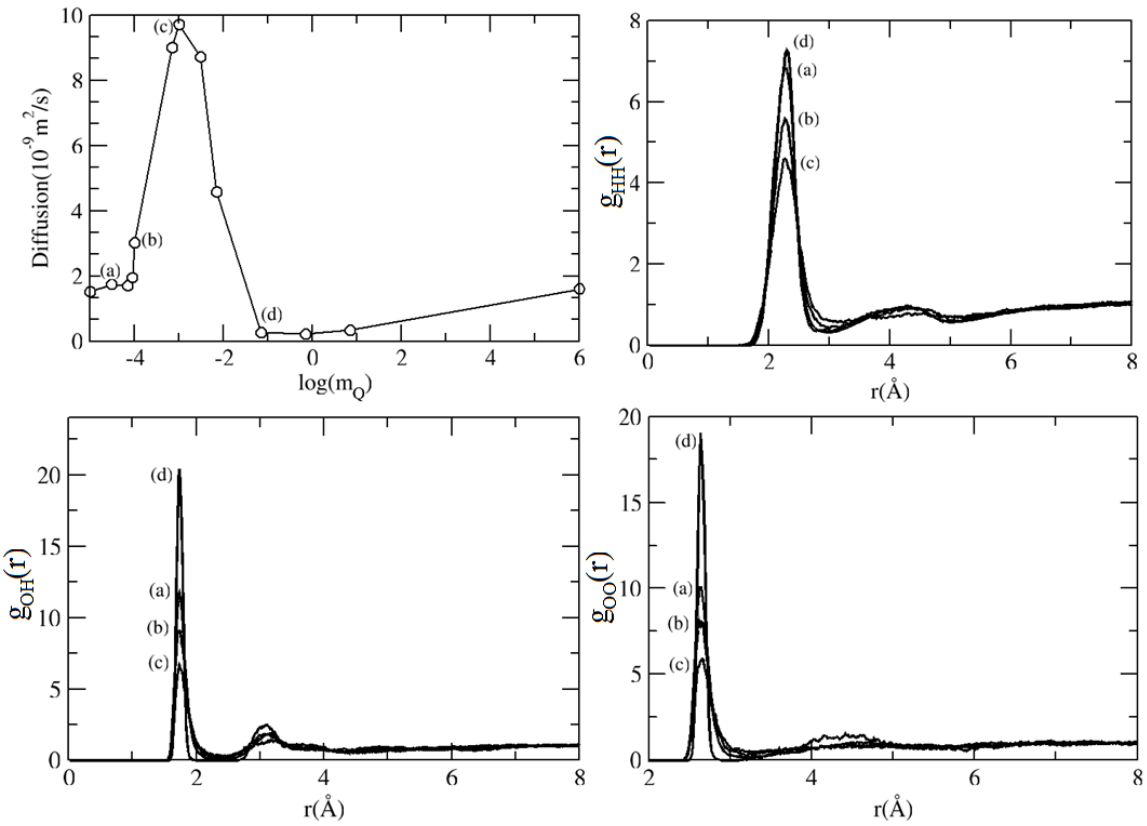

Figure 3.6. The impact of charge "mass" on the diffusion coefficient and radial distribution functions obtained from 20 ps simulations. The final mass chosen for the simulations is identified by (a). The diffusion coefficients are plotted against the logarithm of the charge mass (in units of kcal/mol $(ps/e)^2$). Radial distributions are given for four masses, identified with (a)-(d).

A direct application of a velocity Verlet scheme for integrating the equations of motion requires a time step of less than 0.02 fs in order for H_{NH} to be conserved because of the time scale of the charge fluctuations. This is an unfeasibly small time step, and we have introduced a reversible multiple time step MD algorithm, following Tuckerman *et*

al.[97], to integrate the equations of motion. Details of the force calculations and the equations of motion are provided in Appendix B. The larger time step for the simulations was 0.1 fs, while the atomic charges, and their associated extended Lagrangian variables η_{fq} and p_{fq} , are advanced every 0.01 fs. Fig. 3.7 shows the energy components and H_{NH} as a function of time for a 50 ps simulation. The kinetic energy of the charges is very small (effectively zero on the scale of the figure) since the charge "temperature" is set at 1 K. The potential energy, which includes the contribution from the FC model for electrostatic interactions, stabilizes after 5-10 ps. The short-time fluctuations in H_{NH} are clearly very small but a slight long-term drift is evident even with the small time steps employed here. Throughout the simulation H_{NH} is monitored and fluctuations are within 1% over 10ps.

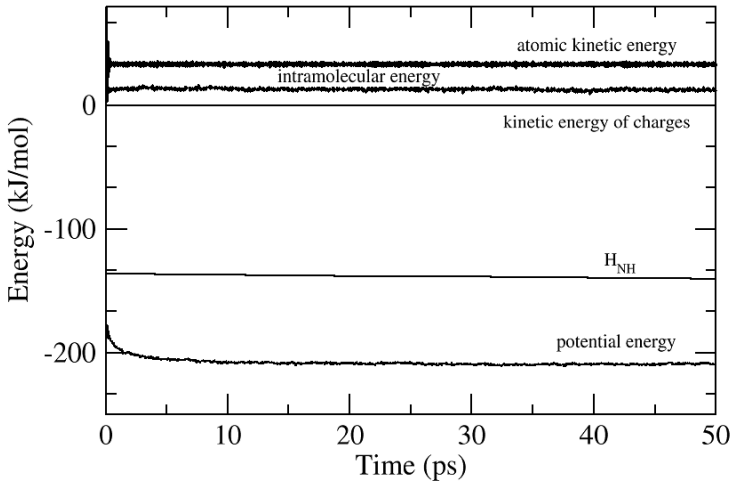

Figure 3.7. The energy components and the conserved quantity H_{NH} as a function of time. The potential energy includes all contributions except for the intramolecular potential which is shown separately. The kinetic energy for the charges is effectively zero throughout the simulation.

The simulations of polarizable, flexible ethanol are performed using the MDMC program[148]. Modifications were introduced to include the charge fluctuation model,

the field-dependent intramolecular potential, and the multiple time step algorithm. The evaluation of forces from the field-dependent intramolecular potential is, by far, the most time-consuming aspect of the computation (see Appendix B). We have parallelized this segment of the code to allow for rapid computation of the forces.

In the simulations, it is possible for atoms to experience fields for which the parameters in Eqs. [2.31]-[2.33] are outside of the range used in building their field-dependent forms. Although this is a rare event, and the model may perform well in such a field, we have chosen to introduce a damping function for each parameter in Eqs. [2.31]-[2.33]. Specifically, we consider the fitted parameters, and extract the minimum and maximum values observed in the 618 fields. These values are given in Tables 3.3-3.5. The damped value, x^{Damp} , of a parameter x is obtained from

$$x_{\min} + \frac{x_{\max} - x_{\min}}{2} e^{-a(x_{\max} - x_{\min})^2/4} \qquad (x \le x_{\min}) \qquad [3.5]$$

$$x - (x - x_{\min}) e^{-a(x - x_{\min})^2} + \frac{x_{\max} - x_{\min}}{2} e^{-a(x_{\max} - x_{\min})^2/4} \qquad (x_{\min} < x \le \frac{x_{\min} + x_{\max}}{2}) \qquad [3.6]$$

$$x + (x_{\max} - x) e^{-a(x - x_{\max})^2} - \frac{x_{\max} - x_{\min}}{2} e^{-a(x_{\max} - x_{\min})^2/4} \qquad (\frac{x_{\min} + x_{\max}}{2} < x \le x_{\max}) \qquad [3.7]$$

$$x_{\max} - \frac{x_{\max} - x_{\min}}{2} e^{-a(x_{\max} - x_{\min})^2/4} \qquad (x_{\max} < x) \qquad [3.8]$$

where x_{min} and x_{max} are the minimum and maximum values of the parameter, respectively. Away from the minimum and maximum values, the damping has a negligible effect. The last term in Eqs. [3.6] and [3.7] is present to ensure continuity of the damped function, and its slope, at the midpoint value of the parameter range. To evaluate the constant a in

Eqs. [3.5]-[3.8], we identify x^* as the damped parameter that satisfies $d^2 x^{Damp} / dx^2 = 0$ and we require that

$$\frac{|x^* - x_{\max}|}{|x_{\max} - x_{\min}|} = 10\% \qquad [3.9]$$

to determine the exponent a. The ratio of 10% is decided based on trial and error. We have found that it leads to a damping function which restricts the parameter to lie within the range $[x_{min}, x_{max}]$ but without altering the value significantly away from the end points. As well, the force contribution from the damping (see Appendix B) is only significant in the region near x_{min} and x_{max}. The ratio of the damped coefficient to the original, $x' = x^{Damp} / x$, is illustrated in Fig. 3.8. We see that x' is close to one over most of the parameter range and deviates by less than 10% near the extreme values of the parameter range. Beyond the range of parameters values obtained from the 618 fields, the damped parameter adopts the maximum or minimum value.

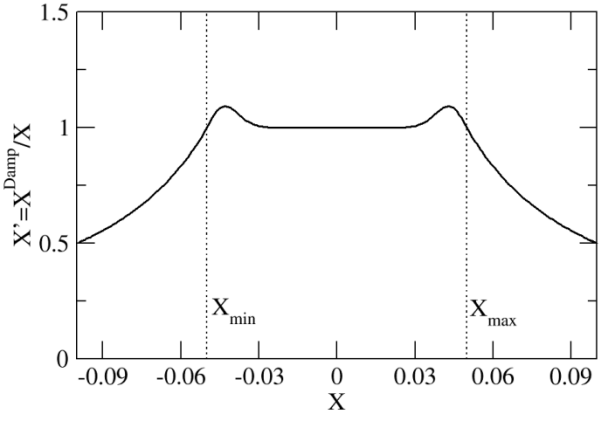

Figure 3.8. The impact of damping on the range of parameter values allowed in the simulation. The solid line shows the ratio of the damped coefficient to the original (see Eqs. [3.5]-[3.8]).

3.3. Results and discussion

In this section, we examine the fluid structure in bulk ethanol. First, we compare our results to experiment and to those of other ethanol models, then we turn to the hydrogen-bonding structure in the bulk.

3.3.1 Bulk ethanol

Fig. 3.9 compares radial distributions from the fCINTRA model, from neutron diffraction[123], and from the non-polarizable OPLS model [127]. The distribution between hydrogen-bonding hydrogens (H(1) in Fig. 2.8) is shown in the top-panel. The first peak in the experimental distribution is relatively broad and all models we have examined (both polarizable and non-polarizable) have narrower peaks. Given this, we have chosen to optimize our model based on the coordination number and peak position. Coordination number is the total number of neighbors around a central atom and can be obtained by integrating over the first peak of the radial distribution [42]. As shown in Table 3.6, these are well reproduced with the fCINTRA model. The small secondary peak in $g_{HH}(r)$, at $r \approx 4.3$ Å, is also well-reproduced by the fCINTRA model. In contrast, the OPLS model places this peak at too large a separation and underestimates the coordination number.

The second distribution, $g_{XH}(r)$, is a combination from the O(2)-H(1), C(3)-H(1), and C(4)-H(1) interatomic pairs. The neutron diffraction experiments[123] were not able to separate these contributions, and the combination in Fig. 3.9 is

$$g_{XH}(r) = 0.303\, g_{H(1)O(2)}(r) + 0.349\, g_{H(1)C(3)}(r) + 0.349\, g_{H(1)C(4)}(r). \qquad [3.10]$$

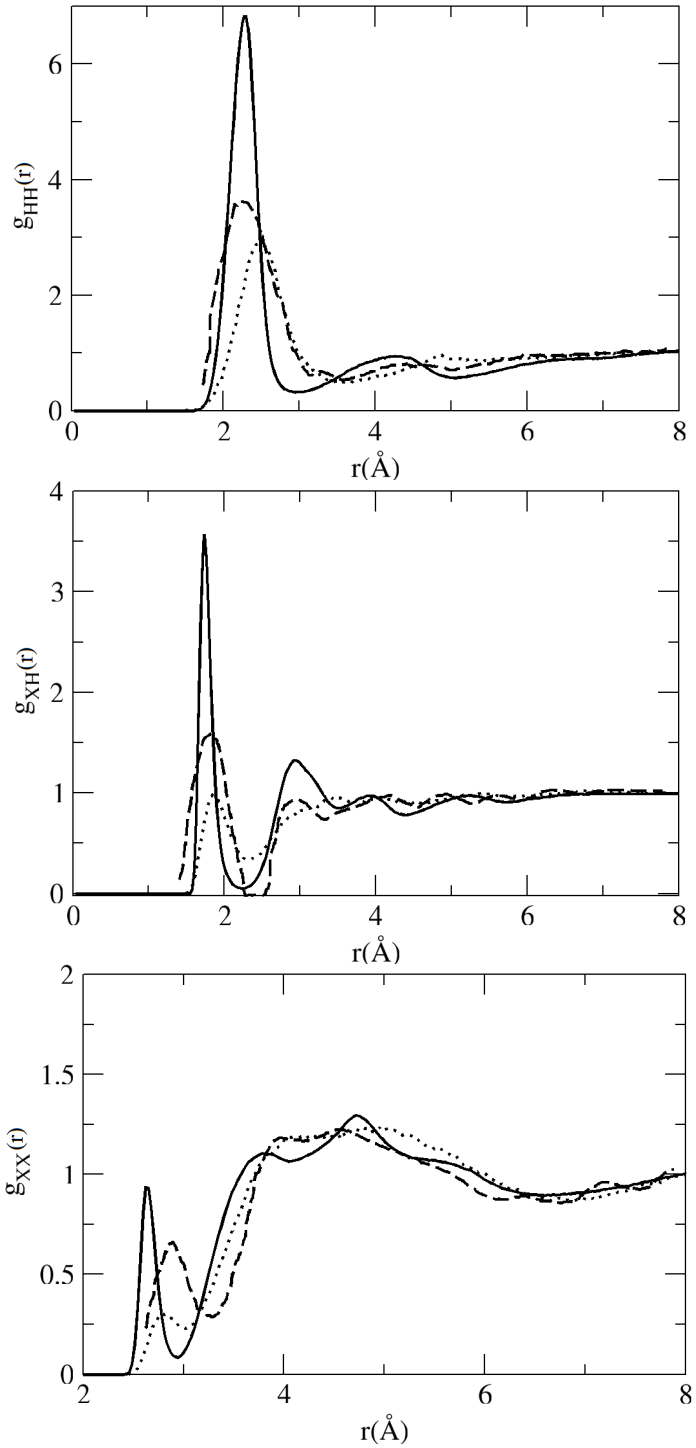

Figure 3.9. A comparison of radial distributions in bulk ethanol obtained from experiment, a non-polarizable model, and the fCINTRA polarizable model. The solid, dotted, and dashed lines correspond to the fCINTRA model, the OPLS model, and the experimental[123] curves, respectively. The topmost panel shows the distribution between hydrogen-bonding hydrogens. The lower panels include multiple contributions from O(2), C(3), and C(4), as discussed in Section 3.3.1.

Table 3.6. Properties of bulk ethanol as predicted from the polarizable, flexible fCINTRA model are compared with experiment. Values for the polarizable OPLS[126] and PIPF[43] models and for the non-polarizable OPLS[127] model are included. The second column reports the average oxygen charge from the simulations. The OPLS-pol and PIPF do not introduce polarization directly into the charge so the tabulated values correspond to the zero-field limit. The third, fifth, and seventh columns report peak positions (PP) in the interatomic distributions. For experiment, this work, and OPLS, X represents the total contribution from O(2), C(3), and C(4). The peak positions for the polarizable OPLS and PIPF models correspond only to oxygen (X=O(3)). Corresponding coordination numbers (CN) are given in the fourth and sixth columns. The self-diffusion coefficient is given in the eighth column, while the dielectric constant, the average dipole moment, and enthalpy of vaporization are given in the following columns. The 7th row identifies the quantities obtained with a fluctuating charge model with a zero-field intramolecular potential. Likewise, the following row refers to the fixed charge limit, with a field-dependent intramolecular potential. The final row ("E shift") corresponds to the field-dependent charges and intramolecular potential implemented with an omitted force contribution (See Section 3.2.6).

	Q_O(|e|)	PP (HH)(Å)	CN (HH)	PP (XH)(Å)	CN (XH)	PP (XX)(Å)	D ($10^{-9}m^2/s$)	ε	Average dipole (D)	ΔH_{vap} (kJ/mol)
Exp.		2.26[123]	2.00[123]	1.82[123]	0.95[123]	2.89[123]	1.20[87]	24.35[132]	3.04[145]	42.30[133]
fCINTRA This work	-0.99	2.30	2.11	1.73	0.96	2.62	1.74	24.89	2.64	45.77
OPLS[126, 127]	-0.68	2.54	1.70	1.86	0.53	2.81	1.10	16.00	2.22	43.00
OPLS-pol[126]	-0.53			1.80		2.62	1.30		2.55	40.70
PIPF[43]	-0.54			1.85	0.99	2.70			2.44	42.17
FC, $U^{\text{intra}}(0)$	-0.95	2.38	1.91	1.79	0.75	2.68	1.45		2.49	
no FC, $U^{\text{intra}}(\vec{E})$	-0.71	2.43	1.90	1.84	0.67	2.78	1.21		3.24	
E shift	-0.98	2.35	2.02	1.76	0.81	2.68	0.59		2.60	

As shown in Fig. 3.9 and Table 3.6, the fCINTRA model reproduces the first peak position and coordination number but is much sharper than the experimental curve. Following the initial peak, due almost entirely to oxygen, the experiments indicate an oscillatory behavior due to contributions from all three atoms. Our polarizable model also shows oscillatory behavior and reproduces the second peak position accurately but the third peak is shifted to smaller separations. The OPLS curve shows far less structure than either the experiment or the fCINTRA distributions and the coordination number is underestimated by roughly 40%.

The final distribution in Fig. 3.9, $g_{XX}(r)$, includes a contribution from several atom pairs, as follows

$$g_{XX}(r) = 0.0924\, g_{O(2)O(2)}(r) + 0.212\, g_{C(3)O(2)}(r) + 0.121\, g_{C(3)C(3)}(r) + 0.212\, g_{C(4)O(2)}(r) + 0.242\, g_{C(4)C(3)}(r) + 0.121\, g_{C(4)C(4)}(r) \quad [3.11]$$

Benmore *et al.*[123] note concerns about contributions from hydrogens remaining in this distribution. As a result, we have opted to focus on overall agreement between experiment and theory for this particular distribution. We find that the position and intensity of the first peak is highly variable. Our final parameters (in Table 3.2) give a peak that appears at smaller separations relative to experiment but the area under this peak is reasonable. The broad secondary structure is also sensitive to model details but, as shown in Fig. 3.9, the fCINTRA model shows the expected double peak followed by a broad shoulder.

Table 3.6 provides a comparison of the properties predicted from the fCINTRA model, from experiment, from the non-polarizable OPLS model, and for two polarizable models. Consider first the charge on O(2). The OPLS-pol and PIPF models do not

include the polarizability directly into the charges. The PIPF model, for example, introduces atomic dipoles to represent the polarizability. However, the static charges employed in these simulations are significantly smaller than the gas phase charge (Table 3.2). The average charges obtained in this work are fairly large but we note parameter sets that gave smaller average charges inevitably led to a high diffusion coefficient and low coordination numbers.

Self-diffusion is overestimated by the fCINTRA model. However, as shown in Fig. 3.6, the diffusion coefficient is highly sensitive to the mass associated with charge fluctuations. Fig. 3.6 suggests that a further reduction in the mass would decrease the diffusion coefficient slightly but the final value would still lie above the experimental value.

The fCINTRA model predicts a dielectric constant, ε, in very close agreement with experiment. The dielectric constant is calculated from[149]:

$$\varepsilon = \varepsilon_{\infty} + \frac{4\pi}{3Vk_bT}(<|\vec{M}|^2> - |<\vec{M}>|^2) \qquad [3.12]$$

where $\vec{M}$ is the total dipole moment of the simulation box:

$$\vec{M} = \sum_{\alpha=1}^{M}\sum_{i=1}^{N_\alpha} Q_{i\alpha}\vec{r}_{i\alpha} \qquad [3.13]$$

Over the course of the simulation $<|\vec{M}|>$ should average to zero and we monitor this quantity as a measure of the convergence of the dielectric. The value given in Table 3.6 includes the contribution from $<|\vec{M}|>^2$, although it should be strictly zero, and it is less than 1% of the reported dielectric constant. In Eq. [3.12], ε_{∞} is calculated from the Clausius-Mossotti equation[150]:

$$\frac{\varepsilon_\infty - 1}{\varepsilon_\infty + 2} = \frac{4\pi}{3}\frac{\alpha}{v} \qquad [3.14]$$

where α is the molecular polarizability (see Appendix A) and v is the molecular volume. The fCINTRA model predicts ε_∞ to be 1.88, which is quite close to the experiment value[132] of 1.93.

The average dipole moment and the enthalpy of vaporization, ΔH_{vap}, are evaluated from the simulations but are not considered in the parameter selection. Relative to the non-polarizable OPLS and the polarizable models, the fCINTRA model predicts the average dipole in closest agreement with experiment although the experimental value is still underestimated by 13%. The distribution of molecular dipole moments is a Gaussian for the fCINTRA model with a standard deviation of 0.308D. The evaluation of the enthalpy of vaporization proceeds as discussed elsewhere[43]. Briefly, ΔH_{vap} is evaluated from

$$\Delta H_{vap} = [E_{intra}(g) - E_i(l) - E_{intra}(l)] + RT - (H^o - H) \qquad [3.15]$$

where $H^o - H$ is obtained from experiment[127]. The calculation of the average gas phase intramolecular energy, $E_{intra}(g)$, proceeds by simulating a "fluid" in which all the intermolecular interactions are omitted. In other words, individual molecules are flexible and polarizable but no longer interact in the fluid. The equations of motion are integrated as discussed in Section 2.4, except that Nosé-Hoover chains[81] are implemented to ensure proper canonical averages. From Table 3.6, the fCINTRA model predicts a vaporization enthalpy in good agreement with experiment, although the experimental value is exceeded by 8%.

The last three rows in Table 3.6 show the properties from sub-models corresponding to simplified versions of the fCINTRA model. All three models result in simulations that are comparable, time-wise, to those for non-polarizable models. The use of the FC model, with zero-field intramolecular potentials, leads to properties that are in reasonable agreement with experiment although the coordination numbers and the average dipole are consistently too small. The use of field-dependent intramolecular potentials with fixed-charges also reduces the coordination numbers and average dipole. In this case, the dipole distribution is bimodal with a peak at 2.34D and a peak at 3.80D. The "E shift" method, in which the forces due to the field-dependence of the intramolecular coefficients (the last term in Eq. [B1]) are neglected, yields a diffusion coefficient that is far too small. This suggests that the coupling term cannot be omitted.

Overall, the fCINTRA model compares favorably with experiment and other polarizable models. The introduction of field-dependence in the charges and the intramolecular potentials leads to accurate predictions for a range of properties including the fluid structure, the diffusion coefficient, the dielectric, the average dipole, and the enthalpy of vaporization. Further model refinement would undoubtedly improve the agreement with experiment. Such improvements would include optimization of all the LJ parameters, further minimization of the charge mass, and perhaps inclusion of field-dependence in all the intramolecular parameters. The limit on the maximum oxygen charge could also be relaxed. The latter may lead to an increase in the average dipole and a decrease in the self-diffusion coefficient, but may adversely impact the dielectric constant and vaporization enthalpy.

3.3.2 Hydrogen bonding

Fig. 3.10 shows three snapshots of the fluid. The left-most panel shows alkyl rich regions with a "loose" hydrogen bonding network separating the regions. Consider the central panel where O(2) and H(1) are emphasized. From the figure, the hydrogen bonding network in the fluid consists of complex chain-like structures. In order to quantify this network, we apply a stringent structural definition of the hydrogen-bond[120]: $r_{HO} < 2.6$ Å, $r_{OO} < 3.5$ Å, and the O-H-O angle is greater than 150 degrees. Using this definition, snapshots have been analyzed to ascertain the hydrogen bond characteristics and the results are collected in Table 3.7. For the fCINTRA model, the average chain length includes roughly 24 molecules. A branch, in which an ethanol molecule hydrogen bonds to three others, occurs on average once or twice every chain. As well, only 1% of the molecules are not participating in a hydrogen-bond at any given time. The statistics collected for the non-polarizable OPLS model show a drastically reduced chain length, with a commensurate increase in the percentage of single molecules. Thus, this nonpolarizable model greatly underestimates the extent and character of hydrogen-bonding in the fluid. The statistics for the "partial" models are also given in Table 3.7. In all cases, the length of the hydrogen bonding chains has decreased. Overall, the FC model with zero-field intramolecular potentials is superior to the other sub-models.

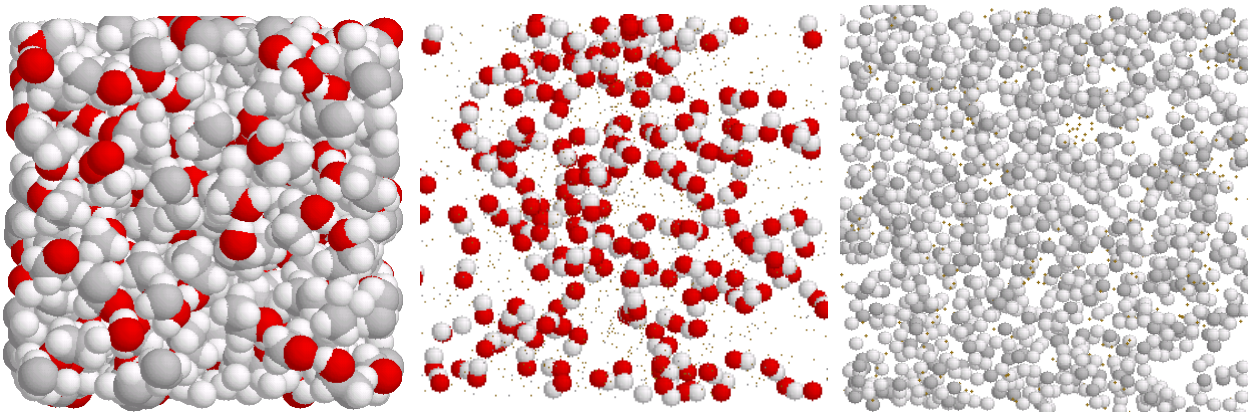

Figure 3.10. Snapshots of bulk ethanol from the fCINTRA polarizable, flexible model. All atoms appear in the snapshot on the right, while the center snapshot emphasizes O(2) and H(1), and the rightmost snapshot shows the carbons and their hydrogens.

Table 3.7. Hydrogen bond statistics evaluated from snapshots of the simulation cell. A chain is defined by a series of hydrogen bonds, the percentage of single molecules identifies the average number of molecules that are not hydrogen bonding, and branches correspond to molecules that simultaneously hydrogen bond to three others.

	Average chain length	Percent single molecules	Branches per chain
fCINTRA This work	23.7	1.0	1.6
OPLS	6.2	23.9	0.6
FC, $U^{\text{intra}}(0)$	21.1	2.7	1.7
no FC, $U^{\text{intra}}(\vec{E})$	13.2	3.7	1.8
E shift	19.4	0.0	3.0

3.4. Conclusions

In this chapter, we have developed a polarizable and flexible model for ethanol. Our approach differs from others[43, 45, 46, 126, 127] in that we allow the intramolecular potential to vary with the field. Atomic charges also fluctuate with the field according to the FC method[46]. At any instant in time, each ethanol molecule in the bulk has a unique set of atomic charges, and its own set of intramolecular potentials. The idea here is that, for each molecule, the electron distribution is unique and leads to distinct atomic charges and intramolecular potentials.

The model we have developed relies heavily on *ab initio* calculations, and we begin with benchmarking of density functionals and basis sets. As well, we collect information on the fields typically experienced by ethanol molecules in the bulk. Following this, an extensive series of B3LYP/6-311++G(d,p) calculations of ethanol, in the presence of 618 fields, is undertaken to develop field-dependent intramolecular potentials. The final ethanol model is obtained by comparison with interatomic distributions[123] and other properties. Although the distribution functions available for comparison are not fully resolved, we find that they do provide a sensitive test of our models. In the end, only four Lennard-Jones parameters are chosen by direct comparison with experiment. In particular, the fluid structure is highly sensitive to the LJ parameters on O(2) and H(1) and small changes in the parameters change the H-bonding in the fluid and lead to significant differences in interatomic distributions.

The stretching and bending motion in ethanol is not strongly field-dependent, and we have chosen to introduce field dependence in only the equilibrium bond angles, leaving the equilibrium bond lengths and the force constants field-independent. On the

other hand, the torsional potential for rotation about the C(3)-O(2) bond, which governs the position of the H-bonding hydrogen, is strongly field-dependent. In some fields, this torsional potential is highly asymmetric, and the global minimum is not at the zero-field value of 180 degrees. An analysis of hydrogen bond characteristics shows that the fCINTRA model predicts longer chains of H-bonded molecules, with very few branching events and few isolated molecules. Other models underestimate the chain lengths and overestimate the fraction of non H-bonding molecules. The fCINTRA model allows the hydrogen to reposition itself in response to the field, thereby optimizing the hydrogen-bond network.

We have analyzed the impact of field-sensitivity of the model by performing a series of simulations on sub-models of fCINTRA. First, the fluid in which the intramolecular potential is field-independent but the charges respond to the field is considered. This model compares favorably with the fCINTRA model although, on average, the hydrogen bonded chains are shorter and the average dipole has been lowered. Second, the intramolecular potential changes with the field, but the atomic charges do not vary. Table 3.6 suggests that this model compares favorably with experiment. However, the model yields a bimodal dipole distribution and the average length for hydrogen-bonded chains is much shorter than for fCINTRA. Finally, both the charges and the intramolecular potential vary but some force terms are omitted. This approach yields a diffusion coefficient well below experiment. Overall, the sub-model in which only the charges fluctuate compares best with fCINTRA.

The implementation of the fCINTRA model presents several challenges. First, the evaluation of the field-dependent intramolecular potential parameters must be

efficient. We have chosen to expand the coefficients into field-analogs of structural quantities. We have also been careful to enforce any expected symmetries in the coefficients. Second, the FC method has only been applied in a few instances[46, 50, 53, 55, 131] and we have found that the simulations are highly sensitive to the choice of charge "mass" and to the definition of the Coulomb overlap. For the latter, we employed a simple interpolation of numerically integrated overlaps(Eq. [2.27]) that was accurate, stable, and efficient (See Section 2.2.1). Third, within the simulations, the molecules experience a range of fields and some of these may lead to intramolecular potential coefficients that lie outside of the range used in the parameterization of the model. We have dealt with this by introducing a damping function that constrains the coefficients to within the interval. Fourth, the charges may "heat up" during the simulation, but we have implemented a Nosé-Hoover thermostat to constrain their temperature to 1K. Finally, the time required for charge fluctuations must be much shorter than for nuclear motion. As a result, a multiple time-step molecular dynamics algorithm is also required.

The polarizable model methodology developed in this chapter offers a viable alternative to *ab initio* simulations. Although the model development requires a large number of initial *ab initio* calculations, the individual calculations are fast. As well, the simulations are far less demanding than full *ab initio* simulations although they are much more time-consuming than for non-polarizable models. In particular, nanosecond simulations are still feasible with the methodology developed in this chapter.

Chapter 4
Chirality transfer: The impact of a chiral solute on an achiral solvent

In this chapter, the chirality transfer from chiral solutes to achiral solvents is discussed. The study is based on MD simulations of two solvents, which are ethanol and benzyl alcohol, and three solutes, which are PAMD, styrene oxide and acenaphthenol. The induced chirality is quantified by a chirality index and the spatial characteristics of the chirality transfer are analyzed.

4.1. Introduction

The impact of solvent on the properties of chiral solutes has been studied in some detail using spectroscopy [24, 30, 31]. Recently, experimental studies have begun to focus on the chirality present in the solvent when it surrounds a chiral solute [26-29].

The chirality transfer from a chiral solute to an achiral solvent, in the isotropic phase, is the focus of this chapter. To our knowledge, this is the first detailed simulation study of chirality transfer in isotropic fluids. With this in mind, we assess the *structural* chirality introduced in the solvent molecules rather than emphasizing a particular property (such as VCD or ORD spectra). This is accomplished with molecular dynamics (MD) simulations of a small number of chiral solutes surrounded by solvent, and the chirality induced in the solvent molecules is assessed via the long-time average of a chirality index. A chirality index proposed by Osipov *et al*.[66] has been chosen for the present work since it can be readily evaluated and satisfies all the requirements noted in

Section 1.4. In this chapter, the Osipov index is evaluated for all solvents in the vicinity of the chiral solute (within 15 Å of specified solute atoms). The excess solvent chirality, as represented by the long-time average of the Osipov chirality index, is evaluated and categorized based on the solvent position about the solute.

In docking processes, including selectivity in chiral chromatography[151-153] and lock-and-key mechanisms in biology,[154, 155] three-point recognition models are often assumed. Here, hydrogen bonding and π-π interactions between aromatic groups are usually present in the recognition models. By analogy with these models, we assume that such interactions also play an important role in the chirality transfer process. To study the impact of these interactions in more detail, we examine two solvents: Ethanol and benzyl alcohol. The former will interact with the chiral solute primarily via a hydrogen bond while the latter can simultaneously form a π- π interaction and a hydrogen bond. Three solutes have been considered: Styrene oxide, acenaphthenol, and *n*-(1-(4-bromophenyl)ethyl)pivalamide (PAMD). Styrene oxide is small, compact, and accessible to the solvent from all sides. Acenaphthenol is larger, but conformationally restricted. PAMD has multiple functional groups, a more complex structure, and many conformers. A comparison between these solutes will provide some indication of the relationship between the chirality transfer and the solute size and properties. We also examine the impact of conformational averaging by comparing the excess solvent chirality about rigid and flexible PAMD.

The MD simulations provide insights into the magnitude and characteristics of the chirality transfer between a chiral solute and its surrounding solvent. However, the level of solvent representation is important for an exploration of chirality transfer. In typical

MD simulations, the molecules are nonpolarizable and the instantaneous molecular environment does not impact any of the parameters defining the molecular force field. The importance of polarizability has been explored for small solvents, including water[44, 46, 47, 130] and alcohols[43, 45, 91, 126], during the past decade. These studies show that the fluid structure, in particular the hydrogen bonding network, is impacted by the response of the molecules to their environment. The relationship between solvent polarizability and chirality transfer is examined here, with the expectation that a polarizable solvent will respond more effectively to a chiral environment, as discussed in Chapter 3 [91]. Several polarizable models for ethanol have been reported [43, 45, 91, 126], but in most cases the molecular flexibility parameters (intramolecular potential) are unchanged by the local environment. Polarizability is included via variations in atomic charges, multipole moments, or by the addition of atomic dipoles. In Chapter 3,[91] we discussed a polarizable ethanol model that allows for fluctuating atomic charges and intramolecular potentials that are field dependent. In this chapter, we explore the impact of solvent representation by evaluating chirality transfer for a fully nonpolarizable solvent, a partially polarizable solvent (atomic charge fluctuations only), and a fully polarizable solvent. We find that chirality transfer is greatly underestimated without allowance for solvent polarization.

In section 4.4.2, we briefly discuss the solvent models, the inclusion of polarizability, the chiral index, and the simulation details. Results from extensive MD simulations are reported in Section 4.4.3 and brief conclusions are presented in Section 4.4.4.

4.2. Methods

4.2.1 Solvent and solute models

The fully polarizable fluctuating charge and intramolecular potential (fCINTRA) model for ethanol is discussed in detail in Chapter 3. In this section, we begin by briefly describing the molecular potentials used to represent benzyl alcohol. The solvents and solutes are shown in Fig. 4.1 along with the atom numbering used throughout this chapter. For benzyl alcohol, a fully polarizable solvent model is not available. We have proceeded to develop a partially polarizable model as follows. First, we employ OPLS parameters[156] for the LJ potential in Eq. [2.12]. For the intramolecular potential, an extensive series of B3LYP/6-311G(d,p) *ab initio* calculations have been performed. Since the aromatic ring is very rigid, only 5 stretches, 9 bends, 2 torsions, and 1 improper torsion are chosen to represent the molecular flexibility. The potential parameters, obtained by least squares fits to the *ab initio* calculations, are given in Table 4.1. Each stretching force constant is extracted from nine energy calculations, as the bond is compressed and stretched away from the equilibrium value. Bending potentials are obtained by least squares fits to nine energy calculations where the angle is varied within sixteen degrees of the equilibrium value. For torsion potentials, the angle is varied from 0 to 360^{o}, in steps of 10^{o}. The improper torsion potential about C(6) is obtained from nine restricted geometry optimizations as C(6) is raised above and below the plane of the neighboring three atoms.

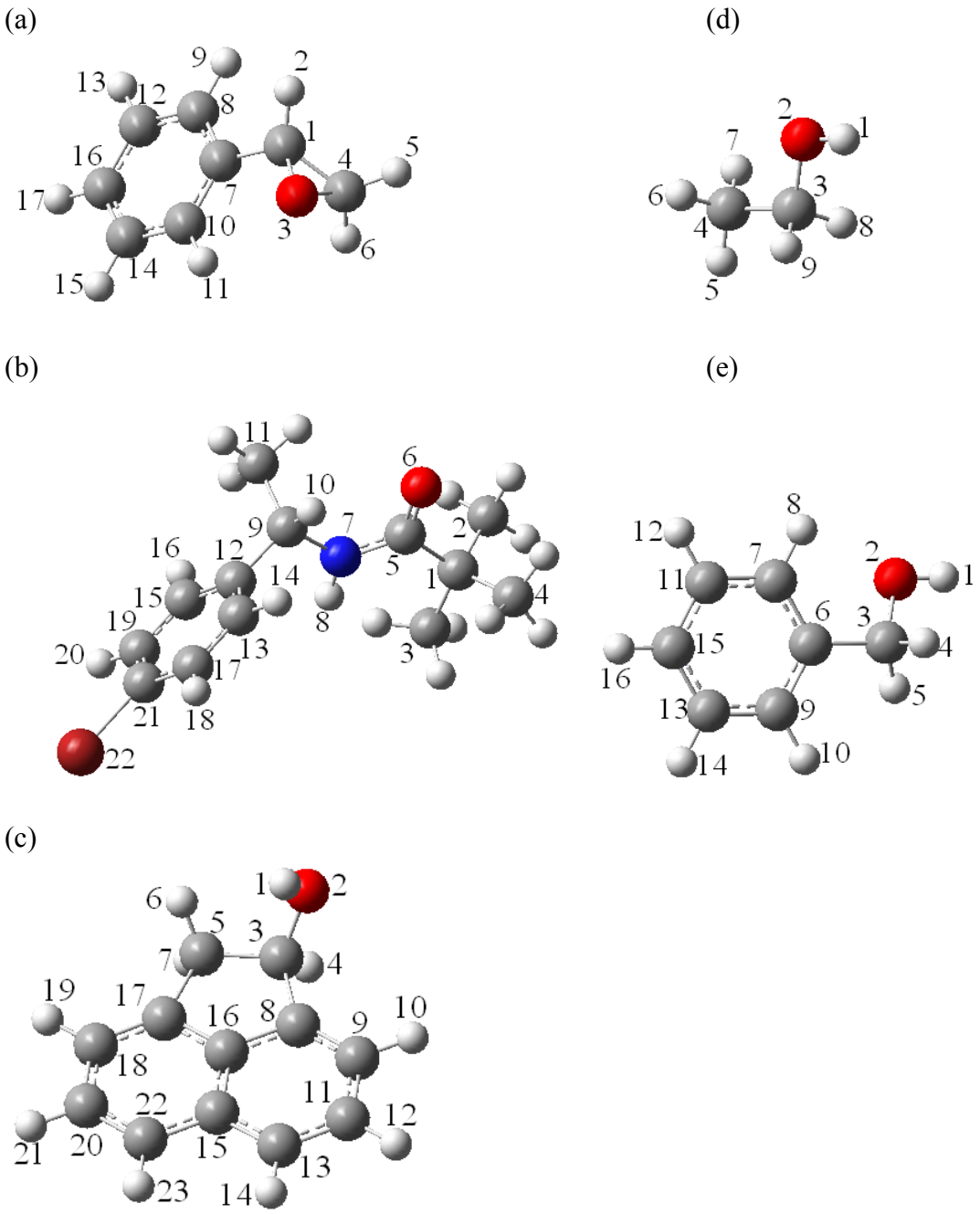

Figure 4.1. The B3LYP/6-311++G(d,p) optimized structures for the solutes (a-c) and the solvents (d and e). S-styrene oxide (a), S-PAMD (b), R-acenaphthenol (c), ethanol (d), and benzyl alcohol (e) are shown. The atom numbering shown above will be used throughout this chapter.

Table 4.1. Intramolecular potential parameters for benzyl alcohol. The first column identifies the atoms (see Fig. 4.1) involved in the potential. When two, three, or four atoms are specified the potential parameters correspond to stretching, bending, or torsion, respectively.

Atom labels	Potential Type	Potential parameters (see Eqs. [2.7]-[2.10])						
1,2	stretch	$k_{s;is}$ =252512 kJ/(Å^2 mol)		$r_{e;is}$ =0.961 Å				
2,3	stretch	$k_{s;is}$ =138317 kJ/(Å^2 mol)		$r_{e;is}$ =1.426 Å				
3,4	stretch	$k_{s;is}$ =151875 kJ/(Å^2 mol)		$r_{e;is}$ =1.099 Å				
3,5	stretch	$k_{s;is}$ =151875 kJ/(Å^2 mol)		$r_{e;is}$ =1.099 Å				
3,6	stretch	$k_{s;is}$ =133458 kJ/(Å^2 mol)		$r_{e;is}$ =1.511 Å				
1,2,3	bend	$k_{\theta;ib}$ =0.0677 kJ/(deg^2 mol)		$\theta_{e;ib}$ =108.7 deg				
2,3,4	bend	$k_{\theta;ib}$ =0.0846 kJ/(deg^2 mol)		$\theta_{e;ib}$ =110.4 deg				
2,3,5	bend	$k_{\theta;ib}$ =0.0846 kJ/(deg^2 mol)		$\theta_{e;ib}$ =110.4 deg				
4,3,5	bend	$k_{\theta;ib}$ =0.0665 kJ/(deg^2 mol)		$\theta_{e;ib}$ =107.5 deg				
2,3,6	bend	$k_{\theta;ib}$ =0.1016 kJ/(deg^2 mol)		$\theta_{e;ib}$ =110.1 deg				
4,3,6	bend	$k_{\theta;ib}$ =0.0728 kJ/(deg^2 mol)		$\theta_{e;ib}$ =109.2 deg				
5,3,6	bend	$k_{\theta;ib}$ =0.0728 kJ/(deg^2 mol)		$\theta_{e;ib}$ =109.2 deg				
3,6,7	bend	$k_{\theta;ib}$ =0.1190 kJ/(deg^2 mol)		$\theta_{e;ib}$ =120.5 deg				
3,6,9	bend	$k_{\theta;ib}$ =0.1190 kJ/(deg^2 mol)		$\theta_{e;ib}$ =120.5 deg				
1,2,3,4	torsion	$C_{it;0}$=2.857 kJ/mol	$C_{it;1}$=-1.774 kJ/mol	$C_{it;2}$=2.466 kJ/mol	$C_{it;3}$=10.030 kJ/mol	$C_{it;4}$=2.260 kJ/mol	$C_{it;5}$=0.690 kJ/mol	$C_{it;6}$=1.364 kJ/mol
2,3,6,7	torsion	$C_{it;0}$=1.364 kJ/mol	$C_{it;1}$=-0.295 kJ/mol	$C_{it;2}$=3.514 kJ/mol	$C_{it;3}$=0.534 kJ/mol	$C_{it;4}$=1.646 kJ/mol	$C_{it;5}$=-0.284 kJ/mol	$C_{it;6}$=-6.480 kJ/mol
3,7,9,6	improper torsion	$k_{ii;t}$=0.0809 kJ/(deg^2 mol)		t_e =-0.9397 deg				

Following the parameterization of the intramolecular potential, fluctuating atomic charges (the FC model) were implemented for benzyl alcohol as follows. In the first instance, the CHARMM-FC transferable parameters[53] were used for the charge fluctuation parameters in Eq. [2.26]. We found that the simulations only converged when

the "mass" governing charge fluctuation was $7x10^{-3}$ kcal/mol (ps^2/e^2) or larger. In practice, this mass must be small enough to allow rapid charge fluctuation in response to molecular motion. Unfortunately, the mass required for benzyl alcohol was large and we found that the average charge on C(3) was unphysical. We proceeded to develop charge-fluctuation parameters *specifically* for benzyl alcohol, following the methodology discussed in Appendix A. adopted previously for ethanol [91]. Briefly, the atomic charges, as evaluated from the CHELPG[110] algorithm applied to B3LYP calculations with the 6-311++G(d,p) basis set, were obtained when the molecule was placed in 30 diverse fields. Based on the fitting of the molecular response, parameters for Eq. [2.26] were extracted. With the new parameters, convergence was achieved for a "mass" as low as $5x10^{-5}$ kcal/mol (ps^2/e^2) and the corresponding atomic charges were reasonable. Table 4.2 presents the fluctuating charge parameters for benzyl alcohol. It is interesting to note that the atomic electronegativities derived specifically for benzyl alcohol were consistently larger than the transferrable CHARMM-FC values. The resulting benzyl alcohol model gives a self diffusion coefficient of 4.27 x 10^{-12} m^2/s, a dielectric constant of 12.13, and a dipole polarizability of 14.67 $Å^3$. These values are in good agreement with the corresponding experimental values of 4.01 x 10^{-12} m^2/s [157], 12.5 (estimated from measured dielectric constants at 20°C and 30°C [158]), and 12.87 $Å^3$ [159, 160], respectively.

The molecular models employed for styrene oxide and PAMD have been described elsewhere [113, 161]. Here we note that these solutes are represented by flexible and nonpolarizable models and that the rings are kept rigid during the simulations, as is also done for benzyl alcohol and acenaphthenol. That is, the ring atoms

move in unison and their motion is represented by translation and rotation about the center-of-mass of the atoms forming the rigid unit.

Table 4.2. Charge fluctuation parameters (see Eq. [2.26]) and zero-field charges for benzyl alcohol. The FC parameters obtained from B3LYP/6-311++G(d,p) calculations (this work) are compared with those of the transferable CHARMM-FC parameter set[54]. The atom numbering follows Fig. 4.1. The J_{ii}^{0}, $\tilde{\chi}_i^{0}$, and Q_i are given in kcal/(mol |e|^2), kcal/(mol |e|), and |e|, respectively.

Atom label	J_{ii}^{0} **(This work)**	J_{ii}^{0} **(CHARMM-FC)**	$\tilde{\chi}_i^{0}$ **(Shifted, This work)**	$\tilde{\chi}_i^{0}$ **(Shifted, CHARMM-FC)**	Q_i
H(1)	608.53	517.26	0.00	0.00	0.414
O(2)	374.67	307.20	159.04	101.66	-0.682
C(3)	270.58	208.92	91.14	50.17	0.304
H(4)	474.71	501.42	78.43	55.08	-0.022
H(5)	474.71	501.42	78.43	55.08	-0.022
C(6)	276.42	225.48	99.10	69.18	0.128
C(7)	266.54	225.48	109.40	69.18	-0.167
H(8)	435.88	454.14	88.25	56.27	0.100
C(9)	266.54	225.48	109.40	69.18	-0.167
H(10)	435.88	454.14	88.25	56.27	0.100
C(11)	269.02	225.48	113.23	69.18	-0.059
H(12)	432.16	454.14	86.64	56.27	0.083
C(13)	269.02	225.48	113.23	69.18	-0.059
H(14)	432.16	454.14	86.64	56.27	0.083
C(15)	274.17	225.48	114.57	69.18	-0.123
H(16)	483.57	454.14	83.87	56.27	0.089

An interaction potential for acenaphthenol was obtained as follows. First, as with benzyl alcohol, *ab initio* B3LYP/6-31G(d) calculations provide the intramolecular potential and, using the CHELPG algorithm, the atomic charges. Second, OPLS

parameters[156] have been chosen for the LJ potential. Fig. 4.2 shows the intramolecular potential for torsion about C(3)-O(2). As shown in the figure, the potential has a well-defined minimum that corresponds to the placement of H(1) above the aromatic region (see Fig. 4.1(c)).

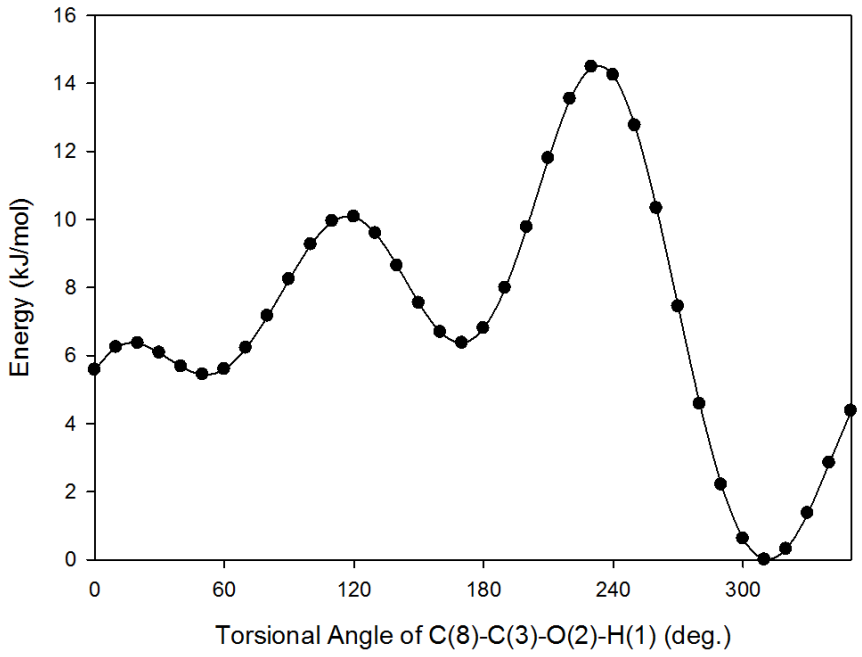

Figure 4.2. The barrier to rotation about the C(3)-O(2) bond of R-acenaphthenol as evaluated from B3LYP/6-31G(d) calculations. The equilibrium structure, corresponding to the minimum, is shown in Fig. 4.1(c).

4.2.2 The assessment of chirality

In Chapter 2, we discussed chirality indexes in detail and introduced the Osipov chirality index[66, 111], G_{0S}^{w} , which is defined in Eq. [2.86]. In the definition of this

chirality index, the powers *m* and *n* and the atomic weights, w_i, are adjustable, and can be chosen to form multiple chirality indexes. In this chapter, we focus on G_{0S}^{w} for solvent molecules near chiral solutes. Instantaneous solvent structures will typically be chiral, leading to a nonzero value for the index. Over long times, the average index of an achiral solvent molecule will be zero as the molecule samples energetically-equivalent configurations, with equal frequency, but with opposite values of the index. If the molecule is in a chiral environment, configurations that are equivalent for the isolated molecule, or when the molecule is in an achiral environment, will no longer be sampled with equal probability. This yields an excess chirality, as reflected by a nonzero value of $< G_{0S}^{w} >$.

The chirality indexes $G_{0S}^{1}, G_{0S}^{q}, G_{0S}^{m}$ for a single ethanol molecule as a function of two torsional angles has been discussed in Chapter 2. The chirality indexes for benzyl alcohol as a function of torsional angle is shown in Fig. 4.3. Relative to ethanol, G_{0S}^{m} is now sensitive to both torsions and G_{0S}^{q} is qualitatively similar for both sets of atomic charges. Two chirality indexes, G_{0S}^{1} and G_{0S}^{q}, have strong correlations in their conformation dependence. The mass-dependent index, G_{0S}^{m}, is distinct from the others in that it depends more strongly on torsions about the C(6)-C(3) bond.

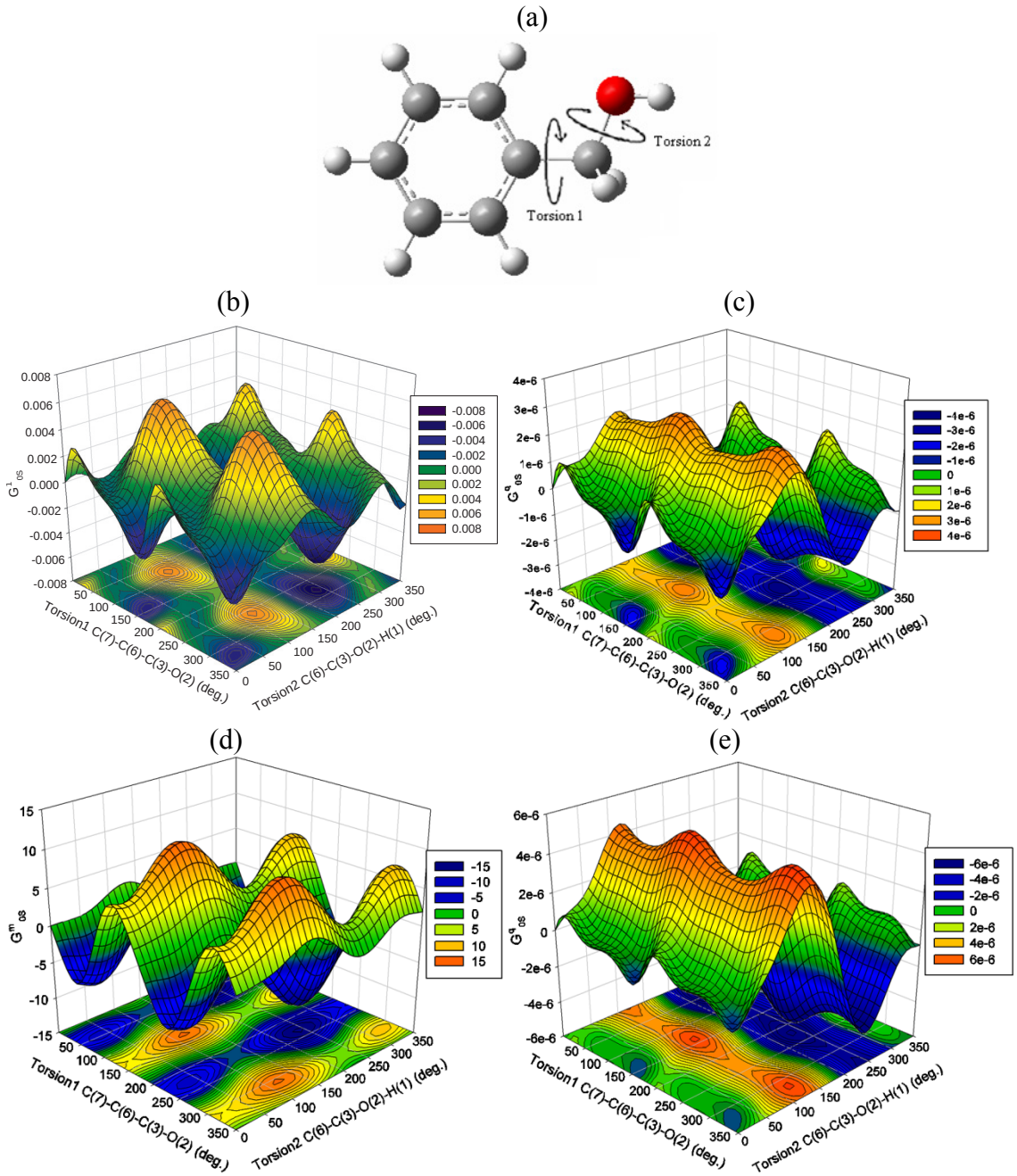

Figure 4.3. The influence of torsional angles on chirality indexes of benzyl alcohol. Panel (a) shows the two torsions under consideration. For the conformation shown in Panel (a), torsion 1 is 0 and torsion 2 is 180 degrees. Panels (b), (c), and (d) show G^{1}_{OS}, G^{q}_{OS}, G^{m}_{OS}, respectively, as the torsional angles vary. The atomic charges from the *ab initio* calculations (see Table 4.2) are used for (c). Panel (e) presents G^{q}_{OS} for a different set of atomic charges that are representative of average atomic charges observed in the simulations: the charges, in units of |e|, for atoms 1-16 are 0.53, -0.84, 0.40, -0.021, -0.021, 0.073, -0.16, 0.087, -0.16, 0.087, -0.064, 0.088, -0.064, 0.088, -0.13 and 0.095, respectively and these that are representative of average atomic charges observed in the simulations.

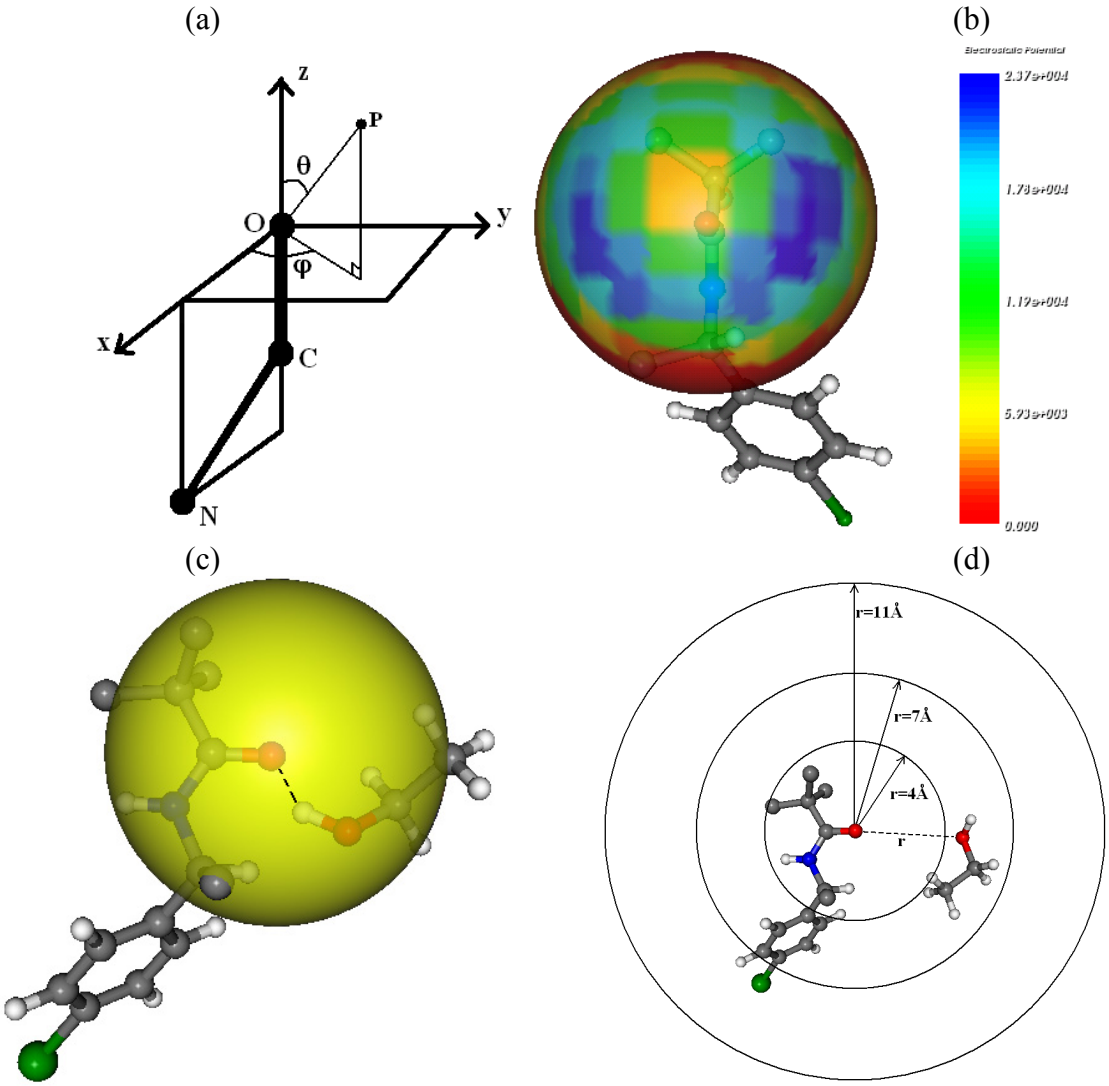

Figure 4.4. The coordinate system used to evaluate chirality indexes for solvent, illustrated for S-PAMD(a). The oxygen lies at the origin of the coordinate system, the carbonyl carbon is on the z-axis, and the amide nitrogen lies in the xz plane. With this coordinate system, the index for an H-bonding solvent is categorized according to two angles (θ and φ) that are used to locate the solvent via its oxygen atom. These angles define a sphere, as shown in (b), which can be used to map out the 3-dimensional variation of the chirality index. The color scale in (b) shows the number of hydrogen-bonded solvents found in the various angle ranges. Panel (c) shows an example of hydrogen-bonding ethanol around S-PAMD. The sphere is centered on the oxygen of S-PAMD with a radius of 3.5Å, which is the maximum O…O distance for H-bonds. The dependence of θ and φ is also important, but is not shown here for simplicity. Panel (d) shows three spheres around the oxygen of S-PAMD. The ethanol is in the second sphere, with an oxygen-oxygen distance between 4 and 7Å.

In what regions around the solute will the excess chirality of the solvent be most significant? To address this question, a solute-based coordinate system is defined as shown in Fig. 4.4(a). This coordinate system will move with the solute within the simulation. It is important to realize that the solute is flexible and the atoms defining the coordinate system undergo intramolecular motion: The coordinate system varies with time (by a limited amount). For all solutes, the oxygen atom is at the origin of the coordinate system. For PAMD, as shown in Fig. 4.4(a), C(5) is on the z-axis and N(7) is in the xz plane. For styrene oxide, C(1) is on the z-axis and C(4) is in the xz-plane while, for acenaphthenol, C(3) and C(5) define the z-axis and the xz-plane, respectively. With the coordinate system in place, the angular space is divided into 648 angular bins (see Fig. 4.4(b)) defined by $\Delta\theta = 10^0$ and $\Delta\varphi = 10^0$. This division allows us to associate a excess chirality with the solvent position about the solute. The resulting average chirality index is referred to as an "angle-dependent" excess chirality, $< G_{0S}^{w} >_{\theta,\varphi}$, and integration of this index over all angles yields $< G_{0S}^{w} >$.

Within the simulations, the chirality indexes are evaluated in two ways. First, the indexes are collected for solvent directly hydrogen-bonded to the chiral solute, as shown in Fig. 4.4(c). The sphere is centered on the oxygen of S-PAMD with a radius of 3.5Å, which is the maximum O···O distance for H-bonds. The dependence of θ and φ is also important, but is not shown here for simplicity. We have found that the chirality transfer to H-bonded solvent is larger than that for other solvents in the vicinity of the solute. As a result, we focus primarily on the H-bonded solvent. However, we also examine a position dependent index $< G_{0S}^{w} >_{r}$ for solvent found within a certain distance of the

solute oxygen (up to 15 Å), as shown in Fig. 4.4(d). For simulations involving polarizable fluids, the charge-weighted index, G_{0S}^{q}, should be more sensitive to the molecular environment due to the field-dependent fluctuation in atomic charges. As a result, emphasis is placed on $< G_{0S}^{q} >$.

4.2.3. Simulation details

Chirality transfer is evaluated from MD simulations of chiral solute (styrene oxide, PAMD, or acenaphthenol) surrounded by solvent (ethanol or benzyl alcohol). Each simulation includes 500 solvent and 4 solute molecules. The solvent density, at 298K, is 0.789g/cm^3 for ethanol[162] and 0.990g/cm^3 for benzyl alcohol. The latter is slightly below the experimental density[162] of 1.044 g/cm^3 but gave a diffusion coefficient consistent with experiment[157]. Periodic boundary conditions are applied in the simulations, with the cutoff chosen as slightly less than half of the box length. Ewald summations, with conducting boundary conditions,[40] are used for the electrostatic interactions. In the case of polarizable fluids, the electrostatic forces are first evaluated according to the Ewald summations, then corrections from the modified electrostatic potential (Eq. [2.26]) are included. The results reported below correspond to a momentum space cutoff of $k^{*2} \leq 27$ and a position space cut-off of $\alpha = 0.1592$ Å^{-1} for benzyl alcohol, and $\alpha = 0.1891$ Å^{-1} for ethanol.

Independent Nosé-Hoover thermostats are used to generate canonical averages for translation and rotation. Only the rigid rings in benzyl alcohol and in the three solutes contribute to the latter. For polarizable models, extended Lagrangian equations of motion

are also applied for charge fluctuation. The relevant conserved quantity in the simulations is

$$H_{NH} = \sum_{j=1}^{N_C}\left(\sum_{\alpha_j}^{M}\sum_{i}^{N_{\alpha_j}}\frac{\vec{p}_{i\alpha_j}^{\,2}}{2m_{i\alpha_j}} + \sum_{\alpha_j}^{M}\sum_{i}^{N_{RU}}\frac{I_{i\alpha_j}\vec{\omega}_{RU}^{\,2}}{2}\right) + \frac{p_{tr}^2}{2W_{tr}} + \frac{p_{rot}^2}{2W_{rot}} + g_{tr}k_BT_{tr}\ln s_{tr} + g_{rot}k_BT_{rot}\ln s_{rot}$$
$$+ \sum_{\alpha}^{M}\sum_{i}^{N_\alpha}\frac{p_{Q;i\alpha}^2}{2m_Q} + \frac{p_{fq}^2}{2W_{fq}} + g_{fq}k_BT_{fq}\ln s_{fq} + U(\vec{E}) \qquad [4.1]$$

where $U(\vec{E})$ is the potential energy from Eq. [2.6], the first sum is the translational kinetic energy evaluated for all atoms except those included in rigid units (RU), and the second sum is the rotational kinetic energy for RUs. $\vec{p}_{i\alpha}$ is the linear momentum of atom *i* in molecule α and $m_{i\alpha}$ is the corresponding mass. $I_{i\alpha}$ and $\vec{\omega}_{RU}$ are the moment of inertia tensor and angular velocity, respectively, of the RU, in the principal axis system. g_{fq}, g_{tr}, g_{rot} are the numbers of degrees of freedom associated with charge fluctuation, translational motion, and rotations, respectively.

A constant temperature of 298 K is obtained with the variables s_{tr} and s_{rot} with associated masses of W_{tr} and W_{rot}, respectively, and momenta of p_{tr} and p_{rot}. For the polarizable models, the atomic charges, $Q_{i\alpha}$, have a mass, m_Q, and associated momentum $p_{Q;i\alpha}$. The variables s_{fq} and p_{fq}, with associated mass W_{fq} = 3.6 x 10^{-3} kcal/(mol·ps^2), are defined to constrain the charges to a temperature of $T_{fq} = 1K$. This temperature is low enough to minimize the energy transfer between the atomic positions and the charges. The charge mass m_Q is set to 5 x 10^{-5} kcal/mol (ps/e)^2, as discussed in Section 4.2.1,

which is small enough to allow a rapid response of the atomic charges to changes in atomic positions.

The time step for all simulations, except for the fCINTRA solvent, is 0.3 fs. As discussed elsewhere,[91] a multiple time step algorithm is required for fCINTRA, and the large and small time steps are 0.1 and 0.01 fs, respectively, for this model. The equilibration period consists of the first 10 000 steps of each simulation. Following this, angle-dependent chirality indexes are collected every 20 iterations.

4.2.4 Convergence of the chirality transfer

The evaluation of the excess solvent chirality requires lengthy simulations due to significant cancellation between instantaneous values of the chirality index. In this section, the convergence is examined in detail and Fig. 4.5 provides the results of several tests of convergence.

The first test examines the chirality transfer about an achiral solute. Consider Fig. 4.5(a). The position and angle-dependent excess chiralities are shown in the left and right panels, respectively. In the right panel, the vertical line at φ=180 corresponds to the "solute" H(1) positioned in the O(2)-C(3)-C(4) plane and the contours identify the most probable locations for H-bonded solvent. The two panels show the results of 17 ns simulations of bulk ethanol, in which four ethanol molecules have been selected and identified as solutes. The left panel shows the radial dependence of the average chirality index $< G^{q}_{0S} >_r$ for solvent molecules with oxygen atoms found at a distance *r* from the oxygen atom of a "solute". As expected, since the "solute" is achiral, the average

chirality index is zero at all separations. The right panel shows the angle-dependent excess chirality, $< G_{0S}^{q} >_{\theta,\varphi}$, for ethanol H-bonded to the solute. As shown in the panel, when divided into angular zones, the chirality transfer is small but not zero. This is exactly analogous to the "chirality" of molecules that are achiral in the isotropic phase but chiral when deposited on a surface [163]. Thus, each side of the ethanol "solute" is seen as chiral, but the two sides together cancel out to yield an overall chirality of zero, as shown in the left panel. The vertical line in the right panel corresponds to the "solute" H(1) positioned in the O(2)-C(3)-C(4) plane. Thus this line defines the two sides of the solute, and symmetry about this line is clearly evident in the panel. The overlaid contours in the right panel identify the most probable angles for finding an H-bonded solvent. As the probability drops, so does the quality of the average chirality index as indicated by the loss of symmetry about $\varphi=180^{o}$ for low probability angles. The legend shows that $< G_{0S}^{q} >_{\theta,\varphi}$ is less than $|10^{-6}|$ despite the fact that instantaneous values may be as large as $|10^{-4}|$. Cancellation is clearly significant and, as a result, lengthy simulations are required to properly capture the small angle-dependent excess chirality.

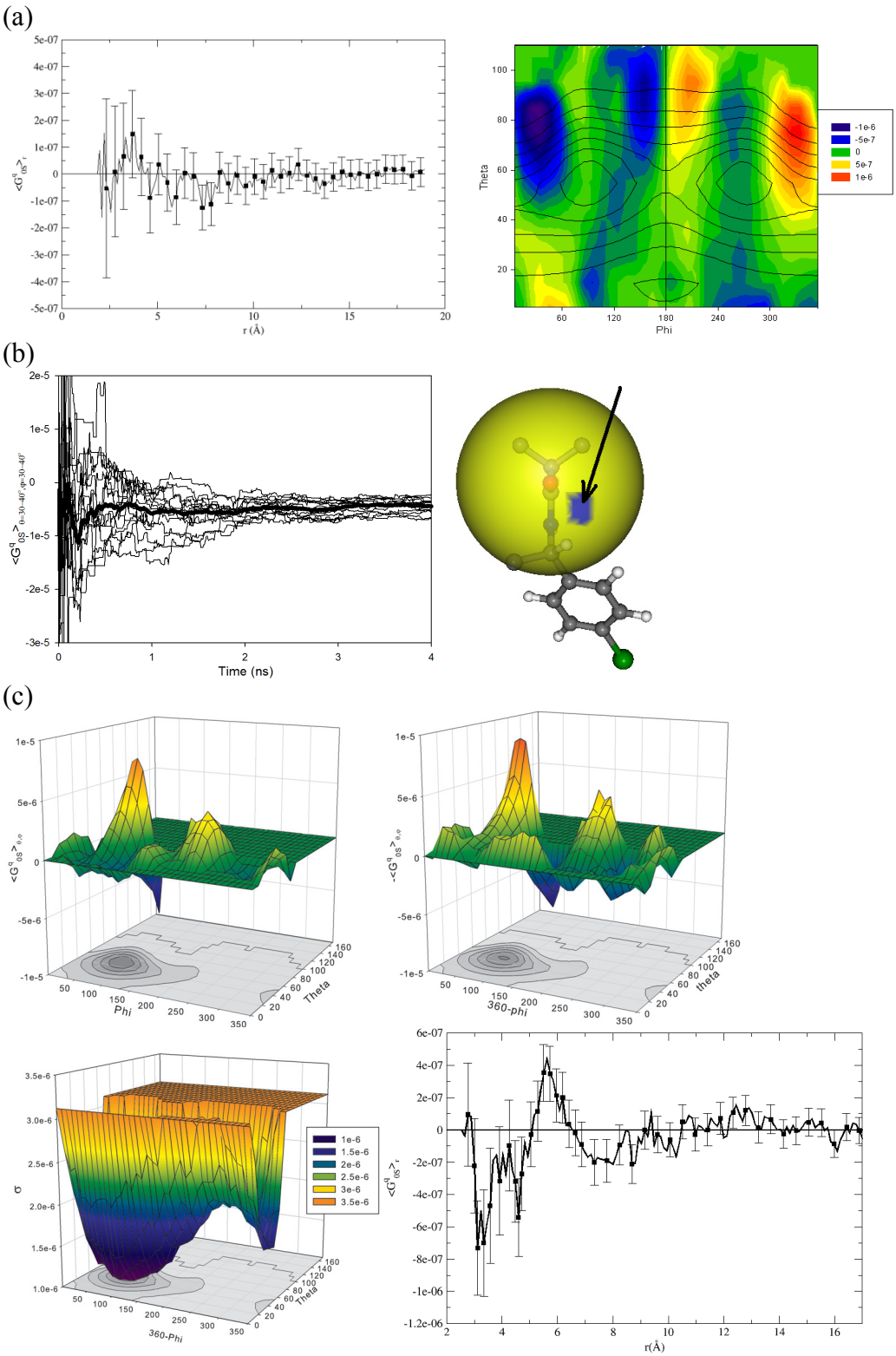

Figure 4.5. Convergence tests for excess chirality. Panel (a) shows results for bulk ethanol where four molecules have been selected and identified as "solutes". Panel (b) shows the convergence of $< G_{0S}^{q} >_{\theta,\varphi}$. Panel (c) shows the excess chirality for ethanol around acenaphthenol.

A comparison of results between independent simulations provides another assessment of convergence. Fig. 4.5(b) shows the convergence of $< G_{0S}^{q} >_{\theta,\varphi}$ for the angular range (θ=30-40^{o} and φ=30-40^{o}) and for hydrogen-bonding ethanol around rigid PAMD. The specific angular location is shown by the arrow in the right panel. Fourteen independent simulations were performed and the average chirality transfer at this position about the solute, as a function of time, is shown. By 4 ns, the chirality transfer for all 14 runs is clearly converging to a value of roughly -4.2 x 10^{-6} e^{4}, where e^{4} is the unit of the chirality index. The average over all 14 runs, indicated by the bold line, has converged after roughly 0.6-0.7 ns of simulation time. This convergence test suggests that 4 ns is adequate, at least in this case.

Fig. 4.5(c) provides a final convergence test of the chirality transfer. The upper left and right panels show results for R- and S-enantiomers, respectively. Note that the upper right panel shows $- < G_{0S}^{q} >_{\theta,\varphi}$ versus 360^{o}-φ for ease of comparison. The lower left panel shows the corresponding standard deviation of the average excess chirality for the S-enantiomer. The lower right panel shows $< G_{0S}^{q} >_{r}$ as a function of oxygen-oxygen distance between ethanol and S-acenaphthenol. Results from 17-19 ns simulations are shown. Before discussing the content of the panels, we note that subsequent presentations of chirality transfer will follow the format shown in these panels. Specifically, the angle-dependent chirality transfer, $< G_{0S}^{q} >_{\theta,\varphi}$, is presented as a color-coded three-dimensional plot. The associated contour diagram, shown beneath the 3D plot, identifies angles where H-bonded solvent is most likely to be found.

The two top panels in Fig. 4.5(c) differ in that they correspond to individual enantiomers of acenaphthenol. By symmetry, the two enantiomers must have angle-dependent chirality transfers that are equal in magnitude but opposite in sign. As well, based on our solute-based coordinate system, φ corresponds to 360^{o}-φ in the mirror-image solute. For ease of comparison, one of the panels presents $-\langle G_{0S}^{q} \rangle_{\theta,\varphi}$ as a function of 360^{o}-φ. Clearly, the two panels are very similar, with slight differences observed in the peak heights and in low probability regions. The third panel shows the standard deviation of the average chirality index for S-acenaphthenol. In the high-probability regions, the standard deviation is less than 1.5×10^{-6} and, clearly, increases in the lower probability regions where fewer hydrogen-bonded solvents are located.

The position-dependent excess chirality for ethanol about R-acenaphthenol is shown in the final panel of Fig. 4.5(c). All solvent molecules are included in this quantity, not just the H-bonded solvent considered in the first two panels. At small separations, where the oxygen-oxygen distance is relatively small, the position dependent index is negative. Following this, the average index climbs close to zero before decreasing again. The position of this second minimum corresponds roughly to the most probable distance for the second solvation layer. These features are statistically significant, as shown in Fig. 4.5(c). Overall, the average index is most negative for the first and second solvation layers, the average index is less negative (or positive) between layers, and is statistically zero once the solvent is more than 10.5 Å from the solute.

Collectively, the convergence studies in Fig. 4.5 illustrate that the chirality transfer from solute to solvent involves considerable cancellation between instantaneous solvent configurations. As a result, simulations of chirality transfer for isotropic fluids

should monitor the fluid properties for a minimum of several nanoseconds. With these considerations in mind, the simulations of chirality transfer in benzyl alcohol and in ethanol are conducted for a minimum of 10 ns and 17 ns, respectively. The chirality transfers reported in Section 4.3 have been averaged over the four solutes in the simulation cell, for a total monitoring time of 40-68 ns. The only exception is the fCINTRA ethanol model where we have found that the chirality transfer converges more quickly and, since the fCINTRA simulations are demanding, we report results for 4 ns.

4.3. Results and discussion

4.3.1 Analyte solvation

Before assessing the chirality transfer, we begin by examining the intermolecular structure, and the hydrogen-bonding, in the bulk solvents and in solvents in the vicinity of solute. Fig. 4.6 shows the radial distribution between oxygens for the bulk solvent and for solvent about the solute. A comparison of hydrogen bonding events in the bulk and near the chiral solutes is presented in Table 4.3. The structural definition of hydrogen bonding[120] has been discussed in Section 3.3.2.

Consider first the hydrogen bonding in ethanol. Styrene oxide disrupts the solvent H-bonding network only weakly, with a few percent fewer ethanol molecules participating in two hydrogen bonds and a small increase in the number that have only one hydrogen bond. The hydrogen-bonding structure of ethanol is disrupted much more significantly around acenaphthenol and PAMD, with a decrease of 13-18% in the number of solvent with two H-bonds and a commensurate increase of 13-18% in the number of solvent in the vicinity of the solute with only one hydrogen bond. A similar situation

occurs for benzyl alcohol: The smaller solute has little impact on the hydrogen-bonding characteristics of the solvent but the larger solutes increase the number of solvent molecules with only one hydrogen bond and decrease the number with two hydrogen bonds.

As shown in Fig. 4.6(a), pure solvents have a strong preference for oxygens separated by roughly 2.6 Å. Both solvents also show a secondary peak at around 4.6 Å. At first glance, benzyl alcohol appears more highly structured in the bulk. However, the different solvent molecular weights lead to a number density of ethanol roughly twice that of benzyl alcohol. This density difference is reflected in the peak heights in Fig. 4.6(a) so that the coordination numbers resulting from the oxygen-oxygen distributions are close for both solvents, as are the hydrogen-bonding statistics in Table 4.3. Figs. 4.6(b) and 4.6(c) provide the distributions between the oxygen of the solvent and the oxygen of the solutes. Clearly, acenaphthenol and PAMD interact much more strongly with the solvent. This is consistent with the statistics in Table 4.3: The solvent interacts strongly with these solutes and this contributes to the disruption of the solvent hydrogen-bonding network. For styrene oxide, the radial distributions show that the solvent interacts very weakly with the solute: it prefers to hydrogen bond with other solvent. Overall, ethanol and benzyl alcohol have similar responses to the solutes.

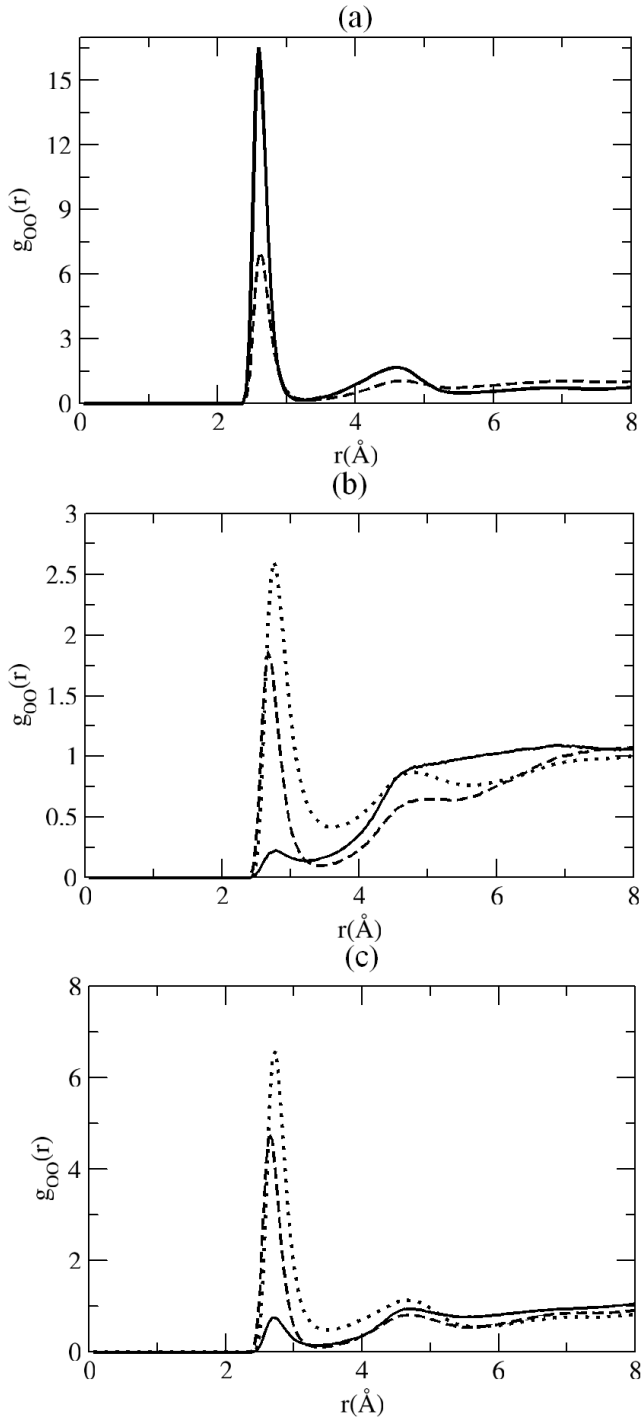

Figure 4.6. Structure of ethanol and benzyl alcohol in the bulk and around the solutes. Radial distribution between the alcohol oxygens in the bulk solvent are shown in panel (a), where the solid and dashed lines refer to benzyl alcohol and ethanol, respectively. The distribution of solvent oxygens about the solute oxygens are shown in panels (b) and (c) for ethanol and benzyl alcohol, respectively. Results for styrene oxide, acenaphthenol and PAMD solutes are represented by solid, dotted and dashed lines, respectively.

Table 4.3. An analysis of solvent hydrogen-bonding and the average chirality of the solutes. The fraction of solvent molecules with 1-3 hydrogen bonds is given in columns 3-5, respectively. Fractions are reported for solvents in the bulk and for solvents in the vicinity of a solute. In this regard, a solvent is considered to be in the vicinity of solute when any solvent atom is within 2.6 Å of any solute atom. The average chirality of the solutes, as evaluated from the long-time average of unweighted, charge weighted, and mass weighted Osipov indexes (Eq. [2.86]) is given in columns 6-8, respectively. Results from 1 ns simulations are given for the FC solvent models. Standard deviations included below have been calculated from 166 sub-averages collected during the simulations. Note that $A(-n)=A\times10^{-n}$.

Solute	**Solvent**	**1 H-bond**	**2 H-bond**	**3 H-bond**	$< G_{0S}^{1} >$	$< G_{0S}^{q} >$	$< G_{0S}^{m} >$
None	Ethanol	0.12	0.80	0.07	0	0	0
S-Styrene Oxide	Ethanol	0.15	0.78	0.04	2.3(-2) ±0.1(-2)	3.5(-7) ±0.2(-7)	2.6(1) ±0.1(1)
R-Acenaphthenol	Ethanol	0.25	0.67	0.04	1.4(-2) ±0.1(-2)	5.2(-6) ±0.2(-6)	9.8(1) ±0.1(1)
S-PAMD	Ethanol	0.30	0.62	0.03	-4.3(-3) ±0.6(-3)	-1.1(-6) ±0.2(-6)	1.7(2) ±0.2(2)
None	Benzyl alcohol	0.15	0.78	0.06	0	0	0
S-Styrene Oxide	Benzyl alcohol	0.16	0.78	0.03	2.5(-2) ±0.1(-2)	2.3(-7) ±0.2(-7)	2.2(1) ±0.1(1)
R-Acenaphthenol	Benzyl alcohol	0.28	0.66	0.03	1.4(-2) ±0.1(-2)	4.6(-6) ±0.5(-6)	9.8(1) ±0.1(1)
S-PAMD	Benzyl alcohol	0.35	0.58	0.02	-2.9(-3) ±0.9(-3)	-1.1(-6) ±0.3(-6)	3.3(1) ±0.3(1)

The average chirality indexes of the three solutes, in both solvent environments, are given in Table 4.3. We have found that the long time average of the indexes converges quickly and this is reflected in the standard deviations. In contrast, the position or angle dependent chirality transfer into the solvent is much more slowly converged, as discussed in Section 4.2.4.

4.3.2 The solvent representation: Is polarizability important?

Typical simulations employ nonpolarizable molecular models so that instantaneous changes in the molecular force field, as represented by the potential parameters, are not allowed. However, the chirality transfer from solute to solvent may involve solvent polarization, since the solvent experiences and responds to the chiral field of the solute. In this section, we examine the excess chirality of ethanol about PAMD as predicted by three solvent models. First, a nonpolarizable solvent model is considered. Second, we examine a partially-polarizable model (the FC model) which shares all the same potential parameters as the nonpolarizable model, except that the atomic charges vary instantaneously. Finally, ethanol is represented by a fully-polarizable model (the fCINTRA model) that is identical to the FC model except that some intramolecular potential parameters fluctuate instantaneously and the fCINTRA-optimized LJ parameters for O(2) and H(1) have been selected. The similarity between these three models provides a clear basis for an assessment of the relationship between solvent polarizability and chirality transfer.

The angle-dependent excess chirality, $< G_{0S}^{q} >_{\theta,\varphi}$, is shown in Fig. 4.7 as a function of solvent position about PAMD. The three panels in Fig. 4.7 differ in that ethanol is represented by the nonpolarizable model, the FC model, and the fCINTRA model. The contour plots in Fig. 4.7 identify the high probability regions for hydrogen-bonded ethanol around PAMD. All three solvent representations give very similar probability distributions: Polarizability has a small impact on the distribution of ethanol around PAMD. In Figs. 4.7(d)-4.7(e), two snapshots of ethanol and PAMD, corresponding to the high probability region around θ=0-10 degrees, are shown. The

hydrogen-bonding is evident in the snapshots but it is important to realize that the ethanol can adopt many positions consistent with these angles and the preservation of H-bonding. Thus, there is substantial cancellation and the instantaneous chirality indexes are large relative to the excess chiralities.

A comparison between Fig. 4.7(a) and Fig. 4.7(c) shows that the nonpolarizable model predicts excess chiralities that are roughly 60 times too small. This is consistent with the expectation that the chirality transfer between the solute and solvent involves polarization of the solvent molecules. In comparison, the index for the FC model is too small by a factor of roughly three. Thus, the incorporation of fluctuating atomic charges allows for adequate solvent response to the nearby chiral solute. A detailed comparison of Figs. 4.7(b) and 4.7(c) shows that the FC solvent representation predicts an angle-dependent index that is qualitatively correct except for the region around $\varphi > 200$ degrees and $\theta > 40$ degrees. Here the FC model predicts a positive average index whereas the fCINTRA model shows a negative index. As shown by the contour plots, the solvent has a low probability of being found within this angular range. Therefore, the average index for these angles is determined to lower precision, as discussed in Section 4.2.4 and illustrated by Fig. 4.5(c).

Simulations with the fCINTRA model are roughly ten times slower than for the FC and nonpolarizable solvent models. Given that the FC representation is in qualitative agreement with the fully-polarizable model, all further results employ the FC solvent representation.

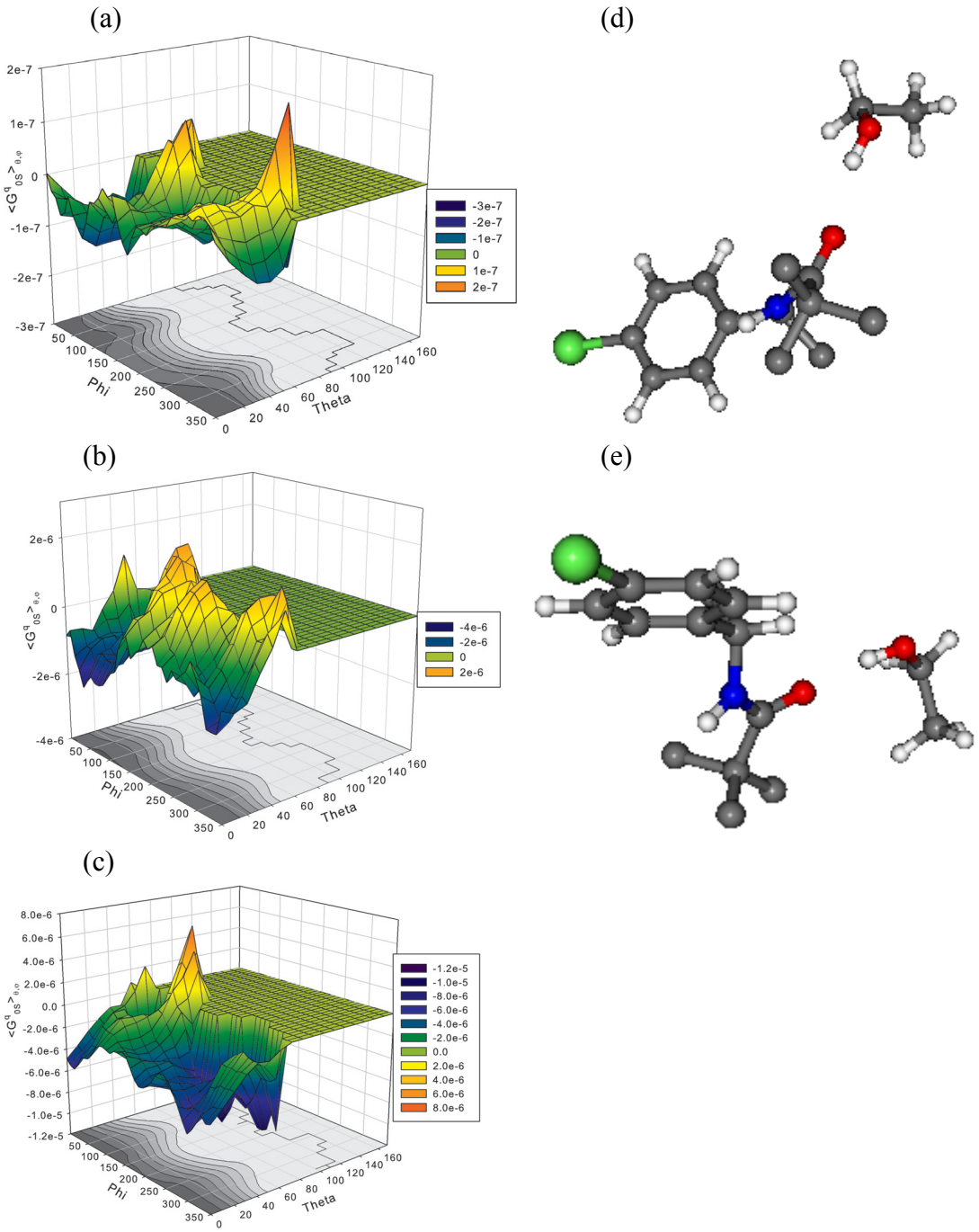

Figure 4.7. The impact of solvent polarizability on chirality transfer: The angle-dependence of $< G^{q}_{0S} >_{\theta,\varphi}$ for ethanol hydrogen-bonded to the oxygen of S-PAMD. Results from MD simulations are shown for a non-polarizable model (a), a fluctuating charge (FC) representation (b) and the fully-polarizable fCINTRA ethanol model (c). Panels (d) and (e) show hydrogen-bonding ethanol in the high probability regions.

4.3.3 Chirality transfer and conformational averaging.

The relationship between conformational changes and chirality transfer is assessed in this section. At first glance, the excess chirality is expected to decrease when the solute is flexible since solute motion should reduce the overall impact of chirality on the solvent. The angle-dependence of this decrease is less evident: Will the excess chirality decrease regardless of the solvent position? In this section, the chirality induced in an ethanol solvent is compared for a rigid, versus a flexible, PAMD solute. We begin by considering solvent hydrogen-bonded to the solute, but continue with an analysis of *all* solvents within a specified distance around PAMD.

Figs. 4.8(a) and 4.8(b) show the angle-dependent chirality indexes for hydrogen-bonded ethanol around rigid and flexible PAMD, respectively. The most significant conformational changes in PAMD arise from torsions: The torsion about the C(7)-C(9) bond is particularly relevant since it repositions the bulky aromatic ring and this may sterically interfere with solvent hydrogen-bonded to O(6). As shown in Fig. 4.8, conformational averaging has a relatively small impact on the overall magnitude of the angle-dependent excess chirality in H-bonded solvent: The angle-dependent index is roughly two times smaller when the solute is flexible. The qualitative variation in excess chirality, as a function of solvent position, is similar for rigid and flexible PAMD, although conformational averaging is found to eliminate the negative region at φ=200 degrees (Fig. 4.8(a)) and broaden the region of negative chirality centered around φ=0 degrees (Fig. 4.8(b)). Due to the latter, the chirality index is consistently negative in the regions where a hydrogen-bonding solvent is most likely to be found (see contour plot in the figure). As a result, the overall excess chirality, $<G^{q}_{0S}>$, is only -5.1x10^{-8} e^{4} for rigid

PAMD but is -2.6×10^{-7} e^4 when the solute is flexible. Thus, the angle-dependent excess chirality decreases as a result of solute flexibility but the overall, angle-averaged value increases due to qualitative changes in the H-bonded solvent, particularly when the solvent is positioned around $\varphi=0$ degrees. From the PAMD-based coordinate system shown in Fig. 4.4(a), this angular range corresponds to solvent near the N(7)-C(5)-O(6) plane (see Fig. 4.1). From Fig. 2.9, these results are consistent with the H-bonded solvent near this plane favoring angles greater than 180^o for torsion 2 when the solute is flexible.

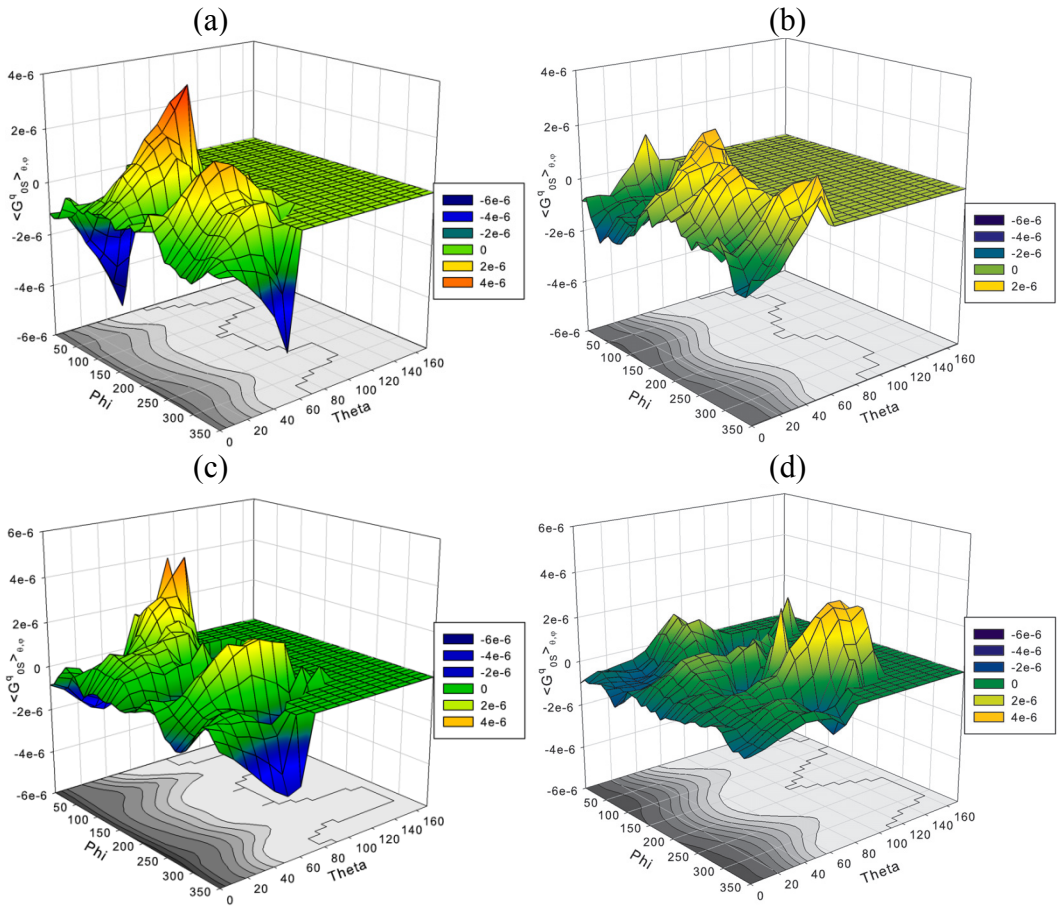

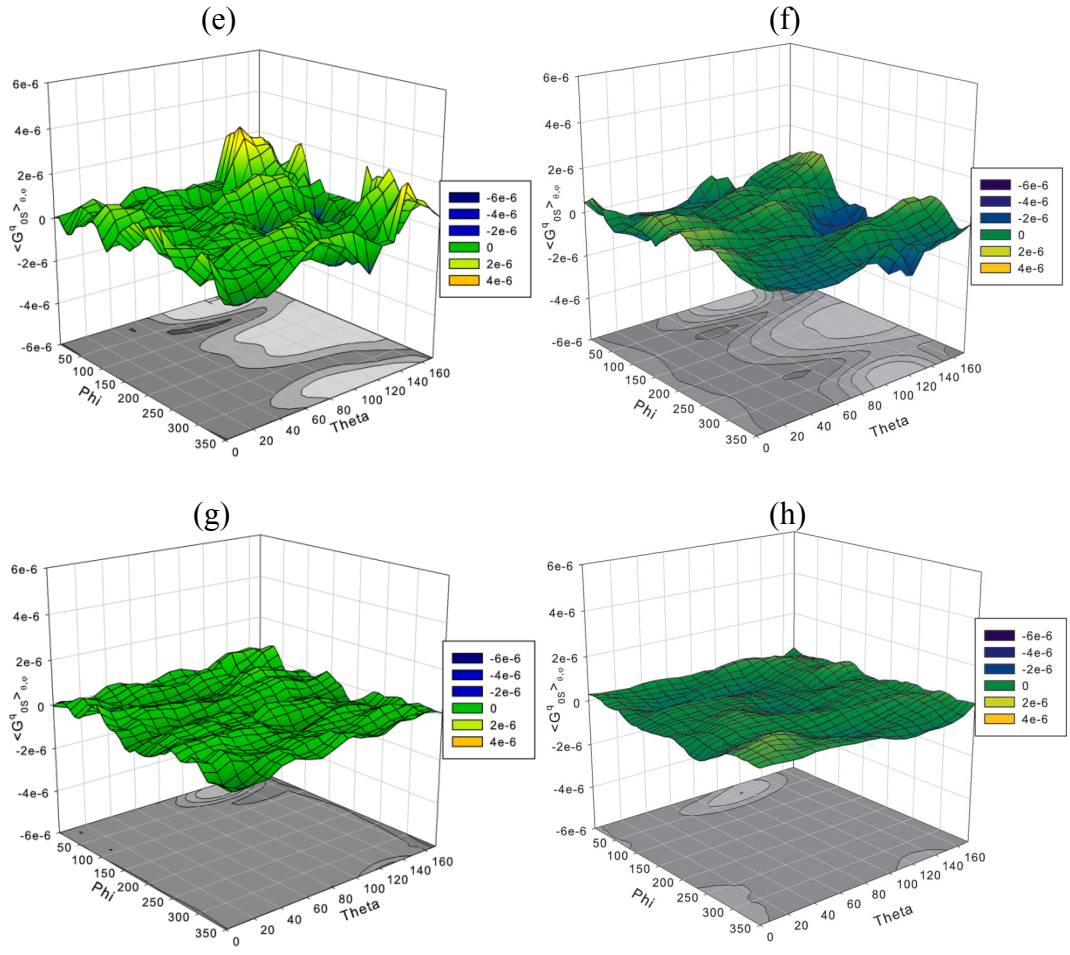

Figure 4.8. The impact of solute flexibility on chirality transfer. Results for ethanol about rigid S-PAMD are shown in (a,c,e, and g) while corresponding results for flexible S-PAMD are given in (b,d,f, and h). Panels (a) and (b) show the charge-dependent chiral indexes of hydrogen-bonded ethanol molecules around the oxygen atom of S-PAMD. Panels (c) and (d) show the average chiral indexes for all ethanol molecules in the first shell around the oxygen of S-PAMD (oxygen-oxygen distance within 4Å). Similarly, Panels (e) and (f), and Panels (g) and (h), consider oxygen-oxygen distances between 4 and 7Å, and between 7 and 11 Å, respectively.

Figs. 4.8(c) and 4.8(d) show angle-dependent excess chiralities for ethanol located in the vicinity of the PAMD oxygen atom when the solute is rigid or flexible, respectively. In particular, the ethanol oxygen should be within 4 Å of the PAMD oxygen and all solvents are considered regardless of whether they H-bond with PAMD. When the solute

is rigid, certain areas about the oxygen are simply inaccessible to the solvent and this is evident in the contour plot of Fig. 4.8(c). Figs. 4.8(c) and 4.8(d) are fairly distinct: The flexibility of the solute has an impact on the spatial characteristics of the chirality transfer when all solvents are considered.

A comparison of Figs. 4.8(b) and 4.8(d) reveals distinctions between H-bonded ethanol and ethanol in the vicinity of the solute oxygen. Specifically, as shown by the contour plots in Figs. 4.8(b) and 4.8(d), hydrogen-bonded ethanol molecules have a restricted orientation relative to the solute and form a subset of the ethanol molecules found near the PAMD oxygen. Thus, Fig. 4.8(d) includes a larger number of ethanol molecules, and these display a broad range of orientations relative to the PAMD. As a result, the excess chirality in Fig. 4.8(d) varies less with the solvent position, although it is important to note that the angle-dependent excess chirality is still negative, although smaller in magnitude, in the primary hydrogen bonding regions. The angle-averaged excess chirality for H-bonded ethanol (Table 4.5) is $-2.6\text{x}10^{-7}$ e^4 whereas the equivalent average (Table 4.4), for all ethanol molecules in the vicinity of the PAMD oxygen, is $-2.2\text{x}10^{-7}$ e^4. The extensive cancellation of instantaneous indexes, to yield the excess chirality, is evident from a comparison with the conformational variations in G^{q}_{0S} shown in Fig. 2.9 , where values as high as $\pm 8\text{x}10^{-5}$ e^4 were obtained.

For solvent "far" from the chiral solute, the local environment is achiral, on average, and the angle-dependent excess chirality should vanish for all angles. Figs. 4.8(e)-(h) show the decrease in the angle-dependent excess chirality as the solvent is farther from the solute. Solvents within 7-11 Å of the PAMD oxygen atom are found to have an angle-dependent chirality index that is roughly ten times smaller than for

solvents located within 4 Å. Thus it is fair to say that the chirality transfer from PAMD to ethanol occurs primarily for solvent within the first few solvation layers about the chiral solute. The last panel of Fig. 4.5(c), for ethanol about R-acenaphthenol, is consistent with this result since the chirality transfer is statistically zero once the oxygens are separated by more than 10.5 Å. Solute conformational averaging hastens this decay, as shown by a comparison of Figs. 4.8(g) and 4.8(h).

Table 4.4. Average excess chirality for solvent around chiral solute. $< G^{1}_{0S} >$, $< G^{q}_{0S} >$ in units of $|e|^4$ where e is the electron charge, and $< G^{m}_{0S} >$ in $(g/mol)^4$ are given for each pair. Standard deviations included below have been calculated from 1666-3332 sub-averages collected during the simulations. r_{OO} is the distance between the solvent oxygen and the solute oxygen. Note that A(-n)=A×10^{-n}.

Solute	**Solvent**	**r_{OO} <4Å**			**4Å< r_{OO} <7Å**			**7Å< r_{OO} <11Å**		
		$< G^{1}_{0S} >$	$< G^{q}_{0S} >$	$< G^{m}_{0S} >$	$< G^{1}_{0S} >$	$< G^{q}_{0S} >$	$< G^{m}_{0S} >$	$< G^{1}_{0S} >$	$< G^{q}_{0S} >$	$< G^{m}_{0S} >$
S-Styrene oxide	ethanol	-2.2(-5) ±0.5(-5)	-6.9(-7) ±1.0(-7)	-3.4(-2) ±0.6(-2)	-1.8(-6) ±0.8(-6)	-9.1(-8) ±3.2(-8)	-4.5(-3) ±0.9(-3)	-1.6(-6) ±0.4(-6)	-3.1(-8) ±1.7(-8)	-1.9(-3) ±0.5(-3)
S-PAMD	ethanol	-5.6(-6) ±4.0(-6)	-2.2(-7) ±0.8(-7)	-1.1(-2) ±0.5(-2)	-1.1(-6) ±0.9(-6)	-1.7(-7) ±0.4(-7)	-7.4(-3) ±1.1(-3)	2.2(-7) ±4.3(-7)	-0.4(-8) ±2.0(-8)	1.6(-4) ±5.5(-4)
R-Acenaphthenol	ethanol	3.4(-6) ±5.5(-6)	1.6(-7) ±1.1(-7)	9.0(-3) ±7.1(-3)	-5.3(-6) ±1.6(-6)	-1.8(-7) ±0.7(-7)	-7.9(-3) ±2.0(-3)	-1.5(-6) ±0.8(-6)	-3.1(-8) ±3.7(-8)	-1.8(-3) ±1.1(-3)
S-Styrene oxide	benzyl alcohol	-1.6(-5) ±0.9(-5)	-8.2(-8) ±1.3(-8)	0.5(-2) ±1.9(-2)	-1.4(-5) ±0.4(-5)	-2.1(-8) ±0.6(-8)	-1.9(-2) ±0.8(-2)	-4.4(-6) ±2.0(-6)	-0.4(-9) ±3.1(-9)	0.8(-3) ±3.9(-3)
S-PAMD	benzyl alcohol	8.4(-5) ±0.7(-5)	1.1(-7) ±0.1(-7)	1.1(-1) ±0.1(-1)	-4.6(-5) ±0.4(-5)	-7.0(-8) ±0.7(-8)	-6.4(-2) ±0.9(-2)	-7.6(-5) ±0.2(-5)	-9.6(-8) ±0.4(-8)	-7.4(-2) ±0.5(-2)
R-Acenaphthenol	benzyl alcohol	-3.8(-5) ±1.0(-5)	-5.4(-8) ±1.4(-8)	2.2(-2) ±2.0(-2)	2.9(-5) ±0.7(-5)	4.4(-8) ±1.1(-8)	8.2(-2) ±1.4(-2)	-1.1(-5) ±0.4(-5)	-1.1(-9) ±5.9(-9)	-1.8(-2) ±0.8(-2)

Table 4.5. Average excess chirality for solvent hydrogen bonded to the chiral solute. $< G^{1}_{0S} >$, $< G^{q}_{0S} >$ in units of $|e|^4$ where e is the electron charge, and $< G^{m}_{0S} >$ in $(g/mol)^4$ are given for each solute-solvent pair. Standard deviations included below have been calculated from 1666-3332 sub-averages collected during the simulations.

Note that $A(-n)=A\times10^{-n}$.

Solute	**Solvent**	**H-bond characteristics**	$< G^{1}_{0S} >$	$< G^{q}_{0S} >$	$< G^{m}_{0S} >$
S-Styrene oxide	ethanol	O-H(solvent)…O(solute)	-3.2(-5) ±1.2(-5)	-7.6(-7) ±1.7(-7)	-6.4(-2) ±1.3(-2)
S-PAMD	ethanol	O-H(solvent)…O(solute)	-7.0(-6) ±5.0(-6)	-2.6(-7) ±0.9(-7)	-1.8(-2) ±0.6(-2)
		N-H(solute)…O(solvent)	3.7(-5) ±1.2(-5)	2.6(-7) ±2.0(-7)	1.5(-2) ±1.3(-2)
R-acenaphthenol	ethanol	O-H(solvent)…O(solute)	8.7(-6) ±9.9(-6)	2.5(-7) ±1.8(-7)	2.2(-2) ±1.3(-2)
		O-H(solute)…O(solvent)	-1.3(-6) ±8.5(-6)	-1.4(-7) ±1.8(-7)	-1.2(-2) ±1.2(-2)
S-Styrene oxide	benzyl alcohol	O-H(solvent)…O(solute)	1.9(-4) ±0.2(-4)	1.1(-7) ±0.2(-7)	4.9(-1) ±0.3(-1)
S-PAMD	benzyl alcohol	O-H(solvent)…O(solute)	1.7(-4) ±0.1(-4)	1.5(-7) ±0.1(-7)	4.4(-1) ±0.2(-1)
		N-H(solute)…O(solvent)	2.0(-4) ±0.2(-4)	4.2(-7) ±0.3(-7)	5.2(-1) ±0.5(-1)
R-acenaphthenol	benzyl alcohol	O-H(solvent)…O(solute)	-1.7(-4) ±0.2(-4)	-5.2(-7) ±0.2(-7)	9.7(-2) ±3.3(-2)
		O-H(solute)…O(solvent)	-6.7(-5) ±1.9(-5)	-2.5(-7) ±0.3(-7)	1.3(-1) ±0.4(-1)

Overall excess chiralities are presented in Table 4.4. The averages have been evaluated over three spatial regions: $r_{oo} \leq 4$Å, 4Å $< r_{oo} \leq 7$Å, and 7Å $< r_{oo} \leq 11$Å. By comparison with the radial distributions in Fig. 4.6, this first region includes the contact peak, the second region includes the second solvation shell and some of the third, while the last region incorporates solvents "far" from the solute. As shown in the table, the chirality transfer systematically decreases from the contact region to the second solvation shell to the outer region. In general, the sign of the chirality transfer may remain unchanged or alternate between regions. However, as illustrated by Fig. 4.5(c), the position-dependent excess chirality may switch signs within these ranges so that the averages in Table 4.4 may include some cancellation.

4.3.4 Contact points and chirality transfer.

In chiral chromatography, the number of interaction points between the analyte and the chiral selector is essential to the recognition process. In this section, we explore the relationship between the number of solute-solvent interactions, and the chirality transferred to nearby solvent molecules.

Fig. 4.9 provides the angle-dependent chirality index for ethanol about the three solutes. The location of hydrogen-bonded solvent, relative to the solute oxygen, is different for all three solutes, as indicated by the contour plots. The angle-dependent chirality indexes are distinct as well. Panels 4.9(d)-4.9(f) indicate the long-time average values for the unweighted, charge-weighted, and mass-weighted indexes at angles corresponding to the most probable location for H-bonded solvent. A representative

snapshot is provided to show an H-bonded solvent molecule in the most probable location and having an instantaneous index of the same sign as the time averaged values.

The angle-dependent chirality index for ethanol about acenaphthenol (Fig. 4.9(b)) has several well-defined regions, but these mostly lie outside the most probable locations for the solvent. Overall, the average index (see Table 4.5) is small. Focusing on the most probable solvent location, the long-time average of each index is negative. From Fig. 2.9, this corresponds to torsion 2 having an average angle greater than 180 degrees. A representative snapshot is provided in Fig. 4.9(e). When ethanol hydrogen-bonds to styrene oxide(Fig. 4.9(a)), the chirality transferred to the solvent is strongly dependent on the position of the solvent. However, the overall excess chirality in Table 4.5 is an order of magnitude smaller than angle-dependent values due to cancellation. From Fig. 4.9(a), the long-time average of each index, for solvent in the most probable location is positive. This corresponds to an average angle for torsion 2 that is less than 180 degrees, as shown in the snapshot in Fig. 4.9(d). Thus, styrene oxide and acenaphthenol have different impacts on the conformations of H-bonded solvent. For ethanol about PAMD, the angle-dependent chirality induced in the solvent is smaller than for the other two solutes (note that the vertical scales are the same in Figs. 4.9(a), (b), and (c)). However the index is consistently negative in regions where the H-bonded solvent is most likely located, and the overall average index, $< G_{0S}^{q} >$, in Table 4.5 is comparable with the other solutes.

Fig. 4.10 gives the overall chirality index for benzyl alcohol about the three solutes. As with ethanol, the angle-dependent excess chirality is qualitatively different for all three solutes. The angle-dependence is largest for acenaphthenol where the index is negative over a significant angular range that includes the most probable angles for H-

bonding solvents. Acenaphthenol has an extended aromatic region, relative to the other two solutes, and it is not surprising that chirality transfer is larger for this solute. Fig. 4.10(e) shows an H-bonded benzyl alcohol positioned at angles consistent with the most probable location for H-bonded solvent about acenaphthenol. The long-time average values for the three indexes, at this location, indicate that the solvent prefers to have torsion 2 between 270-300 degrees and torsion 1 between 140-170 degrees (or equivalently, between 320-350 degrees).

Although it is tempting to directly compare results for ethanol and benzyl alcohol, this is problematic since the chirality index has some residual dependence on the number of atoms in the solvent. As well, the relationship between the index and the molecular structure is complex, although the similarity between Figs. 2.9 and 4.3 implies that some cautionary remarks can be made. With this in mind, we note that Figs. 4.9 and 4.10 suggest that acenaphthenol has the most pronounced impact on the solvent since the angle-dependence in the chirality index is largest for this solute. The stronger impact of acenaphthenol suggests that, for this solute, localized hydrogen-bonded solvent has a stronger preference for certain chiral configurations. This may be related to the overall accessibility of the hydrogen-bonding group following the molecular shape and the restricted conformations available for this solute.

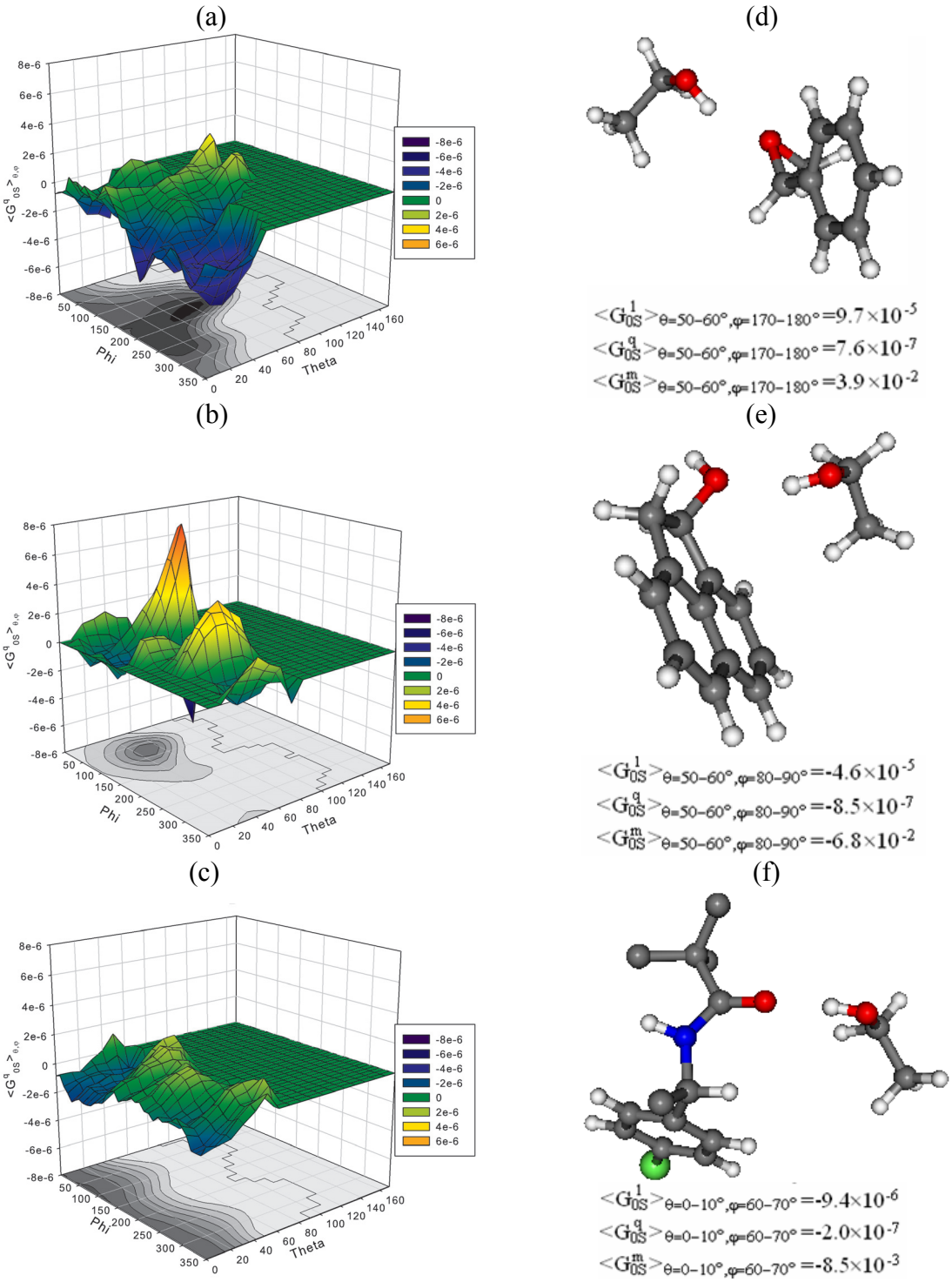

Figure 4.9. Impact of solutes on chirality transferred into hydrogen-bonding ethanol. $< G^{q}_{0S} >_{\theta,\varphi}$ chiral indexes are shown along with illustrative snapshots. The panels are organized as follows: Panels (a) and (d) refer to S-styrene oxide; Panels (b) and (e) refer to R-acenaphthenol; and Panels (c) and (f) refer to S-PAMD.

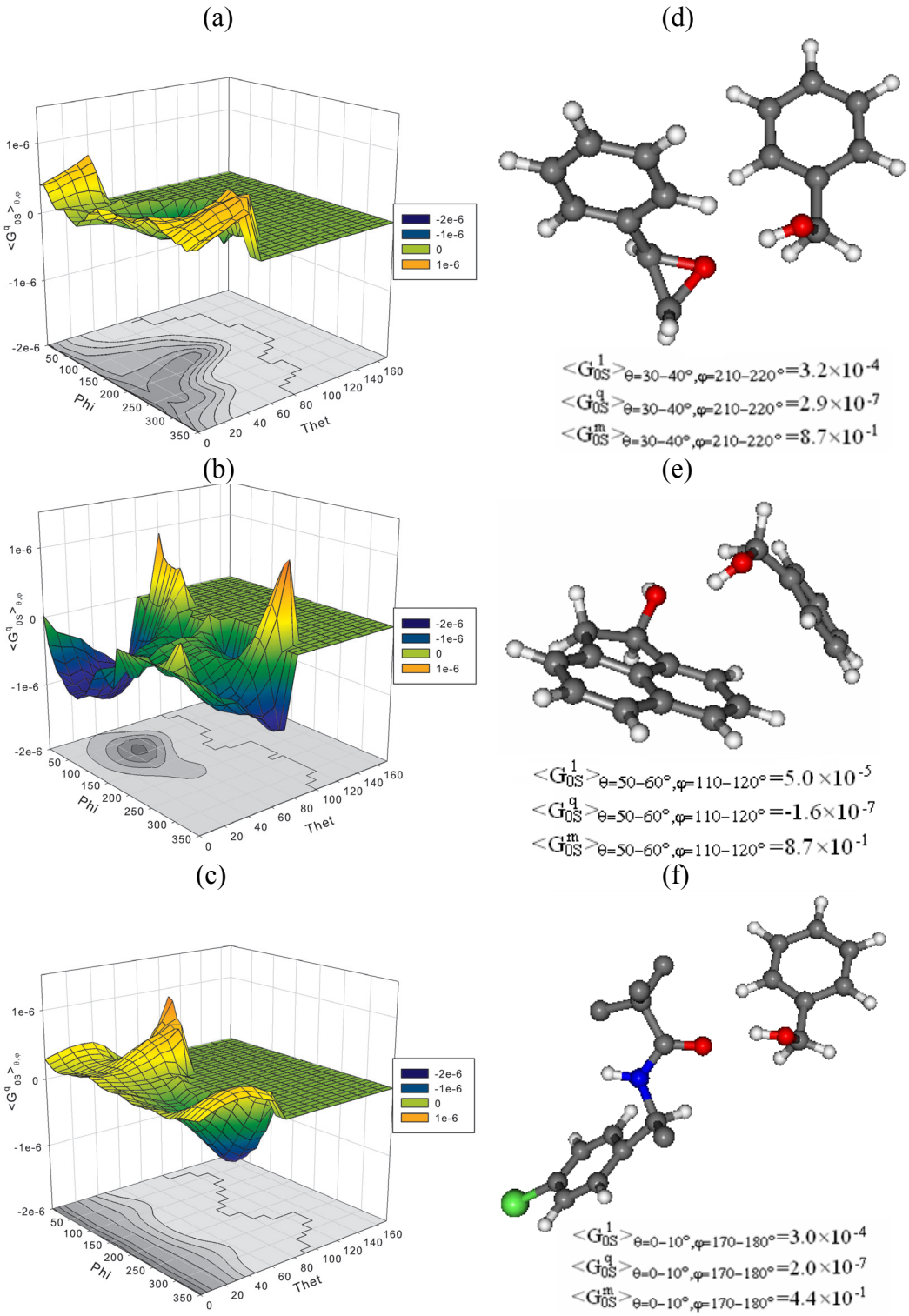

Figure 4.10. Impact of solutes on chirality transferred into hydrogen-bonding benzyl alcohol. The $< G^{q}_{0S} >_{\theta,\varphi}$ chiral indexes are shown along with illustrative snapshots. The panels are organized as follows: Panels (a) and (d) refer to S-Styrene oxide; Panels (b) and (e) refer to R-acenaphthenol; and Panels (c) and (f) refer to S-PAMD.

Table 4.5 gives the angle-averaged chirality index for hydrogen-bonded solvent. For ethanol and benzyl alcohol, the average charge-dependent index $< G_{0S}^{q} >$ is less than 10^{-6} for all solutes. In light of the conformational dependence of this index, shown in Figs. 2.9 and 4.3, these averages clearly reflect significant cancellation so that, overall, the amount of chirality transferred is small. Despite the small overall average, a stronger spatial dependence is present and this is evident in the angular distribution of the average index shown in Figs. 4.9 and 4.10. Thus, within certain spatial regions about the solute, the chirality transfer may be significant and much larger than the angle-averaged value.

In bulk benzyl alcohol, inter-solvent π-π interactions are possible. This situation differs from chromatographic separations where the solvent does not include aromatic rings but the analytes usually do. To explore this fundamental difference, we have also examined the solvation of acenaphthenol in a mixed solvent. Specifically, simulations of a binary *n*-hexane/benzyl alcohol solvent around acenaphthenol were performed. Here, the *n*-hexane is nonpolarizable and is the major solvent component. Interestingly, we found that the angle-dependent chirality transfer to benzyl alcohol was qualitatively very similar to Fig. 4.10(c), but smaller in magnitude. The similarity in the 3D surfaces likely reflects the overall structural constraints placed on an H-bonding solvent molecule. On the other hand, the decrease in magnitude for the mixed solvent suggests that benzyl alcohol samples more conformations in this environment. This follows from the fact that an H-bonded benzyl alcohol will be mostly surrounded by *n*-hexane in the mixed solvent. In the absence of *n*-hexane, the benzyl alcohol molecule H-bonded to the solute will be surrounded by other alcohols, and these H-bond extensively forming a more structured local environment.

4.4. Conclusions

In this chapter, the chirality transfer from a chiral solute to an achiral solvent has been assessed. The importance of solvent polarizability, conformational averaging, and the details of the solvent-solute interactions have been considered. We have found that chirality transfer is most evident for solvent molecules directly H-bonded to the solute. In addition, ethanol and benzyl alcohol both show a clear relationship between excess chirality and position of the solvent relative to the chiral solute. That is, chirality transfer is larger at certain positions about the solute.

Ethanol provided the basis for examining the relationship between solvent polarization and chirality transfer. Here, solvation of PAMD was examined for a nonpolarizable ethanol, a fluctuating charge representation of ethanol, and a fully polarizable ethanol model where the atomic charges and the intramolecular potential vary with the molecular environment. Inclusion of solvent polarization was found to be very important, as the solvent must respond to the chiral field of the solute.

The impact of conformational averaging was explored for PAMD. Here the chirality transfer was assessed for ethanol about a rigid and a flexible PAMD solute. As expected, conformation averaging decreases the magnitude of the angle-dependent chirality transfer, by a factor of roughly two, but it also changes some of the characteristics of the angular dependence of the chirality transfer: In certain regions, the solvent molecules adopt different conformations depending on the flexibility of PAMD. The impact of this is significant for PAMD: Solute rigidity has increased the overall chirality transfer via a reduction in cancellation. Considering PAMD, the chirality

transfer was also assessed as the solvent was farther away from the chiral solute. We have found that the chirality transfer decreases quickly and a 3D representation is essentially featureless for solvent within 7-11 Å from the chiral solute.

The Osipov chirality index[66] formed the basis of the analysis of chirality transfer. Long-time averages of this index, for solvents located at various positions about the solute, identify the excess chirality present in the solvent molecules due to the presence of a chiral solute. Three indexes were examined: One determined by structure alone, another weighed by atomic mass, and a third dependent on atomic charges. The Osipov index is directly related to molecular shape, and can be adapted to emphasize charge fluctuations, proximate atoms, larger atoms, etc. The spatial decomposition of multiple time-averaged indexes can be used to generate an average structure of the solvent about the solute, as a function of the solvent position. This, in turn, may prove useful in predicting the solvent contributions to experimental properties, such as VCD spectra, without the requirement for individual snapshot analysis.

Chapter 5
Chirality transfer from chiral surfaces to nearby solvents

In this chapter, chirality transfer from chiral surfaces to achiral solvents is discussed. The study is based on MD simulations of four solvents (ethanol, 2-propanol, ethanol/*n*-hexane, and 2-propanol/*n*-hexane) and three brush-type selective interfaces (Whelk-O1, DNB-phenylglycine, and DNB-leucine). Emphasis is placed on the location of the chirality transfer zones on each surface and the solvent characteristics in these zones. The spatial characteristics of the chirality transfer and its dependence on the nature of the surface and solvent are examined in detail.

5.1. Introduction

The impact of solvent on chiral high-performance liquid chromatography (HPLC) has been studied extensively, and it is understood that solvent polarity impacts elution times and, to a lesser extent, selection factors. For instance, the role of solvent has been examined for Whelk-O1, where separations are performed under normal phase, reverse phase, and supercritical conditions[164-166]. The effect of solvent has also been studied for phenylglycine-based and leucine-based CSPs, where separations under various mobile phases and binary solvents with different component ratios have been investigated [167-170]. Similarly, Persson *et al.*[171] studied the chiral separation of omeprazole on a

Chiralpak AD column and observed opposite elution orders when using different mobile phases. Roussel *et al*.[172, 173] analyzed elution orders for cellulose tris(3,5-dimethylphenylcarbamate) and cellulose tris(4-methylbenzoate) CSPs under different mobile phases using Circular Dichroism and Optical Rotatory Dispersion (ORD) spectroscopy and found a dependence on the mobile phase. In this chapter, we reverse this perspective and focus instead on the impact of the CSP on nearby solvent molecules. Specifically, we address the question of chirality transfer from the surface to nearby solvent. This transfer may be important because it can, in turn, contribute to the separation mechanism and influence the resolution achieved by the stationary phase.

In Chapter 4, we examined the solute-to-solvent chirality transfer for several small solutes and found that chirality transfer was enhanced for solvent located in specific regions around the solutes. In this chapter, we focus on interfacial chirality transfer and consider three brush-type selective interfaces: Whelk-O1, based on a 1-(3,5-dinitrobenzamido)-1,2,3,4-tetrahydrophenanthrene chiral selector; DNB-phenylglycine, based on a N-(3,5-dinitrobenzoyl)-phenylglycine selector; and DNB-leucine, based on a N-(3,5-dinitrobenzoyl)-leucine selector. Whelk-O1 is commonly used in HPLC and successfully separates a wide range of racemates under various solvent environments[174]. DNB-phenylglycine and DNB-leucine were among the first commercially available HPLC CSPs [175]. DNB-leucine has enhanced enantioselectivity for several classes of compounds[175], benzodiazepines for example. DNB-phenylglycine is suitable for the separation of aryl-substituted cyclic sulfoxides, bi-β-naphthol and its analogs, α-indanol and α-tetralol analogs, and aryl-substituted hydantoins [175]. In chiral chromatography, these CSPs are used in conjunction with

achiral binary or ternary solvents. Molecular dynamics studies of the solvated interfaces has been considered previously[112, 176] but here a wider array of solvents is examined, solvent polarizability is considered, and emphasis is placed on solvent chirality rather than solvent distribution. Typical normal phase solvents consist of alkane-alcohol mixtures, with *n*-hexane most commonly used in conjunction with varying amounts of 2-propanol. With this in mind and to isolate the co-solvent impact, four solvents are considered in this chapter: pure ethanol, pure 2-propanol, 80/20 *n*-hexane/ethanol, and 80/20 *n*-hexane/2-propanol.

Molecular dynamics (MD) simulations of the twelve solvent-surface combinations form the basis of our analysis. The solvent chirality is assessed based on the evaluation of the Osipov chirality index[66], which has been discussed in detail in the previous chapters. Specifically, this index is practical and versatile, has been successfully applied to predict polarization power of chiral dopants[74, 177-180] and to assess excess chirality – the chirality introduced into nearby solvent - around chiral solutes[181]. In any simulation, the solvents explore a range of conformations but, for the systems of interest here, excess chirality results from a small inherent conformational bias and a polarization due to the proximity of the chiral surface. Thus, long simulations are required. The solvent chirality will depend on the solvent's position relative to the chiral selector and, for this reason, we evaluate position dependent chiral indexes.

Section 5.2 begins with a brief discussion of the solvents, chiral surfaces, and the simulation details. Results from extensive MD simulations are reported in Section 5.3 and brief conclusions are presented in Section 5.4.

5.2. Methods

5.2.1 Surface representations

The Whelk-O1, DNB-leucine and DNB-phenylglycine selectors are shown in Fig. 2.10. The atom numbering provided in this figure will be used throughout this chapter. The structures of all three selectors are described in Section 2.7, and more detailed descriptions can be found elsewhere[112, 113].

A side view of a typical simulation cell is shown in Fig. 2.10(d). In order to be consistent with experiment[114-116], the model interface consists of a total of 9 selectors, 27 trimethylsilyl end caps, 36 silanol groups, and an underlying layer of 72 silicon atoms, with a Si-Si distance of 3.2 Å.

5.2.2 Models

The interaction potentials for the system are introduced in Eq. [3.1] in Chapter 3. Both the surface and the solvent contribute to these potentials.

A solvent near a chiral molecule or surface will experience a chiral field and become polarized. Previous simulations have shown that the alcohol prefers the interface[112, 113, 161, 182] and forms hydrogen bonds with the selectors. Thus, chiral polarization is most important for the alcohol and, as a result, a polarizable solvent model has been adopted for ethanol and 2-propanol. Specifically, the electrostatic energy is evaluated from the Fluctuating Charge (FC) model[46] and is given by Eq. [2.26]. The intramolecular potential is not field dependent, but as shown in Chapters 3 and 4, the FC

model is an acceptable alternative. The parameterization of the FC model for ethanol[91] has been discussed in detail in Chapter 3. A suitable flexible and polarizable model (FC model) for 2-propanol has been developed for the simulations of interest in this chapter. Full details of the model are provided in the Appendix C. Briefly, CHARMM parameters are chosen for the Lennard-Jones potential (see Eq. [2.12]). For the intramolecular potential, 19 bends and 3 torsions are employed to represent the molecular flexibility, and an extensive series of B3LYP/aug-cc-pVDZ DFT calculations have been performed. Each bending potential is obtained by least squares fits to nine energy calculations where the angle is varied within sixteen degrees of the equilibrium value. For torsion potentials, the angle is varied from 0 to 360^{o}, in steps of 10 degrees. The FC parameters for Eq. [2.26] are derived by fitting atomic charge response to the presence of electric fields. Similar to previous findings[181] for ethanol, the atomic electronegativities derived specifically for 2-propanol were larger than the transferrable CHARMM-FC values[53] for most atoms. The TraPPE-UA model[134] was chosen for *n*-hexane. This model has been employed in previous solvation studies and is particularly appropriate for alkane-alcohol mixtures, such as the mixed solvents examined in this chapter.

As discussed in Chapter 2, the intramolecular potential consists of four parts: stretching (U^{st}), bending (U^{be}), torsion (U^{tor}) and improper torsion (U^{imp}). In this chapter, improper torsions are employed for carbons joining aromatic rings, for the amide carbons, and for the amide nitrogens. That is, improper torsions are implemented for N(25), C(27), and C(29) of Whelk-O1, N(11), C(13), N(17), C(19), and C(21) of DNB-phenylglycine and DNB-leucine and, in addition, for C(33) in the lateral group of DNB-phenylglycine. Full details on the surface potentials are provided elsewhere[112, 176].

Here, we note that the intramolecular potentials were derived specifically for each CSP, based on extensive exploration of the ground state potential energy surface via *ab initio* calculations.

5.2.3 Chirality indexes

Detailed discussions of the Osipov chirality index[66, 111] can be found in previous chapters. Fig. 5.1 shows several chirality indexes for 2-propanol. The indexes are plotted as a function of the torsional angles and for different combinations of *m* and *n*, the powers in the denominator of Eq. [2.86] that control the range of indexes. With twelve atoms in the molecule, there are 495 unique combinations of four atoms contributing to the sum in Eq. [2.86]. As *m* and *n* increase, the index becomes increasingly dominated by clusters of neighboring atoms. However, even for n=3 and m=3, the index only converges after several hundred terms due, in part, to cancellation between terms. Thus, it is not correct to assume that any of the chirality indexes considered here are dominated by a small group of atoms within the molecule.

Panels (d)-(j) in Fig. 5.1 show that Torsion 1, which rotates the position of the alcohol hydrogen, is the most important contributor to the various chirality indexes. In contrast, Torsion 2 which rotates a methyl group has a small impact. One can combine several chirality indexes to arrive at a new index, $\tilde{G}_{os}^{m}$, that is strongly dependent on Torsion 2 and weakly dependent on Torsion 1. We have arrived at $\tilde{G}_{os}^{m}$ shown in Figs. 5.1(k) and 5.1(l) by trial and error, and by least squares fitting to optimize the combination of indexes. First, by visual inspection G_{0S}^{m}(m=1,n=1) and G_{0S}^{m}(m=1,n=2)

were identified as having very similar dependence on Torsion 1(t1) but distinct variations with Torsion 2(t2). An appropriate combination of these indexes could potentially have the desired t2 dependence. We therefore began by writing $\tilde{G}_{os}^{m}$ as a linear combination of these two indexes. To optimize the combination, torsion 3 was fixed at 180 degrees and torsions 1 and 2 were scanned from 0 to 360 degrees, in 10 degree steps. Following this, the average

$$\bar{G}_{0S}^{m}(t2) = \frac{1}{36}\sum_{t1} \tilde{G}_{0S}^{m}(t1, t2) \qquad [5.1]$$

was evaluated, where the explicit dependence of the index on Torsions 1 and 2 is shown. Then, the optimal linear combination in $\tilde{G}_{os}^{m}$ is obtained by minimizing

$$\sum_{t2}\left(\sum_{t1}\left(\tilde{G}_{0S}^{m}(t1, t2) - \bar{G}_{0S}^{m}(t2)\right)^2\right) \qquad [5.2]$$

The resulting index is $\widetilde{G}_{0S}^{m}$=G_{0S}^{m}(m=1,n=1)-2.681G_{0S}^{m}(m=1,n=2). Panels (k) and (l) show that $\tilde{G}_{os}^{m}$ is only weakly dependent on the position of the alcohol hydrogen but strongly dependent on both methyl torsions. In Section 5.3, $G_{0S}^{1}(m = 3, n = 1)$ and $G_{0S}^{m}(m = 3, n = 2)$ will be used to isolate the chirality induced bias (excess chirality) for Torsion 1. The methyl positions will be determined from $\tilde{G}_{os}^{m}$. $G_{0S}^{q}(m = 3, n = 1)$ will be employed to assess the polarization contribution to chirality transfer.

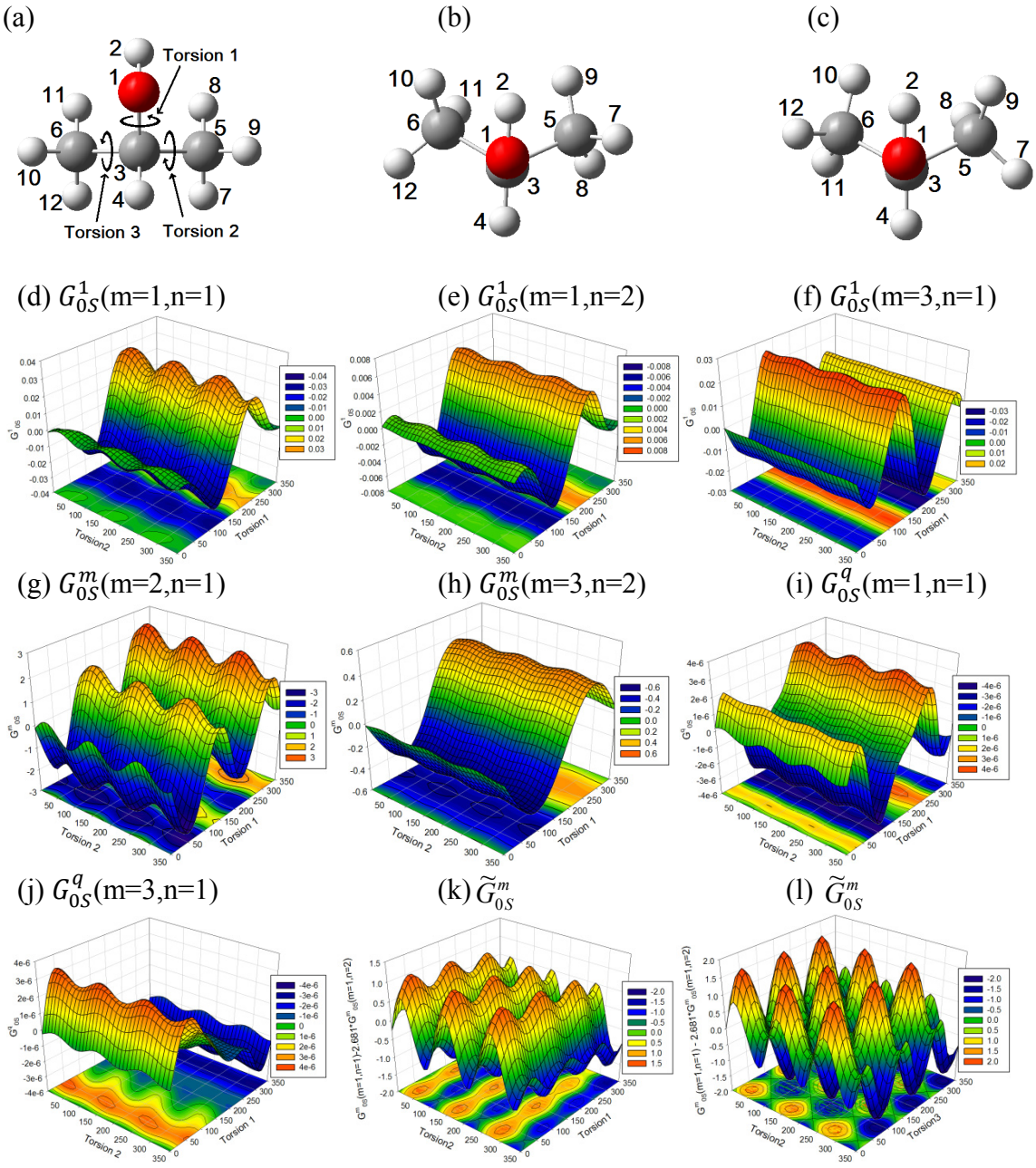

Figure 5.1. The influence of torsional angles on chirality indexes of 2-propanol. As shown in (a), torsions 1, 2, and 3, are defined by atoms H(2)-O(1)-C(3)-H(4), O(1)-C(3)-C(5)-H(7), and O(1)-C(3)-C(6)-H(10), respectively. Panel (b) shows a snapshot in which torsion 1, torsion 2 and torsion 3 are set to 180°, 30°, and 30°, respectively, while panel (c) shows a snapshot in which torsions 1, 2 and 3 are set to 180°, 90°, and 90°, respectively. Panels (d)-(j) show selected chirality indexes as a function of torsion 1 and torsion 2, while torsion 3 is set to 180°. Panels (k) and (l) show the combination index $\widetilde{G}^m_{0S}$. For panel (l), torsion 1 is set to 180°. In (i) and (j), the atomic charges, in unit of |e| are -0.68, 0.37, 0.59, -0.08, -0.30, -0.30, 0.07, 0.07, 0.07, 0.07, 0.07, 0.07, for atoms 1-12, respectively.

The analysis of chirality transfer presented in this chapter focuses on potential hydrogen bonding atomic pairs, for example the hydrogen of 2-propanol with O(28) of Whelk-O1. The indexes will be evaluated as a function of the distance between the two atoms and, specifically, the distance will be divided into two cylindrical coordinates: *z*, the distance between the two atoms in the direction perpendicular to the surface, and *r*, the distance parallel to the surface. The cylinder is centered about a selector atom, as shown in Fig. 5.2, and will move up and down and side to side as the selector moves. However the cylinder axis always remains perpendicular to the underlying Si layer. By choice of convention, we define *z* to be negative when the solvent atom is closer to the underlying Si layer than is the selector atom. With this coordinate system, the excess chirality is calculated as follows: For a given solvent-selector atomic pair (the O of 2-propanol and H(28) of Whelk-O1, for example), when the solvent atom is located between *(r,z)* and *(r+dr, z+dz)* relative to the specific selector atom, the excess chirality, $< G_{0S}^{w} >_{r,z}$ is calculated as follows:

$$< G_{0S}^{w} >_{r,z} = \frac{1}{N_c} \sum_{i=1}^{N_c} G_{0S}^{w} \qquad [5.3]$$

where N_c is the total number of solvent molecules located between *(r,z)* and *(r+dr, z+dz)* over the course of the simulation, *dr*=*dz*=0.12 Å, and G_{0S}^{w} is an instantaneous value of the chirality index for the solvent molecule located at this position. In practice, solvent positions are recorded every 20 iterations, each solvent molecule is identified by its *r* and *z* value, and 27 instantaneous chirality indexes are evaluated and added to the appropriate sum (see Eq. [5.3]). An identical positional breakdown is applied to calculate average atomic charges and molecular dipole moments.

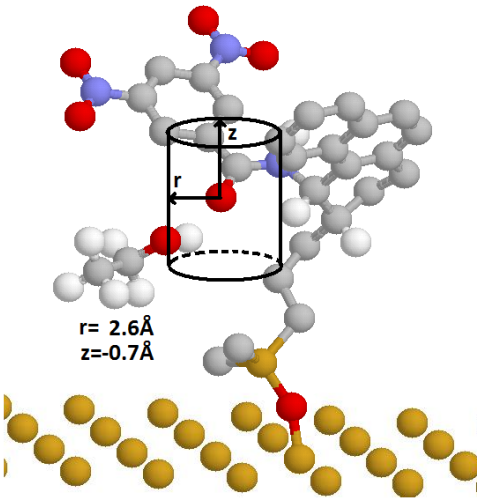

Figure 5.2. The cylindrical coordinate system used in the spatial breakdown of excess chirality, average atomic charges, and average solvent dipole. A chosen selector atom is placed at the center of the cylinder. Averages are collected over solvent molecules located between *(r,z)* and *(r+dr,z+dz)*, where $dr = dz = 0.12$ Å. The cylinder axis is perpendicular to the underlying Si layer.

5.2.4 Simulation details

Surface-to-solvent chirality transfer is evaluated from molecular dynamics simulations of the CSPs (Whelk-O1, DNB-leucine and DNB-phenylglycine) surrounded by solvent. The solvent consists of either pure ethanol, pure 2-propanol, 80/20 *n*-hexane/ethanol, or 80/20 *n*-hexane/2-propanol. The simulation cell, as shown in Fig. 2.10, has solvent confined between an upper and a lower surface that each include nine selectors, end-caps, silanol groups and an underlying layer of Si. The full simulation cell actually has empty space above the upper, and below the lower, surface such that roughly 2/3 of the entire cell is empty. 3D Periodic boundary conditions are applied in the simulations and the space above and below the interfacial region minimizes interactions between neighboring surface-fluid-surface slabs. The distance between the two

underlying Si layers is adjusted so that the solvent density in the center of the simulation cell is close to the experimental density. Each simulation with pure solvent includes 600 solvent molecules, while each simulation with mixed solvents includes 400 solvent molecules.

Electrostatic interactions are evaluated using Ewald summations, including a correction for the rectangular prism shape of the simulation cell[40]. The results reported below correspond to a momentum space cutoff of $k^{*2} \leq 27$ and an Ewald parameter of $\alpha = 0.1916$ Å^{-1}. The FC electrostatic interaction is incorporated into the Ewald summations by replacing the Ewald forces for close intramolecular pairs of atoms where Eq. [2.26] differs from the usual electrostatic potential.

Three Nosé-Hoover thermostats are used to generate canonical averages: one thermostat is applied to translations; another is independently applied to rotations of the rigid ring units in the selectors; and a third constrains the temperature associated with charge fluctuations. The relevant conserved quantity in the simulations is defined by Eq. [4.1] and has been described in detail in Chapter 4.

The initial configuration for the simulations is obtained by placing a large excess of solvent molecules on a cubic lattice between the two surfaces and some are removed at random until the desired number remain. Following this, the surface-to-surface distance is increased until strong overlaps are removed. Then Monte Carlo cycles are performed as the simulation cell is gradually recompressed. Finally, the molecules are assigned random linear and angular velocities consistent with the desired temperature.

Simulations of 10-15 ns are performed for all twelve solvent-surface interfaces. The time step for all simulations is 0.3 fs and the total change in the Nosé-Hoover Hamiltonian, H_{NH}, is 1% over 200 ps. The equilibration time of each simulation is 60 ps. The duration of the equilibration period was decided based upon the dihedral distributions of torsion 2 (O(1)-C(3)-C(5)-H(7)) for 2-propanol. Specifically, in the starting structure of 2-propanol, torsion 2 is set to 60 degrees, and after 50 ps, we find that it becomes equally distributed between the three isoenergetic conformers (60, 180, and 270 degrees). In our previous work on chirality transfer about solutes[181], we found that 4 ns was adequate to get converged results. The excess chirality reported in this work has been averaged over the 18 selectors in the simulation cell, for a total monitoring time of 180–270 ns.

The 2D solvent distribution about the chiral selectors, $g(r,z)$, is collected every 20 iterations along with chirality indexes, atomic charges, and molecular dipoles. Snapshots of the entire simulation cell are collected every 5000 iterations. These snapshots form the basis of the collection of hydrogen bonding statistics, where a hydrogen bond is defined as X—H---Y, where X and Y are either O or N.

5.3. Results and discussion

The chirality transfer between surface and solvent is examined in this section for the three CSPs, Whelk-O1, DNB-phenylglycine, and DNB-leucine, in the four solvents, ethanol, 2-propanol, *n*-hexane/ethanol, *n*-hexane/2-propanol.

In our analysis of excess chirality, we place emphasis on solvent-to-selector hydrogen bonding. Molecular dynamics simulations have been widely used to provide detailed information on the spatial, energetic, and dynamic aspects of hydrogen bonds in condensed phases [183-185]. Analyte-selector hydrogen bonding is invoked in many CSP selective mechanisms[15] and simulations have successfully revealed the importance of H-bonding for these selectors[161]. CH-π interactions are also included in some CSP selectivity mechanisms[161, 186, 187] and will be noted below in regards to chirality transfer to solvent.

5.3.1 Solvation of Chiral Stationary Phases

Before analyzing the selector-solvent chirality transfer, we begin with an analysis of solvent structure about the stationary phases. 2D distributions are presented to show solvent position, relative to specified selector atoms, as a function of distance along the surface (r) and perpendicular to the surface (z). In the mixed solvents, results are shown only for the alcohol component, since *n*-hexane does not interact strongly with the selectors and prefers to be in the bulk. We also focus on the chirality transfer to alcohol since it has the potential to hydrogen bond to the selectors and is most likely to be found at the interface. Solvation studies for these selectors have been published elsewhere[112, 161], although not necessarily for the solvents of interest here.

H-bonding statistics for the three CSPs and the four solvents are presented in Table 5.1. The probabilities in Table 5.1 are consistent with a previous study[112] of H-bonding for DNB-phenylglycine and DNB-leucine, although they are consistently somewhat lower. The selector representation is identical in both studies but a polarizable

alcohol model is used in this chapter along with an all-atom molecular representation of the alcohol.

Table 5.1. Hydrogen bonding statistics for Whelk-O1, DNB-phenylglycine and DNB-leucine selectors in pure ethanol, pure 2-propanol, 80/20 *n*-hexane/2-propanol, and 80/20 *n*-hexane/ethanol. In cases where two solvent and selector atoms are listed, the table gives the percentage of selectors with simultaneous formation of the two specified H-bonds with a single solvent.

Selector component	Solvent component	Percentage in ethanol	Percentage in *n*-hexane/ ethanol	Percentage in 2-propanol	Percentage in *n*-hexane/ 2-propanol
Whelk-O1					
H(26)	O	16.9	16.3	20.3	9.0
O(28)	H	60.6	29.0	39.3	18.3
DNB-phenylglycine					
H(12)	O	5.6	4.9	2.0	2.0
O(14)	H	12.1	9.5	26.0	11.4
H(18)	O	7.2	5.0	7.4	4.1
O(20)	H	33.0	18.4	41.2	22.1
H(12) and O(20)	H and O	0.0	0.0	0.0	0.0
O(14) and H(18)	H and O	0.4	1.1	1.2	1.3
DNB-leucine					
H(12)	O	62.1	23.4	39.9	19.1
O(14)	H	29.9	17.4	33.7	19.6
H(18)	O	55.8	42.9	42.2	37.0
O(20)	H	36.4	15.3	44.8	17.8
H(12) and O(20)	H and O	3.1	2.7	4.8	3.2
O(14) and H(18)	H and O	1.3	1.5	0.7	2.1

The solvent distribution about Whelk-O1 is shown in Fig. 5.3, for all four solvents. Peaks in this distribution identify most probable solvent locations. The arrows in the figure are color-matched to specific solvent molecules in the snapshots. The Whelk-O1 structure places H(26) inside the cleft region and this placement is crucial to chiral selectivity[113, 161]. In particular, the dominant analyte docking arrangement involves

H-bonding to H(26) and, as a result, any solvent in this region must be displaced by analyte in order for chiral recognition to occur. Panels 4(a)-(d) show the 2D distribution of the alcohol oxygen about H(26) in the four solvents. The ridge beginning at around z=2Å, r=0 is due to direct solvent-selector H-bonding. The fact that this ridge occurs for positive z clearly indicates that the solvent H-bonds from above (*i.e.* in the cleft). A second ridge at somewhat higher z is also evident in the panels and this ridge is due to a second solvent, within the cleft region, that is not directly H-bonded to the selector but may H-bond to another solvent. The snapshots in panels (i)-(l) show these in-the-cleft solvents. Solvent-selector H-bonding to the amide oxygen, O(28), occurs frequently and this is evident from the prominence of the ridge at r=2Å in Panels (e)-(h). The solvent prefers to place its hydrogen on the side of O(28), or closer to the surface as evident from the shift in the peak position towards negative z. Thus, this solvent molecule is outside of the cleft region and is less likely to interfere with chiral recognition.

The alcohol placement relative to the Whelk-O1 selector is similar for all four solvents. Overall, 2-propanol is more likely to H-bond to H(26) and this is clear from the stronger peak around z=2Å, r=0 in panels (c) and (d), relative to panels (a) and (b). The 2D distributions in panels (e)-(h) show that the H-bonding probability to O(28) is comparable for ethanol and 2-propanol. The probability for secondary solvents, not directly H-bonded to the selector, increases in 100% alcohol solvents. This is evident from the prominent secondary ridges in 100% alcohol solvents (compare the z=4Å, r=0 ridge in Figs. 5.3(a) and 5.3(b) for example).

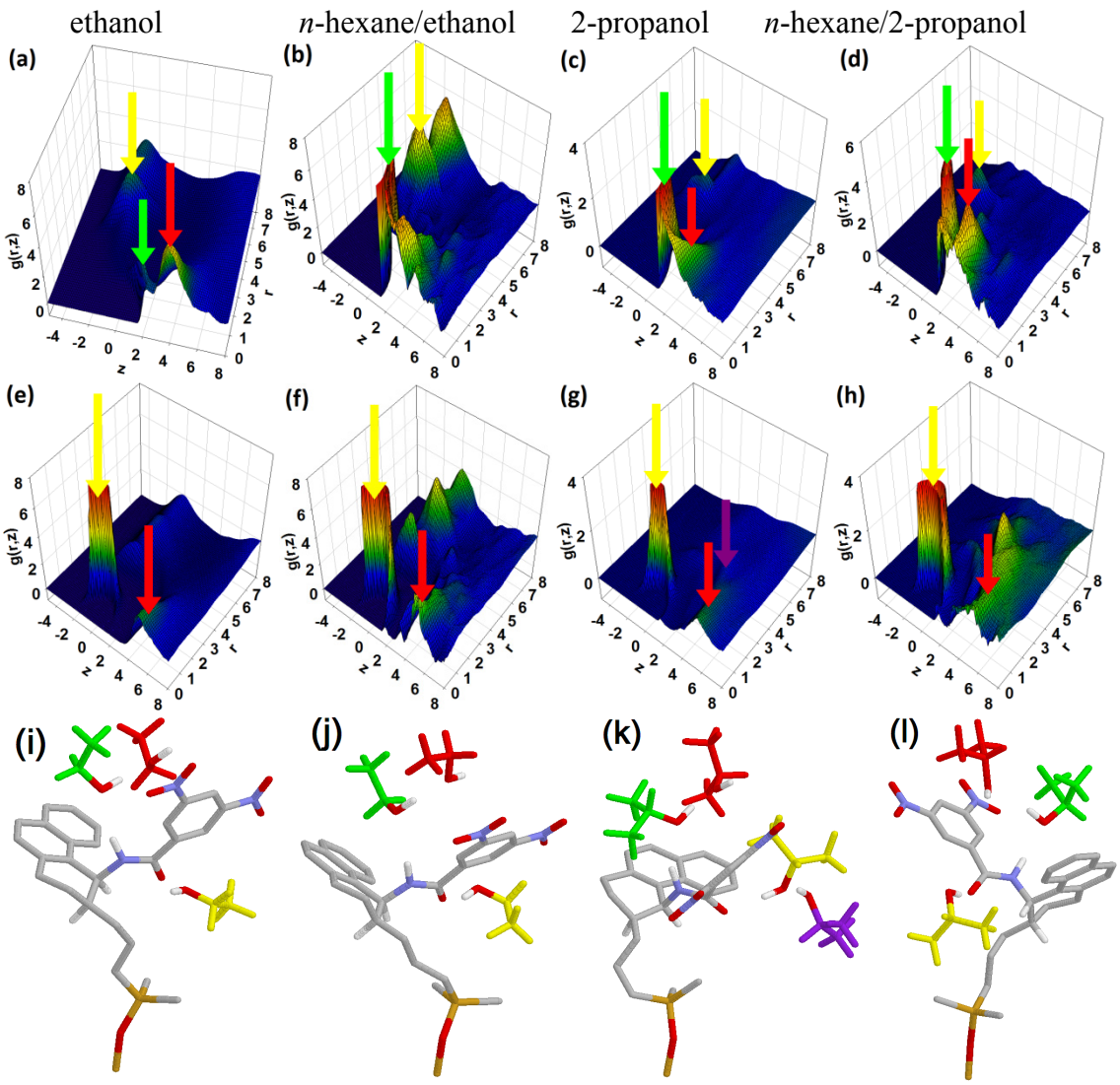

Figure 5.3. 2D solvent-selector distributions for potential H-bonding pairs at the Whelk-O1 interface. The position variables, *z* and *r*, are given in Å. Four solvents are shown: pure ethanol[(a),(e),(i)], *n*-hexane/ethanol [(b),(f),(j)], pure 2-propanol [(c),(g),(k)], and *n*-hexane/2-propanol [(d),(h),(l)]. Distributions between H(26) of the Whelk-O1 selector and the alcohol oxygen, and between O(28) of the Whelk-O1 selector and the alcohol hydrogen, are shown in (a)-(d) and (e)-(h), respectively. Snapshots are provided in (i)-(l). The solvent molecules in the snapshots are color coded to correlate their positions with peaks and ridges in the 2D distributions, as shown by arrows of the same colour in (a)-(h).

2D distributions for *n*-hexane/2-propanol solvated DNB-phenylglycine and DNB-leucine interfaces are provided in Fig. 5.4. The solvent molecules in the snapshots are color coded to correlate their positions with peaks and ridges in the 2D distributions, as shown by arrows of the same colour in (a)-(h). The distribution of O(2-propanol) about H(12), the amide hydrogen closest to the surface, is given in the first row. Results for the DNB-phenylglycine selector (Fig. 5.4(a)) show a very weak distribution between this potential H-bonding pair. In contrast, a strong peak is evident for DNB-leucine (Fig. 5.4(b)) showing that alcohol prefers this selector. The peak location is consistent with direct solvent-selector H-bonding. Steric hindrance due to the lateral phenyl ring may contribute to the lack of H-bonding for H(12) in DNB-phenylglycine. However, as shown in Panels (e) and (f), the upper amide hydrogen, H(18), also has weak H-bonding for DNB-phenylglycine but is much more strongly interacting for DNB-leucine. From Table 5.1, 37% of the H(18) in DNB-leucine are H-bonding to solvent but only 4% are H-bonding for DNB-phenylglycine.

H-bonding to the upper and lower amide oxygens, O(14) and O(20), is common for both selectors. For O(14), the proximity of the underlying surface means that solvent prefers to H-bond from above whereas, for O(20), the solvent preferentially places its hydrogen closer to the surface although H-bonding from the side and above still occurs.

Secondary features, such as the strong ridge at z=4Å in Panel (b) or the broad ridge at r=6Å in Panel (c), are evident in Fig. 5.4. These features arise primarily from

solvents H-bonding to other sites in the selector, or to solvents H-bonded to a solvent that has a solvent-selector H-bond.

DNB-phenylglycine in 2-propanol/*n*-hexane

DNB-leucine in 2-propanol/*n*-hexane

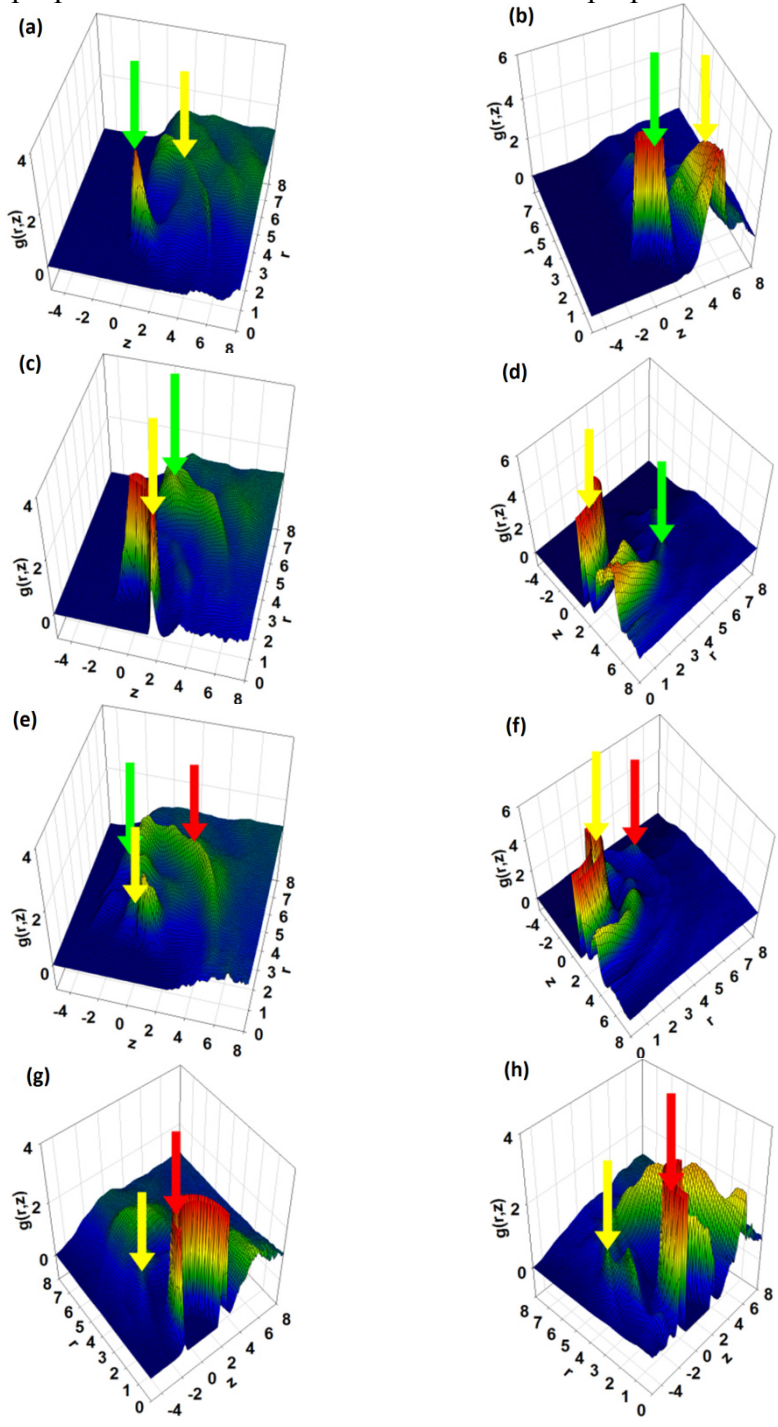

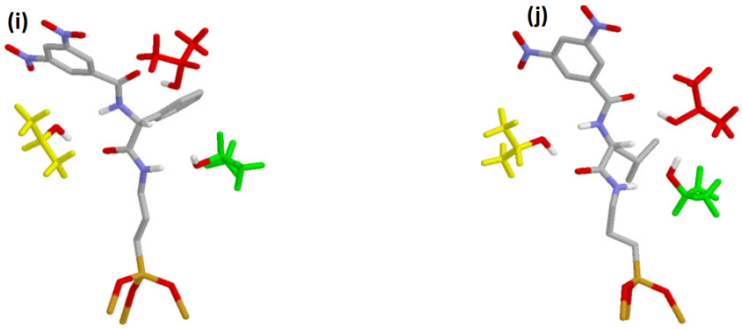

Figure 5.4. 2D distributions from 2-propanol/*n*-hexane solvated DNB-phenylglycine and DNB-leucine interfaces. The position variables, *z* and *r*, are given in Å. Each column refers to a specific stationary phase. Specifically, panels [(a),(c),(e),(g)] and [(b),(d),(f),(h)] show *g(r,z)* for DNB-phenylglycine and DNB-leucine, respectively. Corresponding snapshots are provided in Panels (i) and (j). The first, second, third, and fourth rows show the distribution between H(12)-O(2-propanol), O(14)-H(2-propanol), H(18)-O(2-propanol), and O(20)-H(2-propanol), respectively. The solvent molecules in the snapshots are color coded to correlate their positions with peaks and ridges in the 2D distributions, as shown by arrows of the same colour in (a)-(h).

2D distribution for 2-propanol, ethanol, and ethanol/*n*-hexane about DNB-phenylglycine and DNB-leucine have not been shown but Table 5.1 provides H-bonding statistics. Qualitatively, the 2D distributions are similar to those in Fig. 5.4 but there is a more pronounced quantitative difference between DNB-leucine and DNB-phenylglycine in an ethanol solvent. For DNB-phenylglycine, the overall number of ethanol-selector H-bonds is less than for 2-propanol, and this is particularly true for the pure solvents. In contrast, ethanol forms more H-bonds to DNB-leucine, on average, than does 2-propanol.

In order to correlate solvent position with chirality transfer, the 2D solvent distributions shown in this section will be represented as contour plots in the subsequent sections.

5.3.2 Chirality transfer at interfaces

The alcohol molecules at the interface necessarily explore a broad range of conformations. The excess chirality of interest here results from a small imbalance in the conformational distributions resulting from the chiral environment. It follows that some estimation of the accuracy of the predicted chirality transfers is required. Fig. 5.5 provides a selection of excess chiralities for 2-propanol in 2-propanol/*n*-hexane solvated DNB-phenylglycine and DNB-leucine.

The panels in Fig. 5.5, and in all subsequent presentations of excess chirality, use color coding to identify regions where the excess chirality is negative (blue, indigo) versus regions where it is positive (yellow, orange, red). Green indicates an average close to zero. In the panels, green is also used for regions where solvent is rarely found: We require a minimum of 20000 instantaneous chiralities recorded before presenting an excess chirality for the region. In practice, the solvent is rarely found within the end cap region for steric reasons. In higher probability regions, such as H-bonding areas, the number of instantaneous chirality indexes normally exceeds 200,000. Overlaid on the maps of chirality transfer are contour maps that show the 2D probability distributions analogous to Figs. 5.3 and 5.4. In this way, with color coded maps and contour plots, one can correlate regions of high solvent density with regions of high chirality transfer.

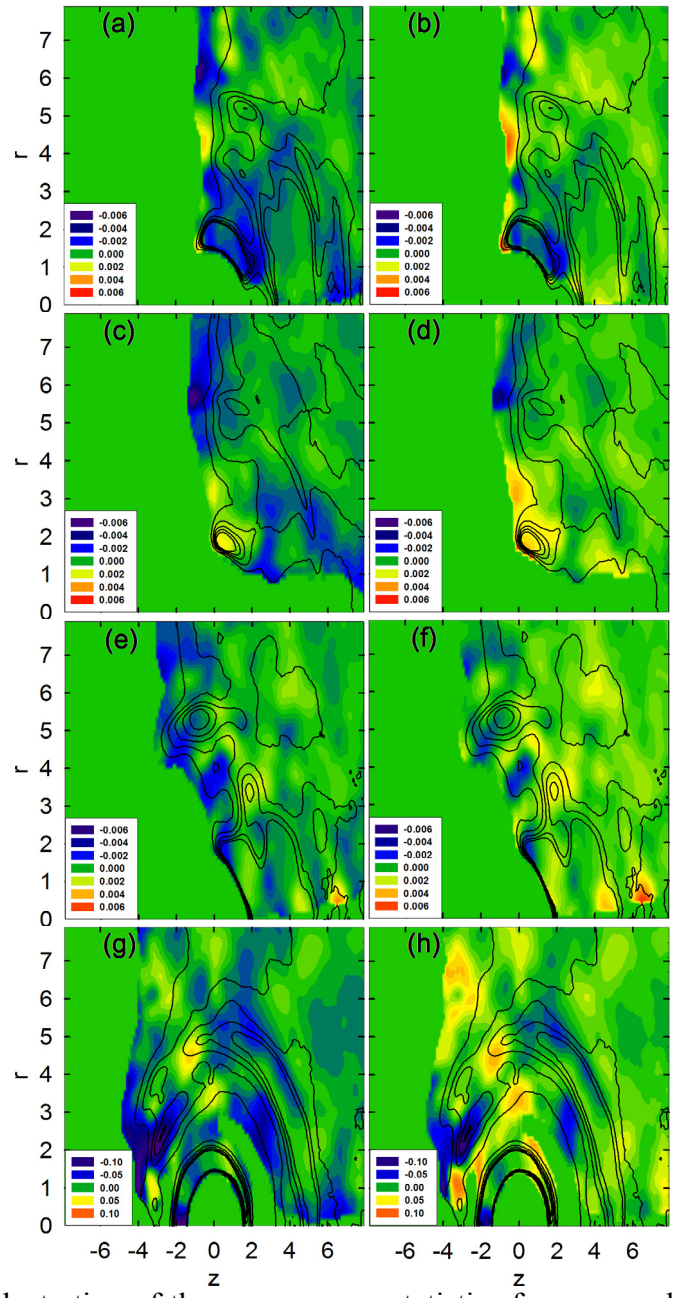

Figure 5.5. An illustration of the convergence statistics for excess chirality. Panels (a) and (b) show ($<\boldsymbol{G}^{\mathbf{1}}_{\mathbf{0S}}(m=3,n=1)>_{r,z}$ - CI95) and ($<\boldsymbol{G}^{\mathbf{1}}_{\mathbf{0S}}(m=3,n=1)>_{r,z}$ + CI95), respectively, for H(12)-O(2-propanol) in the 2-propanol/*n*-hexane solvated DNB-leucine interface. Panels (c) and (d) show ($<\boldsymbol{G}^{\mathbf{1}}_{\mathbf{0S}}(m=3,n=1)>_{r,z}$ - CI95) and ($<\boldsymbol{G}^{\mathbf{1}}_{\mathbf{0S}}(m=3,n=1)>_{r,z}$ + CI95), respectively, for H(12)-O(2-propanol) in the 2-propanol/*n*-hexane solvated DNB-phenylglycine interface. Panels (e) and (f) show ($<\boldsymbol{G}^{\mathbf{1}}_{\mathbf{0S}}(m=3,n=1)>_{r,z}$ - CI95) and ($<\boldsymbol{G}^{\mathbf{1}}_{\mathbf{0S}}(m=3,n=1)>_{r,z}$ + CI95) for H(12)-O(2-propanol) in the 2-propanol/*n*-hexane solvated Whelk-O1 interface. Panels (g) and (h) show ($<\boldsymbol{G}^{\boldsymbol{m}}_{\mathbf{0S}}(m=3,n=2)>_{r,z}$ - CI95) and ($<\boldsymbol{G}^{\boldsymbol{m}}_{\mathbf{0S}}(m=3,n=2)>_{r,z}$ + CI95) for O(20)-H(2-propanol) in the 2-propanol/*n*-hexane solvated DNB-leucine interface. The cylindrical coordinates *r* and *z* are in Å, $<\boldsymbol{G}^{\mathbf{1}}_{\mathbf{0S}}(m=3,n=1)>_{r,z}$ is in Å, and $<\boldsymbol{G}^{\boldsymbol{m}}_{\mathbf{0S}}(m=3,n=2)>_{r,z}$ is in $g^4/(mol^4 \bullet Å^2)$.

The rightmost panels in Fig. 5.5 show $\langle G_{oS}^{w} \rangle_{r,z}$ minus the 95% confidence interval (CI95). The leftmost panels show $\langle G_{oS}^{w} \rangle_{r,z}$ plus the CI95, which is calculated from[188]

$$CI95 = \frac{1.96}{\sqrt{N_c}} \sqrt{\left(\left\langle (G_{0S}^{w})^2 \right\rangle_{r,z} - \left\langle G_{0S}^{w} \right\rangle_{r,z}^2 \right)} \qquad [5.4]$$

where N_c is the number of solvent molecules located between (r, z) and (r+dr, z+dz) about the selector atom during the collection period of the simulation. In calculating CI95, a Gaussian distribution is assumed. Regions of consistent color coding between the right and left panels indicate good statistics. Notice that the color coding is similar in many regions on both panels, and particularly regions of high solvent density, where the error is generally small relative to the overall magnitude of the excess chirality. The largest errors tend to occur for regions of low solvent density, where there are fewer values of the chirality index recorded, and for small r values, due to a smaller collection volume, leading to a reduction of counts.

Before proceeding to a detailed analysis of the chirality transfer, it is worth noting the scale of the chirality transfers in Fig. 5.5. For $\langle G_{oS}^{1}(m = 3, n = 1) \rangle_{r,z}$, the excess chirality induced in 2-propanol can be up-to 20% of the maximum value observed in Fig. 5.1(f). Thus, there is cancellation between instantaneous chirality indexes but the residual remains significant. Likewise, the average value of $\langle G_{oS}^{m}(m = 3, n = 2) \rangle_{r,z}$ can reach up-to 17% of the maximum value. These excess chiralities are much larger than were observed in Chapter 4, where solutes in the bulk were considered. As expected, the immobilization of the chiral selectors onto a surface, and possibly the collective effect of multiple selectors, has lead to a significant chirality transfer into nearby solvents.

5.3.3 Comparisons between selectors: Conformational chirality

In this section, we analyze the chirality transfer to 2-propanol, in the binary 2-propanol/*n*-hexane solvent, when this solvent is near a DNB-leucine, DNB-phenylglycine, or Whelk-O1 interface. In this section, we focus on characterizing conformational bias introduced into the solvent molecules. Solvent polarization due to the chiral interface will be examined in Section 5.3.4 and comparisons between different solvents will be presented in Section 5.3.5.

Fig. 5.6 presents $\langle G_{OS}^{1} \rangle_{r,z}$, $\langle G_{OS}^{m} \rangle_{r,z}$, and $\langle \tilde{G}_{os}^{m} \rangle_{r,z}$, collected around the H-bonding sites (H(12), O(14), H(18), O(20)) of the DNB-leucine selector. The cylindircal coordinates *r* and *z* are in Å, $<G_{0S}^{1}(\text{m=3,n=1})>_{\text{r,z}}$ is in Å, and $<G_{0S}^{m}(\text{m=3,n=2})>_{\text{r,z}}$ is in $g^4/(mol^4 \bullet Å^2)$. H(12) is closest to the underlying surface, and H-bonding imposes steric constraints on the solvent. This solvent is often located on the same side as the lateral isopropyl group of the selector, as shown in the snapshot 5.6(d), which introduces additional steric constraints. Both $\langle G_{oS}^{1} \rangle_{r,z}$ and $\langle G_{oS}^{m} \rangle_{r,z}$ are strongly dependent on Torsion 1, defined by H(2)-O(1)-C(3)-H(4), which orients the alcohol hydrogen relative to the rest of the molecule. Figs. 5.6(a) and 5.6(b) show a significant negative excess chirality for 2-propanol in the high probability region where direct H-bonding to H(12) occurs. One can extract from Fig. 5.1 that simultaneous negative average values for these two indexes means a bias in Torsion 1 towards values between 0 and 60 degrees, where the alcohol hydrogen is gauche to the methine hydrogen. The snapshot in Fig. 5.6(d) provides an illustration of this solvent configuration (Torsion 1 = 48 degrees in the snapshot) .

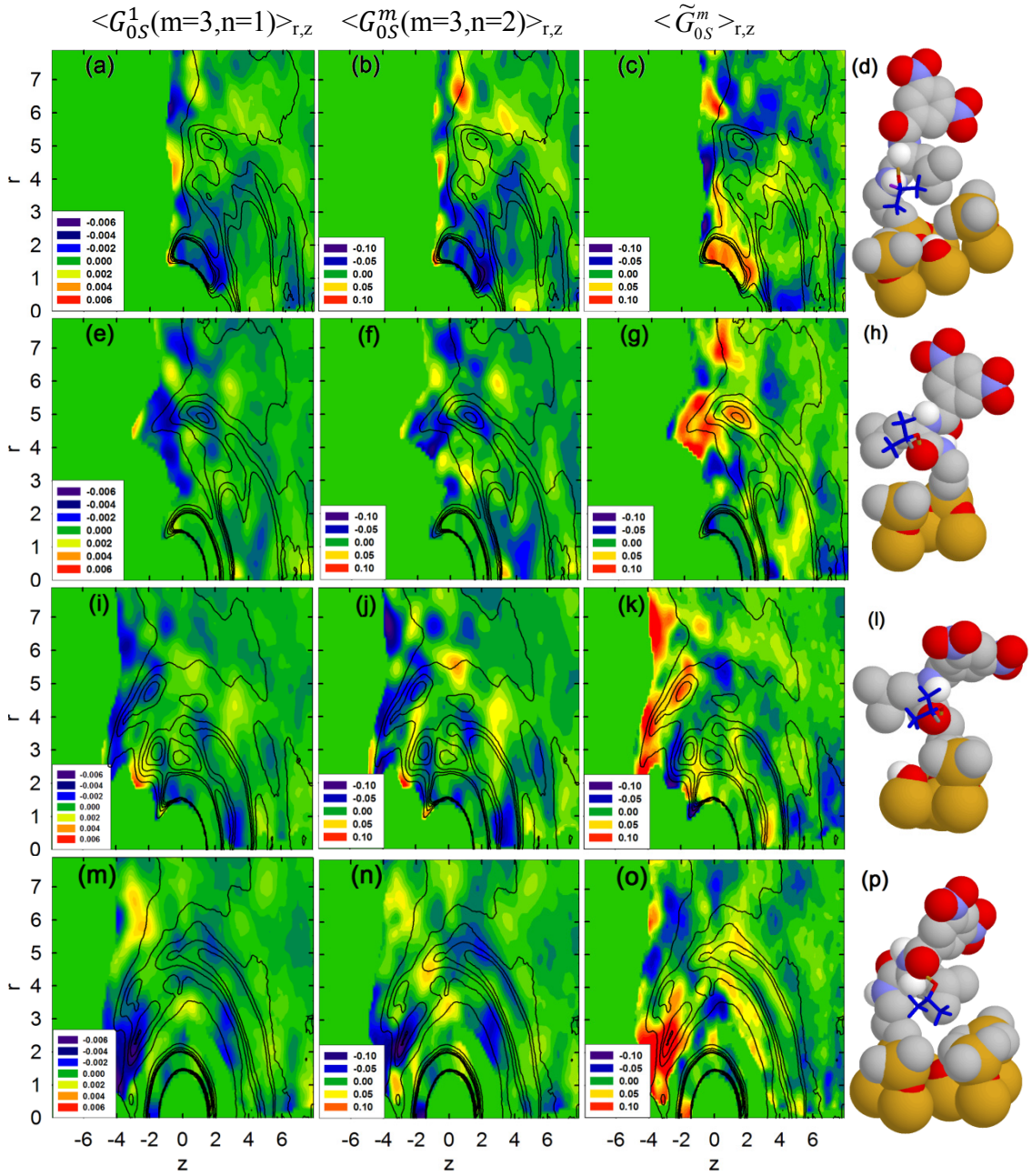

Figure 5.6. 2D distributions of average chirality indexes from the 2-propanol/*n*-hexane solvated DNB-leucine interface. Panels (a), (e), (i) and (m) show <$\boldsymbol{G^1_{0S}}$(m=3,n=1)>$_{r,z}$, panels (b), (f), (j) and (n) show <$\boldsymbol{G^m_{0S}}$(m=3,n=2)>$_{r,z}$, and panels (c), (g), (k) and (o) show the combined index <$\widetilde{G}^m_{0S}$>$_{r,z}$. Panels (d), (h), (l) and (p) show snapshots where the selector, nearby end-caps and silanol groups are shown in space filling representation while 2-propanol is shown in bright colors for contrast. Distance measures *r* and *z* in panels (a)-(d), (e)-(h), (i)-(l), and (m)-(p) refer to H(12)-O(2-propanol), O(14)-H(2-propanol), H(18)-O(2-propanol), and O(20)-H(2-propanol), atom pairs respectively.

Hydrogen bonding to the upper amide hydrogen, H(18), is distinct from the lower amide hydrogen, as shown in Panels 5.6(i) and 5.6(j). First, the H-bonding solvent adopts a wider range of positions and may even be closer to the surface than H(18). Consistent with the greater positional freedom allowed to the solvent, the excess chirality for H-bonding solvent is generally small indicating significant conformational freedom as well. However, there is an indication of some excess chirality around z=-1.0Å, when the solvent is positioned close to the surface while maintaining an H-bond with H(18). A closer inspection of solvents in this location indicates that a non-negligible fraction simultaneously form two H-bonds to the selector, one to O(14) and one to H(18). This forces the alcohol group to point towards the underlying surface, and one methyl group points towards the bulk. The spatial constraints of forming two H-bonds, coupled with steric constraints from the selector lateral group and the underlying surface, lead to a negative excess chirality in this case.

According to Table 5.1 20% of the DNB-leucine selectors have H-bonds to O(14), but these solvents do not have significant excess chirality for several reasons. First, the solvent has some positional flexibility and can H-bond from above or slightly below O(14). Second, the solvent often adopts a position opposite, or tangential to, the lateral group. These factors indicate minimal steric constraints and lead to small excess chirality. It is interesting to note that dual H-bonding with H(18), as discussed in the preceding paragraph, has a smaller contribution for O(14). This follows because these multiple H-bonding solvents tend to occupy positions relative to O(14) that also occur much more frequently for solvents with a single H-bond to the selector.

H-bonding to O(20) is generally characterized by small-to-negligible chirality transfer except for solvents located closer to the underlying surface (ridge ending around z=-2Å in Figs. 5.6(m) and 5.6(n)). Upon close inspection of the corresponding snapshots, we find that a significant fraction of solvents at this location simultaneously form an H-bond to H(12). This forces the alcohol group to point towards the bulk, and one methyl group points towards the underlying surface. On average, these 2-propanol molecules have the methine H and the alcohol H in a gauche configuration, leading to an overall negative excess chirality. Overall, H-bonding to the amide oxygens is probable (see Table 5.1) but is not accompanied by significant chirality transfer to solvent. In contrast, H-boding to the amide hydrogens can be accompanied by steric or energetic constraints that lead to significant excess chiralities.

Panels 5.6(c), 5.6(g), 5.6(k), and 5.6(o) show $< \tilde{G}_{0S}^{m} >_{r,z}$, the combination index introduced to isolate the contribution of methyl torsions. Overall, this index is negligible in regions where $\langle G_{0S}^{1} \rangle_{r,z}$ and $\langle G_{0S}^{m} \rangle_{r,z}$ are small, indicating that "unbiased" solvent conformational averaging occurs in these cases and chirality transfer is small-to-negligible. The largest values of $< \tilde{G}_{0S}^{m} >_{r,z}$ occur for solvent H-bonding to H(12) and the excess $< \tilde{G}_{0S}^{m} >_{r,z}$ is significantly positive. By reference to Figs. 5.1(k) and 5.1(l), this indicates that the methyl groups prefer to orient such that a hydrogen is cis-to-gauche relative to the alcohol oxygen.

Hydrogen bonding to the backbone of DNB-phenylglycine occurs less frequently than for DNB-leucine, as shown in Table 5.1. This is particularly true for the amide hydrogens, where only 2-4% of the selectors have H-bonding to these atoms. The

occurrence of simultaneous multiple H-bonds is also less common for DNB-phenylglycine due to the bulky lateral group and a small number of energetically accessible backbone conformations. The lateral phenyl ring impacts excess solvent chirality in two ways. First, CH-π interactions will encourage certain energy lowering solvent positions and orientations. On the other hand, the ring imposes steric constraints when the solvent is too close and this may bias towards specific conformations.

The excess solvent chirality for 2-propanol in 2-propanol/*n*-hexane about DNB-phenylglycine is shown in Fig. 5.7. The cylindircal coordinates r and z are in Å, $\langle G_{0S}^{1}(\mathrm{m=3,n=1})\rangle_{r,z}$ is in Å, and $\langle G_{0S}^{m}(\mathrm{m=3,n=2})\rangle_{r,z}$ is in $g^4/(mol^4 \bullet Å^2)$. Panels (a) and (b) show a positive excess chirality introduced in 2-propanol molecules that H-bond to H(12) of DNB-phenylglycine (see z=0, r=2Å region). This is in direct contrast to DNB-leucine where solvent hydrogen bonded to H(12) has a negative excess chirality: The change in lateral group has reversed the conformational bias of the nearby solvent. For the other H-bonding atoms (O(14), H(18), and O(20)) of DNB-phenylglycine, a negative excess chirality is induced for a localized subset of the H-bonding solvent. For example, chirality transfer for solvent H-bonded to O(14) is generally small except when the solvent is closer to the underlying surface.

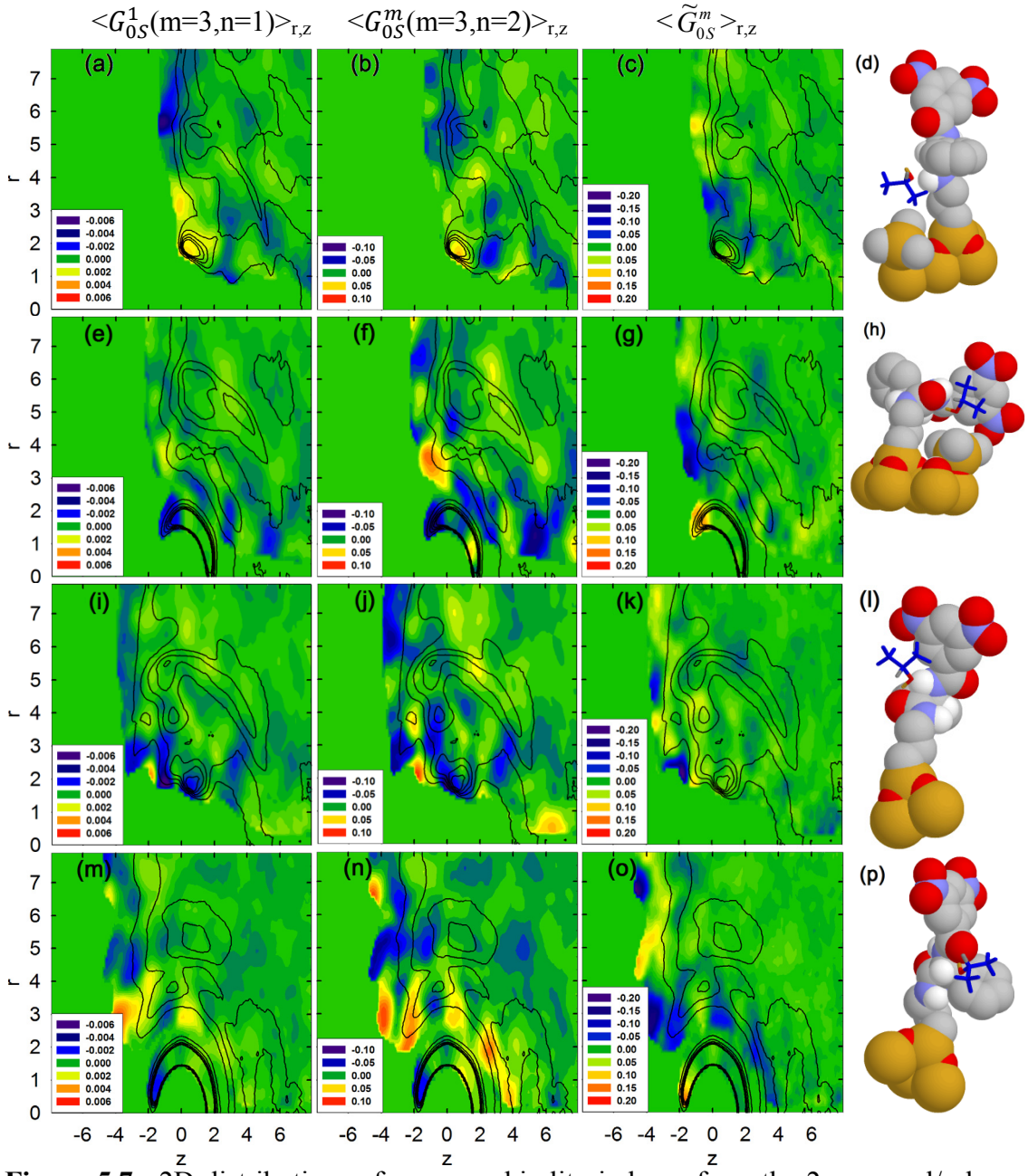

Figure 5.7. 2D distributions of average chirality indexes from the 2-propanol/*n*-hexane solvated DNB-phenylglycine interface. Panels (a), (e), (i) and (m) show <$\boldsymbol{G_{0S}^{1}}$(m=3,n=1)>$_{r,z}$, panels (b), (f), (j) and (n) show <$\boldsymbol{G_{0S}^{m}}$(m=3,n=2)>$_{r,z}$, and panels (c), (g), (k), and (o) show the combined index <$\widetilde{G}_{0S}^{m}$>$_{r,z}$. Panels (d), (h), (l) and (p) show snapshots where the selector, nearby end-caps and silanol groups are shown in space filling representation while 2-propanol is shown in bright colors for contrast. Panels (a)-(d), (e)-(h), (i)-(l), and (m)-(p) represent the H(12)-O(2-propanol), O(14)-H(2-propanol), H(18)-O(2-propanol), and O(20)-H(2-propanol), respectively.

Fig. 5.8 shows the chirality transfer to 2-propanol when it is near a Whelk-O1 selector. This selector is distinct from DNB-leucine and DNB-phenylglycine in many ways. For the purposes of chirality transfer to solvent, it is important to realize that Whelk-O1 has a cleft-like structure, and that the amide linkage is often parallel to the surface. For DNB-leucine and DNB-phenylglycine, in contrast, the selector backbone is more-or-less perpendicular to the underlying surface. The amide hydrogen, H(26), of Whelk-O1 points toward the cleft region and an H-bonding solvent will necessarily occupy the cleft. The cylindircal coordinates r and z are in Å, $<G^{1}_{0S}(\mathrm{m=3,n=1})>_{\mathrm{r,z}}$ is in Å, and $<G^{m}_{0S}(\mathrm{m=3,n=2})>_{\mathrm{r,z}}$ is in $\mathrm{g^4/(mol^4 \bullet Å^{\,2})}$.

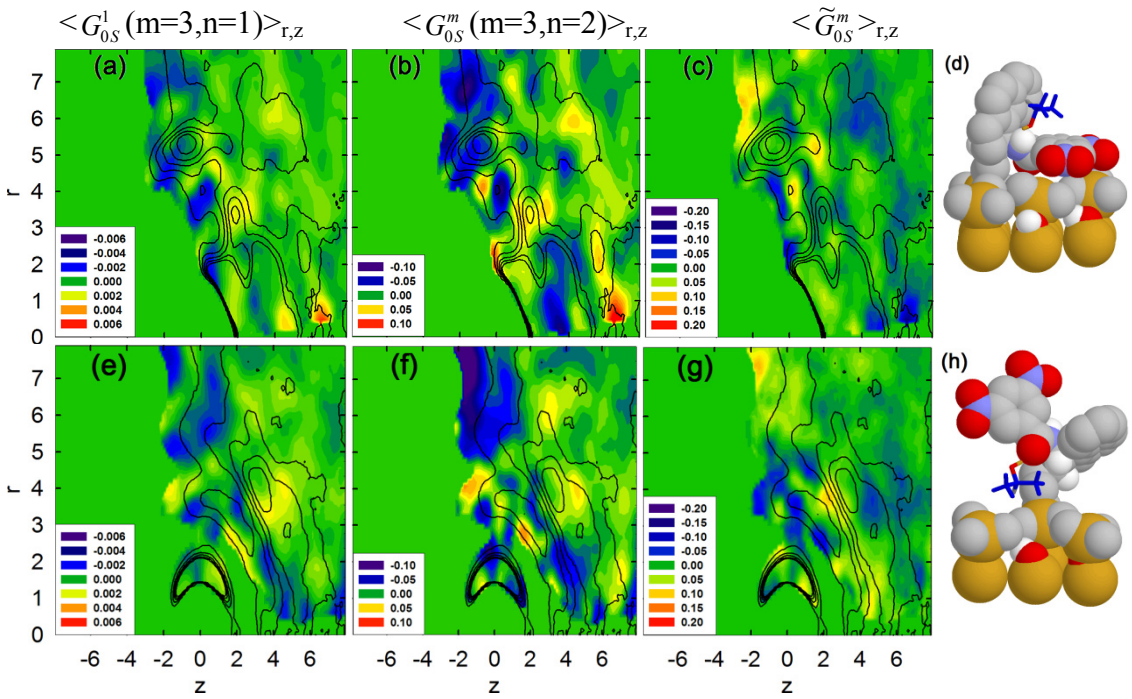

Figure 5.8. 2D distributions of average chirality indexes from the 2-propanol/*n*-hexane solvated Whelk-O1 interface. Panels (a) and (e) show $<G^{1}_{0S}(\mathrm{m=3,n=1})>_{\mathrm{r,z}}$, panels (b) and (f) show $<G^{m}_{0S}(\mathrm{m=3,n=2})>_{\mathrm{r,z}}$ and panels (c) and (g) show the combined index $<\tilde{G}^{m}_{0S}>_{\mathrm{r,z}}$. Panels (a)-(d) and (e)-(h) represent the H(26)-O(2-propanol) and O(28)-H(2-propanol), respectively. Panels (d) and (h) show snapshots of a hydrogen bonding 2-propanol, with methine and methyl groups in blue for emphasis, near a selector.

Fig. 5.3(a), and the contour plots in Figs. 5.8(a)-(c), reflect that there are multiple solvents in the cleft region: an alcohol that H-bonds to H(26) directly and additional solvent. The snapshot in Fig. 5.8(d) shows a typical solvent H-bonding to H(26), and the excess chiralities in Panels (a) and (b) are weakly positive for this solvent in this region, indicating that the alcohol H prefers to orient towards the methyl on the left (see Fig. 5.1(a)). Other in-the-cleft solvents appear at slightly larger separations from H(26) and the simulations show that the chirality transfer to these solvent molecules is significant and, depending on solvent position, the alcohol hydrogen is oriented away from the methyls. From the perspective of chirality transfer, both in-the-cleft solvents experience a significant but distinct conformational imbalance due to the nearby chiral selector.

Hydrogen bonding to O(28) of Whelk-O1 occurs primarily from the side, as noted previously. Regardless of solvent position, this solvent is not in the cleft region, nor is it typically close to the aromatic regions of the selector. Thus, it is the proximity of the end caps that plays the largest steric role. Consistent with this, the excess chirality varies as a function of the solvent distance from the underlying surface. Panel 5.7(h) shows a typical solvent, and the steric constraints due to the nearby end-caps are evident.

5.3.4 Comparisons between selectors: Solvent polarization

Solvent molecules in the vicinity of a chiral selector will respond by biasing towards certain conformations, as discussed in Section 5.3.3. In addition, the solvent will become polarized as the electrons respond to the local chiral environment. Although our molecular dynamics simulations are classical, the alcohol models are polarizable and parameterized based on molecular response to electric fields. In this section, we examine

average atomic charges, and dipole moments for alcohol in the vicinity of the chiral selectors.

Fig. 5.9 shows simulation results for 2-propanol, in a 2-propanol/*n*-hexane solvent, near a DNB-leucine interface. It is immediately clear from Fig. 5.9 that the atomic charges of the oxygen and hydrogen decrease, along with the dipole moment, for solvent near the selector. Thus proximity to the interface is accompanied by a reduction in solvent polarity. The bulk is primarily *n*-hexane, with occasional clusters of 2-propanol molecules. Within these clusters, alcohol-to-alcohol H-bonding occurs. The shift towards lower polarity at the interface indicates that H-bonding between 2-propanol molecules is more polarizing than the alcohol-DNB-leucine interaction, even when the alcohol H-bonds directly to the selector.

The dipole moment shows more variation with solvent location than the atomic charges. Solvent hydrogen bonded to H(12), for example, has an average oxygen charge of around -0.85 |e| and an average hydrogen charge between 0.45 |e| and 0.50 |e| . In contrast, the dipole moment varies from 2.2 to 2.5 Debye. The variation in the dipole moment reflects conformational changes as well as changes in atomic charges. Unfortunately, this conformational effect can occur in the absence of chirality. For instance, *ab initio* calculations indicate that the gas phase molecular dipole of 2-propanol is 1.67 D when torsion 1 is 180 degrees, but is 1.58 D when this torsion is 60 degrees or 300 degrees. A shift towards the latter angles, without biasing towards either one, will decrease the dipole but not introduce chirality.

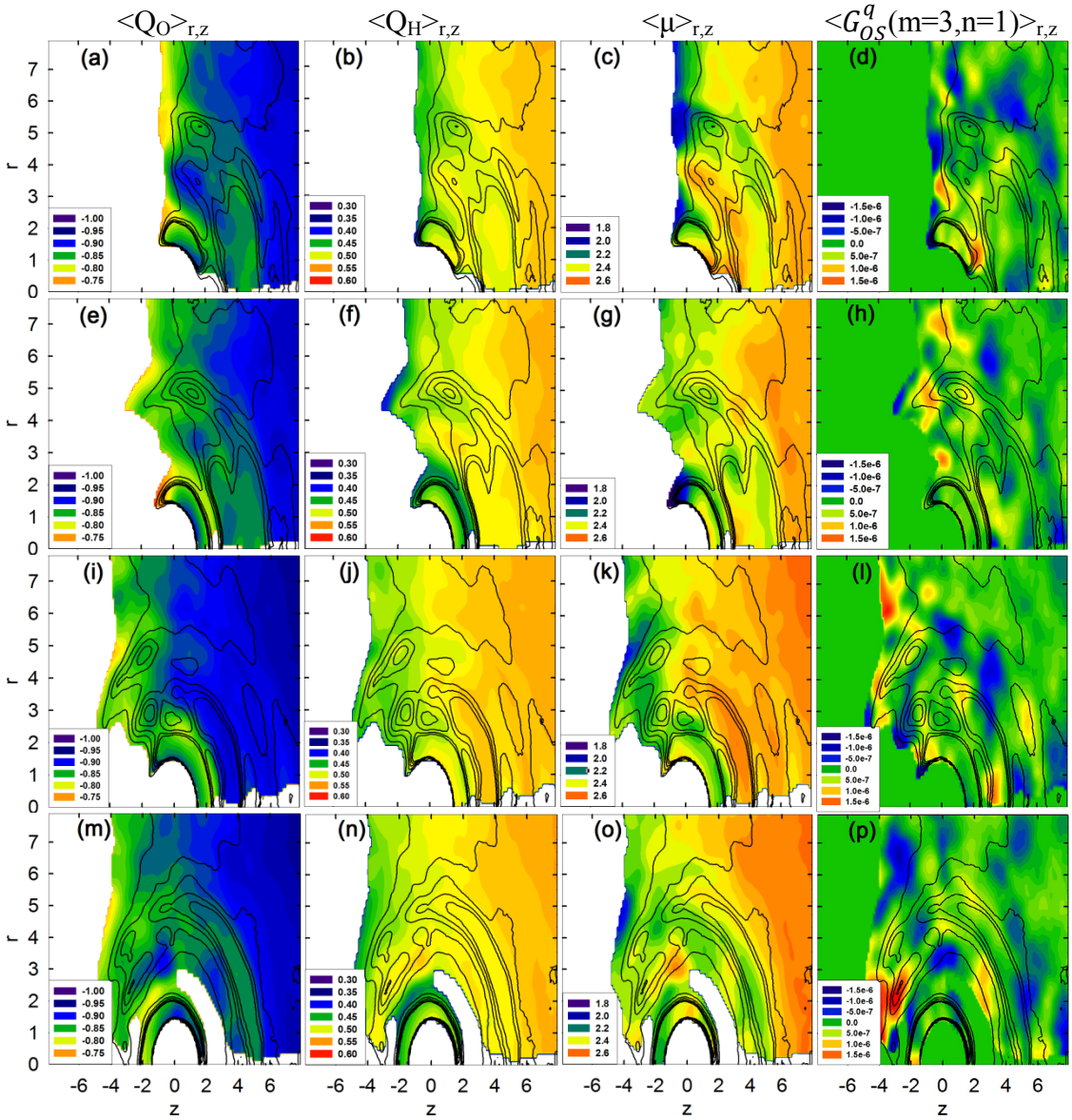

Figure 5.9. Polarization of 2-propanol at the 2-propanol/*n*-hexane solvated DNB-leucine interface. 2D distributions of average charges, dipole moments, and chirality transfer are shown. Panels (a), (e), (i) and (m) represent average atomic charges on O(1), panels (b), (f), (j) and (n) represent average charges for H(2), panels (c), (g), (k) and (o) show average dipole moments in Debye, and panels (d), (h), (l) and (p) represent $<\boldsymbol{G}^{\boldsymbol{q}}_{\boldsymbol{OS}}(m=3,n=1)>_{r,z}$. Panels (a)-(d), (e)-(h), (i)-(l) and (m)-(p) refers to the H(12)-O(2-propanol), O(14)-H(2-propanol), H(18)-O(2-propanol), and O(20)-H(2-propanol) atom pairs, respectively.

To assess chiral polarization, we show $<G_{OS}^{q}(m=3,n=1)>_{r,z}$ in the final column of Fig. 5.9. This chirality index incorporates charge and conformational effects, as does the average dipole, but achiral conformers do not contribute. A closely related index, $<G_{OS}^{1}(m=3,n=1)>_{r,z,}$ was analyzed in Fig. 5.6. We have found that typical charge-dependent indexes strongly depend on the instantaneous charges. Specifically, different combinations of atomic charges lead to very different conformation dependences so that Fig. 5.1(i) and 5.1(j) are expected to change in a nontrivial manner for different charges. However for 2-propanol, different instantaneous atomic charges strongly influence the magnitude of $G_{OS}^{q}(m=3,n=1)$ while leaving the qualitative features reasonably unchanged. We can, as a result, analyze this index in more detail. Both $<G_{OS}^{q}(m=3,n=1)>_{r,z}$ and $<G_{OS}^{1}(m=3,n=1)>_{r,z,}$ have the same instantaneous structural dependence, but the former weights each instantaneous configuration by a combination of atomic charges while the latter gives all atoms an equal weight, regardless of charge. Comparing the first column in Fig. 5.6 with the last column in Fig. 5.9, both indexes show similar positional dependence, except that the charge dependent index typically has opposite sign to $<G_{OS}^{1}(m=3,n=1)>_{r,z}$. Several conclusions can be drawn from the overall correlation between these two chirality indexes. First, regions of small-to-negligible chirality transfer are truly indicative of an absence of excess chirality in the solvent, and inclusion of atomic charge fluctuations does not introduce new features: Both the charges and the structure indicate that the solvent at these positions is, on average, achiral. Second, the correlations between $<G_{OS}^{q}(m=3,n=1)>_{r,z}$ and $<G_{OS}^{1}(m=3,n=1)>_{r,z}$ suggest that the largest contributor to the chirality transfer from DNB-leucine to 2-propanol, in a binary 2-propanol/*n*-hexane solvent, is the introduction of configurational chirality.

$<G_{OS}^{q}(m=3,n=1)>_{r,z}$ includes contributions from configurations and charge distributions. The similarity between $<G_{OS}^{q}(m=3,n=1)>_{r,z}$ and $<G_{OS}^{1}(m=3,n=1)>_{r,z}$ shows that the charge distributions have a secondary impact in this case.

Although Fig. 5.9 shows the polarization induced in 2-propanol due to a nearby DNB-leucine interface, very similar changes in the solvent are observed for a DNB-phenylglycine interface. Similar conclusions also follow from an analysis of the polarization induced by the Whelk-O1 selector. However, it is interesting to note that, for in-the-cleft solvents, the solvent that H-bonds to H(26) has reduced atomic charges and dipole moment. In contrast, other in-the-cleft solvents have charges and dipole moments consistent with molecules in the bulk.

5.3.5 Comparison of different solvents

In this section, we focus on the changes in excess chirality when the solvent composition changes from pure alcohol to alcohol/alkane. In practice, normal phase chiral separations tend to have varying amounts of alcohol in a predominantly nonpolar (typically *n*-hexane) solvent. The analysis in this section will provide some indication of the changes in the alcohol due to the presence of a co-solvent.

Fig. 5.10 provides several chirality indexes, atomic charges, and the dipole moment for alcohol in the vicinity of the amide hydrogen, H(26), of Whelk-O1. Four solvent environments are compared and the trends are representative of those observed for the other CSPs. The spatial extent of the excess chirality is evident from the panels in Fig. 5.10. First, chirality transfer to the alcohol is larger and persists further into the bulk in an alcohol/alkane solvent than in a pure alcohol solvent. Both solvent environments

are fundamentally different and, from our results, the extensive hydrogen bonding network in a 100% alcohol solvent diminishes the selector-to-solvent chirality transfer, both in terms of magnitude and extent. In an alcohol/alkane solvent, the alcohols interact individually with a selector or, at best have one or two nearby alcohols. Thus, the alcohol molecule in this solvent has fewer opportunities to form H-bonds and this increases the impact of the chiral selectors at the surface. In general, the range of the chirality transfer into 2-propanol/*n*-hexane is larger than for ethanol/*n*-hexane: 2-propanol is larger and will be more susceptible to sterically induced chirality transfer from the selector.

The absence of an alkane co-solvent may also impact the details of the chirality transfer. This in not particularly evident for H(26) of Whelk-O1 but, for DNB-leucine and DNB-phenylglycine, the excess chirality may change signs in certain regions around the selector. For example, when ethanol H-bonds to the upper amide oxygen, O(20), of DNB-leucine, the chirality transfer is weakly positive for an ethanol/*n*-hexane solvent but negative in a pure ethanol solvent.

Panels 5.10(e) and 5.10(i) show that the charge on oxygen and on hydrogen are smaller in magnitude for solvent near the surface and that the decrease is reasonably systematic. This is particularly true for pure alcohol, as evident from the strong *z* dependence of the charges shown in panels (f), (h),(j), and (l). This decrease in charge occurs regardless of the solvent environment and, overall, the atomic charges are roughly 10-15% smaller near the surface, relative to the bulk. As expected, the dipole moment also decreases but by a somewhat larger 15-25%. As noted in Section 5.3.3, this contribution does not necessarily result from chirality and this is clear when the relatively featureless $<G_{OS}^{q}(m=3,n=1)>_{r,z}$ is examined for the pure alcohols (Panels (n) and (p)).

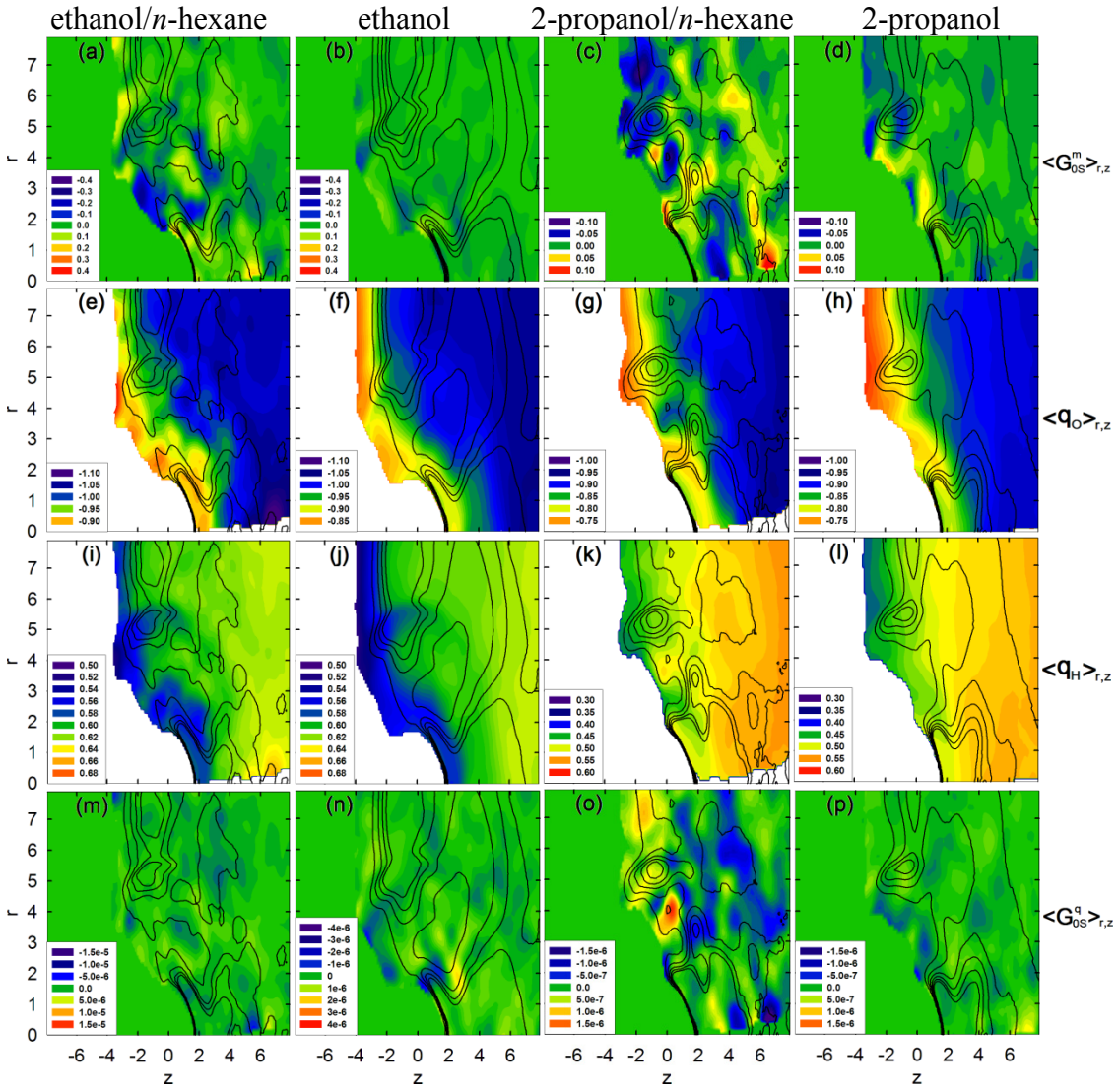

Figure 5.10. 2D distributions of charges and average chirality indexes from the ethanol/*n*-hexane, ethanol, 2-propanol/*n*-hexane and 2-propanol solvated Whelk-O1 interface. Only the H(26)-O(alcohol) is shown. Panels (a), (e), (i) and (m) show ethanol/*n*-hexane, panels (b), (f), (j) and (n) show ethanol, panels (c), (g), (k), and (o) show 2-propanol/*n*-hexane, and panels (d), (h), (l) and (p) show 2-propanol. Panels (a)-(d), (e)-(h), (i)-(l), and (m)-(p) represent $<\boldsymbol{G}_{0S}^{m}$ (m=3,n=2)$>_{r,z}$, $<q_O>_{r,z}$, $<q_H>_{r,z}$, and $<\boldsymbol{G}_{0S}^{q}$(m=3,n=1)$>_{r,z}$, respectively.

5.4. Conclusions

In this chapter, the impact of a nearby chiral surface on solvent is explored. Emphasis is placed on evaluating the extent and characteristics of chirality transferred from the surface to the solvent. The spatial characteristics of this chirality transfer, and its dependence on the nature of the surface and solvent are examined in detail. Molecular dynamics simulations of the solvated chiral interfaces form the basis of the analysis. The chirality induced in the solvent is assessed based on a broad series of related chirality indexes, and combinations of indexes are also employed to isolate specific contributions, such as individual torsions. Three surfaces, employed in chiral chromatography, are considered: The Whelk-O1 interface; a phenylglycine-derived CSP; and a leucine-derived CSP. The solvents consist of ethanol, a binary *n*-hexane/ethanol solvent, 2-propanol, and a binary *n*-hexane/2-propanol solvent. Our results show that chirality transfer is significantly larger at an interface, relative to the transfers observed for chiral solutes in Chapter 4.

The excess chirality is divided into two contributions, a conformational chirality and a polarization contribution. Strictly speaking, these two factors are interrelated and cannot be fully separated. However, with the use of appropriate chirality indexes, we can emphasize the individual contributions. Our simulations reveal that solvents H-bonded to the selectors have reduced atomic charges and reduced dipole moments. While the latter is interesting, it does not necessarily follow from a selector-to-solvent chirality transfer: conformational changes can alter the dipole but a conformational bias is required for

chirality transfer. Chirality indexes suggest that conformational chirality is dominant at these interfaces, with solvent polarization having a smaller secondary effect.

A detailed analysis of conformational chirality reveals that the chirality transfer is largest when the solvent experiences steric constraints or, alternatively, when the solvent forms multiple interactions with the selector. The latter occurs via multiple hydrogen bonds or CH-π interactions. In the absence of these constraints, the chirality transfer is small, as exemplified by the minimal chirality transferred to 2-propanol when it H-bonds to a carbonyl oxygen of DNB-leucine or DNB-phenylglycine. We find that the excess chirality is attributable to local factors and that collective effects, due to the chiral field of multiple selectors, appear to be minimal.

Chirality transfer is more significant and persists to larger distances away from the selector in an alcohol/alkane solvent relative to a pure alcohol solvent. In addition, the spatial range over which the chirality transfer is significant is typically larger for 2-propanol than for ethanol, due mostly to additional steric constraints for the former.

Chapter 6
Conclusions

The main objective of this thesis is to examine chirality transfer from chiral solutes and surfaces to achiral solvents. *Ab initio* calculations are applied to develop polarizable models and intramolecular potentials for solvents and solutes, and MD simulations are used to study the induced chirality in achiral solvents. Five solvents (ethanol, 2-propanol, benzyl-alcohol, ethanol/*n*-hexane, and 2-propanol/*n*-hexane), three solutes (PAMD, acenaphthenol and styrene oxide) and three chiral surface selectors (Whelk-O1, DNB-phenylglycine and DNB-leucine) are the focus of this study.

The methodology for developing a new polarizable and flexible model (the fCINTRA model) is discussed in Chapter 3. In this methodology, the direct coupling between polarization and intramolecular motion, such as bends and torsions, is novel. The methodology integrates the FC method, field-dependent intramolecular potentials, new equations of motion, damping functions for outside-of-range fields, and a reversible multiple time step algorithm. The development of the field-dependent intramolecular potentials of the fCINTRA model relies heavily on extensive *ab initio* calculations that generate information on the molecule's responses to various external electrostatic fields. This methodology has been applied to ethanol as a test case.

MD simulations of bulk ethanol using the fCINTRA model are performed and the physical properties, such as the self-diffusion coefficient, are assessed to evaluate the quality of the model. Comparisons with other models show that the average dipole moment of liquid ethanol predicted by the fCINTRA model is in closest agreement with

experiments and *ab initio* simulation results. The dielectric constant, interatomic distributions and the enthalpy of vaporization are also in close agreement with experiments. Self-diffusion is overestimated by the fCINTRA model, but it has been found that the diffusion coefficient is highly sensitive to the fictitious charge mass and further improvements could be made by reducing the mass. H-bonding analysis with the fCINTRA model predicts longer chains of H-bonded molecules and fewer isolated molecules. In all, the fCINTRA model has many advantages over non-polarizable models and other existing polarizable models, and is a feasible alternative to *ab initio* simulations.

Further development of this model can be made in several aspects. First of all, the computation costs can be decreased. In fCINTRA model, the most time-consuming part in simulations is the evaluation of the electrostatic field derivatives, and thus, any improvement in the EWALD summation algorithm can significantly speed up the computation. For instance, the use of particle-mesh Ewald, which is a faster alternative to EWALD, could greatly reduce the computation time. Second, the model parameters can be refined by reiterating the parameterization process. As shown in Fig. 3.1, the model parameters are developed from the electrostatic fields that are collected in original MD simulations with a non-polarizable model. Since the electrostatic fields are sensitive to models, molecules sometimes experience fields that are outside of the parameterization range in simulations, and a damping function is required to deal with some extreme cases. In order to improve this, the model parameters can be further refined from the electrostatic fields collected from the MD simulations with the fCINTRA model. Ideally, this procedure can be iterated for many times until the electrostatic fields are fully

converged, but it will be a very time consuming process. As described in the previous chapters, the fCINTRA model is able to treat molecules in significantly differing environments, and thus, it can be very useful when applied to biological systems, such as membranes. For instance, when a compound goes across lipid bilayers, it passes through both hydrophobic and hydrophilic regions. The fCINTRA model can correctly describe the behavior of the compound in different environments and can help to uncover some important mechanisms in the process.

In Chapters 4 and 5, the fCINTRA model and other models are used in MD simulations to study chirality transfer from chiral solutes and surfaces to achiral solvents. Chapter 4 focuses on two solvents (ethanol and benzyl alcohol) and three solutes (PAMD, styrene oxide and acenaphthenol). Detailed aspects such as the importance of solvent polarizability and solute flexibility, hydrogen-bonding network, and the solvent-solute interactions have been discussed. In our study, chirality transfer is found to be the most evident at H-bonding sites of chiral solutes, and depends heavily on the positions of the solvents relative to the chiral solute. As expected, solvent polarization is found to be important, and non-polarizable models tend to underestimate the transfer. It is also found that the transfer is the most obvious within the first few solvation shells about the chiral solute.

In Chapter 5, chirality transfer is discussed for chiral surfaces that are used in chiral chromatography, such as Whelk-O1, leucine- and phenylglycine-based CSPs. Four solvents are studied: Pure ethanol, pure 2-propanol, n-hexane/ethanol and n-hexane/2-propanol. Comparing to the solute-solvent chirality transfer, the transfer at interfaces is significantly larger. An in-depth analysis shows that the chirality transfer is a result of

multiple interactions, including H-bonds and CH-π interactions, and steric constrains between the solvents and solutes. The chirality transfer in 2-propanol is found to be larger than in ethanol because of the additional steric constraints for 2-propanol.

The results of chirality transfer analysis can be used to design chiral molecules with different abilities to transfer chirality. For instance, one may wish to find solutes with very localized regions of high chirality transfer or those that transfer chirality over a longer distance.

In complementary to the results in this thesis, *ab initio* studies will be helpful to further investigate the chirality transfer. The interactions between solvent and solute or surface selector can be analyzed in *ab initio* studies, which can give more details on the mechanism and origin of the chirality transfer. For instance, solvent molecules can be placed around a solute molecule and *ab initio* calculations can be used to get the most stable solvent structures in different positions. Further analysis can be focused on the places where the most stable solvent structures are chiral. Because the interactions are relatively weak, high level functionals, such as CCSD(T), and large basis sets, such as aug-cc-pVTZ, will be required to get accurate results.

The study of chirality transfer can be further applied to many areas. It is widely known that in chiral chromatography, the solvent has a strong impact on the separation. With different solvents, the separation factors of the same enantiomers in the same column can differ dramatically, and sometimes even the elution orders are switched. Most of the current studies in this field focus on the direct solvent effects on average structures of analytes, and the influence of the induced chirality within solvents near

surfaces is often neglected. If the induced chirality is evident in solvents near selection sites of chiral surfaces, the analytes will be surrounded by an environment of chiral solvents when interacting with selectors, and thus, the solute-selector interactions and the outcome of the chiral separation will be affected. Therefore, the chirality transfer in solvents can be an important factor in the mechanism of chiral chromatography. The chirality transfer can also be of great importance in spectroscopy. The current theoretical calculations of spectra, such as CD and ORD, are not accurate enough when compared to experiments. In the calculation of these spectra, emphasis has been placed on the direct contributions from chiral solutes and solvent effects on the average structures of solutes. Recently, asymmetric solvation shell of solvent molecules around solutes has also been studied and its effects on spectra have been found to be significant in some cases. However, the solvent molecules are always regarded as internally achiral and no direct contributions to the spectra. From our studies, it can be seen that the chirality transfer can turn achiral solvents into intrinsically chiral and thus can directly affect the spectra. The inclusion of this contribution in theoretical calculations of spectra can be a future direction.

Bibliography

[1] Kelvin, W. T., *Baltimore Lectures on Molecular Dynamics and the Wave Theory of Light*. Clay, C. J.: London, 1904.

[2] Davankov, V. A., *Pure and Applied Chemistry* **1997,** 69, (7), 1469-1474.

[3] Hornok, L., *Cultivation and Processing of Medicinal Plants*. John Wiley & Sons: Chichester,UK, 1992.

[4] Friedman, L.; Miller, J. G., *Science* **1971,** 172, (3987), 1044.

[5] Brenna, E.; Fuganti, C.; Serra, S., *Tetrahedron-Asymmetry* **2003,** 14, (1), 1-42.

[6] Blaschke, G.; Kraft, H. P.; Fickentscher, K.; Kohler, F., *Arzneimittel-Forschung/Drug Research* **1979,** 29-2, (10), 1640-1642.

[7] FDA POLICY STATEMENT FOR THE DEVELOPMENT OF NEW STEREOISOMERIC DRUGS. *Chirality* **1992,** 4, (5), 338-340.

[8] Laird, T., *Chemistry & Industry* **1989**, (12), 366-367.

[9] Stinson, S. C., *Chemical & Engineering News* **2000,** 78, (43), 55.

[10] Thayer, A. M., *Chemical & Engineering News* **2007,** 85, (32), 11-19.

[11] Ager, D. J., *Handbook of chiral chemicals*. 2 ed.; CRC Press: Boca Raton, FL, 2006.

[12] Ahuja, S., *Chiral separations by chromatography*. Oxford University Press: Washington, D.C., 2000.

[13] Karlsson, A.; Pettersson, C., *Journal of Chromatography* **1991,** 543, (2), 287-297.

[14] Pettersson, C.; Karlsson, A.; Gioeli, C., *Journal of Chromatography* **1987,** 407, 217-229.

[15] Berthod, A., *Analytical Chemistry* **2006,** 78, (7), 2093-2099.

[16] Boulton, C. J.; Finden, J. G.; Yuh, E.; Sutherland, J. J.; Wand, M. D.; Wu, G.; Lemieux, R. P., *Journal of the American Chemical Society* **2005,** 127, (39), 13656-13665.

[17] Celebre, G.; De Luca, G.; Maiorino, M.; Iemma, F.; Ferrarini, A.; Pieraccini, S.; Spada, G. P., *Journal of the American Chemical Society* **2005,** 127, (33), 11736-11744.

[18] Eelkema, R.; Feringa, B. L., *Organic & Biomolecular Chemistry* **2006,** 4, (20), 3729-3745.

[19] Gottarelli, G.; Hibert, M.; Samori, B.; Solladie, G.; Spada, G. P.; Zimmermann, R., *Journal of the American Chemical Society* **1983,** 105, (25), 7318-7321.

[20] Gottarelli, G.; Osipov, M. A.; Spada, G. P., *Journal of Physical Chemistry* **1991,** 95, (9), 3879-3884.

[21] Gottarelli, G.; Spada, G. P.; Bartsch, R.; Solladie, G.; Zimmermann, R., *Journal of Organic Chemistry* **1986,** 51, (5), 589-592.

[22] Lemieux, R. P., *Accounts of Chemical Research* **2001,** 34, (11), 845-853.

[23] Todd, S. M.; Ferrarini, A.; Moro, G. J., *Physical Chemistry Chemical Physics* **2001,** 3, (24), 5535-5541.

[24] Kumata, Y.; Furukawa, J.; Fueno, T., *Bulletin of the Chemical Society of Japan* **1970,** 43, (12), 3920-3921.

[25] Fischer, A. T.; Compton, R. N.; Pagni, R. M., Amer Chemical Soc: 2006; 7067-7071.

[26] Yashima, E.; Yamada, M.; Okamoto, Y., *Chemistry Letters* **1994**, (3), 579-582.

[27] Jennings, W. B., *Chemical Reviews* **1975,** 75, (3), 307-322.

[28] Losada, M.; Xu, Y. J., *Physical Chemistry Chemical Physics* **2007,** 9, (24), 3127-3135.

[29] Mukhopadhyay, P.; Zuber, G.; Wipf, P.; Beratan, D. N.; Ch, *Angewandte Chemie-International Edition* **2007,** 46, (34), 6450-6452.

[30] Mukhopadhyay, P.; Zuber, G.; Goldsmith, M. R.; Wipf, P.; Beratan, D. N., *Chemphyschem* **2006,** 7, (12), 2483-2486.

[31] Fidler, J.; Rodger, P. M.; Rodger, A., *Journal of the Chemical Society-Perkin Transactions 2* **1993**, (2), 235-241.

[32] Davankov, V. A., *Chirality* **1997,** 9, (2), 99-102.

[33] Easson, L. H.; Stedman, E., *Biochemical Journal* **1933,** 27, 1257-1266.

[34] Lindner, W., *Mikrochimica Acta* **1991,** 2, (1-6), 113-128.

[35] Mesecar, A. D.; Koshland, D. E., *Nature* **2000,** 403, (6770), 614-615.

[36] Ogston, A. G., *Nature* **1948,** 162, (4129), 963-963.

[37] Pirkle, W. H.; Pochapsky, T. C., *Chemical Reviews* **1989,** 89, (2), 347-362.

[38] Topiol, S.; Sabio, M., *Journal of the American Chemical Society* **1989,** 111, (11), 4109-4110.

[39] Mackerell, A. D., *Journal of Computational Chemistry* **2004,** 25, (13), 1584-1604.

[40] Allen, M. P.; Tildesley, D. J., *Computer Simulation of Liquids*. 1 ed.; Oxford University Press: New York, 1987.

[41] Shirts, M. R.; Pitera, J. W.; Swope, W. C.; Pande, V. S., *Journal of Chemical Physics* **2003,** 119, (11), 5740-5761.

[42] Lamoureux, G.; MacKerell, A. D.; Roux, B., *Journal of Chemical Physics* **2003,** 119, (10), 5185-5197.

[43] Gao, J. L.; Habibollazadeh, D.; Shao, L., *Journal of Physical Chemistry* **1995,** 99, (44), 16460-16467.

[44] Lamoureux, G.; Roux, B., *Journal of Chemical Physics* **2003,** 119, (6), 3025-3039.

[45] Noskov, S. Y.; Lamoureux, G.; Roux, B., *Journal of Physical Chemistry B* **2005,** 109, (14), 6705-6713.

[46] Rick, S. W.; Stuart, S. J.; Berne, B. J., *Journal of Chemical Physics* **1994,** 101, (7), 6141-6156.

[47] Svishchev, I. M.; Kusalik, P. G.; Wang, J.; Boyd, R. J., *Journal of Chemical Physics* **1996,** 105, (11), 4742-4750.

[48] Anisimov, V. M.; Vorobyov, I. V.; Roux, B.; MacKerell, A. D., *Journal of Chemical Theory and Computation* **2007,** 3, (6), 1927-1946.

[49] Drude, P., *The Theory of Optics*. Longmans: Green, New York, 1902.

[50] Rappe, A. K.; Goddard, W. A., *Journal of Physical Chemistry* **1991,** 95, (8), 3358-3363.

[51] Ando, K., *Journal of Chemical Physics* **2001,** 115, (11), 5228-5237.

[52] Krishnan, M.; Verma, A.; Balasubramanian, S., *Proceedings of the Indian Academy of Sciences-Chemical Sciences* **2001,** 113, (5-6), 579-590.

[53] Patel, S.; Brooks, C. L., *Journal of Computational Chemistry* **2004,** 25, (1), 1-15.

[54] Patel, S.; Brooks, C. L. In *Fluctuating charge force fields: Recent developments and applications from small molecules to macromolecular biological systems*, 2006; Taylor & Francis Ltd: 2006; 231-249.

[55] Patel, S.; Mackerell, A. D.; Brooks, C. L., *Journal of Computational Chemistry* **2004,** 25, (12), 1504-1514.

[56] Olano, L. R.; Rick, S. W., *Journal of Computational Chemistry* **2005,** 26, (7), 699-707.

[57] Cicu, P.; Demontis, P.; Spanu, S.; Suffritti, G. B.; Tilocca, A., *Journal of Chemical Physics* **2000,** 112, (19), 8267-8278.

[58] Balasubramanian, D.; Kumar, C., *Applied Spectroscopy Reviews* **1976,** 11, (2), 223-286.

[59] Martin, S. R.; Schilstra, M. J., In *Biophysical Tools for Biologists: Vol 1 in Vitro Techniques*, 2008; Vol. 84, 263-293.

[60] Stephens, P. J.; Devlin, F. J.; Pan, J. J., *Chirality* **2008,** 20, (5), 643-663.

[61] Hassey, R.; Swain, E. J.; Hammer, N. I.; Venkataraman, D.; Barnes, M. D., *Science* **2006,** 314, (5804), 1437-1439.

[62] Buda, A. B.; Derheyde, T. A.; Mislow, K., *Angewandte Chemie-International Edition in English* **1992,** 31, (8), 989-1007.

[63] Jonas, J., *Chemicke Listy* **2001,** 95, (6), 342-343.

[64] Andelman, D.; Orland, H., *Journal of the American Chemical Society* **1993,** 115, (26), 12322-12329.

[65] Harris, A. B.; Kamien, R. D.; Lubensky, T. C., *Physical Review Letters* **1997,** 78, (8), 1476-1479.

[66] Osipov, M. A.; Pickup, B. T.; Dunmur, D. A., *Molecular Physics* **1995,** 84, (6), 1193-1206.

[67] Weinberg, N.; Mislow, K., *Journal of Mathematical Chemistry* **1995,** 17, (1), 35-53.

[68] Buda, A. B.; Heyde, T.; Mislow, K., *Journal of Mathematical Chemistry* **1991,** 6, (3), 243-253.

[69] Buda, A. B.; Mislow, K., *Journal of Molecular Structure (Theochem)* **1991,** 232, 1-12.

[70] Guye, P., *C. R. Hebd. Seances Acad. Sci.* **1890,** 110, 714.

[71] Murrayrust, P.; Burgi, H. B.; Dunitz, J. D., *Acta Crystallographica Section B-Structural Science* **1978,** 34, 1787-1793.

[72] Murrayrust, P.; Burgi, H. B.; Dunitz, J. D., *Acta Crystallographica Section A* **1979,** 35, (SEP), 703-713.

[73] Kamberaj, H.; Osipov, M. A.; Low, R. J.; Neal, M. P., *Molecular Physics*, **2004**, 102, 431-446.

[74] Neal, M. P.; Solymosi, M.; Wilson, M. R.; Earl, D. J., *Journal of Chemical Physics* **2003,** 119, (6), 3567-3573.

[75] Kamberaj, H.; Low, R. J.; Neal, M. P., *Ferroelectrics*, **2005**, 315, 183-196.

[76] Earl, D. J.; Wilson, M. R., Journal of Chemical Physics, **2003**, 119, 10280-10288.

[77] Kamberaj, H.; Low, R. J.; Neal, M. P., *Molecular Physics*, **2006,** 104, 335-357.

[78] Millar, G.; Weinberg, N.; Mislow, K., *Molecular Physics* **2005,** 103, (20), 2769-2772.

[79] Weinberg, N.; Mislow, K., *Theoretica Chimica Acta* **1997,** 95, (3-4), 63-65.

[80] Weinberg, N.; Mislow, K., *Canadian Journal of Chemistry-Revue Canadienne De Chimie* **2000,** 78, (1), 41-45.

[81] Frenkel, D.; Smit, B., *Understanding molecular simulation : from algorithms to applications*. Academic Press: San Diego, 1996.

[82] Morse, P. M., *Physical Review* **1929,** 34, (1), 57-64.

[83] Andersen, H. C., *Journal of Computational Physics* **1983,** 52, (1), 24-34.

[84] Ryckaert, J. P.; Ciccotti, G.; Berendsen, H. J. C., *Journal of Computational Physics* **1977,** 23, (3), 327-341.

[85] Ryckaert, J. P.; Bellemans, A., *Chemical Physics Letters* **1975,** 30, (1), 123-125.

[86] Politzer, P.; Boyd, S., *Structural Chemistry* **2002,** 13, (2), 105-113.

[87] Karger, N.; Vardag, T.; Ludemann, H. D., *Journal of Chemical Physics* **1990,** 93, (5), 3437-3444.

[88] Born, M.; von Karman, T., *Physikalische Zeitschrift* **1912,** 13, 297-309.

[89] Ewald, P. P., *Annalen Der Physik* **1921,** 64, (3), 253-287.

[90] Yeh, I. C.; Berkowitz, M. L., *Journal of Chemical Physics* **1999,** 111, (7), 3155-3162.

[91] Wang, S. H.; Cann, N. M., *Journal of Chemical Physics* **2007,** 126, 214502.

[92] Verlet, L., *Physical Review* **1967,** 159, (1), 98-&.

[93] Anderson, J. B., *Journal of Chemical Physics* **1980,** 73, (8), 3897-3899.

[94] Woodcock, L. V., *Chemical Physics Letters* **1971,** 10, (3), 257-&.

[95] Nose, S., *Journal of Chemical Physics* **1984,** 81, (1), 511-519.

[96] Hoover, W. G., *Physical Review A* **1985,** 31, (3), 1695-1697.

[97] Tuckerman, M.; Berne, B. J.; Martyna, G. J., *Journal of Chemical Physics* **1992,** 97, (3), 1990-2001.

[98] Trotter, H. F., *Proc. Am. Math. Soc.* **1959,** 10, 545.

[99] Hohenberg, P.; Kohn, W., *Physical Review B* **1964,** 136, (3B), B864-&.

[100] Kohn, W.; Sham, L. J., *Physical Review* **1965,** 140, (4A), 1133-&.

[101] Parr, R. G.; Yang, W., *Density-Functional Theory of Atoms and Molecules*. University Press: Oxford, 1989.

[102] Lee, C. T.; Yang, W. T.; Parr, R. G., *Physical Review B* **1988,** 37, (2), 785-789.

[103] Becke, A. D., *Physical Review A* **1988,** 38, (6), 3098-3100.

[104] Abraham, R. J.; Hudson, B., *Journal of Computational Chemistry* **1985,** 6, (3), 173-181.

[105] Bader, R. F. W., *Chemical Reviews* **1991,** 91, (5), 893-928.

[106] Momany, F. A., *Journal of Physical Chemistry* **1978,** 82, (5), 592-601.

[107] Mortier, W. J.; Ghosh, S. K.; Shankar, S., *Journal of the American Chemical Society* **1986,** 108, (15), 4315-4320.

[108] Mulliken, R. S., *Journal of Chemical Physics* **1955,** 23, (10), 1833-1840.

[109] Weiner, S. J.; Kollman, P. A.; Nguyen, D. T.; Case, D. A., *Journal of Computational Chemistry* **1986,** 7, (2), 230-252.

[110] Breneman, C. M.; Wiberg, K. B., *Journal of Computational Chemistry* **1990,** 11, (3), 361-373.

[111] Solymosi, M.; Low, R. J.; Grayson, M.; Neal, M. P., *Journal of Chemical Physics* **2002,** 116, (22), 9875-9881.

[112] Nita, S.; Cann, N. M., *Journal of Physical Chemistry B* **2008,** 112, (41), 13022-13037.

[113] Zhao, C. F.; Cann, N. M., *Journal of Chromatography A* **2007,** 1149, (2), 197-218.

[114] Nawrocki, J., *Journal of Chromatography A* **1997,** 779, (1-2), 29-71.

[115] Pirkle, W. H.; Welch, C. J., *Journal of Liquid Chromatography* **1992,** 15, (11), 1947-1955.

[116] Szczerba, T., Regis Technologies, Inc., *personal communication* **2004**.

[117] Saiz, L.; Padro, J. A.; Guardia, E., *Journal of Physical Chemistry B* **1997,** 101, (1), 78-86.

[118] Yamaguchi, T.; Benmore, C. J.; Soper, A. K., *Journal of Chemical Physics* **2000,** 112, (20), 8976-8987.

[119] Yamaguchi, Y.; Yasutake, N.; Nagaoka, M., *Journal of Physical Chemistry A* **2002,** 106, (2), 404-410.

[120] Andanson, J. M.; Bopp, P. A.; Soetens, J. C., *Journal of Molecular Liquids* **2006,** 129, (1-2), 101-107.

[121] Sarkar, S.; Joarder, R. N., *Journal of Chemical Physics* **1993,** 99, (3), 2032-2039.

[122] Sarkar, S.; Joarder, R. N., *Journal of Chemical Physics* **1994,** 100, (7), 5118-5122.

[123] Benmore, C. J.; Loh, Y. L., *Journal of Chemical Physics* **2000,** 112, (13), 5877-5883.

[124] Narten, A. H.; Habenschuss, A., *Journal of Chemical Physics* **1984,** 80, (7), 3387-3391.

[125] Montague, D. G.; Gibson, I. P.; Dore, J. C., *Molecular Physics* **1982,** 47, (6), 1405-1416.

[126] Gonzalez, M. A.; Enciso, E.; Bermejo, F. J.; Bee, M., *Journal of Chemical Physics* **1999,** 110, (16), 8045-8059.

[127] Jorgensen, W. L., *Journal of Physical Chemistry* **1986,** 90, (7), 1276-1284.

[128] Berendsen, H. J. C.; Postma, J. P. M.; Gunsteren, W. F. v.; Hermans, J., *In Intermolecular Forces*. Dordrecht: Reidel, 1981; p 331.

[129] Berendsen, H. J. C.; Grigera, J. R.; Straatsma, T. P., *Journal of Physical Chemistry* **1987,** 91, (24), 6269-6271.

[130] Rullmann, J. A. C.; Vanduijnen, P. T., *Molecular Physics* **1988,** 63, (3), 451-475.

[131] Banks, J. L.; Kaminski, G. A.; Zhou, R. H.; Mainz, D. T.; Berne, B. J.; Friesner, R. A., *Journal of Chemical Physics* **1999,** 110, (2), 741-754.

[132] Kindt, J. T.; Schmuttenmaer, C. A., Amer Chemical Soc: 1996; 10373-10379.

[133] Wilhoit, R. C.; Zwolinski, B. J., *J. Phys. Chem. Ref. Data, Suppl.* **1973,** 2, 2.

[134] Chen, B.; Potoff, J. J.; Siepmann, J. I., *Journal of Physical Chemistry B* **2001,** 105, (15), 3093-3104.

[135] Gaussian 03, Revision B.04, M. J. Frisch, G. W. Trucks, H. B. Schlegel, G. E. Scuseria, M. A. Robb, J. R. Cheeseman, J. A. Montgomery, Jr., T. Vreven, K. N. Kudin, J. C. Burant, J. M. Millam, S. S. Iyengar, J. Tomasi, V. Barone, B. Mennucci, M. Cossi, G. Scalmani, N. Rega, G. A. Petersson, H. Nakatsuji, M. Hada, M. Ehara, K. Toyota, R. Fukuda, J. Hasegawa, M. Ishida, T. Nakajima, Y. Honda, O. Kitao, H. Nakai, M. Klene, X. Li, J. E. Knox, H. P. Hratchian, J. B. Cross, C. Adamo, J. Jaramillo, R. Gomperts, R. E. Stratmann, O. Yazyev, A. J. Austin, R. Cammi, C. Pomelli, J. W. Ochterski, P. Y. Ayala, K. Morokuma, G. A. Voth, P. Salvador, J. J. Dannenberg, V. G. Zakrzewski, S. Dapprich, A. D. Daniels, M. C. Strain, O. Farkas, D. K. Malick, A. D. Rabuck, K. Raghavachari, J. B. Foresman, J. V. Ortiz, Q. Cui, A. G. Baboul, S. Clifford, J. Cioslowski, B. B. Stefanov, G. Liu, A. Liashenko, P. Piskorz, I. Komaromi, R. L. Martin, D. J. Fox, T. Keith, M. A. Al-Laham, C. Y. Peng, A. Nanayakkara, M. Challacombe, P. M. W. Gill, B. Johnson, W. Chen, M. W. Wong, C. Gonzalez, and J. A. Pople, Gaussian, Inc., Pittsburgh PA, 2003.

[136] Moller, C.; Plesset, M. S., *Physical Review* **1934,** 46, (7), 0618-0622.

[137] Dunning, T. H., *Journal of Chemical Physics* **1989,** 90, (2), 1007-1023.

[138] Kendall, R. A.; Dunning, T. H.; Harrison, R. J., *Journal of Chemical Physics* **1992,** 96, (9), 6796-6806.

[139] Clark, T.; Chandrasekhar, J.; Spitznagel, G. W.; Schleyer, P. V., *Journal of Computational Chemistry* **1983,** 4, (3), 294-301.

[140] Frisch, M. J.; Pople, J. A.; Binkley, J. S., *Journal of Chemical Physics* **1984,** 80, (7), 3265-3269.

[141] Becke, A. D., *Journal of Chemical Physics* **1993,** 98, (7), 5648-5652.

[142] Hamprecht, F. A.; Cohen, A. J.; Tozer, D. J.; Handy, N. C., *Journal of Chemical Physics* **1998,** 109, (15), 6264-6271.

[143] Wilson, P. J.; Bradley, T. J.; Tozer, D. J., *Journal of Chemical Physics* **2001,** 115, (20), 9233-9242.

[144] Perdew, J. P.; Burke, K.; Ernzerhof, M., *Physical Review Letters* **1996,** 77, (18), 3865-3868.

[145] Kaye, G. W. C.; Laby, T. H., *Tables of Physical and Chemical Constants*. Longmans: Harlow,Essex,Great Britain, 1995.

[146] Berardi, R.; Cainelli, G.; Galletti, P.; Giacomini, D.; Gualandi, A.; Muccioli, L.; Zannoni, C., *Journal of the American Chemical Society* **2005,** 127, (30), 10699-10706.

[147] Nita, S.; Cann, N. M.; Horton, J. H., *Journal of Physical Chemistry B* **2004,** 108, (11), 3512-3522.

[148] Cressman, E.; Das, B.; Dunford, J.; Ghenea, R.; Huh, Y.; Nita, S.; Paci, I.; Zhao, C.; Wang, S.; Cann, N. M., *unpublished MCMD program*.

[149] Neumann, M.; Steinhauser, O., *Chemical Physics Letters* **1984,** 106, (6), 563-569.

[150] Buckingham, A. D., *Proceedings of the Royal Society of London Series a-Mathematical and Physical Sciences* **1956,** 238, (1213), 235-244.

[151] Nesterenko, P. N.; Krotov, V. V.; Staroverov, *Journal of Chromatography A* **1994,** 667, (1-2), 19-28.

[152] Pirkle, W. H.; Welch, C. J.; Hyun, M. H., *Journal of Organic Chemistry* **1983,** 48, (25), 5022-5026.

[153] Vidyasankar, S.; Ru, M.; Arnold, F. H., *Journal of Chromatography A* **1997,** 775, (1-2), 51-63.

[154] Copeland, R. A., *Enzymes : a practical introduction to structure, mechanism, and data analysis*. 2nd ed.; John Wiley: New York, 2000; p 149-150.

[155] Fersht, A., *Structure and mechanism in protein science : a guide to enzyme catalysis and protein folding*. W. H. Freeman: New York, 1999; p 248-249.

[156] Jorgensen, W. L.; Maxwell, D. S.; TiradoRives, J., *Journal of the American Chemical Society* **1996,** 118, (45), 11225-11236.

[157] Shukla, P.; Muthukumar, M.; Langley, K. H., *Journal of Applied Polymer Science* **1992,** 44, (12), 2115-2125.

[158] Riddick, J. A.; Bunger, W. B.; Sakano, T. K., *Organic solvents : physical properties and methods of purification*. 4 ed.; Wiley-Interscience: New York, 1986.

[159] Applequi.J; Carl, J. R.; Fung, K. K., *Journal of the American Chemical Society* **1972,** 94, (9), 2952-&.

[160] Vogel, A. I., *Journal of the Chemical Society* **1948**, (NOV), 1814-1819.

[161] Zhao, C. F.; Cann, N. M., *Analytical Chemistry* **2008,** 80, (7), 2426-2438.

[162] Lide, D. R., *CRC Handbook of Chemistry and Physics*. 84 ed.; CRC Press LLC: Boca Raton, Florida, 2003.

[163] Katsonis, N.; Lacaze, E.; Feringa, B. L., Journal of Materials Chemistry **2008**. 18, 2065-2073.

[164] Dungelova, J.; Lehotay, J.; Cizmarik, J.; Armstrong, D. W., *Journal of Liquid Chromatography & Related Technologies* **2003,** 26, (14), 2331-2350.

[165] Pirkle, W. H.; Brice, L. J.; Terfloth, G. J., *Journal of Chromatography A* **1996,** 753, (1), 109-119.

[166] Pirkle, W. H.; Welch, C. J., *Tetrahedron-Asymmetry* **1994,** 5, (5), 777-780.

[167] Berthod, A.; Jin, H. L.; Stalcup, A. M.; Armstrong, D. W., *Chirality* **1990,** 2, (1), 38-42.

[168] Pirkle, W. H.; House, D. W.; Finn, J. M., *Journal of Chromatography* **1980,** 192, (1), 143-158.

[169] Pirkle, W. H.; Welch, C. J., *Journal of Organic Chemistry* **1984,** 49, (1), 138-140.

[170] Pirkle, W. H.; Finn, J. M.; Schreiner, J. L.; Hamper, B. C., *Journal of the American Chemical Society* **1981,** 103, (13), 3964-3966.

[171] Persson, B. A.; Andersson, S.; Ec, *Journal of Chromatography A* **2001,** 906, (1-2), 195-203.

[172] Roussel, C.; Vanthuyne, N.; Serradeil-Albalat, M.; Vallejos, J. C., *Journal of Chromatography A* **2003,** 995, (1-2), 79-85.

[173] Roussel, C.; Del Rio, A.; Pierrot-Sanders, J.; Piras, P.; Vanthuyne, N., *Journal of Chromatography A* **2004,** 1037, (1-2), 311-328.

[174] Welch, C. J.; Szczerba, T.; Perrin, S. R., *Journal of Chromatography A* **1997,** 758, (1), 93-98.

[175] Regis Technologies Inc.; www.registech.com.

[176] Zhao, C.; Cann, N. M., *Journal of Chromatography A* **2006,** 1131, (1-2), 110-129.

[177] Kamberaj, H.; Osipov, M. A.; Low, R. J.; Neal, M. P., *Molecular Physics* **2004,** 102, (5), 431-446.

[178] Kamberaj, H.; Low, R. J.; Neal, M. P., *Molecular Physics* **2006,** 104, (3), 335-357.

[179] Kamberaj, H.; Low, R. J.; Neal, M. P., *Ferroelectrics* **2005,** 315, 183-196.

[180] Earl, D. J.; Wilson, M. R., *Journal of Chemical Physics* **2003,** 119, (19), 10280-10288.

[181] Wang, S. H.; Cann, N. M., *Journal of Chemical Physics* **2008,** 129, (5), 054507.

[182] Nita, S.; Horton, J. H.; Cann, N. M., *Journal of Physical Chemistry B* **2006,** 110, (19), 9511-9519.

[183] Fujii, Y.; Okimoto, N.; Hata, M.; Narumi, T.; Yasuoka, K.; Susukita, R.; Suenaga, A.; Futatsugi, N.; Koishi, T.; Furusawa, H.; Kawai, A.; Ebisuzaki, T.; Neya, S.; Hoshino, T., *Journal of Physical Chemistry B* **2003,** 107, (37), 10274-10283.

[184] Laage, D.; Stirnemann, G.; Hynes, J. T., *Journal of Physical Chemistry B* **2009,** 113, (8), 2428-2435.

[185] Luzar, A.; Chandler, D., *Nature* **1996,** 379, (6560), 55-57.

[186] Tsuzuki, S.; Honda, K.; Uchimaru, T.; Mikami, M.; Tanabe, K., *Journal of the American Chemical Society* **2000,** 122, (15), 3746-3753.

[187] Tsuzuki, S.; Honda, K.; Uchimaru, T.; Mikami, M.; Fujii, A., *Journal of Physical Chemistry A* **2006,** 110, (33), 10163-10168.

[188] Natrella, M. G., *Experimental statistics*. U.S. Dept. of Commerce: Washington, 1963.

[189] Ryckaert, J. P.; Bellemans, A., *Faraday Discussions* **1978,** 66, 95-106.

APPENDIX A
Evaluation of charge fluctuation parameters $\tilde{\chi}_i^0$ and ζ_i.

In this appendix, we briefly discuss our methodology for extracting the electronegativities, $\tilde{\chi}_i^0$, and the Slater exponents ζ_i that determine the atomic charge fluctuations and the Coulombic interaction between intramolecular atomic pairs. Patel and Brooks[53] have analyzed the parameterization of the FC model in considerable detail. Our approach differs from theirs in that we adhere to the Coulomb definition of the $J_{ij}(r_{ij})$ (Eq. [2.27]), we impose symmetry constraints and require that certain atoms have the same values for the parameters, and we rely strictly on *ab initio* calculations to define these quantities.

In the absence of an external field, the electrostatic energy of a single N-atom molecule is:

$$U_{\text{intra}}^{el;0} = \sum_{i=1}^{N} E_i(0) + \sum_{i=1}^{N} \tilde{\chi}_i^0 Q_i^0 + \frac{1}{2}\sum_{i=1}^{N}\sum_{j=1}^{N} J_{ij}(r_{ij}^0) Q_i^0 Q_j^0 \qquad \text{[A1]}$$

where the superscript "0" has been added to the charges to indicate that they correspond to zero-field gas phase values. Recall that the Coulomb overlap and J_{ii}^0 are functions of ζ_i, the exponent in the Slater orbital (Eq. [2.28]). The electrostatic energy for the molecule, confined to its zero-field equilibrium geometry, in the presence of an external field is:

$$U_{\text{intra}}^{el} = \sum_{i=1}^{N} E_i(0) + \sum_{i=1}^{N} \tilde{\chi}_i^0 Q_i + \frac{1}{2}\sum_{i=1}^{N}\sum_{j=1}^{N} J_{ij}(r_{ij}^0) Q_i Q_j + \sum_{i=1}^{N} \Phi_i Q_i \qquad \text{[A2]}$$

where Φ_i is the external electrostatic potential at atom *i*, Q_i is the atomic charge in the presence of the field, $J_{ij}(r_{ij}^0)$ is the Coulomb interaction between atoms *i* and *j* at the zero-field equilibrium interatomic separation r_{ij}^0.

At equilibrium, with or without a field, the electrostatic energy should be a minimum with respect to all the atomic charges. Following Patel and Brooks[53], derivatives of [A2] yield

$$\sum_{j=1}^{N} J_{ij}(r_{ij}^0) Q_j = -(\tilde{\chi}_i^0 + \Phi_i) \quad (i=1, N) \qquad \text{[A3]}$$

and

$$\sum_{j=1}^{N} J_{ij}(r_{ij}^0) Q_j^0 = -\tilde{\chi}_i^0 \qquad (i=1, N) \qquad \text{[A4]}$$

is obtained from derivatives of [A1]. Taking the difference of these equations, we obtain an expression for the response due to the external field

$$\sum_{j=1}^{N} J_{ij}(r_{ij}^0) \Delta Q_j = -\Phi_i \qquad (i=1, N) \qquad \text{[A5]}$$

where $\Delta Q_j = Q_j - Q_j^0$ is the change in the partial charge on atom *j* due to the field. Note that Eq. [A5] no longer includes electronegativities, $\tilde{\chi}_i^0$. The parameters ζ_i, which are directly related to $J_{ij}(r_{ij}^0)$, are obtained by solving Eq. [A5]. With the ζ_i in hand, Eq. [A4] can be solved for the $\tilde{\chi}_i^0$. The parameters are listed in Table 3.2.

Consider the extraction of the ζ_i from Eq. [A5]. The solution of Eq. [A5] requires subjecting individual molecules to a range of fields. The number of fields must equal or exceed the number of atoms in the molecule. In this chapter, the molecular response is extracted from *ab initio* calculations as follows: First, the molecule is fixed at its equilibrium zero-field geometry. Second, 30 perturbing fields are generated by placing a dipolar probe at random locations around the molecule (greater than a distance of 2.0 Å from any atom and less than 4.5 Å from all atoms) and the atomic charges are collected from *ab initio* calculations. The CHELPG algorithm[110], where the atomic charges are varied to best reproduce the molecular electrostatic potential at grid points around the molecule, is used for the charges. In principle, the magnitude and direction of the fields can be chosen arbitrarily but, in practice, they should be reflective of typical fields experienced by the molecule. If the number of fields is equal to the number of parameters, then Eq. [A5] is solved directly. However, one usually assesses the response for a larger number of fields, as we do in this case, and a least-squares procedure is required to solve for the parameters.

Parameter determination based directly on Eq. [A5] proceeds by varying the ζ_i, which determine the $J_{ij}(r_{ij}^0)$, to minimize the difference between the approximate atomic fields predicted from Eq. [A5] and the actual fields used in the *ab initio* calculations. This approach is straightforward but suffers from an important drawback: It selects the ζ_i based on predicted fields, rather than predicted atomic charges. However, Eq. [A5] can be inverted to give, in matrix form, $\Delta Q = -J^{-1}\Phi$, which provides a relationship between the $\left(J_{ij}(r_{ij}^0)\right)^{-1}$ and the charge response due to the external field. Then, following

Patel and Brooks[53], we search for the optimal ζ_i parameters by minimizing the residual[21]

$$\sum_{k=1}^{M}\sum_{i=1}^{N}(\sum_{j=1}^{N}J_{ij}(r_{ij}^{0})^{-1}\Phi_{jk}+\Delta Q_{ik})^{2} \qquad \text{[A6]}$$

where M is the number of perturbations (which is 30 in this case), N is the number of atoms in the molecule, ΔQ_{ik} is the change in the partial charge on atom *k* due to field *i*, as predicted from the *ab initio* calculations, and Φ_{jk} is the *k*-th field on atom *j*.

In minimizing Eq. [A6] the Coulomb integrals, $J_{ij}(r_{ij}^{0})$, are evaluated numerically as discussed in Section 3.2.3. However, since new Coulomb integrals are required at each iteration, we use a coarser grid of $(51)^3$ points for the Simpson's rule integration. The latter was tested and found to yield $J_{ij}(r_{ij}^{0})$ accurate to two decimal places: a sufficient level of accuracy for the minimization of Eq. [A6]. Once the final set of parameters is chosen, Eq. [2.27] is recalculated using a much finer grid as discussed in Section 3.2.3.

Patel *et al.*[53] do not assume a functional form for the $J_{ij}(r_{ij}^{0})$ prior to the minimization. Rather they obtain these elements directly from the minimization of Eq. [A6] and then apply a functional form to reproduce their numerical values. Certainly, our process will be more time consuming since, for each trial ζ_i a number of multiple integrals are required, followed by matrix inversion. However, these calculations are fairly rapid. Banks *et al.*[131] discuss, at length, difficulties in the minimization process. We have not encountered any problems and minimize Eq. [A6] directly. This is partly

due to the small size of the molecule, but we believe that the use of a well-defined Coulomb element from the outset also improves numerical stability.

The optimized zero-field structure has a plane of symmetry defined by C(3), O(2), and H(1). Because of this symmetry plane, the response parameters for H(8) and H(9) should be equal. Likewise, H(5)-H(7) should share the same parameters since, during a simulation, interconversion will occur. We impose this symmetry on the ζ_i, which leaves six independent Slater exponents to vary in turn. The best set of exponents is given in Table 3.2 and the corresponding residual is 4.34 x 10^{-3}.

In principle, the electronegativities are obtained by directly solving Eq. [A4]. However, even with symmetry imposed on the hydrogen ζ_i, Eq. [A4] will not lead to equal $\widetilde{\chi}_i^0$ since the *ab initio* charges are not equal. As a result, we minimize

$$\sum_{i=1}^{N}(\chi_i^0 + \sum_{j=1}^{N} J_{ij}(r_{ij}^0)Q_j^0)^2 \qquad [A7]$$

subject to the constraint of a common electronegativity for H(5), H(6), and H(7) and for H(8) and H(9). The final residual in Eq. [A7] is 7.8 x 10^{-5}.

The final parameters listed in Table 3.2 can be assessed by evaluating the *molecular* polarizability. Following others[53], the polarizability is calculated from

$$\alpha = \frac{1}{3}(\sum_{i=1}^{N}\sum_{j=1}^{N}\Delta x_i J_{ij}^{-1}\Delta x_j + \sum_{i=1}^{N}\sum_{j=1}^{N}\Delta y_i J_{ij}^{-1}\Delta y_j + \sum_{i=1}^{N}\sum_{j=1}^{N}\Delta z_i J_{ij}^{-1}\Delta z_j) \qquad [A8]$$

where Δx_i is the atomic coordinate of atom i relative to the center of geometry. The calculated value is 5.264Å^3, in good agreement with the experimental value[159] of 5.1Å^3.

APPENDIX B
Evaluation of forces

The introduction of a field dependence into the intramolecular potential results in additional force contributions. In this Appendix, we provide the modified equations of motion and the required derivatives of the potential.

The equations of motion for the position of atom α are

$$m_\alpha \frac{d^2\vec{r}_{i\alpha}}{dt^2} = F_{\vec{r}}(\vec{r},Q) - \dot{\eta}_{tr}\vec{p}_{i\alpha} = -\vec{\nabla}_{\vec{r}_{i\alpha}} U - \dot{\eta}_{tr}\vec{p}_{i\alpha}$$

$$= -\frac{\partial U^{el}}{\partial \vec{r}_{i\alpha}} - \frac{\partial U^{\mathrm{LJ}}}{\partial \vec{\mathrm{r}}_{i\alpha}} - \dot{\eta}_{tr}\vec{p}_{i\alpha} - \frac{\partial U^{\mathrm{intra}}}{\partial \vec{\mathrm{r}}_{i\alpha}} - \frac{\partial U^{\mathrm{intra}}}{\partial \vec{E}} \cdot \frac{\partial \vec{E}}{\partial \vec{\mathrm{r}}_{i\alpha}} \qquad \text{[B1]}$$

where m_α is the mass of the atom and the contribution from the extended Lagrangian is included. The second-to-last and last terms on the right capture the explicit and the implicit dependence of the intramolecular potential on the positions. Following Rick *et al.*[46], the equations of motion for the charges are

$$m_Q \frac{d^2 Q_{i\alpha}}{dt^2} = F_Q(\vec{r},Q) - \dot{\eta}_{fq}\vec{p}_{Q;i\alpha} = -\frac{\partial U}{\partial Q_{i\alpha}} + \frac{1}{N_\alpha}\sum_{j=1}^{N_\alpha}\left(\frac{\partial U}{\partial Q_{j\alpha}}\right) - \dot{\eta}_{fq}\vec{p}_{Q;i\alpha}$$

$$= -\frac{\partial U^{el}}{\partial Q_{i\alpha}} + \frac{1}{N_\alpha}\sum_{j=1}^{N_\alpha}\left(\frac{\partial U^{el}}{\partial Q_{j\alpha}} + \frac{\partial U^{\mathrm{intra}}}{\partial \vec{E}} \cdot \frac{\partial \vec{E}}{\partial \mathrm{Q}_{j\alpha}}\right) - \dot{\eta}_{fq}\vec{p}_{Q;i\alpha} - \frac{\partial U^{\mathrm{intra}}}{\partial \vec{E}} \cdot \frac{\partial \vec{E}}{\partial \mathrm{Q}_{i\alpha}} \qquad \text{[B2]}$$

where m_Q is the fictitious mass of the charge and the last term derives from the implicit dependence, via the fields, of the intramolecular potential on atomic charges.

In the evaluation of the field derivatives of the intramolecular potential, we calculate

$$\frac{\partial U^{\text{intra}}}{\partial \vec{E}} = \sum_{coeff} \left(\frac{\partial U^{\text{intra}}}{\partial x^{Damp}} \cdot \frac{\partial x^{Damp}}{\partial x} \cdot \frac{\partial x}{\partial \vec{E}} \right) \qquad [B3]$$

where x is one of the linear parameters from Eqs. [2.31]-[2.33], the sum runs over all coefficients x, and x^{Damp} is the damped value for x (see Eqs. [3.5]-[3.8]). The derivative of the intramolecular potential with respect to the damped coefficients, $\partial U^{\text{intra}} / \partial x^{Damp}$, is obtained directly from Eqs. [2.31]-[2.33]. Consider the derivative of the damped coefficient, x^{Damp}, with respect to x. Beyond the range $[x_{min}, x_{max}]$, the derivative is zero. Within this interval, the derivative of Eqs. [3.6] or [3.7] is taken. Recall that the expressions are equal, and have equal derivatives, when $x=x_{min}$, x_{max}, and $(x_{max}+x_{min})/2$, so that Eqs. [3.5]-[3.8] transition smoothly. The last derivative of Eq. [B3] derives directly from the field-dependence of the expansion coefficients. In other words, this last term vanishes when the intramolecular potential does not depend on the field.

When the expansion coefficients include the multiplicative factor S_y the field-dependence of the potential is obtained from

$$\frac{\partial U^{\text{intra}}}{\partial \vec{E}} = \sum_{coeff} \frac{\partial U^{\text{intra}}}{\partial x'^{Damp}} \cdot \frac{\partial x'^{Damp}}{\partial x'} \cdot \frac{\partial x'}{\partial \vec{E}} = \sum_{coeff} \frac{\partial U^{\text{intra}}}{\partial x'^{Damp}} \cdot \frac{\partial x'^{Damp}}{\partial x'} \cdot \left(AS_y \frac{\partial x}{\partial \vec{E}} + x \frac{\partial (AS_y)}{\partial \vec{E}} \right) \qquad [B4]$$

where we have defined $x' = S_y x$, as a torsion coefficient that enforces proper symmetry. The factor A converts S_y from body-fixed to space-fixed coordinates, and is

$$A = \frac{\vec{E} \cdot [(\vec{r}_C^{\,3} - \vec{r}_O^{\,2}) \times (\vec{r}_O^{\,2} - \vec{r}_H^{\,1})]}{|(\vec{r}_C^{\,3} - \vec{r}_O^{\,2}) \times (\vec{r}_O^{\,2} - \vec{r}_H^{\,1})|} \qquad [B5]$$

with our choice of coordinates. Since the conversion factor is a function of atomic positions, $\partial U^{\text{intra}} / \partial \vec{r}_{i\alpha}$ in Eq. [B1] will also include a contribution from A.

The terms in Eqs. [2.35]-[2.40] are independent of the coordinate system, but their derivatives with respect to the field are not. In particular, the derivatives of the expansion terms required for the evaluation of Eqs. [B3] and [B4] are taken in space-fixed coordinates. We provide only the x-component derivatives below since the y- and z-components can be obtained directly from the expressions provided. For Eq. [2.35], the derivative is

$$\frac{\partial \mid E_H^1 \mid}{\partial E_{Hx}^1} = \frac{E_{Hx}^1}{\mid E_H^1 \mid} \qquad \text{[B6]}$$

where E_{Hx}^1 is the x-component of the field on the atom in question (hydrogen in this case). For Eqs. [2.36] and [2.37], where fields on pairs of atoms are involved, the derivatives are

$$\frac{\partial \mid E_{HO}^{12} \mid}{\partial E_{Hx}^1} = \mid E_O^2 \mid \frac{E_{Hx}^1}{\mid E_H^1 \mid}, \quad \frac{\partial \mid E_{HO}^{12} \mid}{\partial E_{Ox}^2} = \mid E_H^1 \mid \frac{E_{Ox}^2}{\mid E_O^2 \mid}, \qquad \text{[B7]}$$

and

$$\frac{\partial E_{HO}^{12}}{\partial E_{Hx}^1} = E_{Ox}^2, \quad \frac{\partial E_{HO}^{12}}{\partial E_{Ox}^2} = E_{Hx}^1, \qquad \text{[B8]}$$

respectively. For the three-field terms, we have

$$\frac{\partial E_{HOC}^{123}}{\partial E_{Hx}^1} = -(E_{Cx}^3 - E_{Ox}^2), \quad \frac{\partial E_{HOC}^{123}}{\partial E_{Ox}^2} = -2E_{Ox}^2 + E_{Cx}^3 + E_{Hx}^1, \quad \frac{\partial E_{HOC}^{123}}{\partial E_{Cx}^3} = -(E_{Hx}^1 - E_{Ox}^2),$$

[B9]

and

$$\frac{\partial \hat{E}^{123}_{HOC}}{\partial E^{1}_{Hx}} = E^{3}_{Cx} \mid \vec{E}^{2}_{O} \mid^{2} - E^{2}_{Ox}(\vec{E}^{2}_{O} \bullet \vec{E}^{3}_{C}),$$

$$\frac{\partial \hat{E}^{123}_{HOC}}{\partial E^{2}_{Ox}} = 2E^{2}_{Ox}(\vec{E}^{1}_{H} \bullet \vec{E}^{3}_{C}) - E^{1}_{Hx}(\vec{E}^{2}_{O} \bullet \vec{E}^{3}_{C}) - E^{3}_{Cx}(\vec{E}^{1}_{H} \bullet \vec{E}^{2}_{O}), \qquad \text{[B10]}$$

$$\frac{\partial \hat{E}^{123}_{HOC}}{\partial E^{3}_{Cx}} = E^{1}_{Hx} \mid \vec{E}^{2}_{O} \mid^{2} - E^{2}_{Ox}(\vec{E}^{1}_{H} \bullet \vec{E}^{2}_{O}).$$

The derivatives of the four-field term are

$$\frac{\partial E^{1234}_{HOCC}}{\partial E^{1}_{Hx}} = -\mid \vec{E}^{3}_{C} - \vec{E}^{2}_{O} \mid^{2} (E^{4}_{Cx} - E^{3}_{Cx}) + [(\vec{E}^{3}_{C} - \vec{E}^{2}_{O}) \bullet (\vec{E}^{4}_{C} - \vec{E}^{3}_{C})](E^{3}_{Cx} - E^{2}_{Ox})$$

$$\frac{\partial E^{1234}_{HOCC}}{\partial E^{2}_{Ox}} = -2(E^{3}_{Cx} - E^{2}_{Ox})[(\vec{E}^{2}_{O} - \vec{E}^{1}_{H}) \bullet (\vec{E}^{4}_{C} - \vec{E}^{3}_{C})] + \mid \vec{E}^{3}_{C} - \vec{E}^{2}_{O} \mid^{2} (E^{4}_{Cx} - E^{3}_{Cx})$$

$$- (E^{3}_{Cx} + E^{1}_{Hx} - 2E^{2}_{Ox})[(\vec{E}^{3}_{C} - \vec{E}^{2}_{O}) \bullet (\vec{E}^{4}_{C} - \vec{E}^{3}_{C})] + [(\vec{E}^{2}_{O} - \vec{E}^{1}_{H}) \bullet (\vec{E}^{3}_{C} - \vec{E}^{2}_{O})](E^{4}_{Cx} - E^{3}_{Cx})$$

$$\frac{\partial E^{1234}_{HOCC}}{\partial E^{3}_{Cx}} = -2(E^{2}_{Ox} - E^{3}_{Cx})[(\vec{E}^{3}_{C} - \vec{E}^{4}_{C}) \bullet (\vec{E}^{1}_{H} - \vec{E}^{2}_{O})] + \mid \vec{E}^{2}_{O} - \vec{E}^{3}_{C} \mid^{2} (E^{1}_{Hx} - E^{2}_{Ox})$$

$$- (E^{2}_{Ox} + E^{4}_{Cx} - 2E^{3}_{Cx})[(\vec{E}^{2}_{O} - \vec{E}^{3}_{C}) \bullet (\vec{E}^{1}_{H} - \vec{E}^{2}_{O})] + [(\vec{E}^{3}_{C} - \vec{E}^{4}_{C}) \bullet (\vec{E}^{2}_{O} - \vec{E}^{3}_{C})](E^{1}_{Hx} - E^{2}_{Ox})$$

$$\frac{\partial E^{1234}_{HOCC}}{\partial E^{4}_{Cx}} = -\mid \vec{E}^{2}_{O} - \vec{E}^{3}_{C} \mid^{2} (E^{1}_{Hx} - E^{2}_{Ox}) + [(\vec{E}^{2}_{O} - \vec{E}^{3}_{C}) \bullet (\vec{E}^{1}_{H} - \vec{E}^{2}_{O})](E^{2}_{Ox} - E^{3}_{Cx}) \qquad \text{[B11]}$$

The derivatives in Eqs. [B6]-[B11], along with the coefficients in Tables 3.3-3.5, are sufficient to calculate $\partial x / \partial \vec{E}$ in Eqs. [B3] and [B4].

The evaluation of the position and charge derivatives of the electrostatic field are the most time-consuming aspects of the simulation. These derivatives are obtained from the Ewald sums, but since a derivative is required for each atom, the derivatives are *O(N)* more time consuming than the Ewald sums. The field on atom *i* of molecule α is

$$\vec{E}_{i\alpha} = \frac{2\pi}{V} \sum_{\beta=1}^{M} \sum_{j=1}^{N_\beta} \sum_{k} \frac{q_{j\beta}}{k^2} \exp(-\frac{k^2}{4\alpha}) \vec{k} \sin(\vec{k} \bullet \vec{r}_{i\alpha j\beta})$$

$$+\sum_{\beta=1}^{M}\sum_{j=1}^{N_\beta}(1-\delta_{ij}\delta_{\alpha\beta})\sum_k q_{j\beta}\frac{erfc(\alpha r_{i\alpha j\beta})+\frac{2\alpha r_{i\alpha j\beta}}{\sqrt{\pi}}\exp(-\alpha^2 r_{i\alpha j\beta}^2)}{r_{i\alpha j\beta}^3}\vec{r}_{i\alpha j\beta}$$

$$-\sum_{j=1}^{N_\alpha}(1-\delta'_{ij})\frac{q_{j\alpha}}{r_{i\alpha j\alpha}^3}\vec{r}_{i\alpha j\alpha} \qquad \text{[B12]}$$

where the last sum removes the contribution from atoms within the same molecule and separated by less than 4 bonds. δ'_{ij} in the last term is zero for atoms that are separated by four or more bonds, and one otherwise. The derivatives of the *x*-component of this field are

$$\frac{\partial E_{x,i\alpha}}{\partial x_{j\beta}}=(1-\delta_{ij}\delta_{\alpha\beta})\frac{2\pi}{V}\sum_k\frac{q_{j\beta}}{k^2}\exp(-\frac{k^2}{4\alpha})k_x^2\cos(\vec{k}\bullet\vec{r}_{i\alpha j\beta})$$

$$+(1-\delta_{ij}\delta_{\alpha\beta})q_{j\beta}\frac{erfc(\alpha r_{i\alpha j\beta})+\frac{2\alpha r_{i\alpha j\beta}}{\sqrt{\pi}}\exp(-\alpha^2 r_{i\alpha j\beta}^2)}{r_{i\alpha j\beta}^3}$$

$$-(1-\delta_{ij}\delta_{\alpha\beta})3q_{j\beta}\frac{erfc(\alpha r_{i\alpha j\beta})+\frac{2\alpha r_{i\alpha j\beta}}{\sqrt{\pi}}\exp(-\alpha^2 r_{i\alpha j\beta}^2)+\frac{4\alpha^3}{3\sqrt{\pi}}r_{i\alpha j\beta}^3\exp(-\alpha^2 r_{i\alpha j\beta}^2)}{r_{i\alpha j\beta}^5}x_{i\alpha j\beta}^2$$

$$+\delta_{\alpha\beta}(1-\delta'_{ij})(-\frac{q_{j\beta}}{r_{i\alpha j\beta}^3}+3\frac{q_{j\beta}}{r_{i\alpha j\beta}^5}x_{i\alpha j\beta}^2) \qquad \text{[B13]}$$

with the exception of the case where the derivative is with respect to $x_{i\alpha}$. In that case,

$$\frac{\partial E_{x,i\alpha}}{\partial x_{i\alpha}}=-\frac{2\pi}{V}\sum_{\beta=1}^{M}\sum_{j=1}^{N_\beta}\sum_k\frac{q_{j\beta}}{k^2}\exp(-\frac{k^2}{4\alpha})k_x^2\cos(\vec{k}\bullet\vec{r}_{i\alpha j\beta})$$

$$-\sum_{\beta=1}^{M}\sum_{j=1}^{N_\beta}(1-\delta_{ij}\delta_{\alpha\beta})q_{j\beta}\frac{erfc(\alpha r_{i\alpha j\beta})+\frac{2\alpha r_{i\alpha j\beta}}{\sqrt{\pi}}\exp(-\alpha^2 r_{i\alpha j\beta}^2)}{r_{i\alpha j\beta}^3}$$

$$+\sum_{\beta=1}^{M}\sum_{j=1}^{N_\beta}(1-\delta_{ij}\delta_{\alpha\beta})3q_{j\beta}\frac{erfc(\alpha r_{i\alpha j\beta})+\frac{2\alpha r_{i\alpha j\beta}}{\sqrt{\pi}}\exp(-\alpha^2 r_{i\alpha j\beta}^2)+\frac{4\alpha^3}{3\sqrt{\pi}}r_{i\alpha j\beta}^3\exp(-\alpha^2 r_{i\alpha j\beta}^2)}{r_{i\alpha j\beta}^5}x_{i\alpha j\beta}^2$$

$$-\sum_{j=1}^{N_\alpha}(1-\delta'_{ij})(3\frac{q_{j\alpha}}{r_{i\alpha j\alpha}^5}x_{i\alpha j\alpha}^2-\frac{q_{j\alpha}}{r_{i\alpha j\alpha}^3}) \qquad \text{[B14]}$$

The derivative with respect to the *y*-coordinate is

$$\frac{\partial E_{x,i\alpha}}{\partial y_{j\beta}}=(1-\delta_{ij}\delta_{\alpha\beta})\frac{2\pi}{V}\sum_k\frac{q_{j\beta}}{k^2}\exp(-\frac{k^2}{4\alpha})k_x k_y\cos(\vec{k}\bullet\vec{r}_{i\alpha j\beta}) \qquad \text{[B15]}$$

$$-(1-\delta_{ij}\delta_{\alpha\beta})3q_{j\beta}\frac{erfc(\alpha r_{i\alpha j\beta})+\frac{2\alpha r_{i\alpha j\beta}}{\sqrt{\pi}}\exp(-\alpha^2 r_{i\alpha j\beta}^2)+\frac{4\alpha^3}{3\sqrt{\pi}}r_{i\alpha j\beta}^3\exp(-\alpha^2 r_{i\alpha j\beta}^2)}{r_{i\alpha j\beta}^5}x_{i\alpha j\beta}y_{i\alpha j\beta}$$

$$+\delta_{\alpha\beta}(1-\delta'_{ij})3\frac{q_{j\beta}}{r_{i\alpha j\beta}^5}x_{i\alpha j\beta}y_{i\alpha j\beta}$$

with the exception of the case where the derivative is with respect to $y_{i\alpha.}$ In that case,

$$\frac{\partial E_{x,i\alpha}}{\partial y_{i\alpha}}=-\frac{2\pi}{V}\sum_{\beta=1}^{M}\sum_{j=1}^{N_\beta}\sum_k\frac{q_{j\beta}}{k^2}\exp(-\frac{k^2}{4\alpha})k_x k_y\cos(\vec{k}\bullet\vec{r}_{i\alpha j\beta})$$

$$+\sum_{\beta=1}^{M}\sum_{j=1}^{N_\beta}(1-\delta_{ij}\delta_{\alpha\beta})3q_{j\beta}\frac{erfc(\alpha r_{i\alpha j\beta})+\frac{2\alpha r_{i\alpha j\beta}}{\sqrt{\pi}}\exp(-\alpha^2 r_{i\alpha j\beta}^2)+\frac{4\alpha^3}{3\sqrt{\pi}}r_{i\alpha j\beta}^3\exp(-\alpha^2 r_{i\alpha j\beta}^2)}{r_{i\alpha j\beta}^5}x_{i\alpha j\beta}y_{i\alpha j\beta}$$

$$-\sum_{j=1}^{N_\alpha}(1-\delta'_{ij})3\frac{q_{j\alpha}}{r_{i\alpha j\alpha}^5}x_{i\alpha j\alpha}y_{i\alpha j\alpha}\ . \qquad \text{[B16]}$$

Other derivatives of the field can be trivially obtained from the ones provided above.

Field derivatives with respect to charges appear in the equations of motion for the charges, Eq. [B2]. The derivatives are

$$\frac{\partial \vec{E}_{i\alpha}}{\partial Q_{j\beta}} = \frac{2\pi}{V}\sum_{k}\frac{1}{k^2}\exp(-\frac{k^2}{4\alpha})\vec{k}\sin(\vec{k}\bullet\vec{r}_{i\alpha j\beta})$$

$$+(1-\delta_{ij}\delta_{\alpha\beta})\frac{erfc(\alpha r_{i\alpha j\beta})+\frac{2\alpha r_{i\alpha j\beta}}{\sqrt{\pi}}\exp(-\alpha^2 r_{i\alpha j\beta}^2)}{r_{i\alpha j\beta}^3}\vec{r}_{i\alpha j\beta}$$

$$-\delta_{\alpha\beta}(1-\delta'_{ij})\frac{1}{r_{i\alpha j\beta}^3}\vec{r}_{i\alpha j\beta} \qquad \text{[B17]}$$

when $j\beta \neq i\alpha$. The derivative vanishes when $j\beta = i\alpha$. That is,

$$\frac{\partial \vec{E}_{i\alpha}}{\partial Q_{i\alpha}} = 0\,. \qquad \text{[B18]}$$

APPENDIX C
Details of the potentials for 2-propanol

Semi-flexible models for 2-propanol developed in this work are described herein. Models for other solvents and the selectors can be found elsewhere[112, 161, 181].

The intramolecular potential, which dictates the energetic costs for changes in molecular conformations, consists of four parts: bond stretching, angle bending, dihedral torsion, and improper torsion. These potentials are listed in Eqs. [2.7]-[2.10]. In this work, all bonds of 2-propanol are kept fixed using the Rattle algorithm[83] during the simulations, and 19 bends and 3 torsions are employed to represent the molecular flexibility. The equilibrium bond angles are obtained from the global energy minimum and bending potentials are obtained by least squares fits of Eq. [2.8] to nine energy calculations, where the angle is varied within sixteen degrees of the equilibrium value. As shown in Eq. [2.9], the torsions are represented by modified Ryckaert-Bellemans[189] potentials. Each torsional potential is extracted from 36 B3LYP/aug-cc-pVDZ calculations as the angle is varied from zero to 360 degrees, in steps of 10 degrees.

Initial atomic positions and CHELPG charges[110] are extracted from B3LYP/aug-cc-pVDZ global energy minimum. For the nonbonding potential parameters, the CHARMM parameters for Lennard-Jones (LJ) potential and CHELPG charges from the *ab initio* global minimum are applied.

The parameterization of the fluctuating charge model has been discussed in detail in Chapter 3. Briefly, the molecule was placed in 30 diverse fields and atomic charges were evaluated by the CHELPG algorithm applied to B3LYP/aug-cc-pVDZ calculations. Based on the fitting of the molecular response, the $\tilde{\chi}_i^0$ and J_{ii}^0 parameters were extracted. Similar to the findings for ethanol in Chapter 3, the atomic electronegativities derived specifically for 2-propanol were larger than the transferrable CHARMM-FC values[53] for most atoms. All electronic structure calculations are performed using the Gaussian 03 program[135].

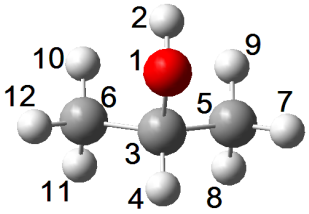

LJ and FC parameters

Atom No.	Atom	σ(Å)	ε (kJ/mol)	CHARMM J_{ii}^0 (kcal/mol·|e|^2)	J_{ii}^0 (this work) (kcal/mol·|e|^2)	CHARMM $\tilde{\chi}_i^o$ (kcal/mol·|e|)	Shifted $\tilde{\chi}_i^o$ (kcal/mol·|e|)	$\tilde{\chi}_i^o$ (this work) (kcal/mol·|e|)	Q_i^0 (|e|)
1	O	0.312	0.7113	307.20	317.07	364.85	101.66	107.41	-0.685
2	H	0.05	0.1000	517.26	544.06	263.19	0.00	0.00	0.369
3	C	0.35	0.2761	196.88	212.95	306.79	43.60	71.68	0.591
4	H	0.25	0.1255	501.42	470.07	319.83	56.64	66.18	-0.084
5	C	0.35	0.2761	240.34	283.89	319.65	56.46	66.16	-0.298
6	C	0.35	0.2761	240.34	283.89	319.65	56.46	66.16	-0.298
7	H	0.25	0.1255	501.42	576.59	315.56	52.37	50.94	0.067
8	H	0.25	0.1255	501.42	576.59	315.56	52.37	50.94	0.067
9	H	0.25	0.1255	501.42	576.59	315.56	52.37	50.94	0.067
10	H	0.25	0.1255	501.42	576.59	315.56	52.37	50.94	0.067
11	H	0.25	0.1255	501.42	576.59	315.56	52.37	50.94	0.067
12	H	0.25	0.1255	501.42	576.59	315.56	52.37	50.94	0.067

Angle bending

Angle	θ(deg)	k_θ(kJ·mol^{-1}·deg^{-2})
3,1,2	108.81	0.065813
4,3,1	108.80	0.090213
5,3,1	108.72	0.121507
6,3,1	108.72	0.121507
5,3,4	108.81	0.077831
6,3,4	108.81	0.077831
6,3,5	112.87	0.107790
7,5,3	110.56	0.066107
8,5,3	110.56	0.066107
9,5,3	110.56	0.066107
8,5,7	108.36	0.060220
9,5,7	108.36	0.060220
9,5,8	108.36	0.060220
10,6,3	110.56	0.066107
11,6,3	110.56	0.066107
12,6,3	110.56	0.066107
11,6,10	108.36	0.060220
12,6,10	108.36	0.060220
12,6,11	108.36	0.060220

Torsions

Torsion	c0, c1, c2, c3, c4, c5, c6 (kJ/mol)
2,1,3,4	7.76,1.89,6.06,10.76,-4.56,-0.94,2.44
1,3,5,7	6.66,-20.53,2.04,28.26,-7.61,-0.96,5.68
1,3,6,10	6.66,-20.53,2.04,28.26,-7.61,-0.96,5.68